METAL OXIDE NANOSTRUCTURES AND THIN FILMS FOR SUSTAINABLE ENERGY APPLICATIONS

Ph.D. Thesis

By

VISHESH MANJUNATH

DEPARTMENT OF METALLURGY ENGINEERING AND MATERIALS SCIENCE

INDIAN INSTITUTE OF TECHNOLOGY INDORE

JULY, 2022

METAL OXIDE NANOSTRUCTURES AND THIN FILMS FOR SUSTAINABLE ENERGY APPLICATIONS

A THESIS

Submitted in partial fulfillment of the requirements for the Award of the degree of

DOCTOR OF PHILOSOPHY

By

VISHESH MANJUNATH
(PHD1701105002)

DEPARTMENT OF METALLURGY ENGINEERING AND MATERIALS SCIENCE
INDIAN INSTITUTE OF TECHNOLOGY INDORE
JULY, 2022

INDIAN INSTITUTE OF TECHNOLOGY INDORE

CANDIDATE'S DECLARATION

I hereby certify that the work which is being presented in the thesis entitled **"METAL OXIDE NANOSTRUCTURES AND THIN FILMS FOR SUSTAINABLE ENERGY APPLICATIONS"** in the partial fulfillment of the requirements for the award of the degree of **DOCTOR OF PHILOSOPHY** and submitted in the **DEPARTMENT OF METALLURGY ENGINEERING AND MATERIALS SCIENCE, INDIAN INSTITUTE OF TECHNOLOGY INDORE**, is an authentic record of my own work carried out during the time period from July, 2017 to July, 2022 under the supervision of Dr. Rupesh S. Devan and Prof. Parasharam M. Shirage, Department of Metallurgy Engineering and Materials Science.

The matter presented in this thesis has not been submitted by me for the award of any other degree of this or any other institute.

Vishesh 02/12/2022

Signature of the student with date

(VISHESH MANJUNATH)

This is to certify that the above statement made by the candidate is correct to the best of my/our knowledge.

Rupesh 2/12/2022

Signature of Thesis Supervisor 1

(Dr. RUPESH S. DEVAN)

2/12/2022

Signature of Thesis Supervisor 2

(Prof. PARASHARAM M. SHIRAGE)

VISHESH MANJUNATH has successfully given his/her Ph.D. Oral Examination held on 2/12/2022

Rupesh 2/12/2022

Signature of Thesis Supervisor 1

(Dr. RUPESH S. DEVAN)

2/12/2022

Signature of Thesis Supervisor 2

(Prof. PARASHARAM M. SHIRAGE)

ACKNOWLEDGEMENTS

I express my sincere thanks to the PSPC (Ph.D. Student Progress Committee) members, Dr. Santosh S. Hosmani (Associate Professor, Department of Metallurgy Engineering and Materials Science) and Dr. Bhargav Vaidya (Assistant Professor, Department of Astronomy, Astrophysics and Space Engineering) for their continuous observation and valuable suggestions to improve the quality of my Ph.D. work. I also thank Dr. Hosmani and Dr. Sunil Kumar (Associate Professor, Department of Metallurgy Engineering and Materials Science) for their valuable suggestions and direct access to their laboratory during my experimental work. I am thankful to Prof. Preeti Bhobe (Department of Physics) and Dr. Somaditya Sen (Associate Professor, Department of Physics) for their help in EXAFS analysis and light sensing studies, respectively. I would also like to thank Dr. Umesh Kshirsagar for his valuable discussions. I extend my gratitude to Dr. Ram Janay Choudhary, UGC-DAE Indore, for timely access to experimental facilities.

I acknowledge the IIT Indore for providing me the financial support under the Teaching Assistantship (TA) category during the entire course of my doctoral work. I wish to thank the Department of Metallurgy Engineering and Materials Science and Sophisticated Instruments Center (SIC) IIT Indore for providing access to various experimental and characterization facilities to complete this research work. I am thankful to Mr. Mayur Dhake for helping me with many technical and non-technical works. Further, I would like to thank all individuals from the support staff of IIT Indore who directly or indirectly contributed to my Ph.D. work.

I am thankful to my colleagues from Nano-architectures Research Group, Dr. Parvez A. Shaikh, Mr. Santosh Bimli, Ms. Sameena Mulani, Mr. Rajender Bunkar, Ms. Manopriya Samtham, Ms. Ekta Choudhary, and Mr. Siddhant Sharma for their company and help during my Ph.D. work. I am also thankful to all my past colleagues from the Nano-architectures Research Group for their constant encouragement and contribution to accomplishing my Ph.D. work. I would also like to thank my seniors and friends from IIT Indore for their company during my Ph.D. work

I would like to thank my co-supervisor, Prof. Parasharam M. Shirage, for his valuable suggestions, guidance, and complete access to his laboratory throughout my Ph.D.

I would like to express my gratitude to my thesis supervisor Dr. Rupesh S. Devan, for his intellectual guidance and encouragement during my Ph.D. I have sincerely benefitted a lot from his valuable suggestions and advice. Apart from my research, I am thankful to him for shaping me into a better human. His support, encouragement, and trust mean a lot to me.

Most importantly, the credit for this all goes to my grandparents (Mrs. Shradhamma Krishnamurthy and Mrs. Vasanti Krishnan) and parents (Mrs. Late Malini and Mr. Manjunath) for making me what I Am today. I would like to thank my family member, Mrs. Rajarajeshwari Mukund, for always supporting me. I would also like to thank my friend Ms. Likhi Dhruv for being an integral part of my Ph.D. I would also like to mention my friends Mr. Salla Nithyanth, Mr. Mohammed Hussain, Mr. Chethan Kandekar, Mr. Himmat Singh Verma, Mr. Goraksh Soni, Mr. Anup Sharma, and Mr. Vinod Chuahan for their support during my Ph.D.

(Vishesh Manjunath)

5th November 2022

Dedicated

To my parents

Mrs. Late Malini & Mr. Manjunath

LIST OF PUBLICATIONS

PAPER-1

V. Manjunath, Y. K. Reddy, S. Bimli, R. J. Choudhary, and R. S. Devan, "22% efficient Kusachiite solar cells of $CuBi_2O_4$ light harvester and ABO_3 buffer layers: A theoretical analysis," ***Mater. Today Commun. 32 (2022)*** **104061).**

PAPER-2

V. Manjunath, S. Bimli, R. Biswas, P. N. Didwal, K. K. Haldar, M. Mahajan, N. G. Deshpande, P. Bhobe, and R. S. Devan, "Experimental investigations on morphology controlled bifunctional NiO nano-electrocatalysts for oxygen and hydrogen evolution," (***Int. J. Hydrog. Energy 47 (2022)*** **39018-39029).**

PAPER-3

V. Manjunath, P. K. Mishra, R. Dobhal, S. Bimli, P. M. Shirage, S. Sen, P. A. Shaikh, and R. S. Devan, "Perovskite-based facile $NiO/CH_3NH_3PbI_3$ heterojunction self-powered broadband photodetector," (***ACS Appl. Electron. Mater. 3 (2021)*** **4548-4557).**

PAPER-4

V. Manjunath, S. Bimli, K. H. Parmar, P. M. Shirage, and R. S. Devan, "Oxidized Nickel films as highly transparent HTLs for inverted planar perovskite solar cells," (***Sol. Energy 193 (2019)*** **387-394).**

PAPER-5

V. Manjunath, S. Bimli, D. Singh, R. Biswas, P. N. Didwal, K. K. Haldar, N. G. Deshpande, P. Bhobe, and R. S. Devan, "Porous nanorods by stacked NiO nanoparticulate exhibiting corn like structure for sustainable environmental and energy applications," ***(Sust. Energy Fuels (2022)*** **Under review).**

LIST OF PUBLICATIONS (Other than the thesis)

1. **V. Manjunath**, S. Bimli, P. A. Shaikh, S. Ogale, and R. S. Devan, "Understanding the role of inorganic carriers transport layer materials and interfaces in emerging perovskites solar cells", **(*J. Mater. Chem. C 10 (2022)* 15725-15780)**

2. M. Alla, **V. Manjunath,*** E. Choudhary,* M. Samtham, S. Sharma, P. A. Shaikh, M. Rouchdi, B. Fares, "Evaluating the potential of lead-free Cs_2BiAgI_6-based double perovskite solar cell," **(*Phys. Status Solidi A: Accepted* DOI: 10.1002/pssa.202200642)**

3. Y. K. Reddy, **V. Manjunath**, S. Bimli, R. S. Devan, "Futuristic kusachiite solar cells of $CuBi_2O_4$ absorber and metal sulfide buffer Layers: Theoretical efficiency approaching 28 %", **(*Sol. Energy 244 (2022)* 75-83)**

4. S. C. Yadav, **V. Manjunath**, A. Srivastava, R. S. Devan, and P. M. Shirage, "Stable lead-free $Cs_4CuSb_2Cl_{12}$ layered double perovskite solar cells yielding theoretical efficiency close to 30%", **(*Opt. Mater. (2022)* 112676).**

5. M. Alla, S. Bimli, **V. Manjunath,*** M. Samtham, A. Kasaudhan, E. Choudhary, M. Rouchdi, and F. Boubker, "Towards lead-free all-inorganic perovskite solar cell with theoretical efficiency approaching 23%," **(*Mater. Technol. (2022)* 1-7).**

6. S. C. Yadav, A. Srivastava, **V. Manjunath**, A. Kanwade, R. S. Devan, and P. M. Shirage, "Properties, performance and multidimensional applications of stable lead-free $Cs_2AgBiBr_6$ double perovskite," **(*Mater. Today Phys. 26 (2022)* 100731).**

7. M. Alla, **V. Manjunath,*** N. Chawki, D. Singh, S. C. Yadav, M. Rouchdi, and F. Boubker, "Optimized $CH_3NH_3PbI_{3-X}Cl_X$ based perovskite solar cell with theoretical efficiency exceeding 30%", **(*Opt. Mater. 124 (2022)* 112044**).

8. N. Jain, A. Mary, **V. Manjunath,** R. Sakla, R. S. Devan, D. A. Jose, and A. R. Naziruddin, "Ruthenium (II) Complexes Bearing Heteroleptic Terpyridine Ligands: Synthesis, Photophysics and Solar Energy Conversion," **(*Eur. J. Inorg. Chem. 2021 (2021)* 5014-5023).**

9. K. H. Parmar, **V. Manjunath,** S. Bimli, P. R. Chikate, R. A. Patil, Y. R. Ma, and R. S. Devan, "Stable and reversible electrochromic behaviors in anodic NiO thin films," **(*Chinese J. Phys. 77 (2022)* 143-150).**

10. N. Jain, A. Mary, **V. Manjunath,** R. Sakla, R. S. Devan, D. A. Jose, and A. R. Naziruddin, "Ruthenium complexes bearing *N*-heterocyclic carbene based CNC and $CN^{\wedge CH_2}C$' pincer ligands: Photophysics, electrochemistry, and solar energy conversion", **(*J. Organomet. Chem. 959 (2022)* 122203).**

Table of Contents

LIST OF FIGURES

LIST OF TABLES

NOMENCLATURE

A	A.E.M	Adsorbate Evolution Mechanism
	A.L.D	Atomic Layer Deposition
B	BET	Brauner-Emmett-Teller
	BHJ	Bulk Hetro-junction
	BJH	Barrett-Joyner-Halenda
	BSO	Barium Stannate
	BTO	Barium Titanate
	BE	Binding Energy
C	CA	Chronoamperometry
	CBm	Conduction Band Minimum
	CBO	Copper Bismuth Oxide
	C_{dl}	Double Layer Capacitance
	CO_2	Carbon di-oxide
	C_s	Specific Capacitance
	CV	Cyclic Voltammetry
D	D^*	Detectivity
	DI	Deionized
	DSSC	Dye-Sensitized Solar Cell
E	ECSA	Electrochemically Active Surface Area
	EDS	Energy Dispersive Spectroscopy
	EIS	Electrochemical Impedance Spectroscopy
	ETL	Electron Transport Layer
	EXAF	Extended X-Ray Absorption Fine Structure
	eV	Electron Volt
F	FESEM	Field Emission Scanning Electron Microscopy
	FF	Fill Factor
	FTO	Fluorine doped Tin Oxide
G	GCD	Galvanostatic charge-discharge
	GofF	Goodness of fit factor
H	HER	Hydrogen Evolution Reaction
	HTL	Hole Transport Layer
	HTM	Hole Transport Material
I	ICSD	Inorganic Crystallographic Database
	I_{Photo}	Photo Current
	I_{SC}	Short Circuit Current
J	J_{SC}	Short Circuit Current Density
L	L_d	Diffusion Length
	LDR	Linear Dynamic Range

	LSV	Linear Sweep Voltammetry
M	MAPI	Methyl ammonium lead tri-iodide
	MOTL	Metal Oxide Transport Layer
N	NEP	Noise Equivalent Power
	NiO	Nickel Oxide
O	OER	Oxygen Evolution Reaction
	1D	One-dimensional
P	PD	Photodetector
	PHJ	Planar Hetero Junction
	P_{in}	Incident Power
	PL	Photoluminescence
	PO	Perovskite Oxide
	PCE	Power Conversion Efficiency
	PV	Photovoltaic
R	R	Responsivity
	R_{ct}	Charge transfer resistance
	RE	Reference Electrode
S	S	Sensitivity
	SAED	Selected Area Electron Diffraction
	SAXS	Small Angle X-Ray Scattering
	SCAPS-1D	Solar Cell Capacitance Simulator-1D
	SCE	Saturated Calomel Electrode
	SnO_2	Tin oxide
	SSO	Strontium Stannate
	STO	Strontium Titanate
T	T	Tolerance Factor
	TEM	Transmission electron microscopy
	T_f	Fall time
	TiO_2	Titanium dioxide
	T_r	Rise Time
	2D	Two-dimensional
V	VBM	Valence Band Maximum
	V_{OC}	Open Circuit Voltage
W	WE	Working Electrode
X	XANES	X-Ray Adsorption Near Edge Structure
	XPS	X-Ray Photoelectron Spectroscopy
	XRD	X-Ray Diffraction
Z	ZnO	Zinc Oxide
	0D	Zero-dimensional

Chapter 1
Introduction

1.1 Overview of sustainable energy

Over the last five decades, rapid industrialization has led to human behavioral changes consuming high energy. The prediction shows that the global energy demand in 2050 will be 30 TW, which is expected to upsurge further to 46 TW by 2100.[1] The increased energy consumption will support economic development; however, it will give rise to greenhouse gas emissions and other issues, which the scientific and industrial community should focus on for controlling environmental pollution, global warming, and other allied problems. Therefore, various approaches are adopted toward sustainability with many arguments and/or agreements, but the balance between energy production, consumption, and carbon emission is the only promising way for a safe, cleaner, and sustainable future. With ever-increasing energy demand, conventional energy sources such as coal, oil, natural gas, etc., are not sustainable to reach the expectations. Therefore, renewable and sustainable energy sources need to be extensively inspected.[2] Though renewable energy is one of the prime solutions which scientists and industry are predominantly exploring, harnessing efficiencies beyond a certain limit has been critical until now. Even after knowing it, the scientific community is putting endless efforts into either developing new technologies or updating the existing ones to expand the horizons for further improvement in efficiency. Overall, excellent renewable energy harnessing technologies can administer future massive energy demand.

Of the several available renewable energy systems, producing hydrogen fuel through water splitting and generating electricity from sunlight using photovoltaic (PV) cells are two prominent approaches that render minimal carbon emissions have attracted the scientific and industrial communities. The low environmental footprint, high gravimetric energy density, and abundance of a hydrogen source signify the advantages of hydrogen as an energy carrier. Electrocatalysis, being efficient and cost-effective, is the most preferred process compared to photocatalysis for splitting water into oxygen and hydrogen fuel. This green hydrogen fuel can be stored and distributed to chemical industries to produce electricity (through fuel cells) without generating post-combustion pollutants. However, using hydrogen as fuel requires appropriate preparedness due to its low volumetric energy density causing safety issues. Therefore, generating electricity from sunlight using the *pn* junctions PV cells is one of the safest and top-notch for scientists and

industrialists. These PV cells have a high power-to-weight ratio, large-scale handling capabilities, and zero or minimal pollution (due to post-operational waste). The photocarriers generated after exposing PV cells to sunlight are later separated to produce current and voltage in the device connected across the appropriate resistive load. The performance of the PV cells is determined by evaluating how efficiently the incident sunlight is converted into electrical energy. However, the efficiency has severely controlled the interfaces in the *pn* junction, the defect density in the material, photoconversion in the material, etc. Nevertheless, maintenance of PV cells during operation, in terms of the dusting of PV panels and protection from harsh environments, requires frequent monitoring.

Overall, water electrolysis and PV systems have the most negligible carbon footprint compared to other renewable technologies. Though the time of sunshine is limited on a particular day, the excess energy from PV panels can be stored in the form of hydrogen fuel when PV panels and water electrolyzers work in tandem, i.e., the electrical output from the PV panels can be fed as input to water electrolyzers to produce hydrogen fuel which can be converted back to electricity on requirement using fuel cells or internal combustion engines. In this process, electrocatalytic water splitting and PV panels do not release carbon into the environment but keep the promise of sustainable energy generation.

Similar to solar cells, photodetectors are *pn*-junction diodes that convert photons into electrical signals giving rise to various modern applications. Ideally, a photodetector instantaneously transforms every photon of the incident optical signal into a free electron, making photocurrent linearly proportional to the incident signal. However, due to practical difficulties in efficient absorption and carrier collection, every incident photon cannot create an electron. The detection wavelength is purely dependent on the properties of the materials used in the photodetector. Consequently, depending on the application, the photodetectors are designed for particular wavelengths or can be tuned for bands of wavelengths. The self-powered photodetectors enable self-powered photodetection to render applications in remote locations without external power. Notably, the self-powered photodetectors can be used with PV panels to monitor the intensity of incident light, calculate the amount of power generated in the solar cells, and align the PV panels to be approaching the sunlight depending on the day and month of the year. Overall, the

photodetectors, PV panels, and electrocatalytic hydrogen generation will be efficient approaches to serve future energy demands in a sustainable manner.

1.2 Sustainable energy applications

Green energy sources play an important role in sustainable energy distribution and controlling the environmental impact. Over the last decade, PV panel installation has drastically increased for water desalination, green hydrogen production, and heat and electricity generation. Similarly, water electrolysis to generate green hydrogen fuel is an important technology for a sustainable future.

1.2.1 Water splitting for hydrogen generation

Presently, 95% of global hydrogen is generated by natural gas or fossil fuels.[3] Industrially processed hydrogen results in low purity with carbonaceous by-products. Therefore, high-quality green hydrogen is produced by sustainable means of water splitting through electrocatalytic and photocatalytic processes. Electrocatalytic water splitting is the most promising approach, in which oxygen evolution reaction (OER) and hydrogen evolution reaction (HER) is pivotal to determining the performance. These two half-reactions, OER and HER, took place at the anode and cathode, respectively. The reaction in an acidic medium is expressed as:

$$Cathode: 2H^+ + 2e^- \leftrightarrow H_2 \quad (1.1)$$

$$Anode: H_2O \leftrightarrow 2H^+ + \frac{1}{2} O_2 + 2e^- \quad (1.2)$$

and in the neutral and alkaline medium as:

$$Cathode: 2H_2O + 2e^- \leftrightarrow H_2 + 2OH^- \quad (1.3)$$

$$Anode: 2OH^- \leftrightarrow H_2O + \frac{1}{2} O_2 + 2e^- \quad (1.4)$$

For these reactions to happen, the thermodynamic standard equilibrium voltage of water splitting is 1.229 V at 298 K, P = 1 atm, and pH = 0. The applied voltages are usually higher than the equilibrium voltages to accomplish electrochemical water splitting. Therefore, overpotential is applied to overcome the intrinsic activation barrier at the anode (η_a), cathode (η_c), and other resistive drops (η_{other}). Thus, total operational potential (E_{op}) is expressed as

$$E_{op} = 1.23\ V + \eta_a + \eta_c + \eta_{other} \quad (1.5)$$

Where, η_a and η_c can be optimized by using efficient oxygen and hydrogen evolution catalyst. This indicates that reduced overpotentials for water splitting can make hydrogen production more economical.

(a) HER mechanism

The most widely accepted HER pathways are either Volmer–Heyrovsky or Volmer-Tafel for electrochemical adsorption and desorption, respectively, represented below,

(i) Electrochemical adsorption (Volmer reaction)

$$H^+ + M^+ + e^- \leftrightarrow \mathrm{M} - H^* \ (acidic) \quad (1.6)$$

$$H_2O + M^+ + e^- \leftrightarrow \mathrm{M} - H^* + OH^- \ (alkaline) \quad (1.7)$$

(ii) Electrochemical desorption (Heyrovsky reaction)

$$\mathrm{M} - H^* + H^+ + e^- \leftrightarrow M^* + H_2 \ (acidic) \quad (1.8)$$

$$\mathrm{M} - H^* + H_2O + e^- \leftrightarrow M^* + OH^- + H_2 \ (alkaline) \quad (1.9)$$

(iii) Chemical desorption (Tafel reaction)

$$2\mathrm{M} - H^* \leftrightarrow 2M^* + H_2 \ (acidic\ and\ alkaline) \quad (1.10)$$

where M-H* represents chemically adsorbed an H atom on a single active site of the electrode surface (M). Even though two pathways, in acidic and alkaline mediums, are used to express the hydrogen evaluation, still reactants and products vary depending on the *pH* of the reaction solution.

(b) OER mechanism

OER mechanism is comprised of four proton and electron transfer steps. The adsorbate evolution mechanism (AEM) is the most widely accepted pathway. OER on a single metal site of metal oxide (M*) is expressed as:

In an acidic solution:

$$H_2O + M^* \leftrightarrow \mathrm{M} - \mathrm{O}H^* + H^+ + e^- \quad (1.11)$$

$$\mathrm{M} - \mathrm{O}H^* \leftrightarrow \mathrm{M} - O^* + H^+ + e^- \quad (1.12)$$

$$\mathrm{M} - O^* + H_2\mathrm{O} \leftrightarrow \mathrm{M} - \mathrm{O}\mathrm{O}H^* + H^+ + e^- \quad (1.13)$$

$$\mathrm{M} - \mathrm{O}\mathrm{O}H^* \leftrightarrow \mathrm{M} + O_2 + H^+ + e^- \quad (1.14)$$

In alkaline solution:

$$\mathrm{O}H^- + M^* \leftrightarrow \mathrm{M} - \mathrm{O}H^* + e^- \quad (1.15)$$

$$\mathrm{M} - \mathrm{O}H^* + \mathrm{O}H^- \leftrightarrow \mathrm{M} - O^* + H_2O + e^- \quad (1.16)$$

$$M - O^* + OH^- \leftrightarrow M - OOH^* + e^- \quad (1.17)$$

$$M - OOH^* + OH^- \leftrightarrow M^* + O_2 + H_2O + e^- \quad (1.18)$$

The OER performance of the electrocatalyst depends on the bonding strength of the absorbents on the M site.

1.2.2 Photodetectors

Photodetectors convert photon flux into electrical signals. Photodetectors with lateral and vertical types of device architectures are in demand for a variety of applications. The active layer of photodetectors is formed by constructing a homo-junction, planar heterojunction (PHJ), or bulk heterojunction (BHJ).[4] Photodetectors consisting of inorganic materials (i.e., metal oxides) in combination with perovskite materials exhibit broadband spectral response and improved performances due to the formation of perovskite/metal oxide heterojunctions which facilitate exciton dissociation and charge-carrier transport. Photodetectors possessing vertical structure with their active layer sandwiched between electrodes, known as photodiode configuration, can be categorized as conventional and inverted configurations, in which the presence of interface layers effectively reduces the dark current and obtain high detectivity accompanied by small noise equivalent power (NEP) and large linear dynamic range (LDR). In photodiodes with the PV effect, an absorbed photon can generate, at best, one electron-hole pair with a quantum efficiency of less than 100%, codetermined by photon-harvesting, exciton dissociation, charge-carrier transport, and collection efficiency.[5] The collection of photogenerated carriers is controlled by the built-in potential due to the different work functions of the two electrodes. An additional reverse bias is often applied to increase the charge collection efficiency. However, the self-powered configuration is refereed when the photodetectors work at 0 bias.

1.2.3 Solar Cells

Among all the renewable energy resources and harvesting approaches, solar energy conversion into electrical energy has shown promise for sustainable development.[6] Solar cells are devices that convert incoming light energy into usable electrical energy. Although myriad efforts have been undertaken in the past 50 years to

achieve high power conversion efficiency (PCE) through different solar cell designs and architectures, a knowledge gap still persists in the comprehensive understanding of how different material interfaces can affect the overall advancement of solar cell technology.[7] The silicon-based solar cell is one of the earliest solar cells making use of crystalline silicon with a bandgap of 1.11 eV, which is well-positioned in the optimum range for wide light absorption. At present, first-generation silicon solar cells continue to show dominance, with significant progress toward high PCE due to the well-matured fabrication technology and earth abundance of the material concerned.[8] Recent oversupply against the demand has also reduced the areal costs of other involved materials, and improved yields have dropped the price of PV technology below the projection.[9] Moreover, over the years, various materials like amorphous-Si, GaAs, CdTe, CIGS, etc., have been successfully deposited and optimized into thin films of required thickness and are used as absorbers in second-generation solar cells to combat this problem further. The advantages of these second-generation solar cells are low production cost, flexibility, lightweight, etc.[10] During the last couple of decades, third-generation solar cells based on nanocrystals, polymers, sensitized dyes, and organic-inorganic perovskites have shown tremendous progress bringing in a high degree of novelty and versatility in both the design of new materials and solar cell architectures.[11-14] Specifically, the emerging perovskite solar cells (PSCs) have gained enormous interest in the last decade, with the corresponding conversion efficiency (~25 %) competing with the first-generation silicon counterparts.[15] Also, the newly introduced perovskite/Si tandem cells are already delivering a remarkable efficiency of 29.5% (Fig. 1.1, Referred from the NREL website).

Hybrid Perovskites are molecularly assembled organic-inorganic compounds that absorb incoming light energy efficiently across a significant portion of the solar spectrum. They can be highly tuned to generate various desired optical and optoelectronic properties. These Organo-inorganic perovskite materials form the ABX_3 structure, where A represents the organic cation (like $CH_3NH_3^+$, Cs^+, etc.), B represents the divalent metal (namely Pb^{2+}, Sn^{2+}, etc.), and X being the halogen (Cl^-, I^-, Br^-). The size of these three ions is strictly confined by the tolerance factor (T) for a stable perovskite structure.[16]

Moreover, the perovskite light absorbers possess a high absorption coefficient in the visible region (~350 to 800 nm), high extinction coefficient (~104 cm^{-1} at 550 nm), long charge diffusion lengths, and ease of processing, which have led to the fabrication of low-cost PSCs at room temperature consuming less amount of material.[17] These intrinsic properties of perovskite light absorbers can be tailored to meet the requirements by merely substituting the ions in the perovskite materials.[18] However, other than the perovskite light absorbers, transport layers have equal importance in solar cell designs to render high efficiency and stability.

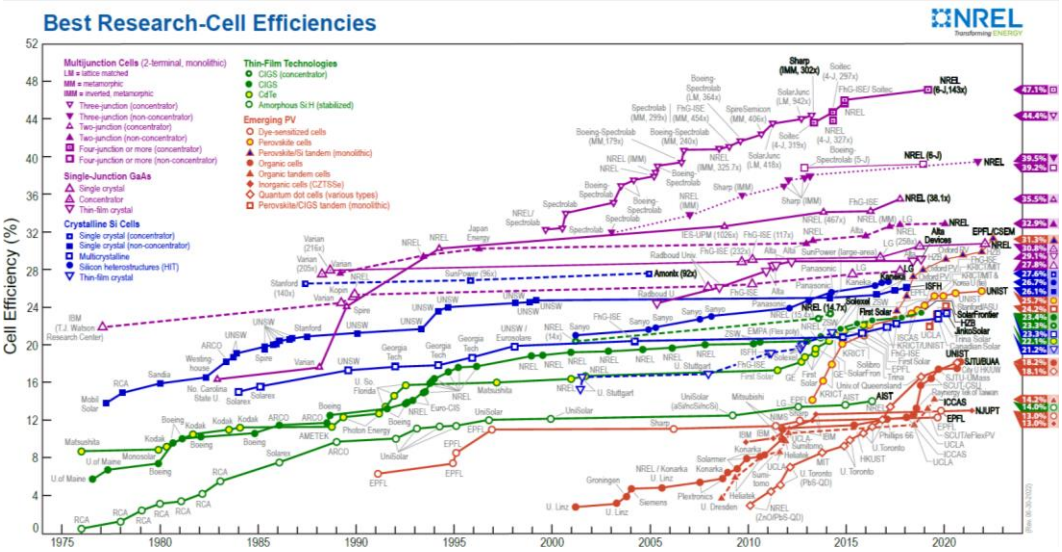

Figure 1.1 Best efficiencies report for various generation of solar cells. (Source, NREL website).

Two carrier-selective transport layers are required to achieve effective carrier extraction at both external terminals. These transport layers preferably perform selective charge carrier extraction (i.e., n- or p-type) by blocking the transport of the other (i.e., p- or n-type). The first deposition of the p or n-type transport layer on the light exposure side of the solar cell, followed by the intrinsic layer, configures the device as the conventional negative-intrinsic-positive (n-i-p) and inverted positive-intrinsic-negative (p-i-n). From the conceptual point of view, both (n-i-p) and (p-i-n) device architectures should give the same efficiency, but it differs due to optical properties, transmittance in the UV-Vis-NIR region, materials compatibility, and its ohmic contact formation

with a transparent side of the electrode. Additionally, investigation on inverted (p-i-n) architecture that alters optical behavior is also reported in the literature.[19] After all, the recombination process involves both types of carriers present within the proximity of charge diffusion length, and the extraction of a particular type of charge carrier at different ends will reduce the recombination. However, other various qualities such as high conductivity for selected carrier type, reducing unfavorable effect at interfaces, closely matching mobilities of charge carriers, tuning bandgap for smooth charge transfer, etc., of interfacial charge carrier type selective transport layers contributed to high efficiency from PSCs

(a) Importance of transport layers

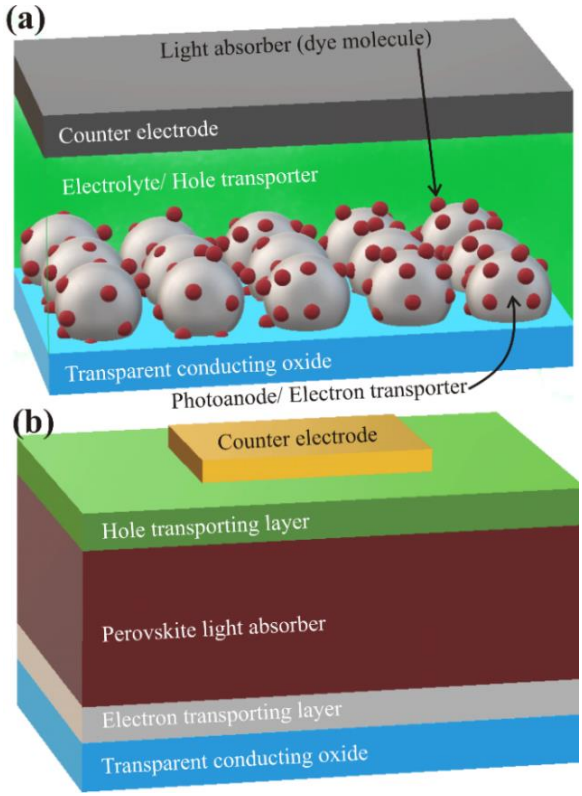

Figure 1.2 Schematics representation of (a) dye-sensitized solar cell (i.e., DSSC) and (b) perovskite solar cells (i.e., PSC).

Transport layers in PSCs perform specific functionalities akin to the functionalities in dye-sensitized solar cells (DSSCs) (Fig. 1.2). The term 'division of labor' has been widely used to understand the functionalities of each component in PSCs.[20] The functionalities of basic components for

PSC include (i) Perovskite light absorber: To absorb the majority of the solar spectrum and create electron-hole pairs, (ii) Transport layers: To selectively dissociate the excitons generated in the light absorber, and (iii) Electrodes: To interface the device to the external circuit with minimal resistance. The systematic synchronization of these basic components in terms of optical, chemical, structural, and electronic properties leads to the high performance of PSCs. Notably, the interface at the transport layer/perovskite absorber plays a crucial role in overall device performance. Depending on the structure of transport layers (i.e., planar or mesoporous) employed, PSCs are classified into planar and mesoporous device architectures (Fig. 1.3). Theoretically, device architecture is identified as a planer device architecture has a larger charge diffusion length (L_d) than the thickness of the perovskite absorber (t) (i.e., $L_d > t$) and it is completely reverse in the mesoscopic device architecture (i.e., $L_d < t$). The structure is further divided into two configurations, regular planar with negative intrinsic positive (n-i-p) and inverted planar with positive intrinsic negative (p-i-n), which facilitates excellent optical transparency to the transport layer and allows maximum light illumination on the perovskite-like absorber.[21] On the other hand, the mesoporous structure demonstrates a large effective interface between the transport layer and perovskite, easing dissociation of exciton generated, but lacks in charge collection efficiency due to grain boundary assisted recombination.[22]

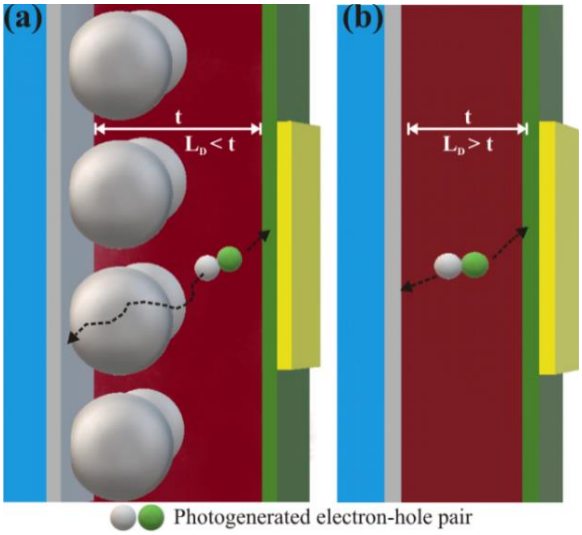

Figure 1.3 Schematic of (a) mesoporous and (b) planar PSC.

(b) Electron transport layers (ETL)

The bandgap and band alignment of the ETLs control and channelize the electron transfer at the ETL/perovskite interface. ETLs, in the form of wide bandgap n-type semiconductors transparent to visible light, absorb the wavelength in the UV range.[52] Moreover, they allow full visible radiance to strike on the perovskite absorber; but this may not be true in inverted device architectures where light strikes through the hole transport layer (HTL) and transparent conducting substrates.[53] Typically, the bandgap values of the ETLs are higher than the perovskite absorbers utilized to fabricate PCSs. Therefore, the CB edge of ETL should be at a lower potential than that of the perovskite absorber to channelize the electrons through the ETL and reduce the leakage of excited charges in the opposite direction. Being n-type, the Fermi levels of ETLs are close to the CB; hence the probability of the VB electron movement from the perovskite to ETL is close to zero and hence ignored (Fig. 1.4). Therefore, a variety of ETLs are explored to control the recombination process and accelerated charge carrier recombination dynamics in search of efficient and stable photovoltaic performance.

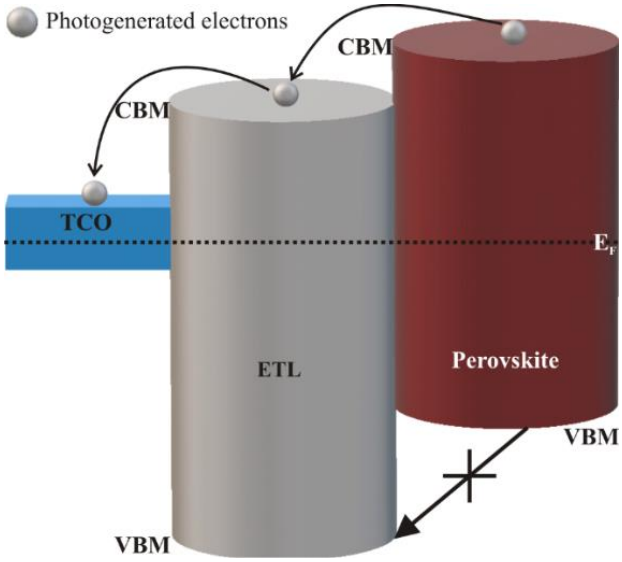

Figure 1.4 Schematic depicting the path of a photogenerated electron from the perovskite light absorber to the external circuit. (CBM: Conduction band minimum and VBM: Valence band maximum)

(c) Hole transport layers (HTL)

HTL is equally essential to transport acceptors or holes generated in the photoactive perovskite layer to the cathode. The HOMO of the hole transport material (HTM) under consideration for the PSCs is required to be located at a higher level than the valence band edge of the perovskite absorber (Fig. 1.5**).** The minimized energy barrier at the perovskite/HTL interface allows easy collection of photogenerated holes. Moreover, the conductivity of HTM, which plays a vital role in charge transfer and charge recombination at the perovskite/HTL interface, can be revamped by governing interface energetics and defect densities. Apart from this, the thermal and chemical stability of HTMs continues to be a concern for long-term and efficient photovoltaic performance. So far, various nanostructured, doped, and passivated HTLs have been explored in PSCs depending on the selected device architecture.

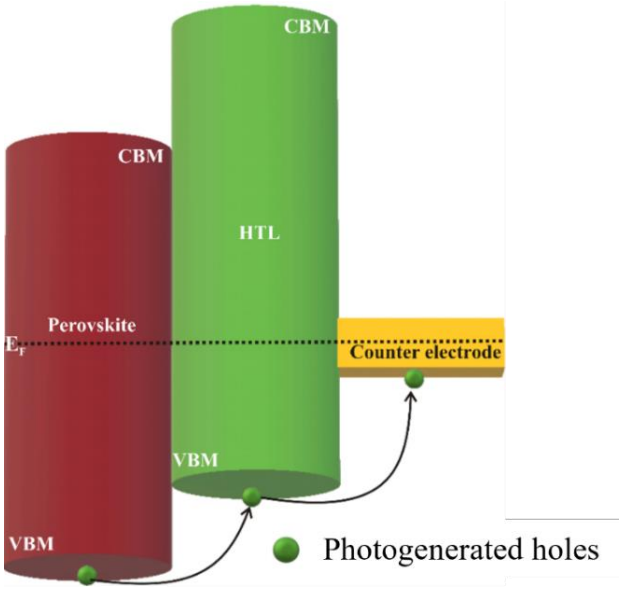

Figure 1.5 Schematic displaying the path of the photogenerated hole from the perovskite light absorber to the external circuit. (CBM: Conduction band minimum and VBM: Valence band maximum)

1.3 Significance of metal oxide and thin film for energy applications

Metal oxides comprise metal cations and oxygen (O) anions, where the ionic radius of the metal cations is lower than that of O anions. Depending on the atomic radium and

periodic occupancy of the metal and oxygen ions, the interstitial sites of cubic, triangular, tetrahedral, and octahedral nature control the physical, chemical, electronic, and structural properties of the metal oxides. The transition metals with +1, +2, and +3 oxidation states from ionic bonds, whereas +4, +5, +6, and +7 oxidation states form covalent bonds with O anion present in the metal oxides. Therefore, the oxides of all kinds of metal ions go from ionic mixtures to covalent bonding and strongly basic to strongly acidic. Oxides of transitional metals, namely Ti, Sn, Mn, Fe, Co, Ni, Cu, and Zn, have been offering precise control over their physicochemical and electronic properties and are explored for various applications, especially in solar cells, water splitting, and photodetectors. Nevertheless, metal oxides downscaled to nanostructure morphologies offering larger volume, better electronic confinement, increased surface-to-volume ratio, and controlled defect states, providing precise control over optical and electrical properties in various morphological forms such as zero-dimensional (i.e., 0D), one-dimensional (i.e., 1D), and two-dimensional (i.e., 2D).[23-25] The same is valid in thin films, hence gaining equal interest in device miniaturization. Specifically, thin films and nanomaterials of metal oxides in pristine, mixed, and/or composite forms are gaining increased interest in the field of sustainable energy, like solar cells, hydrogen fuel, photodetectors, etc.

1.3.1 Water splitting for hydrogen fuel

The metal sites support redox reactions due to different valence sites enabling electrochemical processes. The metal oxides serve as a catalyst in water electrolysis and photocatalysis depending on their band alignment with water oxidation and reduction potentials (0 and 1.23 eV, respectively). Moreover, oxidation states were found to directly impact the water-splitting process and efficiency. Metal oxides offering multiple oxidation sites (i.e., 2+, 3+, and 4+) have gained tremendous research momentum in electrochemistry, which can be able to provide excellent water splitting at relatively reduced overpotentials (~ < 100 mV). Therefore, metal oxides are employed for water splitting through either oxygen evocation reactions (OER) or hydrogen evaluation reactions (HER). CoO_x offering multiple oxidation sites (i.e., Co^{2+}, Co^{3+}, and Co^{4+}) is important in electrocatalytic for water splitting via OER activities. Porous CoO_x with controlled surface oxygen vacancies [26] and CoO

nanoparticles wrapped with porous graphene sheet attracted attention by exhibiting an overpotential of 306 and 348 mV, respectively, toward OERs at 10 mA/cm^2.[27] The Fe-doping in the electrospunned CoO/C nanofibers reduced the overpotential (i.e., 362 mV) and also offered good cyclic stability for 2500 CV cycles with almost no loss in overpotential in an alkaline medium.[28] Likewise, α-MnO_2 requiring an overpotential of 490 mV for OER activity was reduced further by the formation of different phases in order of α-MnO_2 > amorphous MnO_2 > β-MnO_2 > δ-MnO_2.[29, 30] The poor electrical conductance of pristine CuO hinders its usage as an electrocatalyst. Therefore, doping and hetero-structuring strategies are adopted.[31] The less explored electrocatalyst, Fe_2O_3, combined with CuO to form core-shell nanotube arrays over copper foam, provided increased mass transfer and active sites for OER activity (398 mV to reach 100 mA/cm^2).[32] The presence of Fe^{3+} active sites enhances the adsorption of the hydroxyl group from water and improves the overall OER activities. [33] Apart from this, NiO has gained interest due to its higher corrosion resistance and stability. The stoichiometric NiO nanoparticles of diameter 3.3 nm containing Ni^{2+} and Ni^{3+} states showed the highest OER activity with an overpotential of 300 mV.[34] However, The 3D NiO/Ni formed by electro-oxidation of nickel foam required 390 mV for O_2 evolution.[35] Therefore, doping and composite formation of NiO was explored to improve the OER activity. NiO/Co_3O_4@nitrogen-doped-carbon with a high concentration of Co^{3+} and Ni^{3+} on the surface showed a 200 mV overpotential on Ni foam at 10 mA/cm^2 for OER reactions. Fe-cation doping of NiO, i.e., $Fe_xNi_{1-x}O$ nanoparticles (1.5-3.8 nm), provided an overpotential of 297 mV for OER catalytic performance, which was further improved to 297 mV after thin film formation by dispersing $Fe_{0.1}Ni_{0.9}O$ nanoparticles in ethanol.[36] However, one should consider that the 2D metal oxide nanosheets provide a high surface area and offer water oxidation with are reasonable overpotential of 350 mV.[37]

Accounting for the high thermodynamic and acidic stability, metal oxides are employed as electrocatalysts for HER. The perfect stoichiometric metal oxides show unfavorable HER activity. Therefore, oxygen vacancies are generated to modulate the hydrogen adsorption energies, electronic structure, and conductivity. The oxygen defects in the $WO_{2.9}$ nanostructure tuned the hydrogen adsorption energy showed lower

values of Tafel slope (i.e., 50 mV/dec) compared to stochiometric WO_3 (i.e., 120 mV/dec). [38] The rich oxygen vacancies in liquid-exfoliated W-oxide nanosheets provided gap states and acted as a degenerate semiconductor for H_2 evolution with an overpotential of 38 mV at 10 mA/cm^2.[39] Likewise, $TiO_{1.23}$ synthesized by electrochemical cationization delivered excellent HER activity in acidic conditions.[40] The non-metal and or metal doping of metal oxides were also found to enhance the HER activity. The phosphorous doping in MoO_{3-x} nanostructures displays superior performance in H_2 evolution due to the synergy between phosphorous and oxygen vacancies in an acidic medium.[41] However, sulfur doping yield better overpotential than phosphorous.[42] Mo doped in $W_{18}O_{49}$ increases the active surface sites and enhance the HER activity in an acidic medium.[43] Apart from doping and vacancy generation, strain engineering of the metal oxides can also improve HER activity in alkaline conditions. The CoO nanorods with surface strain possessed high oxygen vacancy showing HER activity similar to the reference Pt/C catalyst.[44] Further, the comparison between the trigonal, orthorhombic, and cubic phases of Ti_2O_3 revealed the effect of phase tuning on the HER performance. The smallest charge transfer in cubic Ti_2O_3 results in strong hybridization of Ti(3d) and O(2p) orbitals favoring better H_2 evolution among the Ti_2O_3 polymorphs.[45] On the other hand, one cannot neglect that (i) the ultrathin MnO_2 nanosheets with two monolayer thicknesses improved hydrogen evolution owing to abundant surface oxygen vacancies and Mn^{3+} sites [46] and (ii) the porous structures provide not only large surface sites but also offers efficient pathways for gas diffusion, reactant, and electrolyte transfer.[47] Therefore, morphology engineering of the metal oxides needs to be explored to produce distinctly oriented morphologies in the 0, 1, or 2 dimensional (i.e., 0D, 1D, or 2D) form because the variation in dimension with porous nature can enhance the number of active surface sites and provide connecting pathways resulting in higher HER activity.

1.3.2 Photodetector

Highly sensitive self-powered photodetectors (PDs) are widely used for optical communication, microelectronics, monitoring, etc. Along with various other materials, metal oxides such as tin oxide (SnO_2), gallium oxide (Ga_2O_3), zinc oxide (ZnO),

titanium dioxide (TiO_2), and tungsten oxide (WO_3) are extensively used in photodetectors owing to their different bandgaps. Depending on the bandgap of these metal oxides, the device architecture and detection range of the photodetector can be easily tuned from narrow to wide spectral ranges. Metal oxides, known for high chemical inertness and a variety of morphologic forms, have been synthesized in various 1D and 2D nanostructural forms to tune the optoelectronic properties. Photodetectors fabricated with the WO_3 nanoshale delivering a high surface-to-volume ratio provided photoresponse of 5.1 A/W [48] can be one good example to cite. Nevertheless, the doping or introduction of impurities has also been adopted to search for improved optoelectronic properties. On the other hand, the heterostructures of the metal oxides created more excitement for the development of photodetectors. Therefore, doped metal oxides are combined to form the hetero/homo-structures to gain a better photodetection response in self-powered mode. The energy band alignment between p-Cu_2O and n-ZnO generated a built-in electric field of ~2.2 eV and favored the self-powered operation of the photodetector to provide a better response ranging from UV to visible range (570 nm). [49] The photodetector consisting of NiO/beta-Ga_2O_3 heterojunctions showed a response of 27.43 A/W when illuminated with 245 nm (deep UV).[50] Likewise, the synergistic interactions between the homojunction of p- and n-type SnO_2 worked in the self-powered mode and exhibited the responsivity and detectivity of 1.55 mA/W and 9.8×10^{10} Jones.[51] Hybrid photodetectors of TiO_2 and $CH_3NH_3PbI_3$ (i.e., MAPI) perovskite composite films showed detectivity of the order of 10^{10} Jones under the illumination of a 532 nm laser, which was assigned to the exposure of a high percentage of [001] TiO_2 facets.[52] Nevertheless, the photodetection performance of the perovskite-based device is generally enhanced due to engineering the favorable interface at heterojunctions and the controlled morphology of perovskite films. [53-57] The heterojunction of perovskites with the metal oxides facilitates exciton dissociation and carrier transport resulting in broad spectral response and improved performance.[4] Therefore, several organic and inorganic semiconductors, along with metal halide perovskites, are used to fabricate heterojunction photodetectors.[58-61] Among the variety of inorganic semiconductors, chemically stable NiO is a promising candidate for optoelectronic and

energy/conversion applications.[23, 62-64] Recently, self-powered perovskite-based PDs have attracted intense attention due to their independence, less complicated circuitry, and self-sufficient potential for device operation. These photodetectors depend on PV behavior to produce light current at 0 V bias, which is achieved by forming Schottky junctions with single perovskite crystals and p-i-n junctions.[65-67] Overall, metal oxides are competent materials widely used in multifunctional applications.

1.3.3 Solar cells

The systematic synchronization of metal oxide transport layers (MOTLs) with the perovskite light absorber and metal electrodes in terms of optical, chemical, structural, and electronic properties leads to the high performance of PSCs. The range of coverage, uniformity, and thickness of metal oxide transport layers depends on the coating technique used. Notably, the interface at the MOTL/perovskite absorber plays a crucial role in overall device performance. Moreover, the MOTLs optically protect the perovskite absorber from high-energy UV radiation, enhancing stability. Leijtens et al.[68] have observed higher stability in mesoscopic PSCs sensitized with metal oxide than in non-sensitized PSCs. The surface adsorbed oxygen states of metal oxides possess deep trap sites for the injected electrons upon continuous exposure to the UV spectrum and may leak into the hole transport material. Furthermore, the presence of defects, interstitials, and impurities in the transport layer and, thereby, at its interface with perovskite strongly influence charge mobility, transport, and recombination. The oxygen vacancies and interstitial atoms at the interface are known to create shallow or deep levels near the band edge, which form recombination centers.[69] Therefore, the selection of defect-tolerant interfaces is a prerequisite for smooth charge transfer and to avoid charge recombination. The charge mobilities of the MOTLs, when closely matched with the perovskite light absorber, drastically reduce charge accumulation at the MOTL/perovskite interface and enhance collection efficiency.

Therefore, the engineering of the MOTLs either by doping, faceting, or growing heterostructures is sought to address the charge recombination issues.[70-74] Though a wide range of MOTLs is attempted to efficiently channelize electrons from the

perovskite absorbers into the contacts, the bandgap and band alignment of the transport layers with perovskite light absorbers are fundamental prerequisites for the fabrication of a working device. Usually, wide bandgap semiconductors are employed to allow the maximum visible spectrum illumination onto the perovskite films. Band alignment or band edge alignment channelizes the electrons through the transport layers to reduce the leakage of excited charges in the opposite direction. Besides all these functionalities, ease of processing, earth abundancy, chemical stability, stability under light illumination, non-toxicity, and feasibility of real-time operation are the main concerns to realize the commercial availability of PSCs. Usually, the higher processing temperature of metal oxide has restricted the use of plastic substrates in the PSCs. Overall, the transport layers are known as ETL or HTL, depending on their functionality.

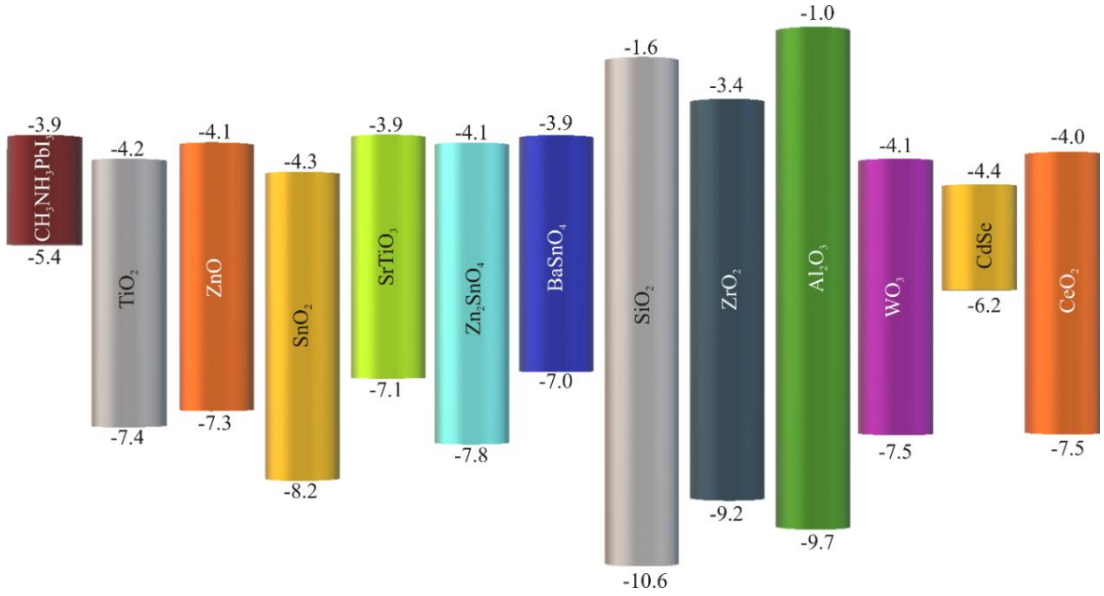

Figure 1.6 Schematic showing the band structures and the band alignment of various inorganic ETLs with perovskite absorber

Inorganic ETLs, engineered into nanostructures for exploiting the nano-regime physical properties, increase the junction interface. Therefore, oxides of various metals such as Titanium (Ti), Tin (Sn), Zinc (Zn), Tungsten (W), Barium (Ba), Strontium (Sr), Aluminium (Al), Iron (Fe), and Indium (In) have been explored for their performance as ETLs in PSCs.[75-79] The band structures of several persuasive metal oxide ETLs are summarized in Fig. 1.6**.** The appearance of these ETLs in various crystalline

polymorphs and their ability to tailor the charge transfer dynamics are of special interest to the PV community. Furthermore, the ETLs can act as a prominent template for the overlaying perovskite layer in PSCs after engineering their phases and crystallinity.

Inorganic HTLs have gained importance in PSCs due to their ability to downsize into nanostructures and increase the junction interface. Since PSCs are the resultant evolution of sensitized solar cells, though, with conceptually newer foundations, redox electrolytes were replaced with solid-state electrolytes or HTLs in PSCs. The expensive solid-state organic spiro-OMeTAD, when introduced in PSCs, degrades perovskite absorbers due to the use of hygroscopic dopants. Therefore, the low-cost inorganic HTLs with high chemical/thermal stability and real scalability have attracted considerable attention from the scientific and industrial community as a replacement for spiro-OMeTAD. Various inorganic materials based on binary oxides, cyanates, and dessafolites such as NiO, VO_x, CoO_x, CuO_x CuI, CuCSN, and $CuGaO_2$ have been investigated for their performance as HTLs in PSCs. [80-83] The band structure positions of selective inorganic HTLs with reference to the perovskite absorber are summarized in **Fig. 1.7.** These metal oxide HTLs are sensibly engineered to alter the charge transfer dynamics and to extract holes efficiently.

Owing to n-type semiconducting properties, suitable bandgap, visible light transmittance, etc., TiO_2 is one of the vastly used materials in modern-day solar cells.[84] The first modern-day organic-inorganic perovskite-based solar cells used TiO_2 nanoparticles as photoanodes.[85] Apart from TiO_2, several metal oxides, namely, ZnO, SnO_2, NiO, CuO, CoO_x, etc., are used as photoanodes or transport layers in dye-sensitized and PSCs. However, NiO is one of the most widely studied HTLs for PSCs due to its chemical inertness, low processing cost, and earth-abundant nature. Nickel oxides with molecular formulas of NiO, NiO_2, and Ni_2O_3 can be engineered to obtain cubic, monoclinic, rhombohedral, and hexagonal crystalline phases. Mainly, p-type semiconducting stoichiometric NiO with a wide bandgap of 3.6 – 4 eV [23] and deep valence band edge (i.e., -5.2 – -5.4 eV) provides excellent band alignment with the perovskite light absorber. The higher conduction band positioning of NiO than

perovskite materials becomes advantageous to conduct holes very efficiently and serves as an excellent electron-blocking layer.

Docampo et al.[86] introduced NiO as HTL in PSCs and gained an efficiency of < 1 % when utilized with a mixed halide perovskite absorber as photoactive material. The low efficiency was attributed to inadequate surface coverage and a large number of pinholes within perovskite films coated over NiO HTL in inverted device architecture. The possibility of improving the PCE after controlling the doping density projected NiO as one of the forthcoming worthwhile HTL candidates. Therefore, various growth mechanisms and thin-film technologies are explored for the synthesis or/and coating of NiO films in ambient atmospheres, such as sputtering, [87] atomic layer deposition (ALD), [88] solvothermal growth, [89] sol-gel, [90] e-beam evaporation, [91] reactive e-beam evaporation, [92] atmospheric pressure spatial atomic layer deposition (AP-SALD), [93] and thermal evaporation followed by oxidation, [94], etc. However, repeated spin coating is observed to be a simple and cost-effective method to gain precise control over the thickness and crystallinity of the NiO nanostructures, though the residual ligands curb the coverage of perovskite absorber and hence the performance of PSCs. Moreover, the thickness of the faceted and corrugated NiO nanocrystalline films controls the hole extraction and transport competence at the HTL/perovskite interface [90] because lower thickness presents higher leakage current and higher thickness offers higher series resistance. The precisely controlled ultra-thin NiO film with negligible absorption loss prepared by ALD blows over the residuals and pinholes. The extremely thin NiO film of 5-7.5 nm thickness, a few times the Debye length (i.e., 1-2 nm for NiO), increases the work function and hole concentration by overlapping the space charge regions. Moreover, the high-temperature treatment improved interfacial properties by dwindling the hydroxylate NiOOH and reducing surface defects related to C-N at the HTL/perovskite interface and conferred 16.4 % PCE.[88] Later on, Liu et al.[95] utilized solution-combustion-based NiO HTL with the two-step processed $MA_{1-y}FA_yPbI_{3-x}Cl_x$ perovskite to gain 19.4 % PCE. Recently, controlled island-like growth of NiO offered lower absorption in the visible region and also increased the effective interface with the perovskite absorber while governing the shunt resistance. [94] Knowing that

mesoporous structures provide a better interface between the HTL and the perovskite, Yin et al.[96] explored the mesoporous nanoforest of 1D NiO nanotube morphology. The hierarchical tube morphology offered a continuous conducting pathway for rapid hole extraction and less charge leakage due to substantially passivated interfacial hole-trapping state density (i.e., 1.274 $\times 10^{16}$ cm^{-3}), which yielded a PCE of 18.77 % with quenched Shockley-Read-Hall recombination losses.

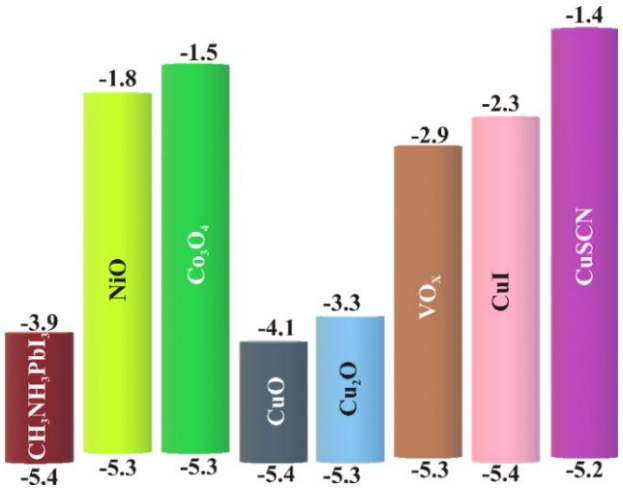

Figure 1.7 Schematics of band alignment of various inorganic HTLs with perovskite absorber.

The Ni^{3+} and Ni^{2+} variations govern the defect levels in NiO and inversely alter the conductivity and optical transmittance of HTL. The spatial localization of HOMO of the perovskite/HTL system on the NiO layer estimated by adopting the relativistic pseudopotentials and pseudo-atomic orbitals predicted the transfer of hole from perovskite in close proximity of NiO surface connected by halogen and lead atoms. [97] Therefore, precise control of the Ni^{3+}/Ni^{2+} ratio by the defect density aligns the VB of HTL with perovskite and provides faster hole extraction with lower energy losses, offering PCE close to 18 %.[91, 97, 98] Nevertheless, significantly reduced oxygen vacancies in the self-doped Ni_2O_3 [99] and NiOOH [100] yielding PCE close to 20 % have gained attention as futuristic HTL to replace NiO; as Ni^{3+} cation sites act as Lewis electron acceptor and bronsted proton acceptor by deprotonating cation amines and oxidizing iodide species. Therefore, different amounts of Cu,[101, 102] Y,[103] La,[104] Fe,[105] Co,[106, 107] Sr,[108] Ag,[109] Na,[110] and Zn,[111, 112], etc. metals and rare earth elements (i.e., Eu, Yb, Tb, Ce, and Nd, etc.)[113] were

doped to enhance the intrinsic conductivity, charge extraction ability, hole mobility, energy level alignment, and optical transparency of the NiO films by reducing the Ni^{2+}/Ni^{3+} vacancy formation energy due to replacement. Even though the segregation of alkaline cations like Li,[114] Cs,[115] and K[116, 117] on the NiO surface improves the PSCs performance due to favorable interaction with perovskite, their time-dependent disparity in the spatial distribution modifies the performance and stability.

Al doping in the lattice of NiO_x not only enhances the electrical conductivity of HTL but also improves the crystalline growth of the perovskite absorber concurrently aligning its energy levels, which dramatically reduces the energetic nonradiative recombination losses and enables quicker hole transportation at the perovskite/HTL interface to deliver 20.84 % PCE.[118] Mg doping is shown to downshift the VB maximum matching it well with the perovskite and lowering the energy redundancy for the hole injection. The reduced energy band offset benefitted the efficient charge collection/transport and curtailed hysteresis, yielding reproducible PCE of 18.5 % from the ambient-stable commercial device of size 10 cm ×10 cm.[119] Interestingly, embedding Au inside the NiO layer to form Au-NiO_x as both electrode and electrode interlayer for the PSCs was attempted to replace the ITO electrode. However, difficulties were encountered in the compact layer formation, reducing the film thickness to control the transmittance and loss of photoexcitation energy due to the self-recombination of opposite charges at the electrode. This hampered the PSC device performance (i.e., PCE = 10. 24 %).[120] Further addition of Cu on the top of Au-NiO film effectively reduced the resistance, but the device delivered a maximum PCE of 11.1 % at the 1 nm Cu layer. The same was reduced further with the increase in the thickness of (i.e., > 1 nm) Cu.[121] UV-ozone irradiation reduced the interface barrier between Cu-doped NiOOH HTL and $MAPbI_3$ perovskite by surface dipole formation and also increased carrier concentration and charge extraction efficiency.[122] Recently, Zhou et al.[123] improved the electrical conductivity of NiO_x film by enhancing Ni^{3+} content after N-doping and achieved a PCE of 17.02 %. The reduced Gibbs free energy on the hydrophilic N-doped NiO_x surface leads to higher nucleation density and, thereby, larger grain growth of perovskite absorber with improved

interfacial contact and passivation of trap state in perovskite layer, thereby suppressing nonradiative recombination.

Cobalt-doping exhibits a synergistic effect and endows the NiO_x film with further improvement of its performance. AS HTL IN PSCs., The p-type Co-doping provides low transparency and high conductance, whereas alkali and alkaline co-dopants bring high transparency with low conductivity. The 10 % Li @ 5 % Co co-doping synergistically enhances the PCE to 20.1 % by providing a shorter carrier lifetime of 0.67 μs and a larger recombination lifetime of 5.24 ms, signifying efficient hole/charge transfer/extraction and suppressed charge carrier recombination, respectively.[124] The synergy between Ag and Li co-dopant with the +1 oxidation states is shown to tailor the optoelectronic properties of NiO. The smallest formation energy of Li and Ag among all related defects creates shallower acceptor levels in NiO and enhanced hole concentration, which effectively optimize the charge extraction/transport and reduce charge accumulation at the interface, therefore boosting the PCE to 19.24%. [125] The Mg^{2+} doping compensates the undesirable positive shift caused in the VB of NiO_x due to the incorporation of Li and promotes the ohmic contact formation at the perovskite interface by reducing barrier height via staircase energy level alignment with $MAPbI_3$ perovskite.[80] However, the inclusion of Co^{2+} in the Mg-Li drop-down affects the device performance severely (i.e., PCE = 13.22 %) for unknown reasons. [126] Apart from this, the polymeric PTAA, DEA, PFBT, PEAI, etc., coatings [127-130] introduced as overlayers for NiO_x HTL effectively modify the interfacial contact and boost the interfacial charge transfer through gradient band alignment and reduce trap state density. The lone-paired functional groups on the polymer coordination with Ni and Pb ions form quasi-2D polymeric-perovskite grain, which blocks the electron transport into HTL and limits the carrier recombination at the interface.

1.4 Motivation

(a) Metal oxides are the most promising functional material which can be engineered into various nanostructure morphology and thin films. Their application in

sustainable energy can be enhanced by modifying and controlling the defects and interfaces at the nanoscale.

(b) The nanostructures of metal oxides are excellent electrocatalysts for water splitting and serve as the buffer layers in thin-film solar cells and photodetectors. Nevertheless, the size and morphology of the metal oxide nanostructures decide the number of exposed active sites which control the efficiency during electrochemical water splitting. Similarly, the roughness, thickness, uniformity, pinholes, etc., of metal oxide thin films directly influence the photoconversion efficiency in solar cells and photodetectors. Especially in the case of metal oxide thin films, the synthesis technique and its repeatability are highly important.

(c) The metal oxide nanostructures with interconnected mesopores provide enhanced surface area, influence mass loading, and facilitate high interaction with electrolyte ions.

(d) The porous material can also serve to accommodate other high-efficiency functional materials.

(e) The semiconducting metal oxide thin films serve in the construction of *pn*-junctions for the fabrication of heterojunction solar cells and photodetectors.

(f) The metal oxide thin films provide the template for the deposition of light harvesters and control the irradiation reaching the light harvester in planar solar cell architecture. In contrast, it protects the absorber from external stimuli like moisture and dust in the inverted solar cell architecture.

Therefore, investigating the influence of metal oxides and their various morphologies on the efficiency of electrocatalytic water splitting is essential to improve the performance in green hydrogen generation. In the last few decades, the synthesis of the nanostructures of transition metal oxides has gained importance due to their excellent physical, chemical, and thermal stability and catalytic activity. Various metal oxide nanostructures and their composites have been developed for electrocatalytic water splitting, but the influence of NiO nanostructure morphologies and porosity in achieving lower overpotential is not well understood.

Moreover, self-powered perovskite-based PDs have attracted intense attention due to their independence, less complicated circuitry, and self-sufficient potential for device

operation. These PDs depend on PV behavior to produce light current at 0 V bias, which is achieved by forming Schottky junctions with single perovskite crystals and p-i-n junctions.[65-67] However, these materials are thermally unstable and degrade in the ambient atmosphere.[67, 131] This becomes a critical issue inhibiting device performance for real-time applications such as optical communication, imaging, sensing, etc.[132-134] Therefore, a systematic study on degradation mechanisms and intrinsic modification within metal halide perovskite in the presence of a metal oxide, like NiO, transport layer is highly desirable.

Despite the use of MOTLs, high-efficiency PSCs are realized by using expensive organic HTLs, which trigger degradation of the perovskite layer and require an inert atmosphere for processing. Therefore, to overcome the problem of perovskite degradation, among all inorganic transport layers, NiO is found to be a more promising and vital candidate for optoelectronic properties because of its excellent chemical stability.[135-137] Moreover, various wet chemical techniques, namely, spin coating, blade coating, spray coating, metric rod coating, etc., are used to synthesize metal oxide thin films, but residual ligands present in them impede their performance.[138] Although the physical deposition methods, such as atomic layer deposition, sputtering, laser deposition, etc., ensure uniformity and reproducibility of the thin films, involves high processing cost. Therefore, using industrially matured thermal evaporation of nickel-metal followed by oxidation to convert to NiO thin films will be an economical solution to the above-cited problems in PSCs.

The ABO_3 perovskite oxide (PO) structures, where the A-site ion is usually a rare-earth element or an alkaline earth metal situated at the center of the lattice, the B-site ion is a transition metal positioned at the lattice corners, possess a bandgap ranging from 1.4 to 3.8 eV are used in solar cells as the n-type buffer/transport layers or photoanodes to form a p-n junction. Additionally, POs offer tunable physical, chemical, and optoelectronic properties, depending on the substitution of the ions and distortion in the ABO_3 structure.[139] Transparency to visible spectra, compatible band energy level alignment with absorber, and minimum recombinations at the interface with absorbers are critical factors for selecting a suitable POs buffer layer for the solar cells. Even though the maximum efficiencies obtained using PO transport layers vary between 12-21 % in the

PSCs, the intervention of the lead iodide layer at the interface degrades the performance drastically. Therefore, the solar cell consisting of metal oxide light harvesters and PO buffer layers is expected to be highly stable and environmentally friendly, unlike the PSC, which is hazardous, moisture and UV sensitive, and suffers from long-term stability.[140] Therefore, evaluating the potential of metal oxide light harvesters and PO buffer layers is of scientific importance. Experimentally evaluating the performance of solar cells with various buffer layers and light harvesters is a myriad task. Nevertheless, Solar Cell Capacitance Simulator-1D (SCAPS-1D), developed at Gent University, Belgium, offers a heterojunction and multi-junction solar cell devices simulation that shall give the prime information about the influence of thickness, defect/impurity levels, temperature, interfacial resistance, etc. of the selected metal oxide buffer and light harvester layers for the solar cell fabrications.

1.5 Objectives of the thesis

This thesis work reports the investigation on the following objectives to answer the questions pertaining to the literature survey. The morphology and porosity-controlled NiO nanostructures are studied for electrocatalytic water-splitting applications. A novel approach is used to synthesize transparent NiO thin films, which can be employed in solar cells and photodetector applications. Further, simulations are provided to identify the all-oxide solar cell providing stabile efficiency in harsh environmental conditions.

The objectives of the thesis are:

- Synthesis of morphology-controlled NiO nanostructures using the cost-effective technique. To optimize the synthesis procedure, obtain different NiO nanostructures and study their crystalline, morphological, chemical, electronic, and electrochemical properties.
- To investigate the influence of morphology and porosity on the electrocatalytic performance of NiO nanostructures for green hydrogen generation.
- To develop the industrially scalable synthesis protocol for well-transparent NiO thin films to use in solar cells and photodetector.

- To study the self-powered photodetection properties of facile NiO/$CH_3NH_3PbI_3$ heterojunction and understand the effect of perovskite degradation on overall performance.
- To fabricate the PSCs at ambient atmospheric conditions and study the influence of interface alteration/degradation on the overall performance of the solar device.
- To simulate the heterojunction and multi-junction oxide solar cell devices consisting of various metal oxide buffers and light harvester layers and identify the best suitable combination for efficient all oxide solar cells.

1.6 References

[1] Hussein A. K., (2015), Applications of nanotechnology in renewable energies-A comprehensive overview and understanding, Renew. Sust. Energy Rev., 42, 460-476, (DOI: 10.1016/j.rser.2014.10.027).

[2] Novas N., Garcia R. M., Camacho J. M., Alcayde A., (2021), Advances in Sol. Energy towards Efficient and Sustainable Energy, Sustainability, 13, 6295, (DOI: 10.3390/su13116295)

[3] Acar C., Dincer I., (2014), Comparative assessment of hydrogen production methods from renewable and non-renewable sources, Int. J. Hydrog. Energy, 39, 1-12, (DOI: 10.1016/j.ijhydene.2013.10.060).

[4] Miao J., Zhang F., (2019), Recent progress on highly sensitive perovskite photodetectors, J. Mater. Chem. C, 7, 1741-1791, (DOI: 10.1039/C8TC06089D).

[5] Wang W., Zhang F., Li L., Zhang M., An Q., Wang J., Sun Q., (2015), Highly sensitive polymer photodetectors with a broad spectral response range from UV light to the near infrared region, J. Mater. Chem. C, 3, 7386-7393, (DOI: 10.1039/C5TC01383F).

[6] Kabir E., Kumar P., Kumar S., Adelodun A. A., Kim K.-H., (2018), Sol. Energy: Potential and future prospects, Renew. Sust. Energy Rev., 82, 894-900, (DOI: 10.1016/j.rser.2017.09.094).

[7] Zheng J., Lau C. F. J., Mehrvarz H., Ma F.-J., Jiang Y., Deng X., Soeriyadi A., Kim J., Zhang M., Hu L., Cui X., Lee D. S., Bing J., Cho Y., Chen C., Green M. A.,

Huang S., Ho-Baillie A. W. Y., (2018), Large area efficient interface layer free monolithic perovskite/homo-junction-silicon tandem solar cell with over 20% efficiency, Energy Environ. Sci., 11, 2432-2443, (DOI: 10.1039/C8EE00689J).

[8] Battaglia C., Cuevas A., De Wolf S., (2016), High-efficiency crystalline silicon solar cells: status and perspectives, Energy Environ. Sci., 9, 1552-1576, (DOI: 10.1039/C5EE03380B).

[9] Green M. A., (2019), How did solar cells get so cheap?, Joule, 3, 631-633, (DOI: 10.1016/j.joule.2019.02.010).

[10] Bagnall D. M., Boreland M., (2008), Photovoltaic technologies, Energy Policy, 36, 4390-4396, (DOI: 10.1016/j.enpol.2008.09.070).

[11] Hillhouse H. W., Beard M. C., (2009), Solar cells from colloidal nanocrystals: Fundamentals, materials, devices, and economics, Curr. Opin. Colloid Interface Sci., 14, 245-259, (DOI: 10.1016/j.cocis.2009.05.002).

[12] Krebs F. C., (2009), Fabrication and processing of polymer solar cells: A review of printing and coating techniques, Sol. Energy Mater. Sol. Cells, 93, 394-412, (DOI: 10.1016/j.solmat.2008.10.004).

[13] Shalini S., Balasundara P. R., Prasanna S., Mallick T. K., Senthilarasu S., (2015), Review on natural dye sensitized solar cells: Operation, materials and methods, Renew. Sust. Energy Rev., 51, 1306-1325, (DOI: 10.1016/j.rser.2015.07.052).

[14] Correa-Baena J.-P., Abate A., Saliba M., Tress W., Jesper Jacobsson T., Grätzel M., Hagfeldt A., (2017), The rapid evolution of highly efficient perovskite solar cells, Energy Environ. Sci., 10, 710-727, (DOI: 10.1039/C6EE03397K).

[15] Kim G., Min H., Lee K. S., Lee D. Y., Yoon S. M., Seok S. I., (2020), Impact of strain relaxation on performance of α-formamidinium lead iodide perovskite solar cells, Science, 370, 108-112, (DOI: 10.1126/science.abc4417).

[16] Green M. A., Ho-Baillie A., Snaith H. J., (2014), The emergence of perovskite solar cells, Nat. Photonics, 8, 506-514, (DOI: 10.1038/nphoton.2014.134).

[17] Jung H. S., Park N. G., (2015), Perovskite solar cells: From materials to devices, Small, 11, 10-25, (DOI: 10.1002/smll.201402767).

[18] Sun S., Hartono N. T. P., Ren Z. D., Oviedo F., Buscemi A. M., Layurova M., Chen D. X., Ogunfunmi T., Thapa J., Ramasamy S., Settens C., DeCost B. L., Kusne A.

G., Liu Z., Tian S. I. P., Peters I. M., Correa-Baena J.-P., Buonassisi T., (2019), Accelerated development of perovskite-inspired materials via high-throughput synthesis and machine-learning diagnosis, Joule, 3, 1437-1451, (DOI: 10.1016/j.joule.2019.05.014).

[19] Bai Y., Meng X., Yang S., (2018), Interface engineering for highly efficient and stable planar p-i-n perovskite solar cells, Adv. Energy Mater., 8, 1701883, (DOI: 10.1002/aenm.201701883).

[20] Sun J., Zhong D. K., Gamelin D. R., (2010), Composite photoanodes for photoelectrochemical solar water splitting, Energy Environ. Sci., 3, 1252-1261, (DOI: 10.1039/c0ee00030b).

[21] Mali S. S., Hong C. K., (2016), p-i-n/n-i-p type planar hybrid structure of highly efficient perovskite solar cells towards improved air stability: synthetic strategies and the role of p-type hole transport layer (HTL) and n-type electron transport layer (ETL) metal oxides, Nanoscale, 8, 10528-10540, (DOI: 10.1039/C6NR02276F).

[22] Pascoe A. R., Yang M. J., Kopidakis N., Zhu K., Reese M. O., Rumbles G., Fekete M., Duffy N. W., Cheng Y. B., (2016), Planar versus mesoscopic perovskite microstructures: The influence of $CH_3NH_3PbI_3$ morphology on charge transport and recombination dynamics, Nano Energy, 22, 439-452, (DOI: 10.1016/j.nanoen.2016.02.031).

[23] Devan R. S., Patil R. A., Lin J.-H., Ma Y.-R., (2012), One-dimensional metal-oxide nanostructures: Recent developments in synthesis, characterization, and applications, Adv. Funct. Mater., 22, 3326-3370, (DOI: 10.1002/adfm.201201008).

[24] Siow J. H., Bilad M. R., Caesarendra W., Leam J. J., Bustam M. A., Sambudi N. S., Wibisono Y., Mahlia T. M. I., (2021), Progress in development of nanostructured manganese oxide as catalyst for oxygen reduction and evolution reaction, Energies, 14, 6385, (DOI: 10.3390/en14196385).

[25] Samtham M., Singh D., Hareesh K., Devan R. S., (2022), Perspectives of conducting polymer nanostructures for high-performance electrochemical capacitors, J. Energy Storage, 51, 104418, (DOI: 10.1016/j.est.2022.104418).

[26] Xu W., Lyu F., Bai Y., Gao A., Feng J., Cai Z., Yin Y., (2018), Porous cobalt oxide nanoplates enriched with oxygen vacancies for oxygen evolution reaction, Nano Energy, 43, 110-116, (DOI: 10.1016/j.nanoen.2017.11.022).

[27] Zhao Y., Sun B., Huang X., Liu H., Su D., Sun K., Wang G., (2015), Porous graphene wrapped CoO nanoparticles for highly efficient oxygen evolution, J. Mater. Chem. A, 3, 5402-5408, (DOI: 10.1039/C5TA00158G).

[28] Li W., Li M., Wang C., Wei Y., Lu X., (2020), Fe doped CoO/C nanofibers towards efficient oxygen evolution reaction, Appl. Surf. Sci., 506, 144680, (DOI: 10.1016/j.apsusc.2019.144680).

[29] Meng Y., Song W., Huang H., Ren Z., Chen S.-Y., Suib S. L., (2014), Structure-property relationship of bifunctional MnO_2 nanostructures: Highly efficient, ultra-stable electrochemical water oxidation and oxygen reduction reaction catalysts identified in alkaline media, J. Am. Chem. Soc., 136, 11452-11464, (DOI: 10.1021/ja505186m).

[30] Singh A., Roy Chowdhury D., Amritphale S. S., Chandra N., Singh I. B., (2015), Efficient electrochemical water oxidation catalysis by nanostructured Mn_2O_3, RSC Adv., 5, 24200-24204, (DOI: 10.1039/C4RA15113E).

[31] Xiong X., You C., Liu Z., Asiri A. M., Sun X., (2018), Co-doped CuO nanoarray: An efficient oxygen evolution reaction electrocatalyst with enhanced activity, ACS Sust. Chem. Eng., 6, 2883-2887, (DOI: 10.1021/acssuschemeng.7b03752).

[32] Gao Y., Zhang N., Wang C., Zhao F., Yu Y., (2020), Construction of Fe_2O_3@CuO heterojunction nanotubes for enhanced oxygen evolution reaction, ACS Appl. Energy Mater., 3, 666-674, (DOI: 10.1021/acsaem.9b01866).

[33] Xu Q.-Q., Huo W., Li S.-S., Fang J.-H., Li L., Zhang B.-Y., Zhang F., Zhang Y.-X., Li S.-W., (2020), Crystal phase determined Fe active sites on Fe_2O_3 (γ- and α-Fe_2O_3) yolk-shell microspheres and their phase dependent electrocatalytic oxygen evolution reaction, Appl. Surf. Sci., 533, 147368, (DOI: 10.1016/j.apsusc.2020.147368).

[34] Fominykh K., Feckl J. M., Sicklinger J., Döblinger M., Böcklein S., Ziegler J., Peter L., Rathousky J., Scheidt E.-W., Bein T., Fattakhova-Rohlfing D., (2014), Ultrasmall dispersible crystalline nickel oxide nanoparticles as high-performance

catalysts for electrochemical water splitting, Adv. Funct. Mater., 24, 3123-3129, (DOI: 10.1002/adfm.201303600).

[35] Han G.-Q., Liu Y.-R., Hu W.-H., Dong B., Li X., Shang X., Chai Y.-M., Liu Y.-Q., Liu C.-G., (2015), Three dimensional nickel oxides/nickel structure by in situ electro-oxidation of nickel foam as robust electrocatalyst for oxygen evolution reaction, Appl. Surf. Sci., 359, 172-176, (DOI: 10.1016/j.apsusc.2015.10.097).

[36] Fominykh K., Chernev P., Zaharieva I., Sicklinger J., Stefanic G., Döblinger M., Müller A., Pokharel A., Böcklein S., Scheu C., Bein T., Fattakhova-Rohlfing D., (2015), Iron-doped nickel oxide nanocrystals as highly efficient electrocatalysts for alkaline water splitting, ACS Nano, 9, 5180-5188, (DOI: 10.1021/acsnano.5b00520).

[37] Pawar S. M., Pawar B. S., Hou B., Kim J., Aqueel Ahmed A. T., Chavan H. S., Jo Y., Cho S., Inamdar A. I., Gunjakar J. L., Kim H., Cha S., Im H., (2017), Self-assembled two-dimensional copper oxide nanosheet bundles as an efficient oxygen evolution reaction (OER) electrocatalyst for water splitting applications, J. Mater. Chem. A, 5, 12747-12751, (DOI: 10.1039/C7TA02835K).

[38] Li Y. H., Liu P. F., Pan L. F., Wang H. F., Yang Z. Z., Zheng L. R., Hu P., Zhao H. J., Gu L., Yang H. G., (2015), Local atomic structure modulations activate metal oxide as electrocatalyst for hydrogen evolution in acidic water, Nat. Commun., 6, 8064, (DOI: 10.1038/ncomms9064).

[39] Zheng T., Sang W., He Z., Wei Q., Chen B., Li H., Cao C., Huang R., Yan X., Pan B., Zhou S., Zeng J., (2017), Conductive tungsten oxide nanosheets for highly efficient hydrogen evolution, Nano Lett., 17, 7968-7973, (DOI: 10.1021/acs.nanolett.7b04430).

[40] Swaminathan J., Subbiah R., Singaram V., (2016), Defect-rich metallic titania ($TiO_{1.23}$): An efficient hydrogen evolution catalyst for electrochemical water splitting, ACS Catal., 6, 2222-2229, (DOI: 10.1021/acscatal.5b02614).

[41] Li L., Zhang T., Yan J., Cai X., Liu S., (2017), P doped MoO_{3-x} nanosheets as efficient and stable electrocatalysts for hydrogen evolution, Small, 13, 1700441, (DOI: 10.1002/smll.201700441).

[42] Geng S., Liu Y., Yu Y. S., Yang W., Li H., (2020), Engineering defects and adjusting electronic structure on S doped MoO_2 nanosheets toward highly active hydrogen evolution reaction, Nano Res., 13, 121-126, (DOI: 10.1007/s12274-019-2582-6).

[43] Zhong X., Sun Y., Chen X., Zhuang G., Li X., Wang J.-G., (2016), Mo doping induced more active sites in urchin-like $W_{18}O_{49}$ nanostructure with remarkably enhanced performance for hydrogen evolution reaction, Adv. Funct. Mater., 26, 5778-5786, (DOI: 10.1002/adfm.201601732).

[44] Ling T., Yan D.-Y., Wang H., Jiao Y., Hu Z., Zheng Y., Zheng L., Mao J., Liu H., Du X.-W., Jaroniec M., Qiao S.-Z., (2017), Activating cobalt(II) oxide nanorods for efficient electrocatalysis by strain engineering, Nat. Commun., 8, 1509, (DOI: 10.1038/s41467-017-01872-y).

[45] Li Y., Yu Z. G., Wang L., Weng Y., Tang C. S., Yin X., Han K., Wu H., Yu X., Wong L. M., Wan D., Wang X. R., Chai J., Zhang Y.-W., Wang S., Wang J., Wee A.T. S., Breese M. B. H., Pennycook S. J., Venkatesan T., Dong S., Xue J. M., Chen J., (2019), Electronic-reconstruction-enhanced hydrogen evolution catalysis in oxide polymorphs, Nat. Commun., 10, 3149, (DOI: 10.1038/s41467-019-11124-w).

[46] Zhao Y., Chang C., Teng F., Zhao Y., Chen G., Shi R., Waterhouse G. I. N., Huang W., Zhang T., (2017), Defect-engineered ultrathin δ-MnO_2 nanosheet arrays as bifunctional electrodes for efficient overall water splitting, Adv. Energy Mater., 7, 1700005, (DOI: 10.1002/aenm.201700005).

[47] Zhu Y., Zhou W., Shao Z., (2017), Perovskite/carbon composites: Applications in oxygen electrocatalysis, Small, 13, 1603793, (DOI: 10.1002/smll.201603793).

[48] Shao D., Yu M., Lian J., Sawyer S., (2014), Optoelectronic properties of three dimensional WO_3 nanoshale and its application for UV sensing, Opt. Mater., 36, 1002-1005, (DOI: 10.1016/j.optmat.2014.01.010).

[49] Lin H.-P., Lin P.-Y., Perng D.-C., (2020), Fast-response and self-powered Cu_2O/ZnO nanorods heterojunction UV-visible (570 nm) photodetectors, J. Electrochem. Soc., 167, 067507, (DOI: 10.1149/1945-7111/ab7e8e).

[50] Jia M., Wang F., Tang L., Xiang J., Teng K. S., Lau S. P., (2020), High-performance deep ultraviolet photodetector based on NiO/β-Ga_2O_3 heterojunction, Nanoscale Res. Lett., 15, 47, (DOI: 10.1186/s11671-020-3271-9).

[51] Liu B., Li M., Fu W., Ye P., E W., Xiao X., Wei H., Lu Y., He Y., (2022), High-performance self-driven ultraviolet photodetector based on SnO_2 p-n homojunction, Opt. Mater., 129, 112571, (DOI: 10.1016/j.optmat.2022.112571).

[52] Jiao S., Fu X., Lian G., Jing L., Xu Z., Wang Q., Cui D., (2017), Ultrathin TiO_2 nanosheets synthesized using a high pressure solvothermal method and the enhanced photoresponse performance of $CH_3NH_3PbI_3$–TiO_2 composite films, RSC Adv., 7, 20845-20850, (DOI: 10.1039/C7RA01073G).

[53] Li F., Ma C., Wang H., Hu W., Yu W., Sheikh A. D., Wu T., (2015), Ambipolar solution-processed hybrid perovskite phototransistors, Nat. Commun., 6, 8238, (DOI: 10.1038/ncomms9238).

[54] Saidaminov M. I., Adinolfi V., Comin R., Abdelhady A. L., Peng W., Dursun I., Yuan M., Hoogland S., Sargent E. H., Bakr O. M., (2015), Planar-integrated single-crystalline perovskite photodetectors, Nat. Commun., 6, 8724, (DOI: 10.1038/ncomms9724).

[55] Alwadai N., Haque M. A., Mitra S., Flemban T., Pak Y., Wu T., Roqan I., (2017), High-performance ultraviolet-to-infrared broadband perovskite photodetectors achieved via inter-/intraband transitions, ACS Appl. Mater. Interfaces, 9, 37832-37838, (DOI: 10.1021/acsami.7b09705).

[56] Zheng Z., Zhuge F., Wang Y., Zhang J., Gan L., Zhou X., Li H., Zhai T., (2017), Decorating perovskite quantum dots in tio2 nanotubes array for broadband response photodetector, Adv. Funct. Mater., 27, 1703115, (DOI: 10.1002/adfm.201703115).

[57] Gao T., Zhang Q., Chen J., Xiong X., Zhai T., (2017), Performance-enhancing broadband and flexible photodetectors based on perovskite/ZnO-nanowire hybrid structures, Adv. Opt. Mater., 5, 1700206, (DOI: 10.1002/adom.201700206).

[58] Li J., Yuan S., Tang G., Li G., Liu D., Li J., Hu X., Liu Y., Li J., Yang Z., Liu S. F., Liu Z., Gao F., Yan F., (2017), High-performance, self-powered photodetectors based on perovskite and graphene, ACS Appl. Mater. Interfaces, 9, 42779-42787, (DOI: 10.1021/acsami.7b14110).

[59] Sutherland B. R., Johnston A. K., Ip A. H., Xu J., Adinolfi V., Kanjanaboos P., Sargent E. H., (2015), Sensitive, fast, and stable perovskite photodetectors

exploiting interface engineering, ACS Photonics, 2, 1117-1123, (DOI: 10.1021/acsphotonics.5b00164).

[60] Liu Y., Jia R., Wang Y., Hu Z., Zhang Y., Pang T., Zhu Y., Luan S., (2017), Inhibition of zero drift in perovskite-based photodetector devices via [6,6]-Phenyl-C_{61}-butyric acid methyl ester doping, ACS Appl. Mater. Interfaces, 9, 15638-15643, (DOI: 10.1021/acsami.7b02413).

[61] Qin L., Wu L., Kattel B., Li C., Zhang Y., Hou Y., Wu J., Chan W.-L., (2017), Using bulk heterojunctions and selective electron trapping to enhance the responsivity of perovskite–graphene photodetectors, Adv. Funct. Mater., 27, 1704173, (DOI: 10.1002/adfm.201704173).

[62] Patil R. A., Devan R. S., Lin J.-H., Ma Y.-R., Patil P. S., Liou Y., (2013), Efficient electrochromic properties of high-density and large-area arrays of one-dimensional NiO nanorods, Sol. Energy Mater. Sol. Cells, 112, 91-96, (DOI: 10.1016/j.solmat.2013.01.003).

[63] Dalavi D. S., Devan R. S., Patil R. S., Ma Y.-R., Patil P. S., (2013), Electrochromic performance of sol-gel deposited NiO thin film, Mater. Lett., 90, 60-63, (DOI: 10.1016/j.matlet.2012.08.108).

[64] Dalavi D. S., Devan R. S., Patil R. S., Ma Y.-R., Kang M.-G., Kim J.-H., Patil P. S., (2013), Electrochromic properties of dandelion flower like nickel oxide thin films, J. Mater. Chem. A, 1, 1035-1039, (DOI: 10.1039/C2TA00842D).

[65] Lu H., Tian W., Cao F., Ma Y., Gu B., Li L., (2016), A self-powered and stable all-perovskite photodetector–solar cell nanosystem, Adv. Funct. Mater., 26, 1296-1302, (DOI: 10.1002/adfm.201504477).

[66] Zhou H., Zeng J., Song Z., Grice C. R., Chen C., Song Z., Zhao D., Wang H., Yan Y., (2018), Self-powered all-inorganic perovskite microcrystal photodetectors with high detectivity, J. Phys. Chem. Lett., 9, 2043-2048, (DOI: 10.1021/acs.jpclett.8b00700).

[67] Li F., Liu M., (2017), Recent efficient strategies for improving the moisture stability of perovskite solar cells, J. Mater. Chem. A, 5, 15447-15459, (DOI: 10.1039/C7TA01325F).

[68] Leijtens T., Eperon G. E., Pathak S., Abate A., Lee M. M., Snaith H. J., (2013), Overcoming ultraviolet light instability of sensitized TiO_2 with meso-superstructured organometal tri-halide perovskite solar cells, Nat. Commun., 4, 2885, (DOI: 10.1038/ncomms3885).

[69] Kim J., Kim K. S., Myung C. W., (2020), Efficient electron extraction of SnO_2 electron transport layer for lead halide perovskite solar cell, NPJ Comput. Mater., 6, 100, (DOI: 10.1038/s41524-020-00370-y).

[70] Hu Q., Wu J., Jiang C., Liu T. H., Que X. L., Zhu R., Gong Q. H., (2014), Engineering of electron-selective contact for perovskite solar cells with efficiency exceeding 15%, ACS Nano, 8, 10161-10167, (DOI: 10.1021/nn5029828).

[71] Yella A., Heiniger L. P., Gao P., Nazeeruddin M. K., Gratzel M., (2014), Nanocrystalline rutile electron extraction layer enables low-temperature solution-processed perovskite photovoltaics with 13.7% efficiency, Nano Lett., 14, 2591-2596, (DOI: 10.1021/nl500399m).

[72] Wang J. T. W., Ball J. M., Barea E. M., Abate A., Alexander-Webber J. A., Huang J., Saliba M., Mora-Sero I., Bisquert J., Snaith H. J., Nicholas R. J., (2014), Low-temperature processed electron collection layers of graphene/tio2 nanocomposites in thin film perovskite solar cells, Nano Lett., 14, 724-730, (DOI: 10.1021/nl403997a).

[73] Karthikeyan V., Maniarasu S., Manjunath V., Ramasamy E., Veerappan G., (2017), Hydrothermally tailored anatase TiO_2 nanoplates with exposed {111} facets for highly efficient dye-sensitized solar cells, Sol. Energy, 147, 202-208, (DOI: 10.1016/j.solener.2017.03.049).

[74] Zhang W., Saliba M., Stranks S. D., Sun Y., Shi X., Wiesner U., Snaith H. J., (2013), Enhancement of perovskite-based solar cells employing core-shell metal nanoparticles, Nano Lett., 13, 4505-4510, (DOI: 10.1021/nl4024287).

[75] Qin P., Paulose M., Dar M. I., Moehl T., Arora N., Gao P., Varghese O. K., Gatzel M., Nazeeruddin M. K., (2015), Stable and efficient perovskite solar cells based on titania nanotube arrays, Small, 11, 5533-5539, (DOI: 10.1002/smll.201501460).

[76] Park M., Kim J.-Y., Son H. J., Lee C.-H., Jang S. S., Ko M. J., (2016), Low-temperature solution-processed Li-doped SnO_2 as an effective electron transporting

layer for high-performance flexible and wearable perovskite solar cells, Nano Energy, 26, 208-215, (DOI: 10.1016/j.nanoen.2016.04.060).

[77] Cao J., Wu B., Chen R., Wu Y., Hui Y., Mao B.-W., Zheng N., (2018), Efficient, hysteresis-free, and stable perovskite solar cells with ZnO as electron-transport layer: Effect of surface passivation, Adv. Mater., 30, 1705596, (DOI: 10.1002/adma.201705596).

[78] Jung K., Lee J., Im C., Do J., Kim J., Chae W.-S., Lee M.-J., (2018), Highly efficient amorphous Zn_2SnO_4 electron-selective layers yielding over 20% efficiency in $FAMAPbI_3$-based planar solar cells, ACS Energy Lett., 3, 2410-2417, (DOI: 10.1021/acsenergylett.8b01501).

[79] Chen C., Jiang Y., Wu Y., Guo J., Kong X., Wu X., Li Y., Zheng D., Wu S., Gao X., Hou Z., Zhou G., Chen Y., Liu J.-M., Kempa K., Gao J., (2020), Low-temperature-processed WO_x as electron transfer layer for planar perovskite solar cells exceeding 20% efficiency, Solar RRL, 4, 1900499, (DOI: 10.1002/solr.201900499).

[80] Chen W., Wu Y., Yue Y., Liu J., Zhang W., Yang X., Chen H., Bi E., Ashraful I., Grätzel M., Han L., (2015), Efficient and stable large-area perovskite solar cells with inorganic charge extraction layers, Science, 350, 944-948, (DOI: 10.1126/science.aad1015).

[81] Zuo C. T., Ding L. M., (2015), Solution-Processed Cu2O and CuO as Hole Transport Materials for Efficient Perovskite Solar Cells, Small, 11, 5528-5532, (DOI: 10.1002/smll.201501330).

[82] Wijeyasinghe N., Regoutz A., Eisner F., Du T., Tsetseris L., Lin Y.-H., Faber H., Pattanasattayavong P., Li J., Yan F., McLachlan M. A., Payne D. J., Heeney M., Anthopoulos T. D., (2017), Copper(I) thiocyanate (CuSCN) hole-transport layers processed from aqueous precursor solutions and their application in thin-film transistors and highly efficient organic and organometal halide perovskite solar cells, Adv. Funct. Mater., 27, 1701818, (DOI: 10.1002/adfm.201701818).

[83] Zhang H., Wang H., Chen W., Jen A. K. Y., (2017), CuGaO2: A Promising inorganic hole-transporting material for highly efficient and stable perovskite solar cells, Adv. Mater., 29, 1604984, (DOI: 10.1002/adma.201604984).

[84] Shakeel Ahmad M., Pandey A. K., Abd Rahim N., (2017), Advancements in the development of TiO2 photoanodes and its fabrication methods for dye sensitized solar cell (DSSC) applications. A review, Renew. Sust. Energy Rev., 77, 89-108, (DOI: 10.1016/j.rser.2017.03.129).

[85] Kojima A., Teshima K., Shirai Y., Miyasaka T., (2009), Organometal halide perovskites as visible-light sensitizers for photovoltaic cells, J. Am. Chem. Soc., 131, 6050-6051, (DOI: 10.1021/ja809598r).

[86] Docampo P., Ball J. M., Darwich M., Eperon G. E., Snaith H. J., (2013), Efficient organometal trihalide perovskite planar-heterojunction solar cells on flexible polymer substrates, Nat. Commun., 4, 2761, (DOI: 10.1038/ncomms3761).

[87] Cui J., Meng F., Zhang H., Cao K., Yuan H., Cheng Y., Huang F., Wang M., (2014), $CH_3NH_3PbI_3$-based planar solar cells with magnetron-sputtered nickel oxide, ACS Appl. Mater. Interfaces, 6, 22862-22870, (DOI: 10.1021/am507108u).

[88] Seo S., Park I. J., Kim M., Lee S., Bae C., Jung H. S., Park N. G., Kim J. Y., Shin H., (2016), An ultra-thin, un-doped NiO hole transporting layer of highly efficient (16.4%) organic-inorganic hybrid perovskite solar cells, Nanoscale, 8, 11403-11412, (DOI: 10.1039/c6nr01601d).

[89] Tang J., Jiao D., Zhang L., Zhang X., Xu X., Yao C., Wu J., Lan Z., (2018), High-performance inverted planar perovskite solar cells based on efficient hole-transporting layers from well-crystalline NiO nanocrystals, Sol. Energy, 161, 100-108, (DOI: 10.1016/j.solener.2017.12.045).

[90] Zhu Z., Bai Y., Zhang T., Liu Z., Long X., Wei Z., Wang Z., Zhang L., Wang J., Yan F., Yang S., (2014), High-performance hole-extraction layer of sol–gel-processed NiO nanocrystals for inverted planar perovskite solar cells, Angew. Chem. Int. Ed., 53, 12571-12575, (DOI: 10.1002/anie.201405176).

[91] Abzieher T., Moghadamzadeh S., Schackmar F., Eggers H., Sutterlüti F., Farooq A., Kojda D., Habicht K., Schmager R., Mertens A., Azmi R., Klohr L., Schwenzer J. A., Hetterich M., Lemmer U., Richards B. S., Powalla M., Paetzold U. W., (2019), Electron-beam-evaporated nickel oxide hole transport layers for perovskite-based photovoltaics, Adv. Energy Mater., 9, 1802995, (DOI: 10.1002/aenm.201802995).

[92] Routledge T. J., Wong-Stringer M., Game O. S., Smith J. A., Bishop J. E., Vaenas N., Freestone B. G., Coles David M., McArdle T., Buckley A. R., Lidzey D. G., (2019), Low-temperature, high-speed reactive deposition of metal oxides for perovskite solar cells, J. Mater. Chem. A, 7, 2283-2290, (DOI: 10.1039/C8TA10827G).

[93] Zhao B., Lee L. C., Yang L., Pearson A. J., Lu H., She X.-J., Cui L., Zhang K. H. L., Hoye R. L. Z., Karani A., Xu P., Sadhanala A., Greenham N. C., Friend R. H., MacManus-Driscoll J. L., Di D., (2018), In situ atmospheric deposition of ultrasmooth nickel oxide for efficient perovskite solar cells, ACS Appl. Mater. Interfaces, 10, 41849-41854, (DOI: 10.1021/acsami.8b15503).

[94] Manjunath V., Bimli S., Parmar K. H., Shirage P. M., Devan R. S., (2019), Oxidized Nickel films as highly transparent HTLs for inverted planar perovskite solar cells, Sol. Energy, 193, 387-394, (DOI: 10.1016/j.solener.2019.09.070).

[95] Liu Z., Chang J., Lin Z., Zhou L., Yang Z., Chen D., Zhang C., Liu S., Hao Y., (2018), High-performance planar perovskite solar cells using low temperature, solution–combustion-based nickel oxide hole transporting layer with efficiency exceeding 20%, Adv. Energy Mater., 8, 1703432, (DOI: 10.1002/aenm.201703432).

[96] Yin X., Zhai J., Song L., Du P., Li N., Yang Y., Xiong J., Ko F., (2019), Novel NiO nanoforest architecture for efficient inverted mesoporous perovskite solar cells, ACS Appl. Mater. Interfaces, 11, 44308-44314, (DOI: 10.1021/acsami.9b15820).

[97] Thakur U. K., Kumar P., Gusarov S., Kobryn A. E., Riddell S., Goswami A., Alam K. M., Savela S., Kar P., Thundat T., Meldrum A., Shankar K., (2020), Consistently high V_{OC} values in p-i-n type perovskite solar cells using Ni^{3+}-doped NiO nanomesh as the hole transporting layer, ACS Appl. Mater. Interfaces, 12, 11467-11478, (DOI: 10.1021/acsami.9b18197).

[98] Feng M., Wang M., Zhou H., Li W., Xie X., Wang S., Zang Z., Chen S., (2020), Optoelectronic Modulation of undoped NiO_x films for inverted perovskite solar cells via intrinsic defect regulation, ACS Appl. Energy Mater., 3, 9732-9741, (DOI: 10.1021/acsaem.0c01330).

[99] Elseman A. M., Luo L., Song Q. L., (2020), Self-doping synthesis of trivalent Ni_2O_3 as a hole transport layer for high fill factor and efficient inverted perovskite solar cells, Dalton Trans., 49, 14243-14250, (DOI: 10.1039/D0DT03029E).

[100] Boyd C. C., Shallcross R. C., Moot T., Kerner R., Bertoluzzi L., Onno A., Kavadiya S., Chosy C., Wolf E. J., Werner J., Raiford J. A., de Paula C., Palmstrom A. F., Yu Z. J., Berry J. J., Bent S. F., Holman Z. C., Luther J. M., Ratcliff E. L., Armstrong N. R., McGehee M. D., (2020), Overcoming redox reactions at perovskite-nickel oxide interfaces to boost voltages in perovskite solar cells, Joule, 4, 1759-1775, (DOI: 10.1016/j.joule.2020.06.004).

[101] Khan F., Rezgui B. D., Kim J. H., (2020), Analysis of PV cell parameters of solution processed Cu-doped nickel oxide hole transporting layer-based organic-inorganic perovskite solar cells, Sol. Energy, 209, 226-234, (DOI: 10.1016/j.solener.2020.09.007).

[102] Wang Y., Mahmoudi T., Hahn Y.-B., (2020), Highly stable and efficient perovskite solar cells based on FAMA-Perovskite-Cu:NiO composites with 20.7% efficiency and 80.5% fill factor, Adv. Energy Mater., 10, 2000967, (DOI: 10.1002/aenm.202000967).

[103] Hu Z., Chen D., Yang P., Yang L., Qin L., Huang Y., Zhao X., (2018), Sol-gel-processed yttrium-doped NiO as hole transport layer in inverted perovskite solar cells for enhanced performance, Appl. Surf. Sci., 441, 258-264, (DOI: 10.1016/j.apsusc.2018.01.236).

[104] Teo S., Guo Z., Xu Z., Zhang C., Kamata Y., Hayase S., Ma T., (2019), The Role of lanthanum in a nickel oxide-based inverted perovskite solar cell for efficiency and stability improvement, ChemSusChem, 12, 518-526, (DOI: 10.1002/cssc.201802231).

[105] Chandrasekhar P. S., Seo Y.-H., Noh Y.-J., Na S.-I., (2019), Room temperature solution-processed Fe doped NiO_x as a novel hole transport layer for high efficient perovskite solar cells, Appl. Surf. Sci., 481, 588-596, (DOI: 10.1016/j.apsusc.2019.03.164).

[106] Lee J. H., Noh Y. W., Jin I. S., Park S. H., Jung J. W., (2019), A solution-processed cobalt-doped nickel oxide for high efficiency inverted type perovskite solar cells, J. Power Sources, 412, 425-432, (DOI: 10.1016/j.jpowsour.2018.11.081).

[107] Xie Y., Lu K., Duan J., Jiang Y., Hu L., Liu T., Zhou Y., Hu B., (2018), Enhancing photovoltaic performance of inverted planar perovskite solar cells by cobalt-doped nickel oxide hole transport layer, ACS Appl. Mater. Interfaces, 10, 14153-14159, (DOI: 10.1021/acsami.8b01683).

[108] Zhang J., Mao W., Hou X., Duan J., Zhou J., Huang S., Ou-Yang W., Zhang X., Sun Z., Chen X., (2018), Solution-processed Sr-doped NiO_x as hole transport layer for efficient and stable perovskite solar cells, Sol. Energy, 174, 1133-1141, (DOI: 10.1016/j.solener.2018.10.004).

[109] Wei Y., Yao K., Wang X., Jiang Y., Liu X., Zhou N., Li F., (2018), Improving the efficiency and environmental stability of inverted planar perovskite solar cells via silver-doped nickel oxide hole-transporting layer, Appl. Surf. Sci., 427, 782-790, (DOI: 10.1016/j.apsusc.2017.08.184).

[110] Di Girolamo D., Phung N., Jošt M., Al-Ashouri A., Chistiakova G., Li J., Márquez J. A., Unold T., Korte L., Albrecht S., Di Carlo A., Dini D., Abate A., (2019), From bulk to surface: Sodium treatment reduces recombination at the nickel oxide/perovskite interface, Adv. Mater. Interfaces, 6, 1900789, (DOI: 10.1002/admi.201900789).

[111] Lee J. H., Noh Y. W., Jin I. S., Jung J. W., (2018), Efficient planar heterojunction perovskite solar cells employing a solution-processed Zn-doped NiO_X hole transport layer, Electrochim. Acta, 284, 253-259, (DOI: 10.1016/j.electacta.2018.07.178).

[112] Wan X., Jiang Y., Qiu Z., Zhang H., Zhu X., Sikandar I., Liu X., Chen X., Cao B., (2018), Zinc as a new dopant for NiO_x-based planar perovskite solar cells with stable efficiency near 20%, ACS Appl. Energy Mater., 1, 3947-3954, (DOI: 10.1021/acsaem.8b00671).

[113] Chen X., Xu L., Chen C., Wu Y., Bi W., Song Z., Zhuang X., Yang S., Zhu S., Song H., (2019), Rare earth ions doped NiO_x hole transport layer for efficient and stable inverted perovskite solar cells, J. Power Sources, 444, 227267, (DOI: 10.1016/j.jpowsour.2019.227267).

[114] Park M.-A., Park I. J., Park S., Kim J., Jo W., Son H. J., Kim J. Y., (2018), Enhanced electrical properties of Li–doped NiO_x hole extraction layer in p–i–n type perovskite solar cells, Curr. Appl. Phys., 18, S55-S59, (DOI: 10.1016/j.cap.2017.11.010).

[115] Chen W., Liu F.-Z., Feng X.-Y., Djurišić A. B., Chan W. K., He Z.-B., (2017), Cesium doped NiOx as an efficient hole extraction layer for inverted planar perovskite solar cells, Adv. Energy Mater., 7, 1700722, (DOI: 10.1002/aenm.201700722).

[116] Yin X., Han J., Zhou Y., Gu Y., Tai M., Nan H., Zhou Y., Li J., Lin H., (2019), Critical roles of potassium in charge-carrier balance and diffusion induced defect passivation for efficient inverted perovskite solar cells, J. Mater. Chem. A, 7, 5666-5676, (DOI: 10.1039/C8TA11782A).

[117] Chen P.-C., Yang S.-H., (2019), Potassium-doped nickel oxide as the hole transport layer for efficient and stable inverted perovskite solar cells, ACS Appl. Energy Mater., 2, 6705-6713, (DOI: 10.1021/acsaem.9b01200).

[118] Parida B., Yoon S., Ryu J., Hayase S., Jeong S. M., Kang D.-W., (2020), Boosting the conversion efficiency over 20% in mapbi3 perovskite planar solar cells by employing a solution-processed aluminum-doped nickel oxide hole collector, ACS Appl. Mater. Interfaces, 12, 22958-22970, (DOI: 10.1021/acsami.0c04618).

[119] Li G., Jiang Y., Deng S., Tam A., Xu P., Wong M., Kwok H.-S., (2017), Overcoming the limitations of sputtered nickel oxide for high-efficiency and large-area perovskite solar cells, Adv. Sci., 4, 1700463, (DOI: 10.1002/advs.201700463).

[120] Lai W.-C., Lin K.-W., Wang Y.-T., Chiang T.-Y., Chen P., Guo T.-F., (2016), Oxidized Ni/Au transparent electrode in efficient $CH_3NH_3PbI_3$ perovskite/fullerene planar heterojunction hybrid solar cells, Adv. Mater., 28, 3290-3297, (DOI: 10.1002/adma.201504621).

[121] Lai W.-C., Lin K.-W., Guo T.-F., Chen P., Liao Y.-Y., (2018), Efficient $CH_3NH_3PbI_3$ perovskite/fullerene planar heterojunction hybrid solar cells with oxidized Ni/Au/Cu transparent electrode, Appl. Phys. Lett., 112, 071103, (DOI: 10.1063/1.5006513).

[122] Kim J., Lee H. R., Kim H. P., Lin T., Kanwat A., Mohd Yusoff A. R. b., Jang J., (2016), Effects of UV-ozone irradiation on copper doped nickel acetate and its

applicability to perovskite solar cells, Nanoscale, 8, 9284-9292, (DOI: 10.1039/C6NR01308B).

[123] Zhou P., Li B., Fang Z., Zhou W., Zhang M., Hu W., Chen T., Xiao Z., Yang S., (2019), Nitrogen-doped nickel oxide as hole transport layer for high-efficiency inverted planar perovskite solar cells, Solar RRL, 3, 1900164, (DOI: 10.1002/solr.201900164).

[124] Wang S., Zhang B., Feng D., Lin Z., Zhang J., Hao Y., Fan X., Chang J., (2019), Achieving high performance and stable inverted planar perovskite solar cells using lithium and cobalt co-doped nickel oxide as hole transport layers, J. Mater. Chem. C, 7, 9270-9277, (DOI: 10.1039/C9TC02526J).

[125] Xia X., Jiang Y., Wan Q., Wang X., Wang L., Li F., (2018), Lithium and silver co-doped nickel oxide hole-transporting layer boosting the efficiency and stability of inverted planar perovskite solar cells, ACS Appl. Mater. Interfaces, 10, 44501-44510, (DOI: 10.1021/acsami.8b16649).

[126] Gokdemir Choi F. P., Moeini Alishah H., Bozar S., Kahveci C., Canturk Rodop M., Gunes S., (2021), First demonstration of lithium, cobalt and magnesium introduced nickel oxide hole transporters for inverted methylammonium lead triiodide based perovskite solar cells, Sol. Energy, 215, 434-442, (DOI: 10.1016/j.solener.2020.12.068).

[127] Du Y., Xin C., Huang W., Shi B., Ding Y., Wei C., Zhao Y., Li Y., Zhang X., (2018), Polymeric surface modification of NiO_x-based inverted planar perovskite solar cells with enhanced performance, ACS Sust. Chem. Eng., 6, 16806-16812, (DOI: 10.1021/acssuschemeng.8b04078).

[128] Liu Y., Duan J., Zhang J., Huang S., Ou-Yang W., Bao Q., Sun Z., Chen X., (2020), High efficiency and stability of inverted perovskite solar cells using phenethyl ammonium iodide-modified interface of NiO_x and perovskite layers, ACS Appl. Mater. Interfaces, 12, 771-779, (DOI: 10.1021/acsami.9b18217).

[129] Yin X., Zhai J., Du P., Li N., Song L., Xiong J., Ko F., (2020), 3 D NiO nanowall hole-transporting layer for the passivation of interfacial contact in inverted perovskite solar cells, ChemSusChem, 13, 1006-1012, (DOI: 10.1002/cssc.201903025).

[130] Han W., Ren G., Li Z., Dong M., Liu C., Guo W., (2020), Improving the performance of perovskite solar cells by surface passivation, J. Energy Chem., 46, 202-207, (DOI: 10.1016/j.jechem.2019.11.004).

[131] Divitini G., Cacovich S., Matteocci F., Cinà L., Di Carlo A., Ducati C., (2016), In situ observation of heat-induced degradation of perovskite solar cells, Nat. Energy, 1, 15012, (DOI: 10.1038/nenergy.2015.12).

[132] Zhang Z., Suchan K., Li J., Hetherington C., Kiligaridis A., Unger E., Scheblykin I. G., Wallentin J., (2021), Vertically aligned $CsPbBr_3$ nanowire arrays with template-induced crystal phase transition and stability, J. Phys. Chem. C, 125, 4860-4868, (DOI: 10.1021/acs.jpcc.0c11217).

[133] Gu L., Tavakoli M. M., Zhang D., Zhang Q., Waleed A., Xiao Y., Tsui K.-H., Lin Y., Liao L., Wang J., Fan Z., (2016), 3D arrays of 1024-pixel image sensors based on lead halide perovskite nanowires, Adv. Mater., 28, 9713-9721, (DOI: 10.1002/adma.201601603).

[134] Bao C., Yang J., Bai S., Xu W., Yan Z., Xu Q., Liu J., Zhang W., Gao F., (2018), High performance and stable all-inorganic metal halide perovskite-based photodetectors for optical communication applications, Adv. Mater., 30, 1803422, (DOI: 10.1002/adma.201803422).

[135] Parmar K. H., Manjunath V., Bimli S., Chikate P. R., Patil R. A., Ma Y.-R., Devan R. S., (2022), Stable and reversible electrochromic behaviors in anodic NiO thin films, Chinese J. Phys., 77, 143-150, (DOI: 10.1016/j.cjph.2022.02.014).

[136] Kitchamsetti N., Chikate P. R., Patil R. A., Ma Y.-R., Shirage P. M., Devan R. S., (2019), Perforated mesoporous NiO nanostructures for an enhanced pseudocapacitive performance with ultra-high rate capability and high energy density, CrystEngComm, 21, 7130-7140, (DOI: 10.1039/C9CE01475F).

[137] Kitchamsetti N., Ramteke M. S., Rondiya S. R., Mulani S. R., Patil M. S., Cross R. W., Dzade N. Y., Devan R. S., (2021), DFT and experimental investigations on the photocatalytic activities of NiO nanobelts for removal of organic pollutants, J Alloys Compd., 855, 157337, (DOI: 10.1016/j.jallcom.2020.157337).

[138] Qiu W., Paetzold U. W., Gehlhaar R., Smirnov V., Boyen H.-G., Tait J. G., Conings B., Zhang W., Nielsen C. B., McCulloch I., Froyen L., Heremans P., Cheyns D.,

(2015), An electron beam evaporated TiO_2 layer for high efficiency planar perovskite solar cells on flexible polyethylene terephthalate substrates, J. Mater. Chem. A, 3, 22824-22829, (DOI: 10.1039/C5TA07515G).

[139] Sun C., Alonso J. A., Bian J., (2021), Recent advances in perovskite-type oxides for energy conversion and storage applications, Adv. Energy Mater., 11, 2000459, (DOI: 10.1002/aenm.202000459).

[140] Leijtens T., Eperon G. E., Pathak S., Abate A., Lee M. M., Snaith H. J., (2013), Overcoming ultraviolet light instability of sensitized TiO_2 with meso-superstructured organometal tri-halide perovskite solar cells, Nat. Commun., 4, 2885, (DOI: 10.1038/ncomms3885).

Chapter 2
Experimental techniques

2.1 Introduction

Downscaling metal oxide to a nano regime and increasing the porosity are the key factors to enhance the surface area of the materials useful for various energy conversion and conservation applications. The porous structures formed after the organized assembling of optimized nanomaterials often increase the number of active sites for catalytic activities. Consequently, mesoporous structures are investigated more for easy evolution of H_2 and O_2 gases. Likewise, the thin films of metal oxide nanostructures are vastly used in modern-day electronic devices to form semiconductor *pn*-junctions with a controlled interface. Therefore, various techniques have been explored to prepare metal oxide nanostructures and thin films. In this chapter, we discussed the processes utilized to synthesize metal oxide nanostructures and thin films.

2.2 Synthesis methods

Considering the ease of operation, reproducibility, and precise control over the nanostructure morphologies, co-precipitation, and hydrothermal synthesis techniques were used for the synthesis of 0D, 1D, and 2D NiO nanostructure morphologies, which are further explored for electrocatalytic hydrogen/oxygen generation through water splitting. Furthermore, thermal evaporation followed by ambient oxidation is used to synthesize NiO thin films for application in photodetectors and solar cells.

2.2.1 Synthesis of 0D & 2D NiO nanostructures by co-precipitation method

Co-precipitation is a cost-effective and fast process useful for the large-scale production of nanomaterials.[1] It yields high-purity nanostructures without using hazardous chemicals at low temperatures and ambient pressure; nevertheless, controlling the crystallinity, size, and shape of the materials is challenging. Here, we aim to gain 0D and 2D nanostructure morphologies by tailoring the concentration of precursor and precipitating agents, reaction time, and processing temperature. All the precursors, reagents, and solvents were used as received without further purification. Nickel nitrate ($Ni(NO_3)_2.6H_2O$) and nickel chloride ($NiCl_2.6H_2O$) were procured from Sigma Aldrich. Sodium hydroxide (NaOH) pellets were obtained from Sisco Research Laboratories Pvt. Ltd. Ammonium hydroxide 0.35% solution (NH_4OH) and potassium hydroxide

(KOH) were procured from Loba Chemie Pvt. Ltd. Iridium oxide (IrO_2) and 5 % Nafion™ 117 solution was procured from Sigma-Aldrich. DI water was used throughout the experiment. All the glassware used in the experiments was physically and chemically inert. The NaOH (Fig. 1, upper panel) and NH_4OH (Fig. 1, lower panel) solutions were added dropwise at a constant rate to the optimized amount of homogeneous aqueous solution of $Ni(NO_3)_2.6H_2O$ prepared at room temperature. Adding NaOH and NH_4OH shoots the pH to 9 and obtains a light blue precipitate for forming 0D and porous 2D NiO morphologies, respectively. This precipitate was aged for 180 mins and subsequently dried and washed several times with DI water. Which subsequently dried at 120 ºC for 3 h and further annealed at 500 ℃ for 4 h in ambient conditions. The optimized amount of 10 mM (Fig. 2.1, upper panel) and 50 mM (Fig. 2.1, lower panel) solution of $Ni(NO_3)_2.6H_2O$ was utilized to tailor the 0D nanoparticles and 2D porous nanoplates morphologies, respectively. The NiO nanostructure morphologies were further characterized to reveal the correlation between morphological and physicochemical properties & electrocatalytic water splitting.

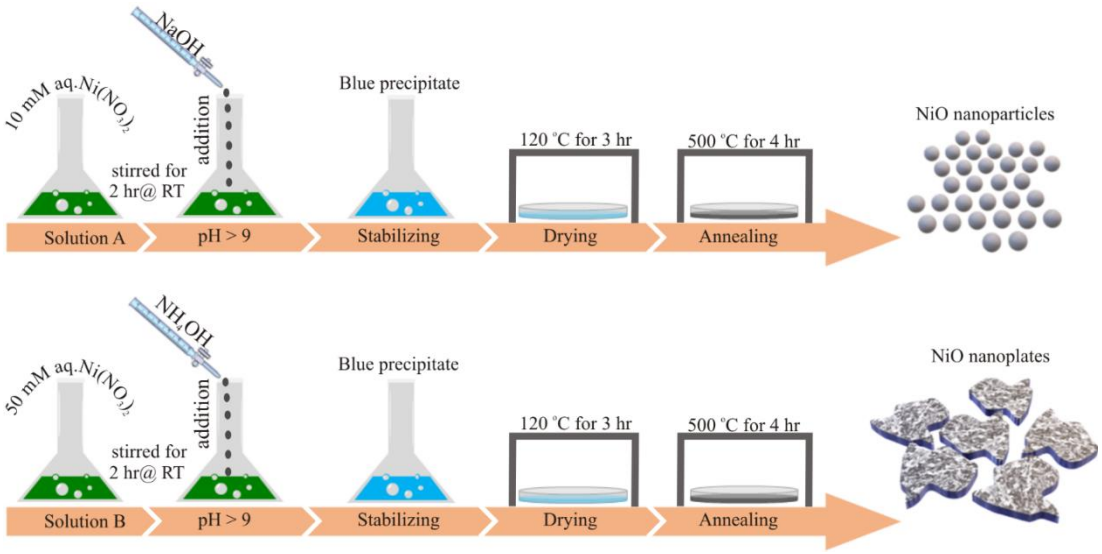

Figure 2.1 Schematics representation of the synthesis of 0D NiO nanoparticles (upper panel) and 2D porous NiO nanoplates (lower panel) using the co-precipitation method.

2.2.2 Synthesis of 1D NiO corn-like nanorods by hydrothermal method

The hydrothermal process governed by the solubility limit of the precursors in boiling water under high pressure is the heterogeneous reaction of aqueous solvents under high temperature and pressure to first dissolve and recrystallize (recover) materials that are relatively insoluble under ordinary conditions. Hydrothermal methods are usually carried out in a sealed container with a Teflon liner known as an 'autoclave' or 'high-temperature autoclave' to maintain high temperature and pressure. The morphology, size, shape, and dimension of the nanostructures can be tuned by varying the reaction time, temperature, *pH* of the solution, and precursor concentration. The pre and post-hydrothermal treatment can lead to nanostructures with high porosity and interconnected particles. Here we have optimized the hydrothermal synthesis protocol to gain the 1D NiO corn-like porous nanorods. All the precursors, reagents, and solvents were used as received without further purification. Nickel chloride ($Ni(NO_3)_2.6H_2O$), sodium oxalate ($NiCl_2.6H_2O$), Iridium oxide (IrO_2), and 5 % Nafion were procured from Sigma Aldrich. Potassium hydroxide (KOH) was procured from Loba Chemie Pvt. Ltd. Double Ionized (DI) water was used throughout the experiment. All the glassware used in the experiments was physically and chemically inert. 0.474 g $NiCl_2.6H_2O$ and 0.126 g $NiCl_2.6H_2O$ were dissolved in a mixed solvent containing 18 ml DI water and 30 ml ethylene glycol under constant stirring for 30 min. The homogeneous solution thus obtained was transferred to a Teflon liner placed in stainless steel autoclave and reacted at 180 ℃ for 12 hr. After natural cooling, the collected product was washed with DI water and ethanol several times. Further, it was dried at 60 ℃ for 2 h and annealed at 400 ℃ for 2 h to gain porous NiO nanorods. The 1D NiO corn-like nanorod morphologies were further characterized to study electrocatalytic water splitting.

2.2.3 Thermal evaporation of Ni to form NiO thin films

The NiO thin films can be formed by various approaches. NiO nanoparticle suspensions used to form NiO film produces residual ligands at low

temperatures and hamper the performance.[2] However, the physical deposition methods, such as atomic layer deposition, sputtering, laser deposition, etc., produce better-performing films with uniformity and reproducibility but involve high processing costs.[3] Therefore, cost-effective thermal evaporation, the oldest physical vapor deposition technique, was used to synthesize NiO thin films. The source material is thermally heated and evaporated (sublimation) from crucibles with an electric current or electron gun under a vacuum ($<10^{-5}$ Torr). The high-temperature heating accelerates vapor particles to move towards substrates and recover back to a solid state (Fig. 2.2). To achieve high melting points of metal, the boat or coil is energized with a large DC current.

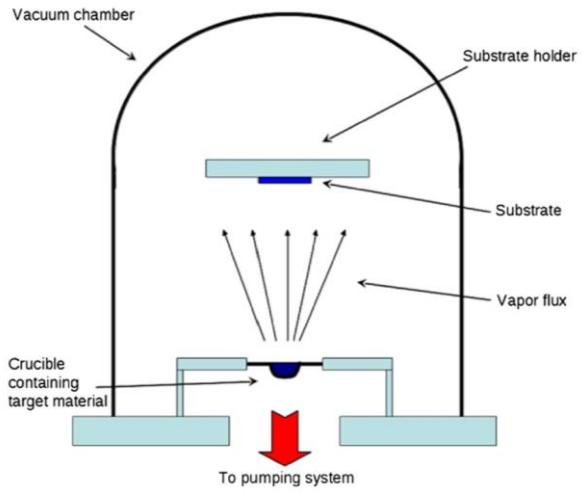

Figure 2.2 Schematic representation of thermal evaporator used for depositing Ni metal films.[4]

(a) Formation of NiO films

Nickel (99.5 %, Alfa Aesar), Lead Iodide (99.9985 %, Alfa Aesar), Methylamine Hydroiodide (TCI), [6, 6]-Phenyl C_{61} Butyric Acid Methyl Ester (PCBM) (Sigma Aldrich), N, N-Dimethylformamide (DMF) (Sigma Aldrich), Dimethyl Sulfoxide (DMSO) (Sigma Aldrich), Chlorobenzene (99.8 %, Sigma Aldrich), Ethanol (SRL Chem) and Isopropyl Alcohol (SRL Chem) were used as received. Fluorine-doped tin oxide coated glass (FTO) was cleaned sequentially with soap solution, DI water, acetone, and isopropyl alcohol and dried with hot air. After that, these films were loaded in the customized thermal

evaporator maintained at a high vacuum of $6x10^{-6}$ Torr and treated further under an argon plasma to maintain the high purity. The masked FTO was loaded over the substrate holder and kept vertically above at a distance of 10 cm from the Ni target. The Ni target was evaporated at an optimized temperature of ~1200℃ at various times, i.e., 70, 100, and 130 sec. and identified as N70, N90, and N130, respectively. Post-evaporated Ni films were further thermally oxidized in a muffle furnace at 580℃ for 3 hours without purging O_2 gas externally into the furnace to obtain NiO thin films of various morphologies.

(b) Fabrication of photodetector and solar cells using NiO thin films

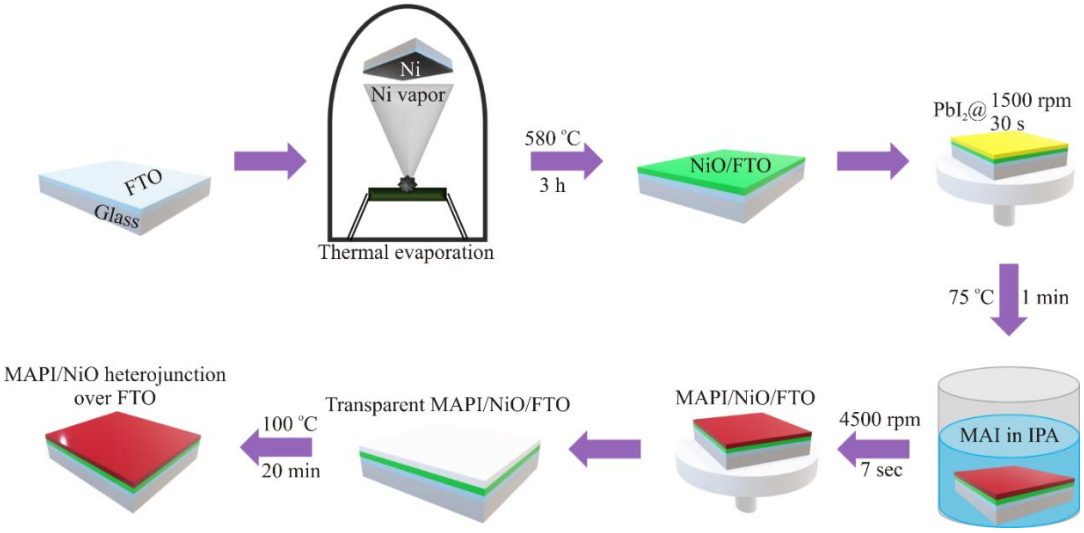

Figure 2.3 Schematic of the fabrication process of NiO/MAPI heterojunction-based photodetector and perovskite solar cell device at ambient atmospheric conditions.

The thermally evaporated NiO thin films were further subjected to the fabrication of photodetectors and solar cells. The schematic of the device fabrication process is shown in Fig. 2.3. MAPI perovskite was deposited in the ambient with a two-step deposition process. 1.2 M lead iodide dissolved in 19:1 (DMF: DMSO) for optimized time and filtered through a 0.45 μm Nylon filter, which was spin-coated on NiO films at 1500 rpm for 30 sec and further dried at 75 ℃ for 60 sec. It was further dipped in the solution of methylamine hydroiodide and isopropyl alcohol for 20 sec (10 mg/ml) to obtain reddish-brown films, which were rinsed in isopropyl alcohol to remove excess growth and

immediately spun at 4500 rpm for 10 sec to form smooth, transparent films. After heating at 100 ℃ for 30 min, transparent thin films converted into reddish-brown films were allowed to cool at room temperature. Further, Au was thermally evaporated through a shadow mask to form a counter electrode. The active area of the device was defined at 0.7 cm^2 for the photodetector. Moreover, PCBM solution in chlorobenzene (15mg/ml) was spin-coated at 3500 rpm for 20 sec over the perovskite layer to form the ETL, and Au metal contact was drawn to fabricate the PSC. Further, photodetection and solar cell studies were performed.

2.3 Material characterization techniques

The synthesized 0D, 1D, and 2D NiO nanostructures were further characterized to analyze their intrinsic and electrochemical properties. The morphology of the synthesized NiO nanostructures is analyzed using Field Emission Scanning Electron Microscopy (FESEM, JEOL, JSM-7610 F Plus). The crystal structure of the NiO is investigated from X-ray diffraction (Empyrean, Malvern-Panalytical, λ = 1.5406 Å) and further confirmed from the high-resolution images and selective area electron diffraction (SAED) obtained from Transmission Electron Microscopy (TEM, JEOL JEM-2100 F). The size distribution of nanoparticles and porous morphology of NiO nanorods are confirmed from the Small Angle X-ray Scattering (SAXS, Empyrean-DY2528, Malvern Panalytical) and BET analysis (QUANTACHROME Autosorb iQ2), respectively. Energy dispersive x-ray spectra (EDS, Oxford Instruments, X-Max^N) of NiO film were recorded to identify the elements of the films and evaluate impurities. The chemical states and electronic structure are analyzed from X-ray photoelectron spectroscopy (XPS, Thermo Scientific Inc. K_α) and Extended X-ray-Absorption Fine Structure (EXAFS, Rigaku R-XAS) analysis. Further, absorption spectroscopy of NiO films was recorded using a UV-Vis spectrophotometer (Shimadzu, UV-2600) to confirm the absorption and band-edge evaluations. Photoluminescence (PL, Dongwoo Optron DM 500i) spectra were obtained by a photoluminescence analyzer. The above-mentioned techniques are widely used in literature; thus, their details are not included in the thesis. However, application-oriented techniques such as electrochemical measurements, photosensing analysis, photovoltaic studies, and theoretical estimations are discussed in the following sections.

2.3.1 Electrochemical analysis

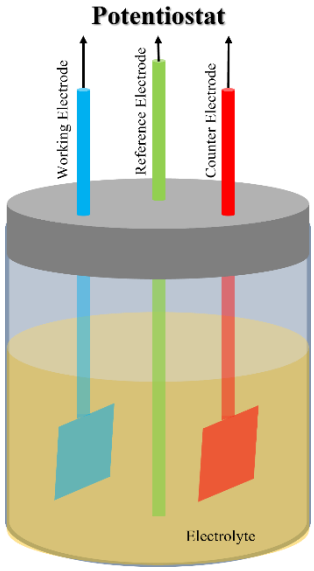

Figure 2.4 Schematic model representing three-electrode system used for electrochemical analysis.

The electrochemical measurements were performed at room temperature in ambient using Metrohm Autolab (Multichannel-204) comprising a standard three-electrode system (Fig. 2.4) equipped with Nova 2.1.4 software. The electrolyte solutions of 1 M KOH and 0.5 H_2SO_4 prepared in DI water and degassed with nitrogen gas for 30 min were used to perform OER and HER measurements, respectively. A glassy carbon electrode was used as the working electrode (3 mm diameter). After loading the catalyst over the working electrode, OER was performed in a conventional three-electrode system consisting of Hg/HgO and platinum electrode as reference and counter electrode, respectively. However, during HER, Ag/AgCl (3 M KCL) was used as a reference electrode, and a graphite rod was used as a counter electrode instead of platinum to avoid its deposition on the electrode surface, which can mislead the experimental results. OER activity was examined from the linear sweep voltammetry (LSV) and cyclic voltammetry (CV) measurements performed in the optimized potential range of 0 to 1 V vs. Ag/AgCl at a scan rate of 10 mV/s and 0.15 to 0.25 V with scan rates varying from 20 to 100 mV/s, respectively. On the other hand, HER activity was investigated from the LSV carried out in the potential

range of 0.2 V to -0.8 V vs. Ag/AgCl at a scan rate of 10 mV/s. The stability of NiO nanostructures for both OER and HER activity is analyzed by comparing the change in overpotential after 2500-3000 LSV cycles at a constant scan rate of 50 mV/s. All potentials were calibrated versus RHE for HER and OER activities using the following Nernst equations, respectively.[5]

$$E_{(RHE)} = E_{(Ag/AgCl)} + 0.059\,pH + E_{Ref} \quad (2.1)$$

$$E_{(RHE)} = E_{(Hg/HgO)} + 0.059\,pH + E_{Ref} \quad (2.2)$$

Moreover, the electrochemically active surface area (ECSA) proportional to the electrochemical double-layer capacitance (C_{dl}) is estimated from the equation[6]

$$ECSA = \frac{C_{dl}}{C_s} \quad (2.3)$$

where C_s is the specific capacitance of a flat working electrode (i.e., 40 μF/cm^2) and C_{dl} is determined from the slope of J_a or J_c *vs.* scan rate. J_a and J_c are anodic and cathodic current densities (mA/cm^2), respectively.

Further, the Tafel plot, ECSA, LSV, and Chronoamperometry(CA) analysis are utilized to interpret the overall hydrogen and oxygen evaluation performance of NiO nanostructures through electrocatalytic water splitting.

(i) Tafel plot

Tafel plot signifies the dependence of steady-state current density and variation of overpotentials (η) can be acquired from the curves of LSV. Tafel slope expresses the kinetics of the electrochemical process in HER, representing possible reaction pathways, rate-determining steps, and basic electrocatalytic performance of the catalyst under equilibrium conditions. The Tafel slope is estimated from the Tafel equation[7]

$$h = a + b \log j \quad (2.4)$$

where η is overpotential (V), a is the log of exchange current density (j_0), j is the current density (mA/cm^2), and b is the Tafel slope.

(ii) Electrochemical active surface area

The ECSA of an electrocatalyst is an essential parameter in determining the exposed active sites in the water-splitting process. The high value of ECSA

signifies the better performance of the catalyst. It is typically determined from double-layer capacitance measurements using Eq. 5 [6]

$$ECSA = \frac{C_{dl}}{C_s} \quad (2.5)$$

where C_s is the specific capacitance of a flat working electrode (F/cm^2), and C_{dl} (F) is determined from the slope of J_a or J_c *vs.* scan rate. J_a and J_c are anodic and cathodic current densities (A/m^2), respectively.

(iii) Linear sweep voltammetry

LSV is a robust electrochemical technique that uses a three-electrode system consisting of working, counter, and reference electrodes. The measurements performed from lower to higher potential sweeps in LSV are useful for irreversible systems where reverse cycling will not provide valuable information. The potential between the working and reference electrodes is regulated, and the current between the working and reference electrodes is recorded to understand and evaluate the electrochemical responses of the materials, namely, oxidation and reduction potentials. A peak or a dip in the potential is noticed depending on the oxidation or reduction of the material.

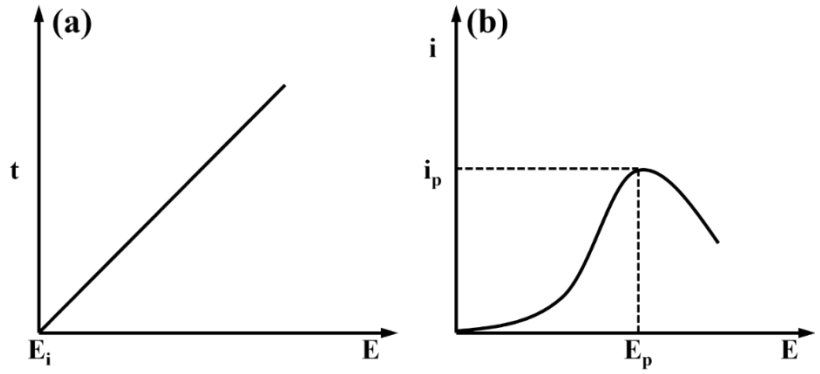

Figure 2.5 Potential waveforms of (a) linear sweep voltammetry and (b) corresponding voltammograms.

In this process, the potential of the working electrode is varied linearly with time (Fig. 2.5), i.e., before starting the reaction (no electrode reaction) to potentials where reduction (negative values) or oxidation (positive values) occurs; therefore, the instantaneous potential is given by

$$E_t = E_i \pm vt \quad (2.6)$$

where E_t is the instantaneous potential (V), E_i is the starting potential (V), and v is the scan rate (V/s).

(iv) Chronoamperometry

The time-dependent variation in the current (faradic process) at an applied potential in electrochemical processes is referred to as CA. Therefore, CA is extensively used in diffusion-controlled electrochemical studies at the electrode. CA experiments are usually performed to examine the electrochemical activity and stability of the electrocatalysts due to the change in electrode current observed with the diffusion of electrolyte ions on the electrode surface. The long-term stability of NiO nanostructures for 20 h as an electrocatalyst was tested using CA at constant overpotential.

2.3.2 Photosensing analysis

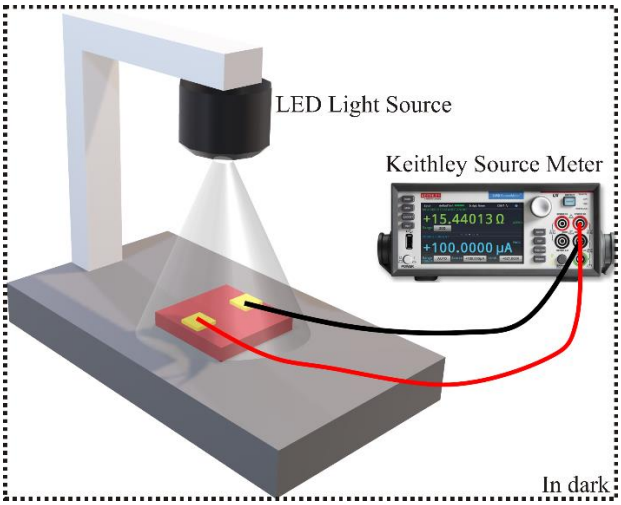

Figure 2.6 Schematics depicting the customized setup for measuring the photodetector response.

Photo-sensing studies on the self-powered PD were performed in the ambient utilizing a customized setup (Fig. 2.6) placed inside a dark box to ensure the absence of any external light. The light source was interfaced with a programmable 'Aurdino board' to control the wavelength and on-off cycles. Keithley source meter interfaced with a computer was used to measure the optical response. Steady LED light sources of various wavelengths, i.e., 290, 450, 540, and 640 nm with a constant power of 1.15 mW, were used to perform

the photosensing studies. A minimum of 4 on/off cycles of photo illumination were studied for each wavelength with the sequential periodicity of 30 s light On and Off. ΔI evaluated for the 90% change (Fig. 2.7) in the I_{light} during light On and Off as shown in Eq. 2.7.[8] The sensitivity (S) at a different probing wavelength was calculated with Eq. 2.8. The ratio of On current to that of Off current was calculated from Eq. 2.9. The ability to generate photocurrent per incident power (P_{in}) per illumination area (A) is given by responsivity (R) shown in Eq. 2.10. Conversely, detectivity (D*) is defined as the ability of the self-powered NiO/MAPI heterojunction to detect minimum optical signal above the noise and is shown in Eq. 2.11.[9, 10] The rise time (T_r), the time required for NiO/MAPI PD to switch from Off state to On state, was defined as the time required for the I_{dark} to reach 90% of I_{light}. Similarly, the fall time (T_f) was the time required to switch from 90 % I_{light} to I_{dark}.

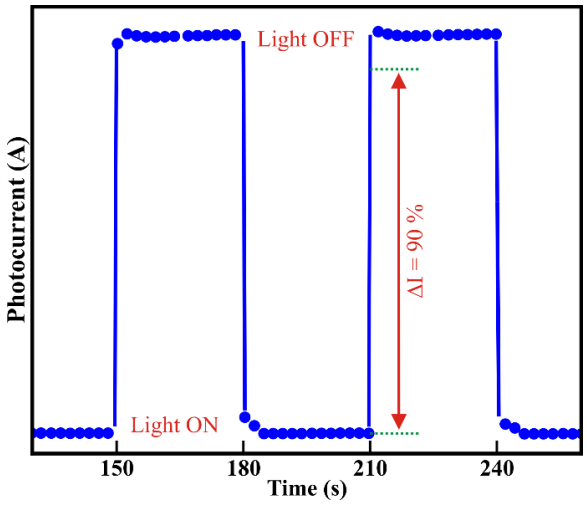

Figure **2.7** Schematics depicting 90 % of photocurrent.

Overall, the key parameter to understand the performance of PD was calculated using the equations [11]

$$\Delta I = 90\%\ of\ I_{light} - I_{Dark} \tag{2.7}$$

$$S = \frac{(90\%\ of\ I_{light} - I_{Dark})}{I_{Dark}} \tag{2.8}$$

$$\frac{On}{off} ratio = \frac{I_{light}}{I_{Dark}} \tag{2.9}$$

$$R = \frac{I_{Photo}}{P_{in}} \tag{2.10}$$

$$D^* = \frac{R}{\sqrt{2qJ_{dark}}} \tag{2.11}$$

where P_{in} is the incident light energy (1000 W/m^2) and J_{dark} is the dark current density (mA/cm^2).

2.3.3 Photovoltaic studies

Figure 2.8 Photographic image of Class AAA solar simulator.

The electromagnetic waves at the surface of the earth are affected by several factors, including diffused radiation. The total radiation received at the earth's surface, called global radiation, accounts for the direct and diffused radiation considering the sun as a spherical source (1.39 million km diameter) at a distance of 1 astronomical unit from the earth. Further, the radiation entering the earth's atmosphere undergoes various path differences due to scattering and absorption by various molecules. Therefore, solar radiation, termed as air mass 0 or AM 0 G before entering the earth's surface, is considered AM 1 G at sea level when the sun is precisely overhead (usually at the equator) and passes through one complete air mass. The air mass is relative to AM 1 G for other zenith angles or high-altitude sites. However, the global standard AM 1.5 G is considered with an irradiance of 1000 W/m^2, which is used in the solar simulator utilized for our present study. Fig. 2.8 shows the photograph of a class AAA solar simulator providing the closest possible spectral match with the solar

spectrum from any source. A typical solar simulator consists of a light source (xenon arc lamp), AM 1.5 G filter, a collimator, and a measurement meter (Keithley meter). The geometry of the simulator ensures a spectrum similar to a 5800 K blackbody with occasional line structures striking the sample. The I-V plot (Fig. 2.8) obtained after illuminating the device under the solar simulator is further analyzed to figure out the performance of the solar devices from the parameters such as short circuit current, open-circuit voltage, fill factor, power conversion efficiency, etc.; as follows[12],

(a) Short circuit current (I_{SC})

I_{SC}, defined as the maximum current flowing through the solar cell at 0 bias (short circuit), is given by Eq. 2.12.

$$I_{SC} = I_S \left[exp\left(\frac{qV}{kT}\right) - 1\right] - I_L \tag{2.12}$$

where I_S is the diode current (A), q is the charge of an electron (eV), V is the open-circuit voltage (V), k is the Boltzman constant (1.380649×10^{-23} $m^2kg.s^{-2}$ K^{-1}), T is the temperature (K), and I_L is photogenerated current (A).

(b) Open cicuit voltage (V_{OC})

V_{OC}, defined as the voltage across the solar cell when the current is 0 (open circuit), is given by Eq. 2.13.

$$V_{OC} = \frac{kT}{q} ln\left(\frac{I_L}{I_S} + 1\right) \approx \frac{kT}{q} ln\left(\frac{I_L}{I_S}\right) \tag{2.13}$$

(c) Fill factor (FF)

FF, defined as the ratio of actual maximum power generated by the solar cell to the ideal power, is given by Eq. 2.14.

$$FF = \frac{V_{MP} \times I_{MP}}{I_{SC} \times V_{OC}} \tag{2.14}$$

where V_{MP} and I_{MP} are open-circuit voltage (V) and short-circuit current (A) at maximum power.

(d) Power conversion efficiency (PCE)

PCE, the ratio of the output power delivered by the solar cell to the incident power (1000 W/m^2), is given by Eq. 2.15.

$$PCE = \frac{I_{SC} \times V_{OC} \times FF}{P_{in} \times AA} \quad (2.15)$$

where AA is the active area of the solar cell (cm^2).

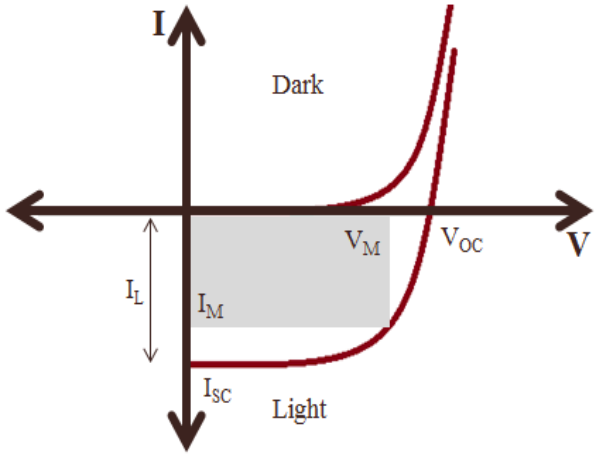

Figure 2.9 The I-V plot of the solar cell in the dark (1st quadrant), under illumination (4th quadrant), and the grey box depicts the FF.

2.3.4 Theoretical analysis of solar cells using SCAPS-1D

Theoretical analysis of all oxide solar cells is performed in the present study to address the degradation issue typically observed at the interface and in the absorber layer of the PSCs. SCAPS-1D program developed at Gent University, Belgium,[13] is utilized to understand the overall performance of the solar cells at various optimized conditions. In fact, SCAPS is an incredible asset that breaks down and simulates heterojunction and multijunction solar cells. SCAPS-1D simulation includes loading the required physical properties of subsequent layers of solar cells to solve the second-order semiconductor differential equation in one direction by applying boundary conditions at the interfaces. Further, the values of the physical and interfacial defects can be varied and evaluated at the boundary conditions (interface of thin films).

The fundamental semiconductor equations extract charge carrier transport parameters under steady-state conditions. Poisson equation (Eq. 2.16), which represents the relationship between space charge density (ρ) and electric field I, is given below by [14, 15]

$$\frac{\rho}{\epsilon} = -\left(\frac{\partial^2 \psi}{\partial x^2}\right) = \frac{q}{\epsilon}[-n(x) + p(x) - N_A^-(x) + N_D^+(x) - n_t(x) + p_t(x)] = \frac{\partial E}{\partial x} \quad (2.16)$$

Continuity equations for the electron (Eq. 2.17) and holes (Eq. 2.18) under the steady-state condition, which dictate the charge transport in the semiconductor, are given by,

$$G_n - \frac{n-n_0}{\tau_n} + n\mu_n \frac{\partial E}{\partial x} + \mu_n E \frac{\partial n}{\partial x} + D_n \frac{\partial^2 n}{\partial x^2} = \frac{\partial n}{\partial t} \quad \text{(for electron)} \quad (2.17)$$

$$G_p - \frac{p-p_0}{\tau_p} + p\mu_p \frac{\partial E}{\partial x} + \mu_p E \frac{\partial p}{\partial x} + D_p \frac{\partial^2 p}{\partial x^2} = \frac{\partial p}{\partial t} \quad \text{(for holes)} \quad (2.18)$$

The charge carrier transport occurring by drift and diffusion for electrons (Eq. 2.19) and holes (Eq. 2.20) are given by,

$$J_n = n\mu_n \frac{\partial E_{Fn}}{\partial x} = q[n\mu_n E + D_n \frac{\partial n}{\partial x}] \quad \text{(for electron)} \quad (2.19)$$

$$J_p = p\mu_p \frac{\partial E_{Fp}}{x} = q[p\mu_p E - D_p \frac{\partial p}{\partial x}] \quad \text{(for hole)} \quad (2.20)$$

where ϵ is the permittivity of the material, ψ is the electrostatic potential, q is the electron charge, $N_D^+(N_A^-)$ is the density of ionized donors (acceptors), n (p) is the electron (hole) concentration, $n_t(p_t)$ is the trapped electron (hole), $G_n(G_p)$ is the electron (hole) generation rates $\tau_n(\tau_p)$ is the electron (hole) lifetime, $D_n(D_p)$ is the diffusion coefficients for the electron (hole), $\mu_n(\mu_p)$ is the electron (hole) mobilities, $E_{Fn}(E_{Fp})$ is the quasi-Fermi levels for the electron (hole), J_n (J_p) is the electron (hole) current density, respectively.

2.4 References

[1] Wu W., Jiang C. Z., Roy V. A. L., (2016), Designed synthesis and surface engineering strategies of magnetic iron oxide nanoparticles for biomedical applications, Nanoscale, 8, 19421-19474, (DOI: 10.1039/C6NR07542H).

[2] Qiu W., Paetzold U. W., Gehlhaar R., Smirnov V., Boyen H.-G., Tait J. G., Conings B., Zhang W., Nielsen C. B., McCulloch I., Froyen L., Heremans P., Cheyns D., (2015), An electron beam evaporated TiO_2 layer for high efficiency planar perovskite solar cells on flexible polyethylene terephthalate substrates, J. Mater. Chem. A, 3, 22824-22829, (DOI: 10.1039/C5TA07515G).

[3] Abzieher T., Moghadamzadeh S., Schackmar F., Eggers H., Sutterlüti F., Farooq A., Kojda D., Habicht K., Schmager R., Mertens A., Azmi R., Klohr L., Schwenzer J. A., Hetterich M., Lemmer U., Richards B. S., Powalla M., Paetzold U. W., (2019),

Electron-beam-evaporated nickel oxide hole transport layers for perovskite-based photovoltaics, Adv. Energy Mater., 9, 1802995, (DOI: 10.1002/aenm.201802995).

[4] Bashir A., Awan T. I., Tehseen A., Tahir M. B., Ijaz M. Chapter 3 - Interfaces and surfaces. In: Awan TI, Bashir A, Tehseen A, editors. Chemistry of Nanomaterials: Elsevier; 2020. p. 51-87.

[5] Singh H., Biswas R., Ahmed I., Thakur P., Kundu A., Panigrahi A. R., Banerjee B., Halder K. K., Lahtinen J., Mondal K., Haldar K. K., (2022), Dumbbell-shaped ternary transition-metal (Cu, Ni, Co) phosphate bundles: A promising catalyst for the oxygen evolution reaction, ACS Appl. Mater. Interfaces, 14, 6570-6581, (DOI: 10.1021/acsami.1c20356).

[6] Prasannachandran R., Vineesh T. V., Anil A., Krishna B. M., Shaijumon M. M., (2018), Functionalized phosphorene quantum dots as efficient electrocatalyst for oxygen evolution reaction, ACS Nano, 12, 11511-11519, (DOI: 10.1021/acsnano.8b06671).

[7] Shinagawa T., Garcia-Esparza A. T., Takanabe K., (2015), Insight on Tafel slopes from a microkinetic analysis of aqueous electrocatalysis for energy conversion, Sci. Rep., 5, 13801, (DOI: 10.1038/srep13801).

[8] Li C., Han C., Zhang Y., Zang Z., Wang M., Tang X., Du J., (2017), Enhanced photoresponse of self-powered perovskite photodetector based on ZnO nanoparticles decorated $CsPbBr_3$ films, Sol. Energy Mater. Sol. Cells, 172, 341-346, (DOI: 10.1016/j.solmat.2017.08.014).

[9] Qi Z., Fu X., Yang T., Li D., Fan P., Li H., Jiang F., Li L., Luo Z., Zhuang X., Pan A., (2019), Highly stable lead-free $Cs_3Bi_2I_9$ perovskite nanoplates for photodetection applications, Nano Res., 12, 1894-1899, (DOI: 10.1007/s12274-019-2454-0).

[10] Hussain A. A., Rana A. K., Ranjan M., (2019), Air-stable lead-free hybrid perovskite employing self-powered photodetection with an electron/hole-conductor-free device geometry, Nanoscale, 11, 1217-1227, (DOI: 10.1039/C8NR08959K).

[11] Hussain A. A., (2020), Constructing Caesium-based lead-free perovskite photodetector enabling self-powered operation with extended spectral response, ACS Appl. Mater. Interfaces, 12, 46317-46329, (DOI: 10.1021/acsami.0c14083).

[12] Hodes G., (2012), Photoelectrochemical cell measurements: Getting the basics right, J. Phys. Chem. Lett., 3, 1208-1213, (DOI: 10.1021/jz300220b).

[13] Niemegeers A., Burgelman M., Herberholz R., Rau U., Hariskos D., Schock H.-W., (1998), Model for electronic transport in Cu(In,Ga)Se_2 solar cells, Prog. Photovolt.: Res. Appl., 6, 407-421, (DOI: 10.1002/(SICI)1099-159X(199811/12)6:6<407::AID-PIP230>3.0.CO;2-U).

[14] Alla M., Bimli S., Manjunath V., Samtham M., Kasaudhan A., Choudhary E., Rouchdi M., Boubker F., (2022), Towards lead-free all-inorganic perovskite solar cell with theoretical efficiency approaching 23%, Mater. Technol., 1-7, (DOI: 10.1080/10667857.2022.2091195).

[15] Alla M., Manjunath V., Chawki N., Singh D., Yadav S. C., Rouchdi M., Boubker F., (2022), Optimized $CH_3NH_3PbI_{3-X}Cl_X$ based perovskite solar cell with theoretical efficiency exceeding 30%, Opt. Mater., 124, 112044, (DOI: 10.1016/j.optmat.2022.112044).

Chapter 3

0D and 2D NiO nanostructures for hydrogen evolution

3.1 Introduction

With the depletion of fossil fuels, it is vital to find alternate fuel sources. Among all available fuel sources, water splitting by either cathodic hydrogen evolution reaction (HER) or anodic oxygen evolution reaction (OER) has been established as the most economical and clean source which can pave the way to a sustainable future.[1] In general, both HER and OER in acidic and alkaline mediums, respectively, are imperative to determine the overall efficiency of water splitting.[2] At the cathode, HER occurs at a smaller overpotential than the thermodynamic potential due to the involvement of $2e^-$ and $2H^+$. However, OER involves the transfer of $4e^-$ and $4OH^-$ ions at the anode, becoming the rate-determining step in overall water splitting.[3] Precious metals like Pt and Ru, or/and Ir oxides, are of attraction to the scientific community for HER and OER, respectively, delivering relatively better water-splitting efficiencies.[4] However, researchers have devoted efforts to find cheaper alternatives in transitional metal-based chalcogenides, intermetallics, carbides, nitrides, phosphides, and layered materials.[5, 6] Nevertheless, these alternatives possess toxic elements like Se, S, P, and N. Therefore, water-splitting electrocatalyst comprises first-row transitional metals, such as Nickel (Ni), Cobalt (Co), Iron (Fe), etc., and their derivatives have fascinated researchers due to superior electrochemical stability and redox chemistry.[7] Conversely, metal oxides have gained tremendous research momentum due to their multifunctional applications in solar cells,[8-16] gas sensors,[17] electrochromic films,[18, 19] energy storage,[20, 21] photodetectors,[22], etc. Further, nanostructure morphologies offering larger volume, better electronic confinement, and increased surface-to-volume ratio, along with controlled defect states, provide precise control over optical and electrical properties in various morphological forms (i.e., 0D, 1D, and 2D), which influences the overall performance.[23] The use of 0D nanostructures in the form of quantum dots (QD) and nanoparticles as electrocatalysts or co-catalyst with another host for producing hydrogen are of great interest because of their unique electronic and surface properties.[24] On the other hand, the 2D nanomaterials such as heteroatomic graphene, transition metal dichalcogenides, layered double hydroxides, graphite carbon nitride (g-C_3N_4), etc. are also appropriate candidates for efficient catalysis owing to their high specific surface area, remarkable mechanical properties, and high activity, and stability.[5, 25, 26] Flexibility in the charge

transfer directions of 2D nanomaterials can significantly contribute to reducing the overpotential for OER and HER activity. Moreover, in contrast to 0D nanomaterials, the heterostructures of 2D nanomaterials can shift the edges of the conduction and lithium-ions, leading to a significant shift in the potential for hydrogen and oxygen evolution reactions.[27] Therefore, considerable efforts need to be focused on understanding the effect of morphology on electrocatalytic water splitting using metal oxide nanostructures.

Nickel oxide (NiO) has gained considerable attention due to its flexibility in tailoring the crystalline phases, i.e., cubic, monoclinic, rhombohedral, and hexagonal, and the chemical composition, i.e., NiO, Ni_2O, and Ni_2O_3 for multifunctional applications.[28] Despite these advances, because of the low conductivity and limited catalytic sites, the HER or OER performance of bare NiO still needs to be improved. Therefore, several dopants,[6] composites, defect engineering, and modulation of electronic structures of NiO are explored to enhance the water-splitting efficiency.[26, 29] NiO hollow spheres synthesized by the spray drying method could deliver OER and HER activity at a relatively higher overpotential of 370 mV and 424 mV (at the current density of 10 mA/cm^2), respectively.[30] HER activity of ultra-thin NiO nanosheets (an overpotential of 57 mV at the current density of 10 mA/cm^2) was improved further by forming its hybrids with platinum nanoparticles.[31] However, in search of further improvements, Fe-doped NiO mesoporous nanosheet arrays deposited over Ni foam were explored to gain better OER activities. Still, it required an overpotential of 206 mV to achieve a current density of 10 mA/cm^2.[32] Nevertheless, the composite of NiO and Co_3O_4 formed to gain better HER, and OER activities could deliver the low Tafel slope of 101 and 61 mV/dec, respectively.[33] The NiO@$Co_{0.5}Fe_{0.5}P$ core-shell heterostructures revealed OER and HER activities at an overpotential of 262 and 73 mV at a current density of 10 mA/cm^2, respectively.[34] Notably, the small overpotential of 49.48 mV at a current density of 10 mA/cm^2 towards HER reactions was achieved from the hierarchical porous prism arrays comprising Ni-NiO embedded in graphite carbon grown over nickel foam.[35] However, to our knowledge, hardly any articles in the literature report the effect of morphology on the electrocatalytic water-splitting capabilities of NiO nanostructures.

Numerous techniques such as hydrothermal,[36] sol-gel,[37] co-precipitation,[38] thermal combustion,[39] electrospinning,[34] ball milling,[41] pulse ablation,[42]

aerosol,[43] flame pyrolysis,[44] molten salt protected pyrolysis,[45, 46] have been explored for the synthesis of a variety of NiO morphologies. In the present study, the co-precipitation method, which provides control over shape, dimensionality, and size with high yield, has been opted to tailor the 0D and 2D morphologies of NiO. The synthesized NiO nanostructures are characterized thoroughly to understand the crystal structure, chemical states, and morphology variation. Further, the nanostructures are employed for overall water splitting. Although NiO nanoparticles and nanoplates showed OER and HER activity, superior performance is recorded for 0D NiO nanoparticles owing to their increased electrochemically active sites. Additionally, the measurements showcased the excellent stability of 0D NiO nanoparticles in both basic and acidic mediums for overall water splitting.

3.2 Experimental Section

3.2.1 Chemical and reagents

All the precursors, reagents, and solvents were used as received without further purification. Nickel nitrate ($Ni(NO_3)_2.6H_2O$) and nickel chloride ($NiCl_2.6H_2O$) were procured from Sigma Aldrich. Sodium hydroxide (NaOH) pellets were obtained from Sisco Research Laboratories Pvt. Ltd. Ammonium hydroxide 0.35% solution (NH_4OH) and potassium hydroxide (KOH) were procured from Loba Chemie Pvt. Ltd. Iridium oxide (IrO_2) and 5 % Nafion™ 117 solution was procured from Sigma-Aldrich. DI water was used throughout the experiment. All the glassware used in the experiments was physically and chemically inert.

3.2.2 Synthesis of NiO nanostructures

NaOH solution was added dropwise at a constant rate to the optimized amount of homogeneous aqueous solution of $Ni(NO_3)_2.6H_2O$ prepared at room temperature to shoot the pH to 9 and obtain a light blue precipitate. This precipitate was aged for 180 min and subsequently dried and washed several times with DI water. Further, the precipitate was dried at 120 ^oC for 3 h and annealed at 500 °C for 4 h in ambient conditions. The optimized amount of 10

mM (Fig. 2.1, upper panel) and 50 mM (Fig. 2.1, lower panel) solution of $Ni(NO_3)_2.6H_2O$ was utilized to tailor the 0D nanoparticles and 2D porous nanoplates morphologies, respectively. The NiO nanostructure morphologies were further characterized to reveal the correlation between morphological and physicochemical properties and electrocatalytic water splitting.

3.2.3 Characterization

The morphology of the synthesized NiO nanostructures is analyzed using Field Emission Scanning Electron Microscopy (FESEM, JEOL, JSM-7610 F Plus). The crystal structure of the NiO is investigated from X-ray diffraction (Empyrean, Malvern-Panalytical, $\lambda = 1.5406$ Å) and further confirmed from the high-resolution images and selective area electron diffraction (SAED) obtained from Transmission Electron Microscopy (TEM, JEOL JEM-2100 F). The size distribution and porous morphology of the NiO are confirmed from the Small Angle X-ray Scattering (SAXS, Empyrean Malvern Panalytical) analysis. The chemical states and electronic structure are analyzed from X-ray photoelectron spectroscopy (XPS, Thermo Scientific Inc. K-alpha) and Extended X-ray-Absorption Fine Structure (EXAFS, Rigaku R-XAS) analysis.

3.2.4 Electrochemical measurements

Initially, a homogenous electrocatalyst ink is prepared by dissolving and sonicating 3.5 mg of catalyst in a mixed solvent containing 600 µL of DI water and 380 µL of ethanol. 20 µL 5% Nafion solution is added to the ink, then sonication for another 20 min. Finally, the as-prepared ink is drop-cast over the glassy carbon electrode of 3 mm diameter and dried in a vacuum desiccator at ambient conditions to further used as the working electrode (WE) to study the overall water splitting. The typical mass of 0.247 mg/cm^2 loaded electrocatalyst is used to perform electrochemical measurements at room temperature in ambient using Metrohm Autolab (Multichannel-204) comprising a standard three-electrode system equipped with Nova 2.1.4 software. The electrolyte solutions of 1 M KOH and 0.5 H_2SO_4 prepared in DI water and degassed with nitrogen gas for 30 min are subjected to perform OER and HER measurements,

respectively. OER was performed in a conventional three-electrode system consisting of Hg/HgO and platinum electrode as reference and counter electrode, respectively. However, during HER, Ag/AgCl (3 M KCL) was used as a reference electrode, and a graphite rod was used as a counter electrode instead of platinum to avoid its deposition on the electrode surface, which can mislead the experimental results. OER activity was examined from the LSV and CV measurements performed in the optimized potential range of 0 to 1 V vs. Ag/AgCl at a scan rate of 10 mV/s and 0.15 to 0.25 V with scan rates varying from 20 to 100 mV/s, respectively. On the other hand, HER activity was investigated from the LSV carried out in the potential range of 0.2 V to -0.8 V vs. Ag/AgCl at a scan rate of 10 mV/s. The long-term stability of NiO nanoparticles for 20 h is tested using CA at a constant overpotential of 373 and 268 mV for OER and HER activity, respectively. The stability of NiO nanoparticles for both OER and HER activity is analyzed by comparing the change in overpotential after 2500 LSV cycles at a constant scan rate of 50 mV/s. All potentials were calibrated versus RHE using the Nernst equations 2.1 and 2.2. Moreover, the ECSA proportional to the C_{dl} is estimated from equation 2.3 [47-49]

3.3 RESULT AND DISCUSSION

3.3.1 X-ray diffraction

Rietveld refinement of the XRD pattern shown in Fig. 3.1 indicates the observed and calculated patterns, difference curves, and the Bragg reflections and confirms the crystallinity of NiO nanostructures. Both 0D NiO nanoparticles and 2D NiO nanoplates crystalized into a cubic structure with an $Fm\bar{3}m$ space group. The characteristic XRD peaks of both 0D NiO nanoparticles (Fig.3.1(a)) and 2D NiO nanoplates (Fig. 3.1(b)) observed at 2θ of 37.33°, 43.38° and 63.03° corresponds to (111), (020) and (022) planes, respectively (ICSD No. 1010093). The value of goodness of fitting factors such as R_{EXP}, R_{WP}, R_P, GoF, and the estimated lattice parameters (i.e., a, b, c) and cell volume (V) of 0D NiO nanoparticles and 2D porous nanoplates are listed in Table 3.1. Overall, the

Rietveld analysis confirms the formation of cubic crystalline pure NiO phase in 0D nanoparticles and 2D nanoplates.

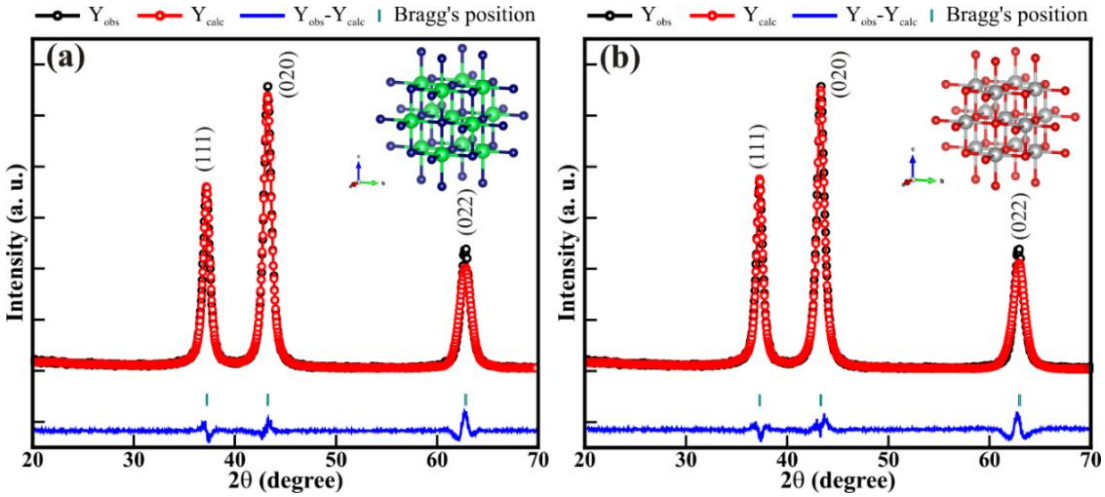

Figure 3.1 Rietveld refinement of XRD pattern of (a) 0D NiO nanoparticles and (b) 2D NiO nanoplates. The inset shows the crystal structure of the corresponding nanostructures.

Table 3.1 Various parameters estimated from the Rietveld refinement of the XRD spectra of NiO nanoparticles and nanoplates.

Parameters	0D NiO nanoparticles	2D porous NiO nanoplates
R_{Brag}	0.763	1.02
R_p	6.93	8.71
R_{EXP}	5.97	6.11
R_{wp}	9.02	11.9
RF	0.460	0.514
GoF	2.28	3.82
a=b=c (Å)	4.185	4.177
V (g/cc)	73.32	72.89

3.3.2 Microscopic and structural analysis

The surface morphology and crystal structure of the NiO nanostructures are evaluated from the FESEM and TEM analysis. The high magnification FESEM images in Fig. 3.2 show the distribution of homogenous NiO

nanoparticles (Fig. 3.2(a)) and NiO nanoparticles. The close observation of Fig. 3.2(b) shows the growth of porous 2D NiO nanoplates. The TEM image in the inset of Fig. 3.2(a)) confirms the formation of 0D NiO nanoparticles of diameter size < 10 nm. Where inset of Fig.3.2(b) represents that the porous layers of NiO lead to the growth of 2D nanoplates, but the actual number of atomic layers present in the NiO nanoplates is still unknown.

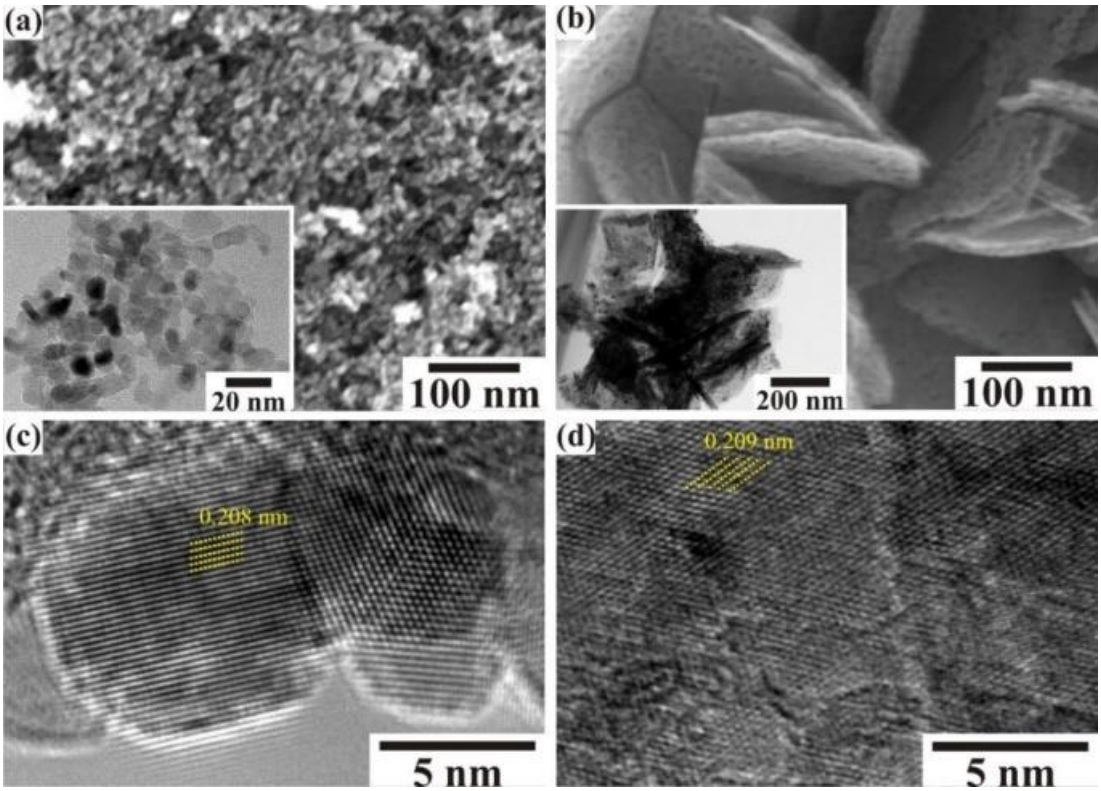

Figure 3.2 High magnification FESEM images of (a) 0D NiO nanoparticles and (b) 2D porous NiO nanoplates and (c, d) their corresponding high-resolution TEM images. The inset of (a) and (b) shows the TEM images of the corresponding nanostructure morphologies. The yellow lines in (c) and (d) indicate the interplanar spacing of the NiO nanoparticles and NiO nanoplates nanostructures.

Further, HRTEM images validate the crystal structure of both nanostructures. The HRTEM image in Fig. 3.2(c) revealed the well-crystalline nature of NiO nanoparticles with clearly visible textural boundaries. The uniformly distributed ordered lattice planes, with an interplanar spacing of 0.208 nm corresponding to the (020) plane, confirmed the formation of single-

crystalline NiO nanoparticles in the cubic crystalline phase. However, the HRTEM images Fig. 3.2(d) show ordered lattice planes throughout with some discontinuities, representing the alteration due to the porous nature of the nanoplates. The interplanar spacing of 0.209 nm observed for porous NiO nanoplates is akin to that of NiO nanoparticles and assigned to the (020) plane, ascertaining the formation of cubic crystalline NiO nanoplates. This confirms the tailoring of 0D and 2D nanostructure morphology of NiO without altering the cubic crystalline phase while controlling the concentration of precursors and precipitating agents in the reaction mixture.

3.3.3 Small-angle X-ray scattering

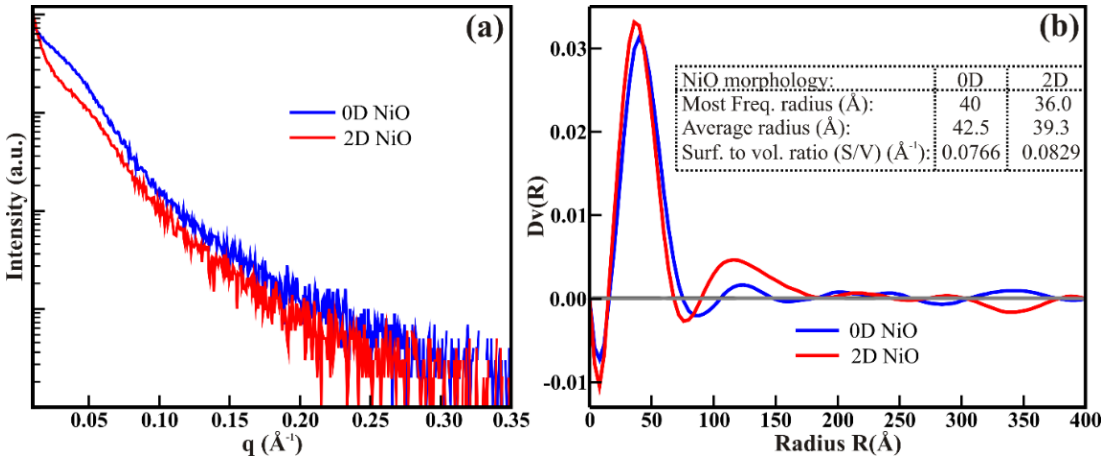

Figure 3.3 (a) SAXS profile and (b) corresponding fitting of the 0D NiO nanoparticles and porous 2D NiO nanoplates.

Further, the SAXS profile of the 0D NiO nanoparticles and porous 2D NiO nanoplates recorded in the 2θ range of 0 to 5° is shown in Fig. 3.3(a), and their analysis/fitting performed using EasySAXS software is provided in Fig. 3.3(b). The best-fitting outcome is provided in the inset of Fig. 4(b). Most of the 0D NiO nanoparticles assumed to be spherical in shape are of diameter 8 nm, exhibiting a surface-to-volume ratio of 0.77/Å. The average diameter of the nanoparticles is 8.5 nm. On the other hand, most of the porous present on the 2D NiO nanoplates assumed to be spherical is of diameter 7.2 nm and delivers a surface-to-volume ratio of 0.082/Å. The average diameter of pores on nanoplates is 7.9 nm. Even though the surface-to-volume ratio of pores on nanoplates is

relatively better, the formation of nanopores has failed to augment the accessible surface area in the nanoplates like the nanoparticle. This demonstrates that the 0D nanoparticles can provide a much larger accessible surface area for electrocatalytic reactions than the wider 2D nanoplates despite the small pores over them.

3.3.4 BET adsorption-desorption isotherm

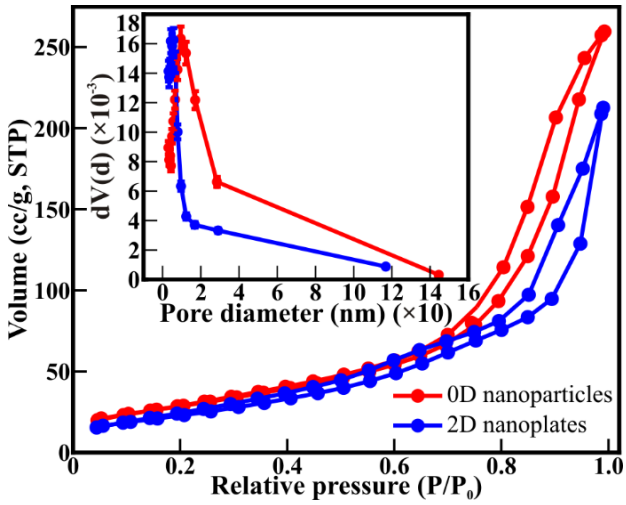

Figure 3.4 BET adsorption-desorption isotherms of the 0D NiO nanoparticles and porous 2D NiO nanoplates. The inset represents the corresponding BJH pore size distribution.

The surface area and porosity play a significant role in catalytic water-splitting activities.[50] Therefore, pore size distribution and surface area are estimated from N_2 adsorption-desorption (Fig. 3.4). A distinct hysteresis loop observed for NiO nanoparticles, and nanoplates morphologies are of type IV isotherm and indicate the porous nature. The specific surface area of 106.02 m^2/g obtained for 0D NiO nanoparticles is relatively larger than the 2D nanoplates (i.e., 87.46 m^2/g). The larger pore volume of 0.40 cc/g of the 0D NiO nanoparticles than that of 2D NiO nanoplates (i.e., 0.32 cc/g) is expected to provide better larger surface-active sites for the electrocatalytic activities. The pore size distributions (inset of Fig. 5) are observed in the range of 3 to 144 and 3 to 116 nm for nanoparticles and porous nanoplates, respectively. However, an

average (mean) pore diameter of 9.45 and 5.67 nm observed for 0D and 2D morphologies of NiO, respectively, indicates the more accessible surface area/sites from the 0D nanoparticles compared to porous 2D nanoplates. Overall, BET analysis is akin to the SAXS profile and confirms that the 0D NiO nanoparticles offer higher electrochemically active sites on the surface for OER and HER activity than the wider 2D NiO nanoplates despite the tiny pores over them.

3.3.5 X-ray photoelectron spectroscopy

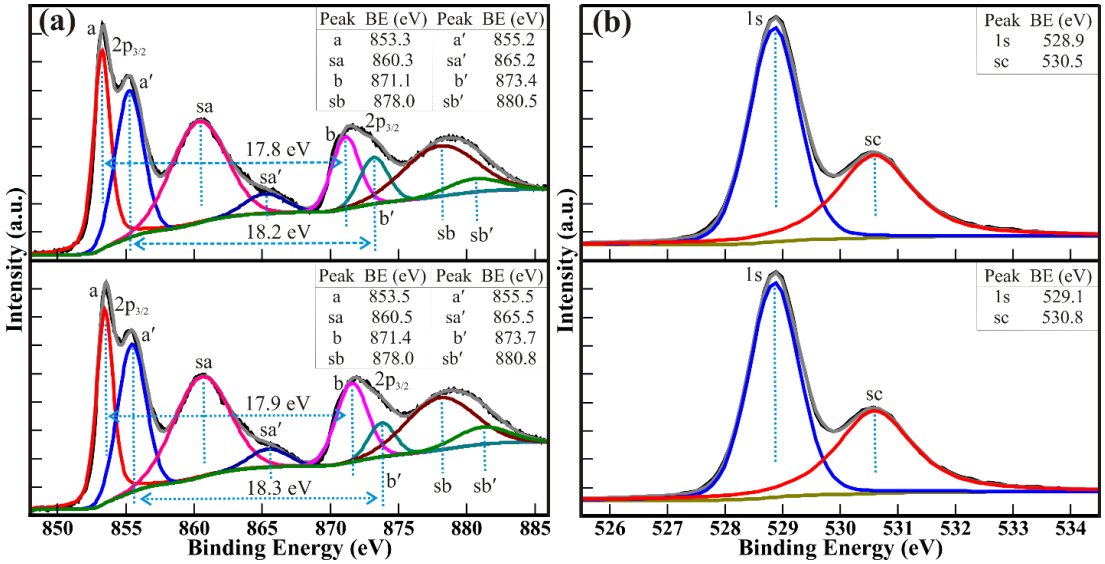

Figure 3.5 High-resolution XPS spectra of (a) Ni(2p) and (b) O(1s) core levels of 0D NiO nanoparticle (lower panel) and 2D porous NiO nanoplates (upper panel).

XPS spectroscopy is used to analyze the chemical compositions and electronic states of the NiO nanostructures. Fig.3.5 shows the high-resolution XPS spectra of Ni(2p) and O(1s) core levels of the NiO nanostructures. The XPS spectra are deconvoluted with Voigt function fitting, followed by a Shirley background to precisely determine the features of Ni(2p) and O (1s). The XPS spectrum of core Ni(2p) levels for NiO nanoplates (Fig. 3.5(a) upper panel) shows two distinct peaks accompanied by their shake-up satellite peaks located at the binding energies of 853.3 (≡ a), 860.3 (≡ sa), 871.1 (≡ b) and 878.0 (≡ sb)

eV, respectively, which is deconvoluted into 8 peaks. The peaks at 853.3 (≡ a) and 871.1 eV (≡ b) correspond to core levels of $Ni^{2+}(2p_{3/2})$ and $Ni^{2+}(2p_{1/2})$, respectively. The deconvolution gives rise to two relatively lower intensity peaks at binding energy (i.e., BE) of 855.5 (≡ a′) and 873.7 (≡ b′) eV are assigned to $Ni^{3+}(2p_{3/2})$ and $Ni^{3+}(2p_{1/2})$ core levels, respectively, indicating trace amounts of Ni_2O_3. The corresponding shake-up satellite peaks are observed at BE of 865.2 (≡ sa′) and 880.5 (≡ sb′) eV. Likewise, the peak of O(1s) (Fig. 3.5(b) upper panel) is deconvoluted into two peaks at the BE of 528.9 and 530.5 eV, which corresponds to the O(1s) core level of O^{2-} ions of NiO nanoplates and surface contamination or defect sites on the surface.[22, 44, 45] Similarly, the chemical states of the 0D NiO nanoparticles are analyzed with high-resolution XPS. The deconvoluted peaks of Ni(2p) (Fig. 3.5(a) lower panel) are very much akin to that of 2D NiO nanoplates, representing that the change in morphology from 0D to 2D has not altered the chemical stoichiometry of the NiO. The minor existence of Ni_2O_3 with the NiO in both the nanoparticles and nanoplates might assist in enhancing the overall electrocatalytic activities by collectively offering $Ni^{2+,}$ and Ni^{3+} cites.

3.3.6 X-ray absorption near-edge structure (XANES) and extended X-ray absorption fine structure (EXAFS) spectroscopy

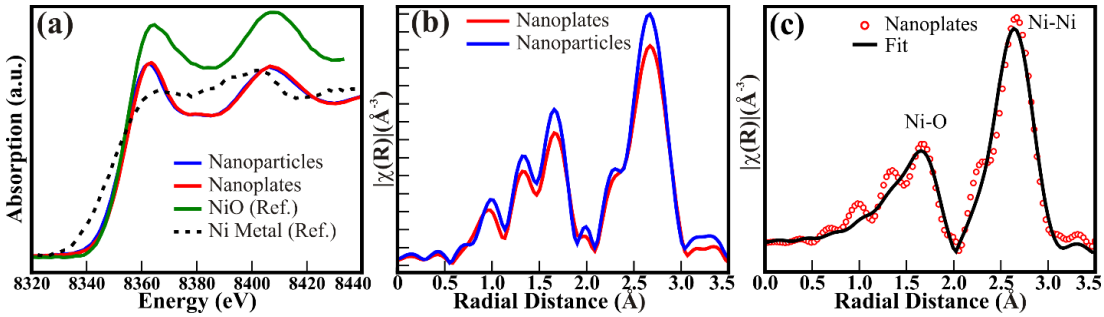

Figure 3.6 (a) Nickel K edge XANES, (b) x-ray absorption fine structure spectra in (b) R space, and (c) k-space of the NiO nanoparticles and nanoplates.

The 2+ oxidation state of Ni ions present in the bulk of the samples was confirmed by carrying out the X-ray absorption near-edge structure (XANES) spectroscopy. The Ni K-edge absorption spectra for NiO particles, as well as the

nanoplates, were recorded at room temperature, in transmission geometry, and lab-based tunable X-ray source. The obtained spectra are as shown in Fig. 3.6. A distinct shift of the absorption edge towards higher energy as compared to the standard Ni metal foil and a good match with the standard NiO (Alfa Aesar, 3N purity) reference sample confirm the 2+ oxidation state of the Ni ions present in the bulk of the samples. Furthermore, the Extended X-ray Absorption Fine Structure (EXAFS) spectra for both compounds were analyzed in the back Fourier-transformed R–space and *k*–space, and plots are presented in Fig. 3.6(b) and (c), respectively. The bond distance of the first coordination shell around Ni ions is estimated to be ~ 2.111 ± 0.007 Å, with the coordination number fixed to 6 (Fig. 3.6(c)). Thus, the octahedral environment around the Ni ions is confirmed in both compounds.

3.3.7 Oxygen evolution reaction (OER)

With commercial IrO_2 as the reference catalyst, the OER activity of 0D NiO nanoparticles and 2D porous NiO plates is studied in a 1 M KOH solution. Fig. 3.7(a) shows the LSV plots of nanoparticles, porous nanoplates, and IrO_2 catalysts. Nanoparticles and porous nanoplates exhibit an overpotential of 373 and 476 mV, respectively, to achieve a current density of 10 mA/cm^2, at which the reference IrO_2 catalyst showed an overpotential of 354 mV. Moreover, the boost in the current density at a potential of >1.35 V indicates the active transitions between Ni^{2+}/Ni^{3+}. The higher boost in the current density of 0D nanoparticles represents the existence of plentiful Ni^{2+}/Ni^{3+} transition assisting to enhance OER activity than 2D porous nanoplates, which is in line with the XPS analysis. The reaction kinetics of electrocatalytic OER activity is analyzed from the corresponding Tafel plots shown in Fig. 3.7(b). The Tafel slopes of 139, 136, and 75 mV/dec are obtained for nanoparticles, porous nanoplates, and reference IrO_2 catalysts, respectively. The proximity of Tafel slopes of nanoparticles and porous nanoplates suggests analogous OER kinetics and catalytic rate towards OER performance. Nevertheless, relatively lower overpotential and Tafel slope indicate better electrocatalytic performance for

nanoparticles than the nanoplates. Therefore, the CA stability test of nanoparticles is performed for 20 h at an overpotential of 373 mV to confirm the commercial durability. After the initial loss of ~10.5%, the current density remains stable at 9.10 mA/cm^2 for over 20 h (Fig. 3.7(c)), which indicates the long-term stability of the nanoparticles. Additionally, the long-term stability of nanoparticles is verified from LSV cycles executed in 1 M KOH electrolytes. A mere 13 mV change in the overpotential of nanoparticles at a current density of 10 mA/cm^2 after 2500 consecutive LSV cycles (Fig. 3.8) confirms their superior stability towards OER activity.

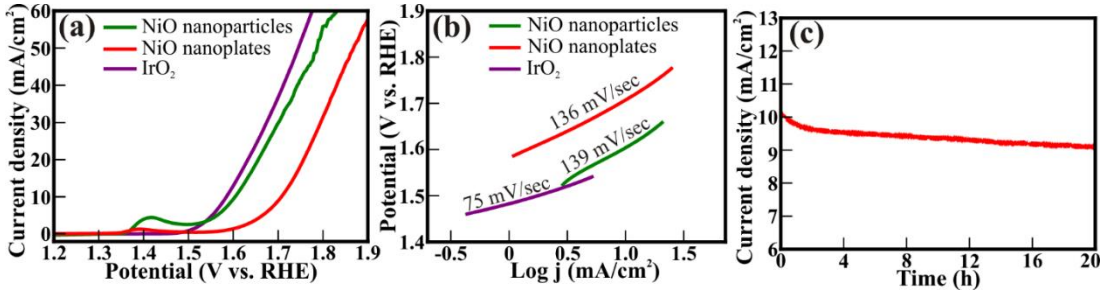

Figure 3.7 (a) Polarization curves (LSV plot) and (b) corresponding Tafel plots of 0D NiO nanoparticles and 2D porous NiO nanoplates for OER activity. (c) Chronoamperometry stability test of NiO nanoparticles at an applied overpotential of 373 mV for 20 h in 1 M KOH.

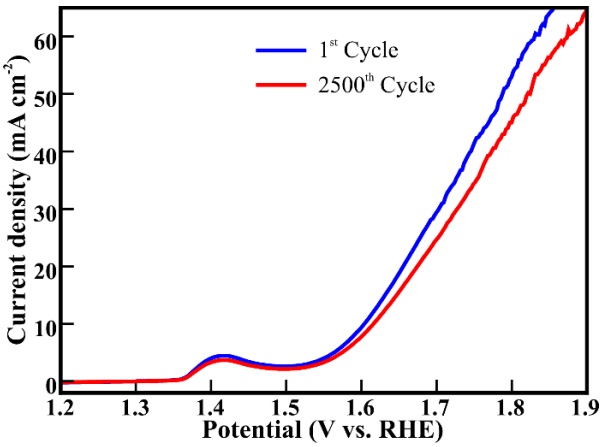

Figure 3.8 Polarization curves (LSV) of NiO nanoparticles for 1st and 2500th cycles of continuous operation in 1 M KOH towards OER activity.

Further, to confirm the electrocatalytic stability of the NiO nanoparticle, the structural, morphological, and chemical properties were analyzed from XRD,

FESEM, and EDS analysis. The Rietveld refinement of the XRD pattern of 0D NiO nanoparticles after the CA stability test for 20 h in a basic medium is shown in Fig. 3.9(a). The NiO nanoparticles retained the cubic structure with an $Fm\bar{3}m$ space group. The characteristic XRD peaks positions at 2θ of 37.33°, 43.38°, and 63.03° corresponds to (111), (020), and (022) planes, respectively (ICSD No. 1010093), showed no shift after continuous CA measurements. The value of goodness of fitting factors such as R_{Bragg} (= 8.14), R_{EXP} (= 7.65), R_P (= 11), and GoF (= 6.77), the estimated lattice parameters (i.e., a = b = c = 4.181 Å) and cell volume (= 73.093 g/cc) of 0D NiO nanoparticles after and before CA analysis remained almost identical. Likewise, the morphology and size distribution (i.e., < 10 nm) of NiO nanoparticles after CA analysis for 20 h (Fig. 3.9(b)) remained identical to that of before electrochemical water splitting activities. Moreover, the EDS spectra show distinct peaks (Fig. 3.9(c)), illustrating the existence of Ni and O without any other foreign elements after the electrochemical water-splitting reaction. This confirmed the excellent structural, morphological and chemical stability of 0D NiO nanoparticles towards water splitting activity even after electrocatalytic reaction for 20 h.

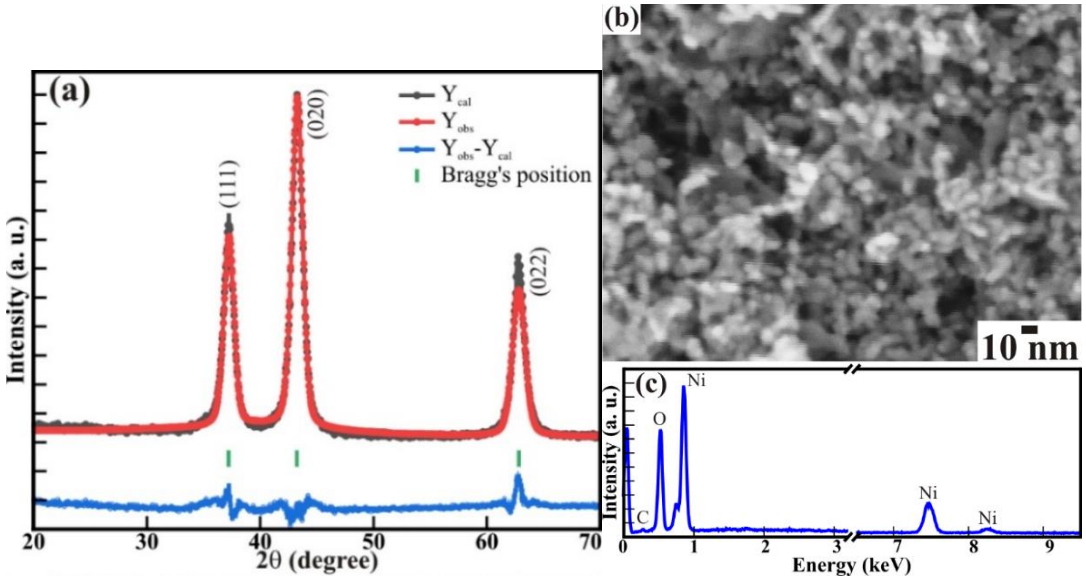

Figure 3.9 (a) Rietveld refinement of XRD pattern, (b) FESEM image, and (c) EDS spectra collected after CA stability test of NiO nanoparticles at an applied overpotential of 373 mV for 20 h in 1 M KOH.

3.3.8 Electrochemical impedance spectroscopy (EIS)

The electrochemical impedance spectroscopy (EIS) studies performed on NiO nanostructures to determine the charge-transfer resistance (R_{ct}) during the OER process are shown in Fig. 3.10. The EIS spectra are fitted to evaluate the charge-transfer resistance and the resistance offered by the NiO. The resistance (R_s) at the interface of NiO and water is relatively larger in the nanoplates (i.e., 22.93 Ω) than in the nanoparticles (i.e., 8.53 Ω). The two semicircular arcs identified for NiO nanoparticles represent the resistance at the textural boundaries (i.e., R_{ct1} = 95.3 Ω) and the bulk/core (i.e., R_{ct2} = 25.3 Ω) of the nanoparticle. However, the single semicircular arc of the NiO nanoplates represents the resistance along the surface (R_{ct1} = 237.48 Ω). The relatively lower R_s and R_{ct} values observed for the NiO nanoparticles indicates higher charge-transfer kinetics across the NiO nanoparticles than that of the NiO nanoplates.

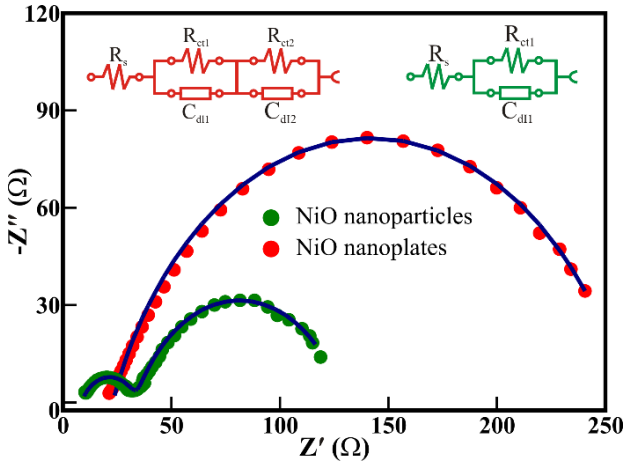

Figure 3.10 Electrochemical impedance spectra of NiO nanostructured catalyst at an applied potential of 0.6 V (vs. Ag/AgCl).

Further, the ECSA of NiO nanoparticles and nanoplates is evaluated from the CV measurements performed at different scan rates from 20 to 100 mV/s, respectively (Fig. 3.11(a and b)). The anodic (J_a) and the cathodic (J_c) double-layer charging currents, estimated from the CV curves at a fixed potential of 0.2 V (*vs.* Ag/AgCl), are plotted against corresponding scan rates (Fig. 3.11(c and d)). The estimated C_{dl} of 0.878 and 0.521 mF/cm for the nanoparticles and porous

nanoplates illustrate the ECSA of 21.95 and 13.02 cm^2, respectively. This represents that the 0D NiO nanoparticles provide more exposed active sites, subsequently offering higher OER activity than 2D porous nanoplates. The comparative evaluation of the OER performance of both NiO nanostructures is provided in Table 3.2.

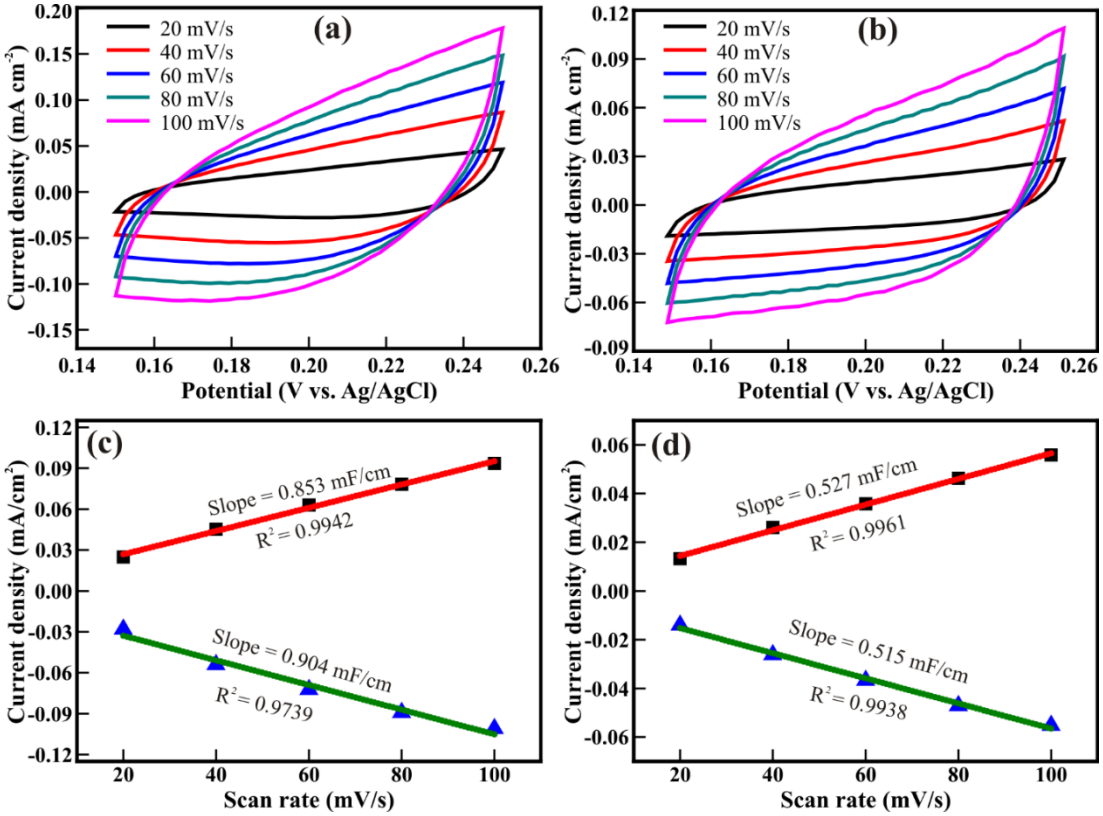

Figure 3.11 Cyclic voltammetry curves of (a) NiO nanoparticles, (b) NiO plates, and (c and d) are their corresponding plot of J_a and J_c against scan rate for the determination of double layer capacitance (C_{dl}).

3.3.9 Hydrogen evolution reaction (HER)

Furthermore, the NiO nanostructures are probed for HER activity. The LSV plots of NiO nanostructures towards HER activity are shown in Fig. 3.12(a). The 0D nanoparticles exhibited lower overpotential (268 mV) than 2D porous nanoplates (384 mV) at a current density of 10 mA/cm^2. However, the reference Pt/C catalyst showed an overpotential of 32 mV. The corresponding Tafel slope (Fig. 3.12(b)) evaluated for 0D nanoparticles, 2D porous nanoplates, and

reference Pt/C is 201, 326, and 36 mV/dec, respectively. However, relatively lower overpotential and Tafel slope of 0D nanoparticles confirm significantly better catalytic activity towards HER than 2D porous nanoplates. Consequently, a stability test is performed at an overpotential of 268 mV to ascertain the commercial durability of 0D nanoparticles toward HER activity (Fig. 3.12(c)). The CA indicates that the current density remains stable for 20 h at 10.04 mA/cm^{2,} which signifies excellent stability.

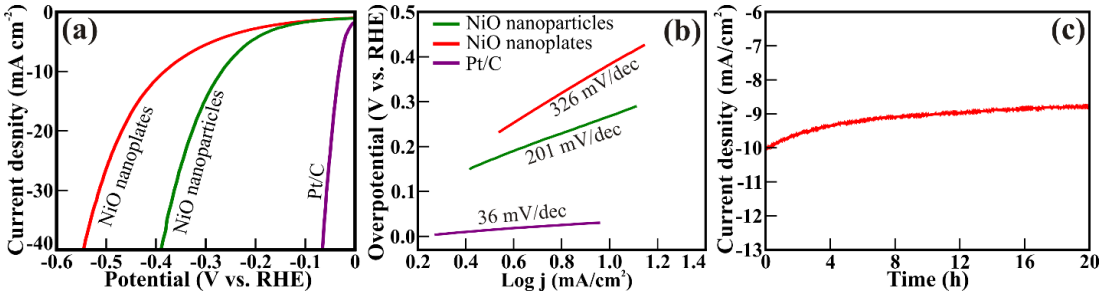

Figure 3.12 (a) Polarization curves (LSV plot) and (b) corresponding Tafel plots of 0D nanoparticles and 2D porous nanoplates for HER activity. (c) Chronoamperometry stability test of NiO nanoparticles at an applied overpotential of 268 mV for 20 h in 0.5 M H_2SO_4.

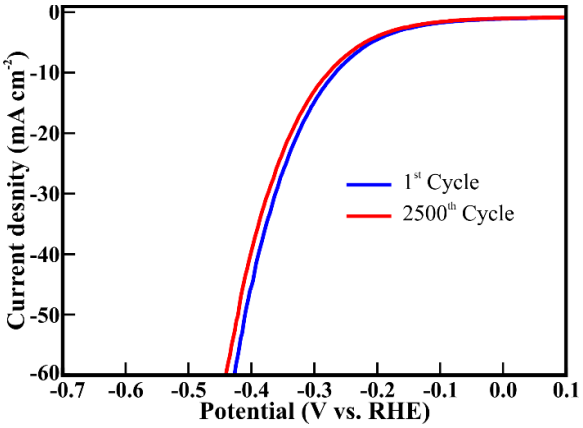

Figure 3.13 Polarization curves (LSV) of NiO nanoparticles for 1st and 2500th cycles of continuous operation in 0.5 M H_2SO_4 towards HER activity.

Furthermore, the long-term stability of 0D nanoparticles towards HER activity is confirmed from LSV performed in 0.5 M H_2SO_4 (Fig. 3.13). A mere 11 mV increase in overpotential at a current density of 10 mA/cm^2 after 2500 continuous LSV cycles confirm the exceptional stability of 0D nanoparticles

towards HER activity in an acidic medium. The comparative evaluation of the HER performance of both NiO nanostructures is provided in Table 3.2. Overall, the pristine 0D NiO nanoparticles synthesized by a simple co-precipitation method have shown better water-splitting performance compared to the NiO nanostructure morphologies and heterostructures with Carbon or Graphene oxides reported in the literature (Table 3.2). Moreover, the literature reports the enhancement in the water-slitting performance of NiO after forming heterostructures with other metal oxides. Therefore, the present 0D NiO nanoparticles have the ability to improve the overall water-splitting performance when combined to form heterostructure with Fe, Ru, or Co-based metal oxides, which form the basis of future work.

Table 3.2 Comparative performance of various NiO nanostructures towards OER and HER activity.

Catalyst	Over potential (mV)@10 mA/cm^2		Tafel Slope (mV/dec)		Ref.
	OER	HER	OER	HER	
0D NiO nanoparticles	373	268	139	201	This work
2D porous NiO nanoplates	476	384	136	326	
NiO hallow microspheres	370	424	156	105	[26]
Triple phase NiO/Ru@Ni foam	-	39	-	75	[46]
NiO@$Co_{0.5}Fe_{0.5}P$ core-shell nanostructures	262	-	-	-	[30]
$NiCo_2O_3$@mesoporous carbon	281	-	96.8	-	[52]
MoS_2@NiO nanocomposite	-	406	-	44	[53]
Thermally oxidized porous NiO	310	-	54	-	[54]
NiO_x/Ni	390	-	69.8	-	[55]
Carbon-Anchored NiO Nanotablets	320	-	49	-	[56]
A-NiO nanoparticles/rGO	201	397	-	-	[57]
A-NiO nanoparticles/GO	274	465	-	-	
NiO nanoparticles/GO	453	625	-	-	

3.4 Conclusion

In conclusion, we have introduced the morphology-controlled NiO nanostructures as a single electrocatalyst efficient for oxygen and hydrogen evolution. The cubic crystal phase of 0D NiO nanoparticles and 2D NiO nanoplates is confirmed from XRD and TEM

analysis. The larger surface area of discrete nanoparticles and nanoplates of diameter/thickness <10 nm played a significant role in the oxygen and hydrogen evolution. The stoichiometry, 2+ octahedron coordination, and existence of Ni^{2+}/Ni^{3+} in NiO nanostructures are confirmed by XPS and XANES analysis. The distinct 0D nanoparticles provided a relatively larger surface area and hence electrochemically active surface sites and delivered the overpotentials of 373 and 268 mV for OER and HER activity, respectively, performed better than 2D porous NiO nanoplates. The chronoamperometric measurements and consecutive LSV cycles showed the long durability of 0D NiO nanoparticles in both basic and acidic mediums for overall water electrolysis.

3.5 References

[1] Zhao Y., Nakamura R., Kamiya K., Nakanishi S., Hashimoto K., (2013), Nitrogen-doped carbon nanomaterials as non-metal electrocatalysts for water oxidation, Nat. Commun., 4, 2390, (DOI: 10.1038/ncomms3390).

[2] Ahmed I., Biswas R., Patil R. A., Halder K. K., Singh H., Banerjee B., Kumar B., Ma Y-R., Haldar K. K., (2021), Graphitic carbon nitride composites with MoO_3-decorated Co_3O_4 nanorods as catalysts for oxygen and hydrogen evolution, ACS Appl. Nano Mater., 4, 12672-12681, (DOI: 10.1021/acsanm.1c03238).

[3] Singh H., Biswas R., Ahmed I., Thakur P., Kundu A., Panigrahi AR., Banerjee B., Halder K. K., Lahtinen J., Mondal K., Haldar K. K., (2022), Dumbbell-shaped ternary transition-metal (Cu, Ni, Co) phosphate bundles: A promising catalyst for the oxygen evolution reaction, ACS Appl. Mater. Interfaces., 14, 6570-6581, (DOI: 10.1021/acsami.1c20356).

[4] McCrory C. C. L., Jung S., Ferrer I. M., Chatman S. M., Peters J. C., Jaramillo T. F., (2015), Benchmarking hydrogen evolving reaction and oxygen evolving reaction electrocatalysts for solar water splitting devices, J. Am. Chem. Soc., 137, 4347-4757, (DOI: 10.1021/ja510442p).

[5] Bao J., Wang Z., Xie J., Xu L., Lei F., Guan M., (2019), A ternary cobalt–molybdenum–vanadium layered double hydroxide nanosheet array as an efficient bifunctional electrocatalyst for overall water splitting, ChemComm., 55, 3521-3524, (DOI: 10.1039/C9CC00269C).

[6] Wei Z., Sun W., Liu S., Qi J., Kang L., Li J., Lou S., Xie J., Tang B., Xie Y., (2021), Lanthanum-doped α-$Ni(OH)_2$ 1D-2D-3D hierarchical nanostructures for robust bifunctional electro-oxidation, Particuology, 57, 104-111. (DOI: 10.1016/j.partic.2021.01.002).

[7] Gao R., Yan D., (2020), Recent development of Ni/Fe-based micro/nanostructures toward photo/electrochemical water oxidation, Adv. Energy Mater., 10, 1900954, (DOI: 10.1002/aenm.201900954).

[8] Manjunath V., Bimli S., Parmar K. H., Shirage P. M., Devan R. S., (2019), Oxidized Nickel films as highly transparent HTLs for inverted planar perovskite solar cells, Sol. Energy, 193, 387-394, (DOI: 10.1016/j.solener.2019.09.070).

[9] Karthikeyan V., Maniarasu S., Manjunath V., Ramasamy E., Veerappan G., (2017), Hydrothermally tailored anatase TiO_2 nanoplates with exposed {111} facets for highly efficient dye-sensitized solar cells, Sol. Energy, 147, 202-208, (DOI: 10.1016/j.solener.2017.03.049).

[10] Didwal P. N., Pawar K. S., Chikate P. R., Abhyankar A. C., Pathan H. M., Devan R. S., (2016), Titania sensitized with SPADNS dye for dye sensitized solar cell, J. Mater. Sci.: Mater. Electron., 27, 12446-12451, (DOI: 10.1007/s10854-016-5431-3).

[11] Alla M., Manjunath V., Chawki N., Singh D., Yadav S. C., Rouchdi M., Boubker F., (2022), Optimized $CH_3NH_3PbI_{3-X}Cl_X$ based perovskite solar cell with theoretical efficiency exceeding 30%, Opt. Mater., 124, 112044, (DOI: 10.1016/j.optmat.2022.112044).

[12] Alla M., Bimli S., Manjunath V., Samtham M., Kasaudhan A., Choudhary E., Rouchdi M., Boubker F., (2022), Towards lead-free all-inorganic perovskite solar cell with theoretical efficiency approaching 23%, Mater. Technol., 1-7, (DOI: 10.1080/10667857.2022.2091195).

[13] Manjunath V., Reddy Y. K., Bimli S., Choudhary R. J., Devan R. S., (2022). 22% efficient Kusachiite solar cells of $CuBi_2O_4$ light harvester and ABO_3 buffer layers: A theoretical analysis, Mater. Today Commun., 32, 104061, (DOI: 10.1016/j.mtcomm.2022.104061).

[14] Yadav S. C., Manjunath V., Srivastava A., Devan R. S., Shirage P. M., (2022), Stable lead-free $Cs_4CuSb_2Cl_{12}$ layered double perovskite solar cells yielding theoretical

efficiency close to 30%, Opt. Mater., 132, 112676, (DOI: 10.1016/j.optmat.2022.112676).

[15] Yadav S. C., Srivastava A., Manjunath V., Kanwade A., Devan R. S., Shirage P. M., (2022), Properties, performance and multidimensional applications of stable lead-free $Cs_2AgBiBr_6$ double perovskite, Mater. Today Phys., 26, 100731, (DOI: 10.1016/j.mtphys.2022.100731).

[16] Reddy Y. K., Manjunath V., Bimli S., Devan R. S., (2022), Futuristic kusachiite solar cells of $CuBi_2O_4$ absorber and metal sulfide buffer layers: Theoretical efficiency approaching 28%, Sol. Energy., 244, 75-83, (DOI: 10.1016/j.solener.2022.08.034).

[17] Chikate P. R., Sharma A., Rondiya S. R., Cross R. W., Dzade N. Y., Shirage P. M., Devan R. S., (2021), Hierarchically interconnected ZnO nanowires for low-temperature-operated reducing gas sensors: Experimental and DFT studies, New J. Chem., 45, 1404-14014, (DOI: 10.1039/D0NJ05231K).

[18] Patil R. A., Devan R. S., Liou Y., Ma Y-R., (2016), Efficient electrochromic smart windows of one-dimensional pure brookite TiO_2 nanoneedles, Sol. Energy Mater. Sol. Cells., 147:, 40-45, (DOI: 10.1016/j.solmat.2015.12.024).

[19] Parmar K. H., Manjunath V., Bimli S., Chikate P. R., Patil R. A., Ma Y-R., Devan R. S., (2022), Stable and reversible electrochromic behaviors in anodic NiO thin films, Chinese J. Phys., 77, 143-150, (DOI: 10.1016/j.cjph.2022.02.014).

[20] Kitchamsetti N., Ma Y-R., Shirage P. M., Devan R. S., Mesoporous perovskite of interlocked nickel titanate nanoparticles for efficient electrochemical supercapacitor electrode, (2020), J. Alloys Compd., 833, 155134, (DOI: 10.1016/j.jallcom.2020.155134).

[21] Kitchamsetti N., Choudhary R. J., Phase D. M., Devan R. S., (2020), Structural correlation of a nanoparticle-embedded mesoporous $CoTiO_3$ perovskite for an efficient electrochemical supercapacitor, RSC Adv., 10, 23446-23456, (DOI: 10.1039/D0RA04052E).

[22] Manjunath V., Mishra P. K., Dobhal R., Bimli S., Shirage P. M., Sen S., Shaikh P. A., Devan R. S., (2021), Perovskite-based facile $NiO/CH_3NH_3PbI_3$ heterojunction self-powered broadband photodetector, ACS Appl. Electron. Mater., 3, 4548-4557, (DOI: 10.1021/acsaelm.1c00679).

[23] Daulbayev C., Sultanov F., Bakbolat B., Daulbayev O., (2020), 0D, 1D and 2D nanomaterials for visible photoelectrochemical water splitting. A review, Int. J. Hydrog. Energy, 45, 33325-33342, (DOI: 10.1016/j.ijhydene.2020.09.101).

[24] Chen L., Liang J. M., Zhang Q. C., Hu X. W., Peng W. C., Li Y., Zang F., Fan X., (2022), Quasi zero-dimensional MoS_2 quantum dots decorated 2D $Ti_3C_2T_x$ MXene as advanced electrocatalysts for hydrogen evolution reaction, Int. J. Hydrog. Energy, 47, 10583-10593, (DOI: 10.1016/j.ijhydene.2021.12.185).

[25] Wei Y. H., Gao F., Du J. G., Jiang G., (2022), Modulation of the B_4N monolayer as an efficient electrocatalyst for hydrogen evolution reaction, Int. J. Hydrog. Energy, 47, 11511-11519, (DOI: 10.1016/j.ijhydene.2022.01.177).

[26] Xie J., Yang X., Xie Y., (2020), Defect engineering in two-dimensional electrocatalysts for hydrogen evolution, Nanoscale, 12, 4283-4294, (DOI: 10.1039/C9NR09753H).

[27] Lu X., Tao T., Chen L., Lu S., Zhang Y., Xie J., Wu Z., (2022), Intercalation of coordination polymer to regulate interlayer of 2D layered MoS_2 for hydrogen evolution reaction, Int. J. Hydrog. Energy, 47, 18347-18356, (DOI: 10.1016/j.ijhydene.2022.04.052).

[28] Devan R. S., Patil R. A., Lin J-H., Ma Y-R., (2012), One-dimensional metal-oxide nanostructures: Recent developments in synthesis, characterization, and applications, Adv. Funct. Mater., 22, 3326-3370, (DOI: 10.1002/adfm.201201008).

[29] Xie J., Qi J., Lei F., Xie Y., (2020), Modulation of electronic structures in two-dimensional electrocatalysts for the hydrogen evolution reaction, ChemComm., 56,11910-11930, (DOI: 10.1039/D0CC05272H).

[30] Mondal A., Paul A., Srivastav D. N., Panda A. B., (2018), NiO hollow microspheres as efficient bifunctional electrocatalyst for overall water splitting, Int. J. Hydrog. Energy, 43, 21665-21674, (DOI: 10.1016/j.ijhydene.2018.06.139).

[31] Ma G., Zhang X., Zhou G., Wang X., (2021), Hydrogen production from methanol reforming electrocatalysis at NiO nanosheets supported Pt nanoparticles, Chem. Eng. J., 411, 128292, (DOI: 10.1016/j.cej.2020.128292).

[32] Wu Z., Zou Z., Huang J., Gao F., (2018), Fe-doped NiO mesoporous nanosheets array for highly efficient overall water splitting, J. Catal., 358, 243-252, (DOI: 10.1016/j.jcat.2017.12.020).

[33] QayoomMugheri A., AneelaTahira, Aftab U., IshaqAbro M., Chaudhry S. R., Amaral L., Ibupoto Z. H., (2019), Co_3O_4/ NiO bifunctional electrocatalyst for water splitting, Electrochim. Acta, 306, 9-17, (DOI: 10.1016/j.electacta.2019.03.092).

[34] Zhao H., Liang J., Zheng Q., (2022), Construction of core-shell heterostructure NiO@$Co_{0.5}Fe_{0.5}P$ as efficient bifunctional electrocatalysts for overall water splitting, J. Alloys Compd., 905, (DOI: 10.1016/j.jallcom.2022.164264).

[35] Zhou W., Lu X-F., Chen J-J., Zhou T., Liao P-Q., Wu M., Li G-R., (2018), Hierarchical porous prism arrays composed of hybrid ni-nio-carbon as highly efficient electrocatalysts for overall water splitting, ACS Appl. Mater. Interfaces, 10, 38906-38914, (DOI: 10.1021/acsami.8b13542).

[36] Yao X., Li P., Yu B., Yang F., Li J., Zhao Y., Li Y., (2017), Hydrothermally synthesized NiO-samarium doped ceria nano-composite as an anode material for intermediate-temperature solid oxide fuel cells, Int. J. Hydrog. Energy, 42, 22192-22200, (DOI: 10.1016/j.ijhydene.2017.02.008).

[37] Sta I., Jlassi M., Kandyla M., Hajji M., Koralli P., Krout F., Kompitsas M., Ezzaouia H., (2016), Surface functionalization of sol-gel grown NiO thin films with palladium nanoparticles for hydrogen sensing, Int. J. Hydrog. Energy, 41, 3291-3298, (DOI: 10.1016/j.ijhydene.2015.12.109).

[38] Wang Z., Lin J., Xu H., Zheng Y., Xiao Y., Zheng Y., (2021), Zr-doped NiO nanoparticles for low-temperature methane combustion, ACS Appl. Nano Mater., 4, 11920-11930, (DOI: 10.1021/acsanm.1c02487).

[39] Baygi N. J., Saghir A. V., Beidokhti S. M., Khaki J. V., (2020), Modified auto-combustion synthesis of mixed-oxides TiO_2/NiO nanoparticles: Physical properties and photocatalytic performance, Ceram. Int., 46, 15417-15437, (DOI: 10.1016/j.ceramint.2020.03.087).

[40] Dong S., Wu D., Gao W., Hao H., Liu G., Yan S., (2020), Multi-dimensional templated synthesis of hierarchical Fe_2O_3/NiO composites and their superior ethanol

sensing properties promoted by nanoscale p–n heterojunctions, Dalton Trans., 49, 1300-1310, (DOI: 10.1039/C9DT04185K).

[41] Ryu K., Lee K-J., (2020), Grinding behavior of WO_3, NiO, Fe_2O_3 by ultrasonic milling parameters control and preparation of nanocomposite powder, Adv. Powder Technol., 31, 3867-3873, (DOI: 10.1016/j.apt.2020.07.024).

[42] Favet T., Cottineau T., Keller V., El Khakani M. A., (2020), Comparative study of the photocatalytic effects of pulsed laser deposited CoO and NiO nanoparticles onto TiO_2 nanotubes for the photoelectrochemical water splitting, Sol. Energy Mater. Sol. Cells., 217, 110703, (DOI: 10.1016/j.solmat.2020.110703).

[43] Chang Y-T., Hung K-Y., Young H-T., Li K-M., Chen R K., (2022), Aerosol jet printing of nickel oxide nanoparticle ink with ultraviolet radiation curing for thin-film temperature sensors, Int. J. Adv. Manuf. Technol., 118, 1957-1965, (DOI: 10.1007/s00170-021-08046-7).

[44] Won J. M., Hong Y. J., Kim J. H., Choi Y. J., Kang Y. C., (2016), Electrochemical properties of core-shell structured NiO@SiO_2 ultrafine nanopowders below 10nm for lithium-ion storages, Electrochim. Acta, 190, 835-842, (DOI: 10.1016/j.electacta.2015.12.197).

[45] Xie J., Guo Y., Lou S., Wei Z., Hao P., Lei F., Tang Bo., (2020), A molten-salt protected pyrolysis approach for fabricating a ternary nickel–cobalt–iron oxide nanomesh catalyst with promoted oxygen-evolving performance, Chem. Commun., 56, 4579-4582, (DOI: 10.1039/D0CC01613F).

[46] Guo Y., Lei F., Qi J., Cao S., Wei Z., Lou S., Hao P., Xie J., Tang B., (2020), Molten-salt-protected pyrolysis for fabricating perovskite nanocrystals with promoted water oxidation behavior, ACS Sustain. Chem. Eng., 8, 16711-16719, (DOI: 10.1021/acssuschemeng.0c06971).

[47] Deng H., Zhang C., Xie Y., Tumlin T., Giri L., Karna S. P., Lin J., (2016), Laser induced MoS_2/carbon hybrids for hydrogen evolution reaction catalysts, J. Mater. Chem. A, 4, 6824-6830, (DOI: 10.1039/C5TA09322H).

[48] Prasannachandran R., Vineesh T. V., Anil A., Krishna B. M., Shaijumon M. M., (2018), Functionalized phosphorene quantum dots as efficient electrocatalyst for oxygen evolution reaction, ACS Nano, 12, 11511, (DOI: 10.1021/acsnano.8b06671).

[49] McCrory C. C. L., Jung S., Peters J. C., Jaramillo T. F., (2013), Benchmarking heterogeneous electrocatalysts for the oxygen evolution reaction, J. Am. Chem. Soc., 135, 16977-16987, (DOI: 10.1021/ja407115p).

[50] Shafiq F., Tahir M. B., Hussain A., Sagir M., Rehman J. U., Kebaili I., Alrobei H., Alzaid M., (2022), The construction of a highly efficient p-n heterojunction $Bi_2O_3/BiVO_4$ for hydrogen evolution through solar water splitting, Int. J. Hydrog. Energy, 47, 4594-4600, (DOI: 10.1016/j.ijhydene.2021.11.075).

[51] Zhong C., Zhou Q., Li S., Cao L., Li J., Shen Z., Ma H., Liu J., Lu M., Zhang H., (2019), Enhanced synergistic catalysis by a novel triple-phase interface design of NiO/Ru@Ni for the hydrogen evolution reaction, J. Mater. Chem. A, 7, 2344-2350, (DOI: 10.1039/C8TA11171E).

[52] Zhang Y., Wang X., Luo F., Tan Y., Zeng L., Fang B., Liu A., (2019), Rock salt type $NiCo_2O_3$ supported on ordered mesoporous carbon as a highly efficient electrocatalyst for oxygen evolution reaction, Appl. Catal. B-Environ., 256, (DOI: 10.1016/j.apcatb.2019.117852).

[53] Mugheri A. Q., Ali S., Narejo G. S., Otho A. A., Lal R., Abro M. A., Memon S. H., Abbasi F., (2020), Electrospun fibrous active bimetallic electrocatalyst for hydrogen evolution, Int. J. Hydrog. Energy, 45, 21502, (DOI: 10.1016/j.ijhydene.2020.06.005).

[54] Babar P. T., Lokhande A. C., Gang M. G., Pawar B. S., Pawar S. M., Kim J-H., (2018), Thermally oxidized porous NiO as an efficient oxygen evolution reaction (OER) electrocatalyst for electrochemical water splitting application, J. Ind. Eng. Chem., 60, 493-497, (DOI: 10.1016/j.jiec.2017.11.037).

[55] Han G-Q., Liu Y-R., Hu W-H., Dong B., Li X., Shang X., Chai Y-M., Liu Y-Q., Liu C-G., (2015), Three dimensional nickel oxides/nickel structure by in situ electro-oxidation of nickel foam as robust electrocatalyst for oxygen evolution reaction, Appl. Surf. Sci., 359, 172-176, (DOI: 10.1016/j.apsusc.2015.10.097).

[56] Sekar S., Kim DY., Lee S., (2020), Excellent oxygen evolution reaction of activated carbon-anchored NiO nanotablets prepared by green routes, Nanomaterials, 10, 1382, (DOI: 10.3390/nano10071382).

[57] Jo S. G., Kim C. S., Kim S. J., Lee J. W., (2021), Phase-controlled NiO nanoparticles on reduced graphene oxide as electrocatalysts for overall water splitting, Nanomaterials, 11, 3379, (DOI: 10.3390/nano11123379).

Chapter 4

1D NiO porous corn-like nanorods for hydrogen evolution

4.1 Introduction

The utilization of multifunctional materials in energy generation, energy storage, and CO_2 capture shall address the global energy crises and environmental pollution. However, finding functional materials pertinent to multiple applications is a timely need to address these issues. Among all the available functional materials, metal oxides render various unique properties owing to their completely filled 's' orbitals and partially filled 'd' orbitals.[1] Accounting from the unique properties like wide bandgaps,[2] high dielectric constants,[3] tunable optoelectronic characteristics,[4], etc., the metal oxides are applied in different functional applications such as solar cells,[5, 6] photodetector,[7, 8] supercapacitors,[9] battery electrodes,[10] gas sensors,[11] electrochromism,[12], etc. Moreover, the metal oxides can be downscaled into nanostructures with different shapes and morphologies, providing an increased surface-to-volume ratio and significantly larger textural boundaries.[13] Currently, layered, nanoparticulate, and mesoporous structures have gained considerable attention from researchers to gain enhanced chemical and physical properties. However, such structures compromise the conductivity and, thereafter, electron/ion transport/diffusion, owing to the larger charge transfer resistance. Therefore, the synthesis of highly porous oriented structures of interconnecting nanoparticles offering a larger surface area is of scientific importance. The porous 1D nanostructure morphologies are anticipated to offer fast charge transport in the axial direction, which benefits nanodevices and nanoelectronics applications.[14] Therefore, porous 1D metal oxide nanostructures with larger surface area and high aspect ratio can serve in electrocatalysis, carbon dioxide (CO_2) capture, supercapacitors, etc.

Compared to other metal oxides, nickel oxide, capable of existing in NiO, NiO_2, and Ni_2O_3 forms with cubic, monoclinic, rhombohedral, and/or hexagonal crystalline phases [1], is an excellent candidate for a variety of applications. Therefore, NiO thin films and nanostructures in the form of nanospheres,[15] nanoflakes,[16] nanotubes,[17] nanofibers,[18] pinecones,[19], etc., are independently explored for applications in energy storage, sensors, photocatalysis, etc. The hydrothermally synthesized NiO nanoflakes and urchinlike nanostructures, [20, 21] 2D nanoflakes and 1D nanorods of NiO synthesized by decomposition of $NiC_2O_4 \cdot 2H_2O$,[22] and NiO nanorods grown over Ni foil by calcinating Ni foil dipped in LiOH[23] described the potentials of 1D nanostructures in stable energy

storage performance, but their specific capacitance limited to 140 to 290 F/g. On the contrary, NiO micro flower of particulate nanowire-weaving nanosheets [24] and Metal-Organic-Frameworks derived mesoporous NiO nanorod [25] performed well for supercapacitor and Li-ion batteries and disclosed the necessity of porous 1D morphology providing a larger surface area accounting for enhanced specific capacitance. Moreover, the NiO nanostructures are explored for electrocatalytic water-splitting processes due to the coexistence of Ni^{2+} and Ni^{3+} ions. NiO hollow spheres offering a larger surface area provide the overall water spitting at an overpotential of 370 and 424 mV for OER and HER activity at the current density of 10 mA/cm^2. [26] Introduction of reduced-graphene-oxide in the Ni/NiO nanostructures delivered O_2 and H_2 evolution at an overpotential of 480 and 582 mV, respectively.[27] However, the NiO nanoparticle/graphene oxide composite [28] and Ni-NiO@3Dgraphene composites.[29] synthesized in search of an excellent water splitting process could not serve the purpose and restrict further improvement with the overpotentials of 453 and 625 mV and 1640 and 310 mV, respectively, for OER and HER. Nevertheless, MoS_2@NiO nanocomposites provided a relatively better overpotential of 406 mV; the water splitting was limited to the HER only.[30] Therefore, the synthesis of porous NiO nanostructures providing a larger surface area for abundant electrocatalytic active sites would benefit from achieving better water-splitting performance. Overall, such porous NiO nanostructure consisting of interconnected nanoparticles is expected to deliver multifunctional properties and serve for applications in energy storage, hydrogen fuel generation, CO_2 capture, etc.

In this study, 1D NiO nanorods comprising interlocked NiO nanoparticles are synthesized by the solvothermal method. The as-synthesized NiO nanorods were comprehensively characterized to understand the crystallinity, morphology, porosity, chemical states, and local chemical environment. Further, in an attempt to understand the multifunctional property of the synthesized NiO nanorods for sustainable energy applications, the nanorods were employed as a catalyst for greenhouse CO_2 capture, an electrode for supercapacitor, and an electrocatalyst for water splitting to generate hydrogen fuel. Interestingly, the porous NiO nanorods formed by interconnecting nanoparticles showed excellent CO_2 uptake, good energy storage performance, and low overpotential for OER and HER. Additionally, the NiO nanorods as an electrode for supercapacitors and

electrocatalysts for water splitting showed excellent capacitance retention and stability in acidic and basic mediums, respectively.

4.2 Experimental section

4.2.1 Synthesis of NiO nanorods

All the precursors, reagents, and solvents were used as received without further purification. Nickel chloride ($Ni(NO_3)_2.6H_2O$), sodium oxalate ($NiCl_2.6H_2O$), Iridium oxide (IrO_2), and 5 % Nafion were procured from Sigma Aldrich. Potassium hydroxide (KOH) was procured from Loba Chemie Pvt. Ltd. Double Ionized (DI) water was used throughout the experiment. All the glassware used in the experiments was physically and chemically inert. 0.474 g $NiCl_2.6H_2O$ and 0.126 g $NiCl_2.6H_2O$ were dissolved in a mixed solvent containing 18 ml DI water and 30 ml ethylene glycol under constant stirring for 30 min. The homogeneous solution thus obtained was transferred to a Teflon liner placed in stainless steel autoclave and reacted at 180 ℃ for 12 hr. After natural cooling, the collected product was washed with DI water and ethanol several times. Further, it was dried at 60 ℃ for 2 h and annealed at 400 ℃ for 2 h to gain porous NiO nanorods.

4.2.2 Characterization

The morphology of the synthesized NiO product is analyzed using Field Emission Scanning Electron Microscopy (FESEM, JEOL, JSM-7610 F Plus). The crystal structure of the NiO is investigated from X-ray diffraction (Empyrean-DY2528, Malvern Panalytical, λ_{Cu} = 1.5405 Å) and further confirmed from the high-resolution images and selective area electron diffraction (SAED) obtained from Transmission Electron Microscopy (TEM, JEOL JEM-2100 F). The size distribution of nanoparticles and porous morphology of NiO nanorods are confirmed from the Small Angle X-ray Scattering (SAXS, Empyrean-DY2528, Malvern Panalytical) and BET analysis (QUANTACHROME Autosorb iQ2), respectively. The chemical states and electronic structure are analyzed from X-ray photoelectron spectroscopy (XPS,

Thermo Scientific Inc. K_α) and Extended X-ray-Absorption Fine Structure (EXAFS, Rigaku R-XAS) analysis.

4.2.3 Gas adsorption-desorption measurements

Gas adsorption-desorption studies were performed using QUANTACHROME Autosorb iQ2 gas analyzer, and obtained isotherms were analyzed using ASIQwin software. The sample was degassed for 10 h in a high vacuum to eliminate moisture and other adsorbed gases before CO_2 capture. Barrett-Joyner-Halenda (BJH) and Brunauer-Emmett-Teller (BET) models were used to estimate porosity and specific surface area, respectively, in the N_2 gas environment. The equilibrium CO_2 adsorption isotherms were obtained at 273 and 298 K and further used to calculate isosteric heat of adsorption (-Qst or ΔHads) from the Clausius-Clapeyron equation [31, 32]

$$\ln\left(\frac{P_2}{P_1}\right) = \frac{-Q_{st}}{R}\left(\frac{1}{T_2} - \frac{1}{T_1}\right) \quad (4.1)$$

where P_2 and P_1 are the pressures (bar) corresponding to two different isotherms at temperatures T_2 (i.e., 298 K) and T_1 (i.e., 273 K), respectively, for the same volume of gas adsorbed, & R is the universal gas constant (i.e., 8.3145 J/mol·K).

4.2.4 Electrochemical measurements for supercapacitor

Initially, 1×1 cm of nickel foam was ultrasonically treated in concentrated HCl and further washed with DI water and ethanol to remove the oxide contamination on the surface, if any. The homogeneous ink consisting of 10 mg of NiO nanorods and 10 µL of Nafion was drop cast on nickel foam and dried at ambient overnight to prepare the working electrode for the supercapacitor. The energy storage performance is evaluated from CV, galvanostatic charge-discharge (GCD), and cyclic stability measurements performed in 1M KOH aqueous electrolyte in the three-electrode configuration using an electrochemical workstation (Metrohm Autolab PGSTAT204), where NiO/Ni-foam is the working electrode, platinum is the counter electrode, and saturated calomel electrode (SCE) is the reference electrodes. The specific capacitance (C_s) of NiO nanorods is estimated from the CV and GCD curves using equations

$$C_S = \frac{\int idV}{m\vartheta\Delta V} \quad \text{for CV} \quad (4.2)$$

$$C_s = \frac{I}{m}\int \frac{dt}{V} \quad \text{for GCD} \quad (4.3)$$

where C_s is the specific capacitance of NiO nanorods (F/g), m is the mass of active electrode materials (g), υ is the scan rate (mV/s), ΔV is the applied potential range (V), I is the applied current (A), and V is applied potential in the GCD.

Further, the charge storage mechanism is evaluated from current density variation to the scan rate of porous NiO nanorods expressed from Eq. 4.3.

$$i_p = a\upsilon^b \text{ or } \log(i_p) = \log(a) + b\ log(\upsilon) \quad (4.4)$$

where a and b are constants, and i_p is the current density. The estimated value of b represents the diffusion (if b = 0.5) and surface (if b = 1) controlled process.

4.2.5 Electrocatalytic water splitting

The homogeneous ink is prepared using a 3.5 mg NiO catalyst, 600 μL DI water, 380 μL ethanol, and 20 μL 5% Nafion solution. The as-prepared ink is drop-cast on a glassy carbon electrode and dried overnight under ambient conditions. Typically, 0.25 mg/cm^2 catalyst loaded over a 3 mm diameter was used as the working electrode to study water-splitting performance. The electrocatalytic performance was investigated in a standard three-electrode system using an electrochemical workstation equipped with Nova 2.1.4 software (Metrohm Autolab, Multichannel-204). The OER and HER performance were determined using electrolyte solutions of 1 M KOH and 0.5 M H_2SO_4 degassed with nitrogen gas for 30 min, respectively. OER was performed in a conventional three-electrode system of Hg/HgO reference and platinum counter electrode. OER activity was examined from the LSV and CV measurements performed in the optimized potential range of 0 to 1 V at a scan rate of 10 mV/s and 0.15 to 0.25 V at various scan rates between 20 to 100 mV/s, respectively. However, HER activity is evaluated using Ag/AgCl (3 M KCl) reference electrode along with a graphite rod as a counter electrode instead of platinum to avoid deposition on the electrode surface, which can mislead the hydrogen evolution. HER activity was investigated from LSV in the potential range of 0.2 V to -0.8 V vs.

Ag/AgCl at a scan rate of 10 mV/s. The long-term stability of NiO porous nanorods for 25 h is tested using CA at a constant overpotential of 441 and 345 mV for OER and HER activity, respectively. The change in overpotential after 3000 LSV cycles at a constant scan rate of 50 mV/s was investigated to estimate the stability of NiO nanorods for both OER and HER activity. The potentials were calibrated versus RHE using the Nernst equation for HER (Eq. 2.1) and OER (Eq. 2.2). Moreover, the ECSA is estimated from Eq. 2.3. [33]

4.3 Results and discussions

4.3.1 Structural and morphological analysis

The surface morphological features and crystalline phase of the NiO are examined from FESEM, TEM, and XRD analysis. The Rietveld refinement was done on the XRD pattern using FullProf software to identify the crystal structure and lattice parameter. Fig. 4.1(a) shows the observed and calculated patterns, Bragg's positions, and difference curves for the space group Fm-3m (ICSD No. 9008693). The NiO nanorods crystallized into a cubic crystal system with a space group. The reasonably good fit of the diffraction peaks at 2θ = 37.33°, 43.38°, 63.03°, 75.60°, and 79.61° represents (111), (020), (022), (131), and (222) peaks, respectively. The values of fitting factors, such as R_{Brag}, R_P, R_{Exp}, R_{Wp}, R_f, and GoF, are 0.343, 4.83, 4.71, 6.38, 0.307, and 1.84, respectively. The estimated values of lattice parameters (i.e., a=b=c) and cell volume (V) for NiO nanorods are 4.184 Å and 72.287 cc/g, respectively. The FESEM image in Fig. 4.1(b) indicates the formation of porous nanorods consisting of corn-like features along the surface of each rod. Corn-like features are observed due to the regular interconnected arrangement of the nanoparticles. Moreover, these interconnected nanoparticles formed porous NiO nanorods of width < 50 nm. These distinct porous NiO rods are well separated with clear visible textural boundaries. The profound insights not revealed to a large extent by FESEM are thoroughly exposed from TEM analysis. The TEM image confirmed that the NiO nanorods are formed through the interconnection of randomly aligned distinct NiO nanoparticles (Fig. 4.1(c)). Moreover, the nanoparticles with clearly visible

textural boundaries have all dimensions < 15 nm. The SAED pattern of the NiO nanorods shown in the inset of Fig. 4.1(c) represents distinct circular rings with bright diffraction spots corresponding to the individual planes of the cubic crystalline NiO nanorods. The high-resolution TEM image revealed the existence of well-crystalline distinct NiO nanoparticles of dimension ~ 8 nm with clearly visible textural boundaries identified by yellow lines (Fig. 4.1(d)). The interplanar spacing of 0.208 and 0.241 nm corresponds to (020) and (111) planes, respectively, confirming the formation of cubic crystalline NiO nanoparticles, which is in good agreement with the XRD analysis. These analyses confirm the formation of highly crystalline porous NiO nanorods with interlocked NiO nanoparticles.

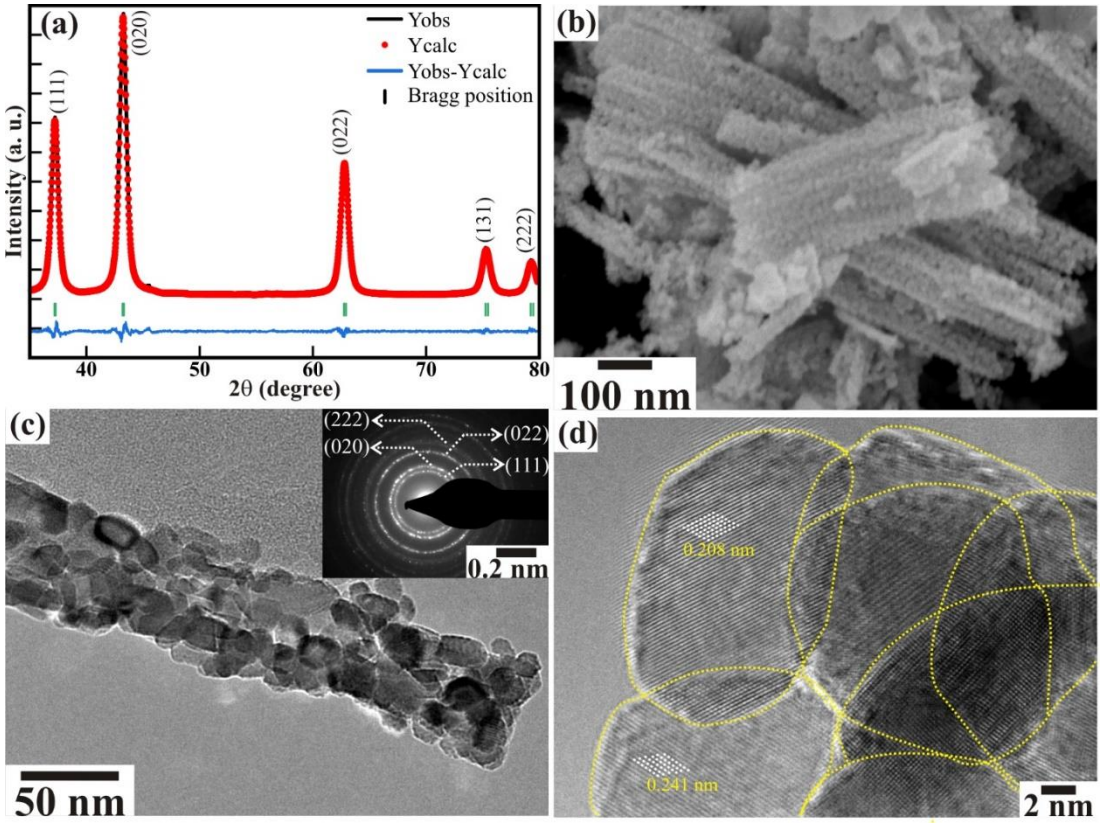

Figure 4.1 (a) Rietveld refinement of XRD pattern, (b) High magnification FESEM image, (c) TEM image, and (e) High-resolution TEM image of NiO nanorods. The inset of (c) is the SAED pattern of NiO nanorods. The yellow dotted lines in (e) are the guidelines to the eye indicating discrete Ni nanoparticles present in the nanorods.

4.3.2 X-ray photoelectron spectroscopy

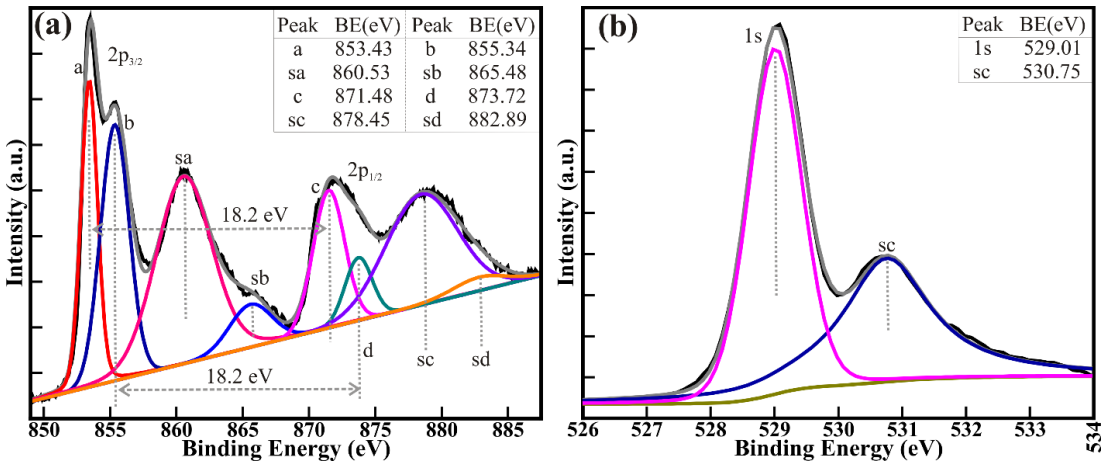

Figure 4.2 High-resolution XPS spectra of (a) Ni(2p) and (b) O(1s) core levels of NiO nanorods. The spectra are deconvoluted via the Voigt curve fitting function within Shirley's background.

The electronic and chemical states of the porous NiO nanorods are investigated from XPS. The deconvoluted XPS spectra of Ni(2p) and O(1s) core levels are shown in Fig. 4.2. The four distinct peaks in Fig. 4.2(a) represent two peaks of Ni(2p) core levels and their corresponding shake-up satellites, which are deconvoluted into eight distinct peaks. The peaks located at the BE of 853.43 (≡ a), 855.34 (≡ b), 871.48 (≡ c), and 873.72 (≡ d) eV correspond to the $Ni^{2+}(2p_{3/2})$, $Ni^{3+}(2p_{3/2})$, $Ni^{2+}(2p_{1/2})$, and $Ni^{3+}(2p_{1/2})$, respectively. Whereas the peak at a BE of 860.53 (≡ sa), 865.48 (≡ sb), 878.45 (≡ sc), and 882.89 (≡ sd) signify their respective shake-up satellite peaks. The relatively lower intensity peaks of $Ni^{3+}(2p_{3/2})$ and $Ni^{3+}(2p_{1/2})$ than that of $Ni^{2+}(2p_{3/2})$ and $Ni^{2+}(2p_{1/2})$ represent the existence of NiO and Ni_2O_3 phases, where Ni_2O_3 is in the minority. Likewise, the O(1s) core level, shown in Fig. 4.2(b), is deconvoluted into two distinct peaks located at binding energies of 529.01 and 530.75 eV, corresponding to O^{2-} ions and defect sites on the surface or surface contamination, respectively. Furthermore, the separation of 324.42 eV in the position of Ni($2p_{3/2}$) and O(1s) core levels is much smaller compared to the non-stoichiometric Ni_2O_3 (i.e., 321.7 eV) and metallic Ni (321.7 eV).[34] Overall, this specifies the formation of stoichiometric NiO nanorods along with a minor

amount of non-stoichiometric Ni_2O_3 phase. The existence of negligible traces of Ni_2O_3 has positively assisted the porous NiO nanorods in delivering multifunctional properties.

4.3.3 XANES and EXAFS spectroscopy

The room temperature Ni *K*-edge absorption spectrum was recorded in transmission geometry using a lab-based tunable X-ray source to confirm the oxidation state of Ni ions in porous NiO nanorods. The obtained spectra of X-ray absorption near-edge structure (XANES) are shown in Fig. 4. A distinct shift in absorption edge towards higher energy compared to standard Ni metal and a good match with the standard NiO (Alfa Aesar, 3N purity) reference sample represents the existence of Ni^{2+} oxidation state in NiO nanorods (Fig. 4.3(a)). Moreover, the fitting of the Extended X-ray Absorption Fine Structure (EXAFS) spectrum in the back Fourier-transformed *k* – space is presented in Fig. 4.3(b). This fitting provides the value of ~ 2.108 ± 0.015 Å as bond distance and 0.005+/- 0.002 as the corresponding thermal mean square factor of the first coordination shell around Ni ions, along with the fixed coordination number of 6. This demonstrates the octahedral environment around the Ni ions in particulate porous NiO nanorods.

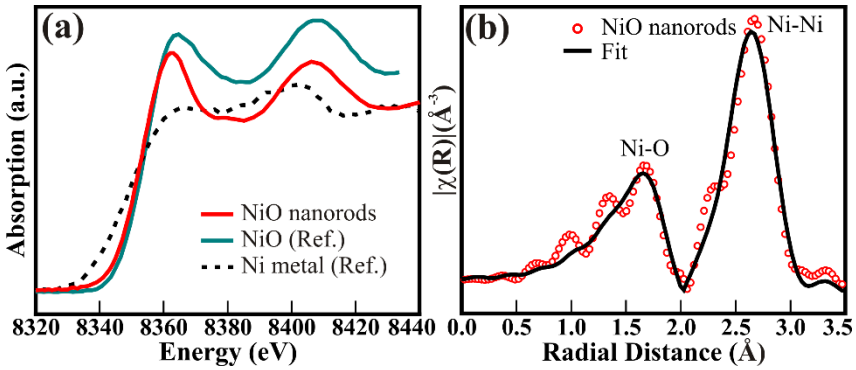

Figure 4.3 (a) Nickel K edge XANES and (b) x-ray absorption fine structure spectra in k-space of the particulate porous NiO nanorods.

4.3.4 SAXS and N_2 adsorption-desorption isotherm

The size of interlocked nanoparticles in the particulate NiO nanorods is estimated from the fitting/analysis of the SAXS profile collected in the range 2θ

= 0 to 5° (Fig. 4.4(a)). The most frequent radius of 6.5 nm corroborates the ~13 nm diameter of distinct NiO nanoparticles present in the nanorods offering porous nature. These interconnecting nanoparticles shaped nanorods of an average radius of 23.56 nm might represent the average diameter of ~47.12 nm for the NiO nanorods. These values of the diameter of nanoparticles and nanorods are akin to those estimated from the FESEM or TEM analysis, nevertheless, confirmed differentiation between the nanoparticles and nanorods from SAXS is challenging in the present case. The nanosized particles have resulted in a relatively higher surface-to-volume ratio (S/V) of 0.0279/Å. Further, the surface features were analyzed by N_2 gas adsorption-desorption isotherms at 77K (Fig. 4.4(b)). The NiO nanorods showed type IV isotherm (H3 hysteresis), indicating slit-like pores. The BET surface area of 84.731 m^2/g was estimated for the particulate porous NiO nanorods. The corresponding BJH pore size distribution (inset of Fig. 4.4(b)) illustrated the average pore diameter of 3.744 nm. These results strongly complement the values obtained from SAXS analysis and reveal more effective processes projecting the multifunctionality of porous NiO nanorods.

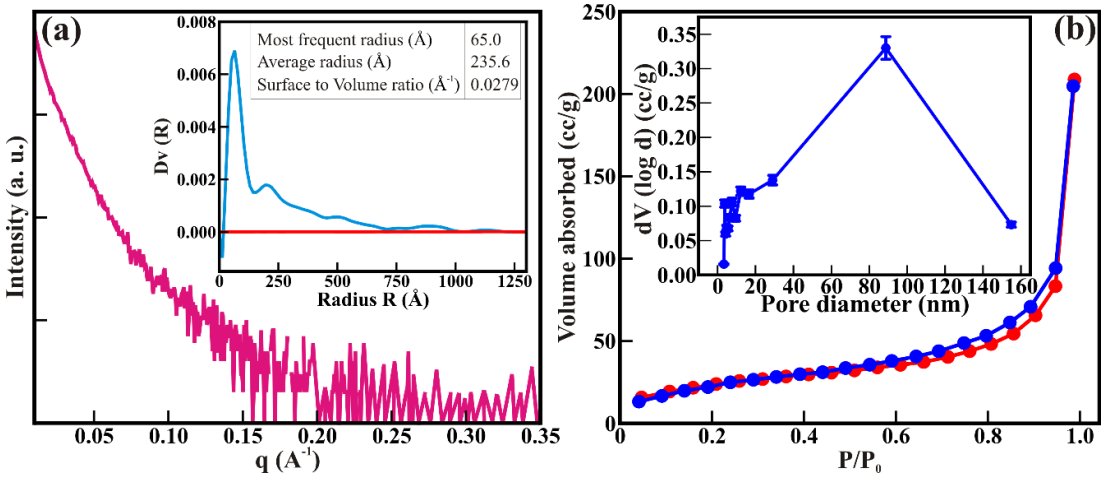

Figure 4.4 (a) SAXS profile of the particulate NiO nanorods; the inset shows corresponding best fitting/analysis using Easy-SAXS software. (b) N_2 adsorption-desorption isotherm and BJH pore diameter distribution (in the inset) of the particulate porous NiO nanorods.

4.3.5 CO_2 capture

The porous NiO nanorods comprising interconnected nanoparticles showed excellent porosity and surface-to-volume ratio, therefore employed for CO_2 capture. The CO_2 uptake of 0.63 and 0.47 mmol/g was recorded at 273 and 298 K, respectively (Fig. 4.5(a)). The lower value of CO_2 uptake at higher temperatures (298 K) indicates the exothermic type of adsorption. Therefore, the isosteric heat of CO_2 adsorption ($-Q_{st}$) was evaluated from the Clausius-Clapeyron equation to understand the nature of CO_2 adsorption over NiO nanorods (Fig. 4.5(b)). The $-Q_{st}$ values in the range of 8.53 kJ/mol to 7.41 kJ/mol indicates the physisorption of CO_2 gas over porous NiO nanorod surface, which also indicates the ease of regeneration of NiO nanorods. Additionally, the decrease in the $-Q_{st}$ values with an increase in the CO_2 uptake suggests the saturation of the active interaction sites at higher CO_2 loading.

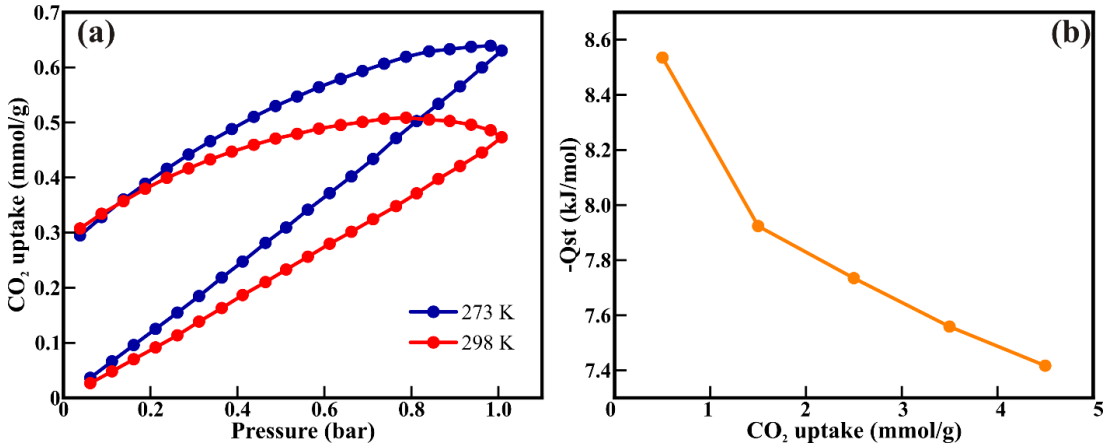

Figure 4.5 (a) The CO_2 adsorption-desorption isotherm at 273 and 298 K. (b) Isosteric heat of CO_2 adsorption over NiO nanorods calculated from CO_2 adsorption isotherm at 273 and 298 K using Clausius-Clapeyron equation.

4.3.6 Supercapacitor

The electrochemical energy storage performance of porous nanorods is evaluated from CV and GCD analysis (Fig. 6). The CV curves of NiO nanorods recorded at different scan rates from 5 to 100 mV/s at an optimized applied potential of 0.1 to 0.6 V (vs. SCE/V) (Fig. 4.6(a)) shows the pair of well-defined redox peaks due to Ni^{2+}/Ni^{3+} redox couples during charging (i.e., oxidation) and

discharging (i.e., reduction), signifies the reversible redox mechanism. The Ni^{2+}/Ni^{3+} redox couples assist the diffusion and extraction of OH^- ions from the surface of nanoparticles existing in the NiO nanorods. Moreover, the oxidation and reduction peaks have shifted at relatively higher and lower applied potentials, respectively, with an increase in the scan rate, representing the battery-type behavior. The NiO nanorods delivered a C_s (calculated from Eq. 4.2) of 368 F/g at a scan rate of 5 mV/s due to the significantly accessible surface area deep inside the porous rod body for flawless electron transfer for the facile diffusion of OH^- ions. Nevertheless, the C_s value was reduced to 177.9 F/g at a higher scan rate of 100 mV/s, at which the OH^- ions (or charges) encountered a significant barrier for diffusion. Fig. 4.6(b) illustrates the correlation between the peak current density (i_p) and the scan rate (υ) to identify the charge storage mechanism in the NiO nanorod electrode. Linear behavior is observed between peak current density and the scan rate. The estimated b value of 0.75 for anodic processes in NiO nanorods justifies the mixed behavior, i.e., both diffusion and surface charge storage mechanisms in the porous NiO nanorods. GCD studies performed at different current densities of 0.5 – 5 A/g indicate a reversible energy storage reaction mechanism in the NiO nanorods (Fig. 4.6(c)). The current density-dependent C_s values of the mesoporous NiO nanorods (Fig. 4.6(d)) were evaluated from the GCD curves using Eq. 4.3. C_S of 350.5 F/g obtained at the current density of 0.5 A/g has linearly decreased to 263.8 F/g at a current density of 5 A/g. The long-term cycling performance is crucial in analyzing the durable performance of supercapacitors. Therefore, the GCD cyclic performance of NiO nanorods was examined at the current density of 1 A/g (Fig. 4.6(e)). The 76.84% retention of initial capacitance after 2500 continuous charge-discharge cycles indicates the long-term cyclic stability of NiO nanorods. Furthermore, specific power and specific energy were evaluated to illustrate the electrochemical performance of the NiO electrode materials. Fig. 4.6(f) represents the relation between the specific energy and specific power of the active NiO nanorods electrode estimated in three electrode configurations. The NiO nanorods delivered maximum specific energy of 12.17 Wh/kg at a specific power of

193.68 W/kg and maximum specific power of 2035.49 W/kg at a specific energy of 9.15 Wh/kg. These significant energy and power density values are attributed to the large surface area and abundantly accessible activation sites provided by well-interconnected NiO nanoparticles forming porous nanorods.

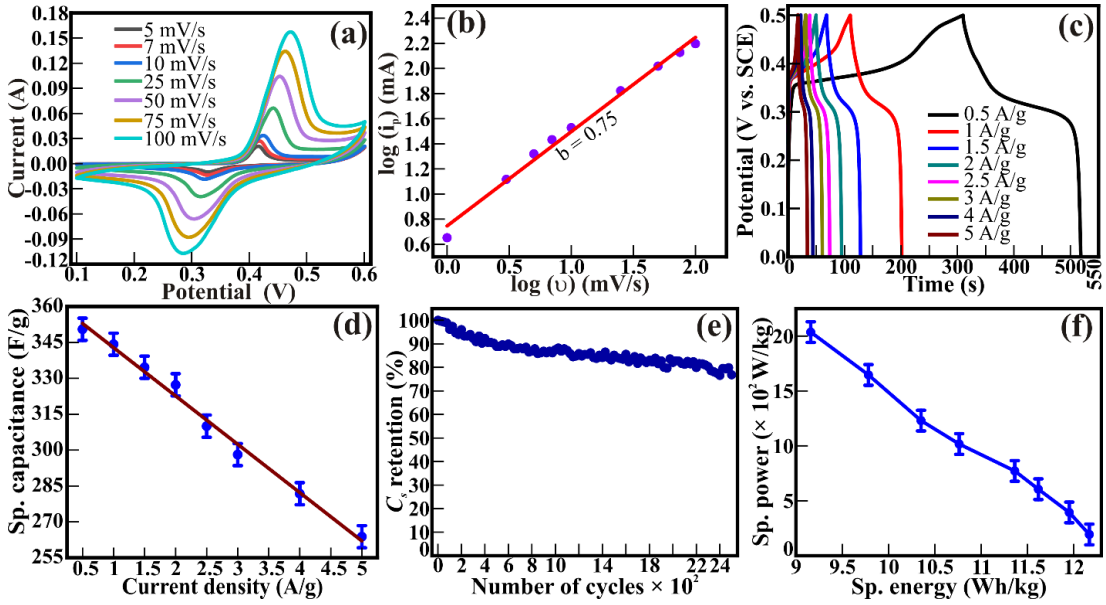

Figure 4.6 (a) CV curves of porous NiO nanorods at various scan rates. (b) Variation in the peak current density and the scan rate of the cathodic peak current. (c) GCD curves and (d) current density-dependent specific capacitance calculated from GCD curves, (e) Capacitance retention evaluated at 1 A/g, and (f) Ragone plot of porous NiO nanorods.

4.3.7 Water electrolysis

The OER activity of the porous NiO nanorods consisting of interconnected NiO nanoparticles was studied in a 1M KOH solution. Fig. 4.7(a) shows the LSV plots of the NiO nanorods and the commercial IrO_2 reference catalyst. The NiO nanorods demonstrate an overpotential of 441 mV to achieve a current density of 10 mA/cm^2, at which the reference catalyst exhibited an overpotential of 354 mV. Moreover, the boost in the current density at a potential of >1.35 V represents the existence of abundant active transitions between $Ni^{2+}/Ni^{3,}$ assisting in enhanced OER activity, which is in line with the XPS analysis. The reaction kinetics of electrocatalytic OER activity is analyzed from

the corresponding Tafel plots shown in Fig. 7(b). The Tafel slope of 108 and 75 mV/dec was observed for NiO nanorods and IrO_2 reference catalyst, respectively (Fig. 4.7(b)). The relatively closer proximity of Tafel slopes of NiO nanorods and IrO_2 reference catalyst suggests similar reaction kinetics and catalytic rate towards OER activity. The reliability of the electrocatalyst was analyzed by performing a CA stability test for 25 h at an overpotential of 441 mV (Fig. 4.7(c)). The current density remains stable for 25 h at 8.73 mA/cm^2 (13.03% loss), which signifies excellent stability. Additionally, the long-term stability is analyzed with consecutive LSV cycles, as shown in Fig. 4.9 (Left panel). A slight increase in overpotential of 11 mV observed for NiO nanorods after 3000 consecutive LSV cycles confirm the superior stability for OER activity.

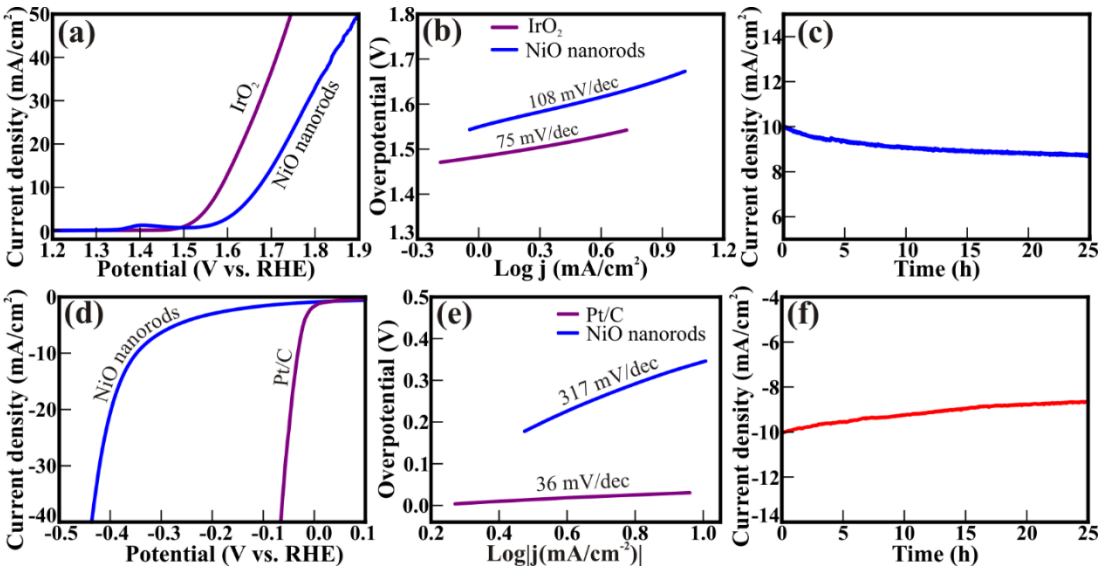

Figure 4.7 (a) Polarization curve (LSV plots) and (b) corresponding Tafel plot of porous NiO nanorods towards OER activity. (c) Chronoamperometry stability test of NiO nanorods at an overpotential of 441 mV for 25 h in 1M KOH. (d) Polarization curve (LSV plot) and (e) corresponding Tafel plot of porous NiO nanorods for HER activity. (f) Chronoamperometry stability test of NiO nanorods at an applied overpotential of 345 mV for 25 h in 0.5 M H_2SO_4.

Furthermore, the HER activity of NiO nanorods was studied in 0.5M H_2SO_4. The LSV plots towards HER activity (Fig. 4.7(d)) show an overpotential of 345 mV and 32 mV for NiO nanorods and reference Pt/C electrocatalyst,

respectively, at the current density of 10 mA/cm^2. The corresponding Tafel slope (Fig. 4.7(e)) evaluated for NiO nanorods and Pt/C electrocatalysts are 317 mV/dec and 36 mV/ dec, respectively. The stability test is performed at an overpotential of 345 mV to understand the performance of the NiO nanorods towards HER activity (Fig. 4.7(f)). The CA indicates that the current density reduced with time and reached 8.65 mA/cm^2 (~13.8 %) after 25 h stability study, demonstrating relatively stable HER activity. Additionally, the long-term stability of NiO nanorods was also ascertained from consecutive LSV cycles. A 12.5 mV increase in overpotential at the current density of 10 mA/cm^2 after 3000 consecutive LSV cycles confirms the exceptionally good stability of particulate porous NiO nanorods towards HER activity in an acidic medium (Fig. 4.8, right panel). Overall, nano-particulate porous 1D NiO nanorods showed excellent potential to produce hydrogen fuel through water electrolysis (Table 4.1).

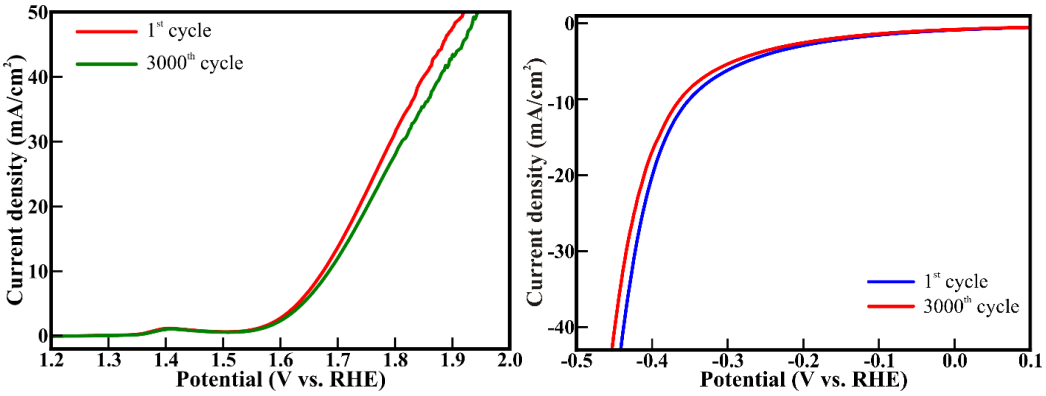

Figure 4.8 Polarization curves (LSV) of porous NiO nanorods for 1st and 3000th cycles of continuous operation in 1 M KOH towards OER activity (Left panel) and 0.5 M H_2SO_4 towards HER activity (Right panel).

Table 4.1. Comparative performance of various NiO nanostructures towards OER and HER activity.

Catalyst	Over potential (mV)@10 mA/cm^2		Tafel Slope (mV/dec)		Ref.
	OER	HER	OER	HER	
1D NiO nanoparticulate porous nanorods	441	345	108	317	This work
Ni/NiO@rGO	480	582	41	63	[27]

NiO hollow microsphere	370	424	156	105	[26]
Ni-NiO@3D graphene	1640	310	55	78	[29]
NiO nanoparticles/GO	453	625	-	-	[28]
MoS_2@NiO nanocomposite	-	406	-	44	[30]

Further, to confirm the electrocatalytic stability of the NiO nanorods consisting of interconnected NiO nanoparticles, the structural, morphological, and chemical properties were analyzed from XRD, FESEM, and EDS. The Rietveld refinement of the XRD pattern of NiO nanorods after the CA stability test for 25 h in a basic medium is shown in Fig. 4.9(a). The NiO nanorods retained the cubic structure with an $Fm\bar{3}m$ space group. The characteristic XRD peaks positions at 2θ of 37.33°, 43.38°, 63.03°, 75.60°, and 79.61° represent (111), (020), (022), (131), and (222) peaks, respectively (ICSD No. 1010093), showed no shift after continuous CA measurements. The value of goodness of fitting factors such as R_{Bragg} (= 2.32), R_{EXP} (= 9.03), R_P (= 8.34), and GoF (= 15.816), the estimated lattice parameters (i.e., a = b = c = 4.175 Å) and cell volume (= 73.80 g/cc) of NiO nanorods after and before CA analysis remained almost identical. Likewise, the morphology of NiO nanoparticles after CA analysis for 25 h (Fig. 4.9(b)) remained identical to that of before electrochemical water splitting activities. Moreover, the EDS spectra show distinct peaks (Fig. 4.9(c)), illustrating the existence of Ni and O without any other foreign elements after the electrochemical water-splitting reaction. The C is observed due to the use of carbon tape during the EDS measurement. This confirmed the excellent structural, morphological and chemical stability of NiO nanorods toward water splitting activity even after electrocatalytic reaction for 25 h.

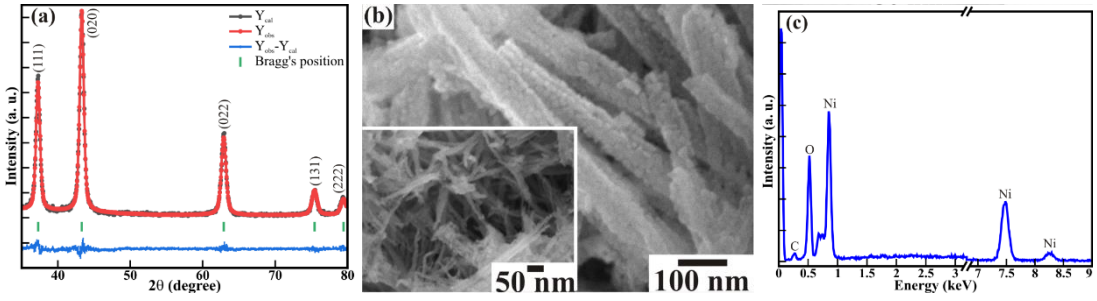

Figure 4.9 (a) XRD, (b) FESEM, and (c) EDS analysis of the NiO nanorods after the CA stability test for 25 h in a basic medium.

4.3.8 Electrochemical impedance spectroscopy (EIS)

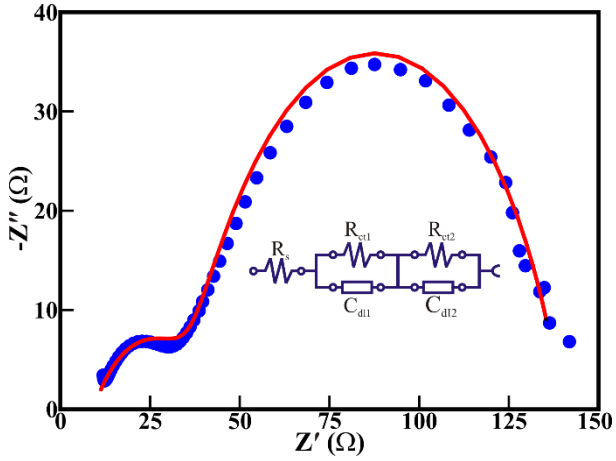

Figure 4.10 Electrochemical impedance spectrum of NiO nanorod electrocatalyst at an overpotential of 441 mV towards OER activity.

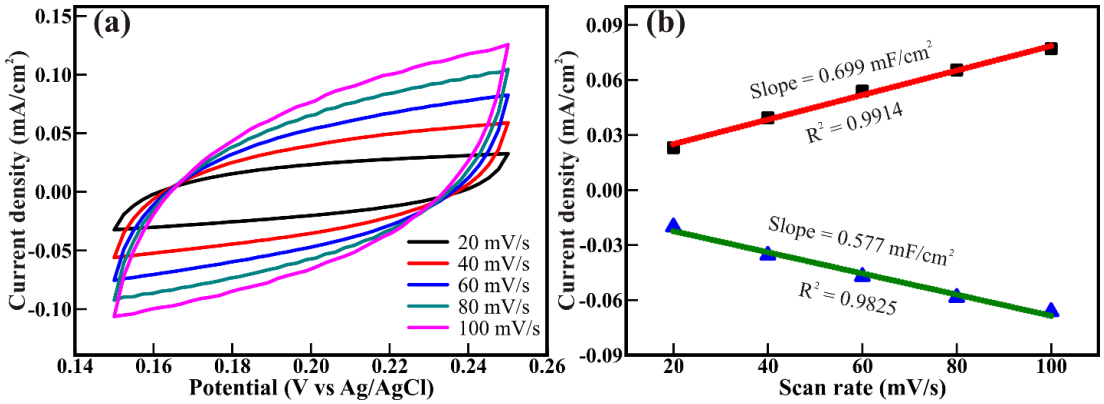

Figure 4.11 (a) Cyclic voltammetry curves of porous NiO nanorods and (b) corresponding plot of J_a and J_c against scan rate for the determination of double layer capacitance (C_{dl}).

Electrochemical impedance spectroscopy (EIS) study was performed to analyze the charge transfer process during OER activity (Fig. 4.10). The interfacial resistance (R_s) of 9.26 Ω is observed at the interface of the electrocatalyst and electrolyte. Moreover, the resistance at the textural boundary (R_{Ct1}) and the core/bulk of NiO nanorods (R_{Ct2}) are 28.9 and 102 Ω, respectively, indicating the active contributions of both the textural boundaries and core of NiO nanoparticles in the electrocatalytic OER activities. Further, the ECSA of porous NiO nanorods is evaluated from the CV measurements performed at

different scan rates from 20 to 100 mV/s(Fig. 4.11(a)). The anodic (J_a) and cathodic (J_c) double-layer charging currents, estimated at a fixed potential of 0.2 V (*vs*. Ag/AgCl), are plotted against corresponding scan rates (Fig. 4.11(b)). The estimated C_{dl} of 0.623 mF/cm for the particulate porous NiO nanorods illustrates the ECSA of 15.57 cm^2. This represents that the porous NiO nanorods formed of interconnected NiO nanoparticles deliver more open-up active sites, consequently administrating higher electrochemical as well as adsorption activity.

4.4 Conclusion

In conclusion, we have hydrothermally synthesized porous NiO nanorods formed by interconnecting cubic crystalline NiO nanoparticles with the Fm-3m space group. The surface morphological and structural analysis confirm the assembly of porous NiO nanorods of diameter ~47.12 nm due to the interlinking of nanoparticles of diameter ~13 nm, providing a surface-to-volume ratio of 0.0279/Å. The BET analysis revealed a surface area of 84.731 m^2/g and an average pore diameter of 3.74 nm originating from interlocked NiO nanoparticles. The high-resolution XPS and EXAF confirm the 2+ octahedron coordination and the existence of Ni^{2+}/Ni^{3+} transitions in the NiO nanorods. The excellent regenerative CO_2 capturing ability with CO_2 uptake of 0.63 mmol/g at 273K and the competent electrochemical energy storage ability with good retention (i.e., 76.84 % @ 2500 cycle), specific energy (i.e., 12.17 Wh/Kg at 0.5 A/g) and specific power (i.e.,2035.49 W/kg at 5A/g) indicate the potentials of porous NiO nanorods as electrode materials for CO_2 capture and electrochemical supercapacitor. Moreover, porous NiO nanorods provided a larger surface area and subsequent electro-catalytically active surface sites and delivered overpotentials of 441 and 345 mV for OER and HER activity, respectively, and showed long-term stability of NiO nanorods in both basic and acidic mediums for overall water electrolysis. Overall, the present study indicates that, like nano-particulate porous NiO nanorods, any stable materials providing hetero-architectural porous structure with a larger surface area and easily accessible active sites can be a potential candidate for multifunctional devices in the future.

4.5 References

[1] Devan R. S., Patil R. A., Lin J.-H., Ma Y.-R., (2012), One-dimensional metal-oxide nanostructures: Recent developments in synthesis, characterization, and applications, Adv. Funct. Mater., 22, 3326-3370, (DOI: 10.1002/adfm.201201008).

[2] Bao Y., Zhang F., (2022), Electronic engineering of ABO_3 perovskite metal oxides based on d^0 electronic-configuration metallic ions toward photocatalytic water splitting under visible light, Small Structures, 3, 2100226, (DOI: 10.1002/sstr.202100226).

[3] Cheema S. S., Shanker N., Wang L.-C., Hsu C.-H., Hsu S.-L., Liao Y.-H., et. al, (2022), Ultrathin ferroic HfO_2–ZrO_2 superlattice gate stack for advanced transistors, Nature, 604, 65-71, (DOI: 10.1038/s41586-022-04425-6).

[4] Zhai X.-P., Gao L.-F., Zhang H., Peng Y., Zhang X.-D., Wang Q., Zhang H.-L., (2022), Defect Engineering of Ultrathin WO3 Nanosheets: Implications for Nonlinear Optoelectronic Devices, ACS Appl. Nano Mater., 5, 1169-1177, (DOI: 10.1021/acsanm.1c03791).

[5] Wang Y., Liu Y., Tong J., Shi X., Huang L., Xiao Z., Wang G., Pan D., (2022), A general and facile solution approach for deposition of high-quality metal oxide charge transport layers, Sol. Energy Mater. Sol. Cells, 236, 111511, (DOI: 10.1016/j.solmat.2021.111511).

[6] Manjunath V., Bimli S., Parmar K. H., Shirage P. M., Devan R. S., (2019), Oxidized Nickel films as highly transparent HTLs for inverted planar perovskite solar cells, Sol. Energy, 193, 387-394, (DOI: 10.1016/j.solener.2019.09.070).

[7] Mandavkar R., Kulkarni R., Lin S., Pandit S., Burse S., Ahasan Habib M., Pandey P., Hee Kim S., Li M.-Y., Kunwar S., Lee J., (2022), Significantly improved photo carrier injection by the MoS_2/ZnO/HNP hybrid UV photodetector architecture, Appl. Surf. Sci., 574, 151739, (DOI: 10.1016/j.apsusc.2021.151739).

[8] Manjunath V., Mishra P. K., Dobhal R., Bimli S., Shirage P. M., Sen S., Shaikh P. A., Devan R. S., (2021), Perovskite-based facile NiO/$CH_3NH_3PbI_3$ heterojunction self-powered broadband photodetector, ACS Appl. Electron. Mater., 3, 4548-4557, (DOI: 10.1021/acsaelm.1c00679).

[9] Kitchamsetti N., Samtham M., Didwal P. N., Kumar D., Singh D., Bimli S., Chikate P. R., Basha D. A., Kumar S., Park C.-J., Chakraborty S., Devan R. S., (2022), Theory abide experimental investigations on morphology driven enhancement of electrochemical energy storage performance for manganese titanate perovskites electrodes, J. Power Sources, 538, 231525, (DOI: 10.1016/j.jpowsour.2022.231525).

[10] Feng Z., Zhang Y., Sun J., Liu Y., Jiang H., Cui M., Hu T., Meng C., (2022), Dual ions enable vanadium oxide hydration with superior Zn2+ storage for aqueous zinc-ion batteries, Chem. Eng. J., 433, 133795, (DOI: 10.1016/j.cej.2021.133795).

[11] Li Q., Zeng W., Li Y., (2022), Metal oxide gas sensors for detecting NO_2 in industrial exhaust gas: Recent developments, Sens. Actuators B: Chem., 359, 131579, (DOI: 10.1016/j.snb.2022.131579).

[12] Parmar K. H., Manjunath V., Bimli S., Chikate P. R., Patil R. A., Ma Y.-R., Devan R. S., (2022), Stable and reversible electrochromic behaviors in anodic NiO thin films, Chinese J. Phys., 77, 143-150, (DOI: 10.1016/j.cjph.2022.02.014).

[13] Eivazzadeh-Keihan R., Bahojb Noruzi E., Chidar E., Jafari M., Davoodi F., Kashtiaray A., Ghafori G. M., Masoud H. S., Javanshir S., Ahangari C. R., Maleki A., Mahdavi M., (2022), Applications of carbon-based conductive nanomaterials in biosensors, Chem. Eng. J., 442, 136183, (DOI: 10.1016/j.cej.2022.136183).

[14] Yuan F., Xia Y., Lu Q., Xu Q., Shu Y., Hu X., (2022), Recent advances in inorganic functional nanomaterials based flexible electrochemical sensors, Talanta, 244, 123419, (DOI: 10.1016/j.talanta.2022.123419).

[15] Miao Y., Zhang X., Sui Y., Hu E., Qi J., Wei F., Meng Q., He Y., Sun Z., Ren Y., Zhan Z., (2020), Nanospherical Cu_2O/NiO synthesized by electrochemical dealloying as efficient electrode materials for supercapacitors, Mater. Lett., 265, 127300, (DOI: 10.1016/j.matlet.2020.127300).

[16] Kitchamsetti N., Chikate P. R., Patil R. A., Ma Y.-R., Shirage P. M., Devan R. S., (2019), Perforated mesoporous NiO nanostructures for an enhanced pseudocapacitive performance with ultra-high rate capability and high energy density, CrystEngComm, 21, 7130-7140, (DOI: 10.1039/C9CE01475F).

[17] Lei Y., Xu T., Ye S., Zheng L., Liao P., Xiong W., Hu J., Wang Y., Wang J., Ren X., He C., Zhang Q., Liu J., Sun X., (2021), Engineering defect-rich Fe-doped NiO

coupled Ni cluster nanotube arrays with excellent oxygen evolution activity, Appl. Catal. B: Environ., 285, 119809, (DOI: 10.1016/j.apcatb.2020.119809).

[18] Macdonald T. J., Xu J., Elmas S., Mange Y. J., Skinner W. M., Xu H., Nann T., (2014), NiO nanofibers as a candidate for a nanophotocathode, Nanomaterials, 4, 256-266, (DOI:

[19] Han K., Huang H., Gong Q., Si T., Zhang Z., Zhou G., (2018), Temperature-induced hierarchical tremella-like and pinecone-like NiO microspheres for high-performance supercapacitor electrode materials, J. Mater. Sci., 53, 12477-12491, (DOI: 10.1007/s10853-018-2532-9).

[20] Zheng Y.-z., Ding H.-y., Zhang M.-l., (2009), Preparation and electrochemical properties of nickel oxide as a supercapacitor electrode material, Mater. Res. Bull., 44, 403-407, (DOI: 10.1016/j.materresbull.2008.05.002).

[21] Liu X.-M., Zhang X.-G., Fu S.-Y., (2006), Preparation of urchinlike NiO nanostructures and their electrochemical capacitive behaviors, Mater. Res. Bull., 41, 620-627, (DOI: 10.1016/j.materresbull.2005.09.006).

[22] Wang D., Wang Q., Wang T., (2013), Controlled synthesis of porous nickel oxide nanostructures and their electrochemical capacitive behaviors, Ionics, 19, 559-570, (DOI: 10.1007/s11581-012-0781-1).

[23] Pang H., Lu Q., Zhang Y., Li Y., Gao F., (2010), Selective synthesis of nickel oxide nanowires and length effect on their electrochemical properties, Nanoscale, 2, 920-922, (DOI: 10.1039/C0NR00027B).

[24] Ci S., Wen Z., Qian Y., Mao S., Cui S., Chen J., (2015), NiO-microflower formed by nanowire-weaving nanosheets with interconnected Ni-network decoration as supercapacitor electrode, Sci. Rep., 5, 11919, (DOI: 10.1038/srep11919).

[25] Pang H., Guan B., Sun W., Wang Y., (2016), Metal-organic-frameworks derivation of mesoporous NiO nanorod for high-performance lithium ion batteries, Electrochim. Acta, 213, 351-357, (DOI: 10.1016/j.electacta.2016.06.163).

[26] Mondal A., Paul A., Srivastava D. N., Panda A. B., (2018), NiO hollow microspheres as efficient bifunctional electrocatalysts for overall water-splitting, Int. J. Hydrog. Energy, 43, 21665-21674, (DOI: 10.1016/j.ijhydene.2018.06.139).

[27] Narwade S. S., Mali S. M., Digraskar R. V., Sapner V. S., Sathe B. R., (2019), Ni/NiO@rGO as an efficient bifunctional electrocatalyst for enhanced overall water splitting reactions, Int. J. Hydrog. Energy, 44, 27001-27009, (DOI: 10.1016/j.ijhydene.2019.08.147).

[28] Jo S. G., Kim C.-S., Kim S. J., Lee J. W., (2021), Phase-controlled NiO nanoparticles on reduced graphene oxide as electrocatalysts for overall water splitting, Nanomaterials, 11, 3379, (DOI: 10.3390/nano11123379)

[29] Ullah N., Zhao W., Lu X., Oluigbo C. J., Shah S. A., Zhang M., Xie J., Xu Y., (2019), In situ growth of M-MO (M = Ni, Co) in 3D graphene as a competent bifunctional electrocatalyst for OER and HER, Electrochim. Acta, 298, 163-171, (DOI: 10.1016/j.electacta.2018.12.053).

[30] Mugheri A. Q., Ali S., Narejo G. S., Otho A. A., Lal R., Abro M. A., Memon S. H., Abbasi F., (2020), Electrospun fibrous active bimetallic electrocatalyst for hydrogen evolution, Int. J. Hydrog. Energy, 45, 21502, (DOI: 10.1016/j.ijhydene.2020.06.005).

[31] Giraldo L., Rodriguez-Estupiñán P., Moreno-Piraján J. C., (2019), Isosteric Heat: Comparative study between clausius–clapeyron, csk and adsorption calorimetry methods, Processes, 7, 203, (DOI: 10.3390/pr7040203)

[32] Guha N., Gupta A. K., Chatterjee S., Krishnan S., Singh M. K., Rai D. K., (2021), Environmentally benign melamine functionalized silica-coated iron oxide for selective CO_2 capture and fixation into cyclic carbonate, J. CO_2 Util., 49, 101575, (DOI: 10.1016/j.jcou.2021.101575).

[33] Prasannachandran R., Vineesh T. V., Anil A., Krishna B. M., Shaijumon M. M., (2018), Functionalized phosphorene quantum dots as efficient electrocatalyst for oxygen evolution reaction, ACS Nano, 12, 11511, (DOI: 10.1021/acsnano.8b06671).

[34] Kitchamsetti N., Ramteke M. S., Rondiya S. R., Mulani S. R., Patil M. S., Cross R. W., Dzade N. Y., Devan R. S., (2021), DFT and experimental investigations on the photocatalytic activities of NiO nanobelts for removal of organic pollutants, J. Alloys Compd., 855, 157337, (DOI: 10.1016/j.jallcom.2020.157337).

Chapter 5

NiO thin films based self-powered photodetector

5.1 Introduction

The field of optoelectronics has been transformed with the advent of metal halide perovskites that possess unique optoelectronic properties, namely, direct tunable bandgap, large charge diffusion length, high absorption coefficient, photon recycling, etc.,[1] which can be further tuned by merely varying the chemical composition of ABX_3 (where A and B are cations and X is halide anion) metal halide perovskite structures.[2] Therefore, these perovskite halides have shown promise towards various optoelectronic applications in solar cells,[3-6] microlasers,[7] PDs,[8] and light-emitting diodes,[9-10], etc. However, PDs, intelligent optoelectronic devices that convert optical input signals to electrical outputs, attract attention due to their advancement in sensing, imaging, communication, and environmental monitoring. Although several semiconducting materials were employed in the PDs depending on the absorption range and bandgap, the invention of broadband PDs utilizing MAPI perovskites has triggered excitement due to its high photocurrent (I_{photo}).[11] Dou et al.[12] demonstrated perovskite PDs with solution-processed $CH_3NH_3PbI_{3-x}Cl_x$. After which, various perovskite PDs are described in the literature.[13-16] Generally, to enhance the performance of perovskite-based photodetection, three main strategies used are (i) engineering device structures,[17] (ii) controlling the morphology of perovskite films,[18] and (iii) construction of heterojunctions.[19-21] Among these strategies, heterojunction facilitates exciton dissociation and carrier transport resulting in broad spectral response and improved performance.[8,13,22-25] Therefore, several organic and inorganic semiconductors, along with metal halide perovskites, were used to fabricate heterojunction PDs.[13,26-28] Among the inorganic semiconductors, nickel oxide (NiO) with high chemical stability is of prime importance and is a promising candidate for optoelectronic and energy/conversion applications.[29-32]

Recently, self-powered perovskite-based PDs have attracted intense attention due to their independence, less complicated circuitry, and self-sufficient potential for device operation. These PDs depend on PV behavior to produce light current at 0 V bias, which is achieved by forming Schottky junctions with single perovskite crystals and p-i-n junctions.[33-35] However, these materials are thermally unstable and degrade in the ambient atmosphere.[35-36] This becomes a critical issue inhibiting device performance for real-time applications such as optical communication, imaging, sensing, etc.[37-39]

Therefore, a systematic study on degradation mechanisms and intrinsic modification within metal halide perovskite in the presence of a foreign layer is highly desirable.

In this work, high-performance self-powered NiO and MAPI heterojunction PD are engineered in the ambient to observe a broad spectral response ranging from ultra-violet (UV) to visible spectra. The performance of self-powered PDs is probed at five different wavelengths of 290±5 nm (UV), 450±5 nm (Blue), 540±5 nm (Green), and 640±5 nm (Red) provides a thorough outline of the entire UV-VIS spectra (Fig. 5.1), which has been scarcely investigated in earlier reported studies. To account for the figure-of-merits of the PD, the responsivity (R), detectivity (D*), sensitivity (S), and On/Off ratio were measured at each probing wavelength. The self-powered PD delivered a responsivity of 33.39 mA/W for UV light, followed by 6.48, 2.57, 2.29, and 5.79 mA/W for blue, green, red, and white lights, respectively, at zero bias. Additionally, high detectivity in the order of 1010 Jones was observed. Further, the stability of the self-powered PD was studied for up to 58 days. Though the X-ray diffraction studies revealed the degradation of MAPI films contributed to the reduction in current, optimized content of PbI_2 in MAPI films enhanced PDs performance due to the reduction of dark current. Overall, our findings suggest that NiO and MAPI heterojunction is promising to fabricate low-cost and high-performance self-powered PDs for optoelectronic applications.

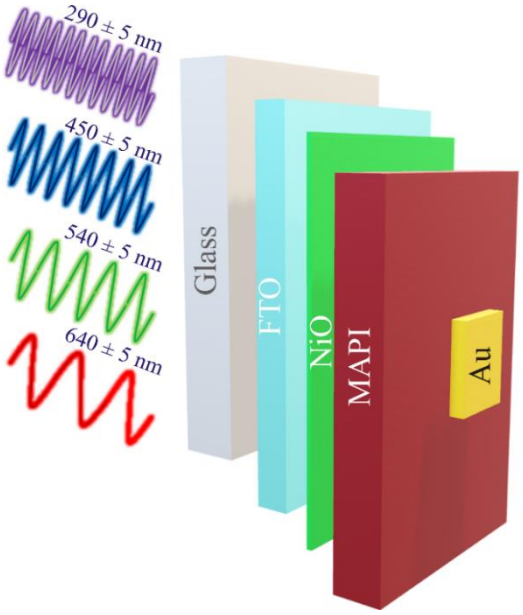

Figure 5.1 Schematic of the self-powered NiO and MAPI heterojunction PD engineered to perform at different wavelengths in the UV-VIS region.

5.2 Experimental section

5.2.1 Chemicals and reagents

Nickel (99.5%, Alfa Aesar), Lead Iodide (99.9985%, Alfa Aesar), Methylamine Hydroiodide (TCI), N, N-Dimethylformamide (DMF) (Sigma Aldrich), Dimethyl Sulfoxide (DMSO) (Sigma Aldrich), Ethanol (SRL Chem), and Isopropyl Alcohol (SRL Chem) were used as received.

5.2.2 Device fabrication

The device was fabricated in the piecemeal processing of FTO, NiO, MAPI, and Au constituents. The schematic of the device fabrication process is shown in Fig. 2.3. FTO-coated glass substrates were ultrasonically cleaned sequentially with soap solution, DI water, acetone, and ethanol, which were further dried in hot air. The as-cleaned substrates were coated with highly transparent NiO thin films following the recipes reported in previous studies.[6] Initially, high-purity nickel metal (i.e., 99.5%) was thermally evaporated over FTO substrates and further oxidized for 3 hr in ambient at 580°C to form NiO thin films. MAPI perovskite was deposited in the ambient with a two-step deposition process. 1.2 M lead iodide dissolved in 19:1 (DMF: DMSO) was spin-coated on NiO films at 1500 rpm for 30 sec and further dried at 75 °C for 60 sec. It was further dipped in methylamine hydroiodide and isopropyl alcohol solution for 20 sec (10 mg/ml) to obtain reddish-brown perovskite films, which were rinsed in isopropyl alcohol to remove excess growth of perovskite and immediately spun at 4500 rpm for 10 sec to form smooth and transparent films. Transparent thin films converted into reddish-brown films upon heating at 100 °C for 30 min were allowed to cool at room temperature. Further, Au was thermally evaporated through a shadow mask to form a counter electrode. The active area of the device was defined at 0.7 cm^2.

5.2.3 Characterization

The surface morphology and thickness of each layer deposited were analyzed from Field Emission Scanning Electron Microscopy (FESEM, JEOL,

JSM-7610 F). Absorption spectra of NiO and MAPI films were recorded using a UV–Vis spectrophotometer (Shimadzu, UV-2600) to confirm the absorption range and bandgap. The structural and chemical variations in the MAPI films were recorded using an X-ray diffractometer (Bruker D2 Phaser) to understand the effect of light exposure on the device's performance. I-V conductance was measured using a Keithley Source meter 2401. Photo-sensing studies on the self-powered PD were performed in the ambient utilizing a customized setup, placed inside a dark box to ensure the absence of any external light. Steady LED light sources of various wavelengths, i.e., 290, 450, 540, 640 nm, and white light with a constant power of 1.15 mW, were used to perform the photosensing studies. A minimum of 4 on/off cycles of photo illumination was studied with the sequential periodicity of 30 s light On and Off for each wavelength. ΔI evaluated at the 90 % change in the I_{light} during light On and Off as shown in Eq. 5.1 and 5.2.[40] The sensitivity (S) of the NiO/MAPI heterojunction at a different probing wavelength was calculated with Eq. 5.3. The ratio of On current to that of Off current was calculated from Eq. 5.4. The ability to generate photocurrent per incident power (P_{in}) per illumination area (A) given by responsivity (R) is shown in Eq. 5.5. Conversely, detectivity (D*) defined as the ability of the self-powered NiO/MAPI heterojunction to detect minimum optical signal above the noise is shown in Eq. 5.6.[41-42] The rise time (T_r), the time taken by NiO/MAPI PD to switch from Off state to On state, was defined as the time required for the I_{dark} to reach 90% of I_{light}. Similarly, the fall time (T_f) was the time required for NiO/MAPI PD to switch from 90 % I_{light} to I_{dark}. Moreover, the content of PbI_2 is evaluated from Eq. 5.7. The critical parameter to understand the performance of PD was calculated using the following equations,

$$I_{Photo} = I_{light} - I_{dark} \tag{5.1}$$

$$\Delta I = 90\%\ of\ I_{light} - I_{dark} \tag{5.2}$$

$$S = \frac{(90\%\ of\ I_{light} - I_{dark})}{I_{dark}} \tag{5.3}$$

$$\frac{On}{Off} ratio = \frac{I_{light}}{I_{dark}} \tag{5.4}$$

$$R = \frac{I_{Photo}}{P_{in}} \tag{5.5}$$

$$D^* = \frac{R}{\sqrt{2qJ_{dark}}} \quad (5.6)$$

$$Content\ of\ PbI_2 = \frac{Intensity\ of\ PbI_2}{Intensity\ of\ PbI_2 + Intensity\ of\ MAPI} \times 100 \quad (5.7)$$

where P_{in} is the incident light energy, J_{dark} is the dark current density, and q is the electronic charge.

5.3 RESULTS AND DISCUSSIONS

5.3.1 Microstructure and band diagram

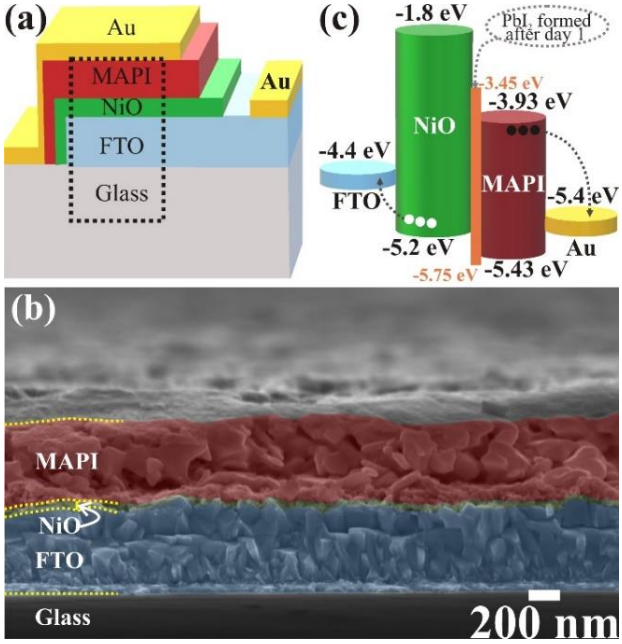

Figure 5.2 (a) Schematics of the fabricated NiO/MAPI photodetector. (b) Cross-sectional FESEM image of the NiO/MAPI photodetector (as highlighted with dotted lines in (a)). Pale blue, green, and red colors highlight the FTO, NiO, and MAPI, respectively. (c) Schematics of the corresponding band diagram.

The self-powered PD was fabricated with FTO/NiO/MAPI/Au device architecture. The schematic of the fabricated self-powered PD is shown in Fig. 5.2(a). The corresponding cross-section FESEM image of NiO and MAPI heterojunction formed over FTO coated glass substrate is shown in Fig. 5.2(b). The thin layer of NiO is stacked between FTO and MAPI. Three distinct layers were observed in the cross-sectional FESEM image and highlighted with pale blue (for FTO), green (for NiO), and red (for MAPI) colors. The estimated

thickness of FTO, NiO, and MAPI films was ~ 550-575, ~35-45, and~ 500-530 nm, respectively. The observed thickness of NiO film is akin to our previously reported data.[6] The corresponding band diagram of the NiO/MAPI heterojunction where PbI_2 evolved with time (Fig. 5.2(c)) is prepared utilizing the energy levels from the literature,[6,43] reveals that the well-aligned energy levels of NiO and MAPI heterojunction can facilitate the collection of photogenerated charge carriers. However, the PbI_2 formed from MAPI progress with time and tailors the energy levels alignment, which is expected to alter the PDs performance. Further the band bending occurring during the operation of the NiO/MAPI self-powered photodetector developing a built-in potential of ~2.13 eV is shown in Fig. 5.3.

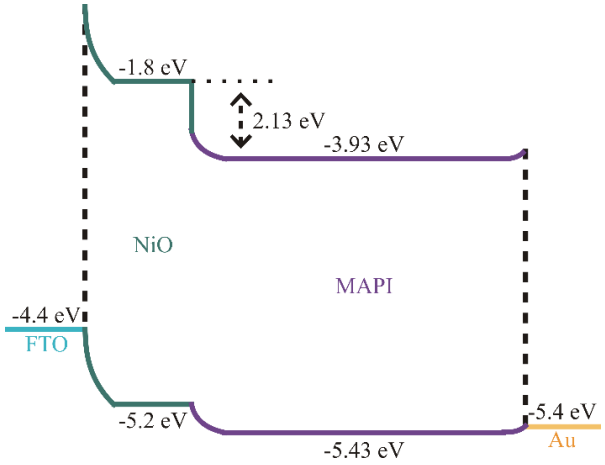

Figure 5.3 Schematic for energy level band bending of self-powered NiO/MAPI photo detector.

5.3.2 UV-Visible spectroscopy

UV-Vis spectroscopy was used to record the absorption spectra of the fabricated NiO/MAPI heterojunction. The UV-Vis absorption spectroscopy of NiO thin films synthesized over FTO-coated glass substrates (Fig. 5.4) showed minimum absorption in the visible range (400 – 800 nm), allowing maximum visible wavelength to irradiate MAPI films. The NiO thin film absorption onset was observed at ~378 nm, and the corresponding bandgap of 3.28 eV was estimated by Tauc's plot (inset of Fig. 5.4).

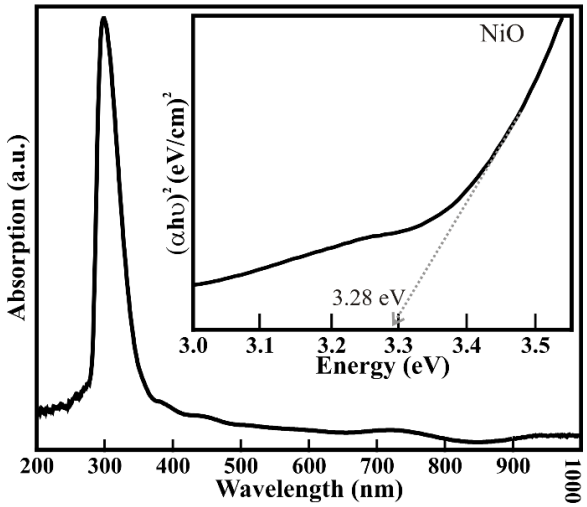

Figure 5.4 UV-Vis absorption spectrum and Tauc's plot (inset) for estimating the bandgap of NiO films coated over FTO substrates.

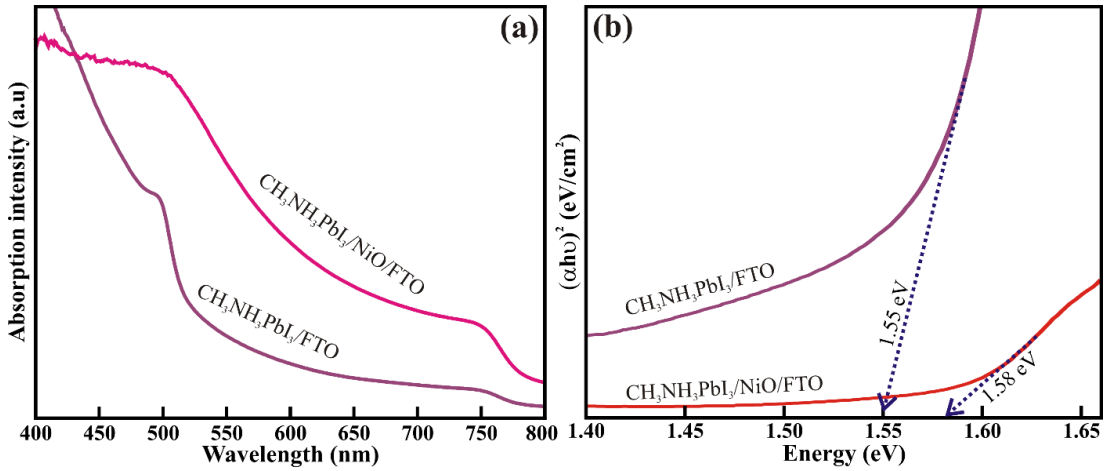

Figure 5.5 (a) UV-Vis absorption spectrum and corresponding (b) Tauc's plot for estimating bandgap of MAPI films coated over plain FTO (i.e., $CH_3NH_3PbI_3$/FTO) and NiO coated FTO substrates (i.e., $CH_3NH_3PbI_3$/NiO/FTO corresponds to NiO/MAPI).

Further, the absorption range and corresponding bandgaps of plain MAPI films and MAPI coated over NiO (i.e., NiO/MAPI) film are shown in Fig. 5.5(a) and (b), respectively. The pristine MAPI coated over FTO (i.e., FTO/MAPI) and MAPI film over NiO (i.e., FTO/NiO/MAPI) in NiO/MAPI heterojunction showed an excellent absorption range in the visible spectrum. A slight extension of the absorption range over 750 nm may be possible due to sub-band states arising from pinholes in the films. The bandgaps of 1.55 and 1.58 eV obtained

for FTO/MAPI and FTO/NiO/MAPI heterojunction, respectively, exhibited insignificant variations akin to the literature.[44-45] Even though NiO absorbs UV and MAPI absorbing visible spectrum independently, the NiO/MAPI heterojunction altogether absorbs both UV and Visible spectrum. However, the visible range absorption of MAPI film over NiO in heterojunction was higher than the MAPI film over FTO substrate, indicating NiO as a template enhanced visible range absorption.

5.3.3 Field emission scanning electron microscopy

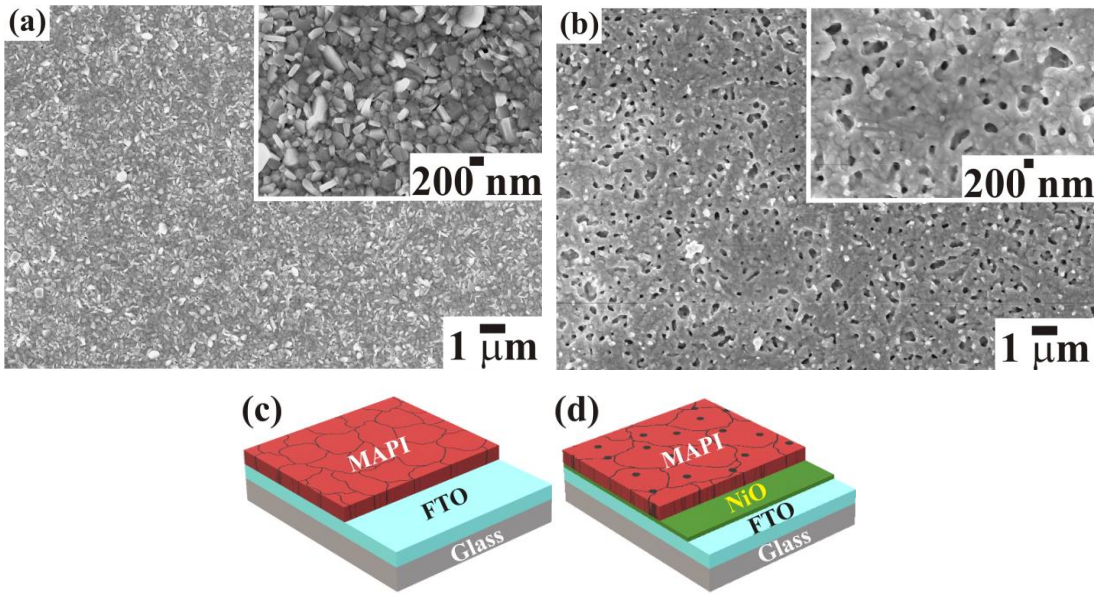

Figure 5.6 Top view FESEM images of the (a) plain MAPI films coated over FTO. (b) MAPI films coated over NiO film. Inset shows their respective high-magnification images. Schematics of (c) plain MAPI films coated over FTO and (d) MAPI films with pinholes coated over NiO film.

Fig. 5.6 shows the FESEM micrographs of MAPI film deposited over plain FTO substrate (Fig. 5.6(a)) and NiO-loaded FTO substrate (Fig. 5.6(b)). Uniform grain growth of MAPI on the FTO substrates resulted in the formation of plain MAPI film over a large area. The high magnification micrographs to the inset of Fig. 5.6(a) revealed no pinholes in the plain MAPI films. Fig. 5.6(c) depicts the schematics of uniform grains of MAPI films coated over an FTO substrate. However, NiO over the FTO substrate has led to the formation of non-

uniform grains along with a few secondary grains of MAPI. The high magnification FESEM image to the inset of Fig. 5.6(b) revealed a large number of pinholes of diameter between ~50 to 300 nm in MAPI film coated over NiO. Fig. 5.6(d) represents the schematic of many pinholes produced in the MAPI films coated over the NiO, typically observed with thermally evaporated metal oxide underlayer,[6,46] which can be tailored under controlled thickness or roughness of NiO film. Overall, plain MAPI films showed a larger area uniformity than MAPI films in NiO/MAPI heterojunction.

5.3.4 Photodetector studies

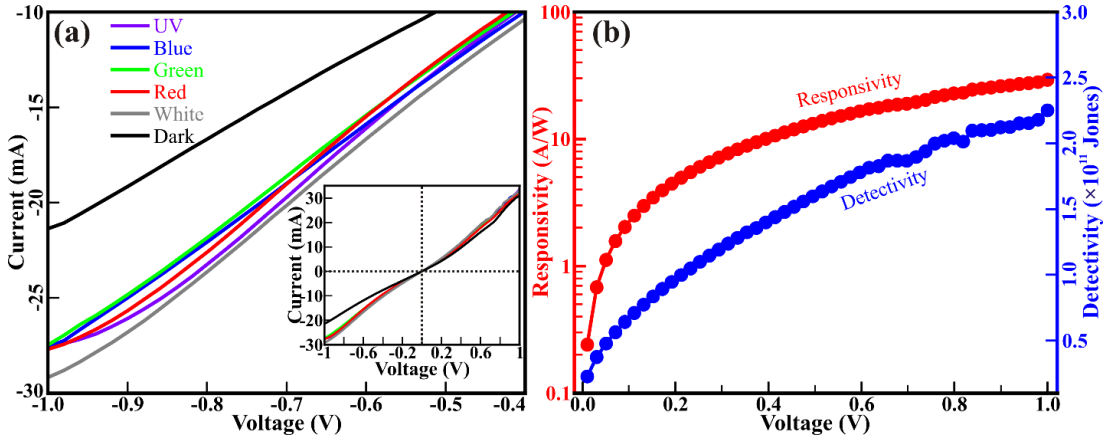

Figure 5.7 (a) I-V curves of NiO/MAPI heterojunction photodetector in the dark and under illumination. (b) Variation of responsivity and detectivity of NiO/MAPI heterojunction under white light illumination at the applied bias of 0 to + 1 V.

NiO/MAPI heterojunction formed over FTO coated glass substrate was subsequently tested for its application as UV and Visible light PDs. I-V curves in Fig. 5.7(a) highlight the apparent difference in dark current and light current under the illumination of different wavelengths. Additionally, the I-V curves at the applied voltage of -1 to 1 V are shown in the inset of Fig. 5.7(a). Further, Fig. 5.8 (Left panel) highlights the distinct variation in I_{dark} and I_{light} at 0 bias for different wavelengths. This illustrates that photogenerated carriers at NiO and perovskite films, upon illumination for UV and visible light, produced a higher current for a fixed voltage than the dark. The built-in potential at the NiO/MAPI

heterojunction facilitates to operate in self-powered mode (i.e., at 0 V). The low shunt resistance in NiO/MAPI resulting from pinholes in MAPI and NiO films might have produced insignificant rectification. Consequently, the conductance of NiO/MAPI heterojunction was measured at a minimum voltage of 10 mV. The variation in conductance after illumination at different wavelengths is shown in Fig. 5.8 (right panel). The least conductance of 0.020 Ω^{-1} observed in the dark has increased further after illumination. UV illumination delivered the highest conductance of 0.029 Ω^{-1}, followed by white (i.e., 0.027 Ω^{-1}), blue (i.e., 0.026 Ω^{-1}), red (i.e., 0.02586 Ω^{-1}), and green (i.e., 0.02546 Ω^{-1}) light illumination. The variation in conductance depending on the probing wavelength can be attributed to the absorption intensity of NiO/MAPI heterojunction at these wavelengths.

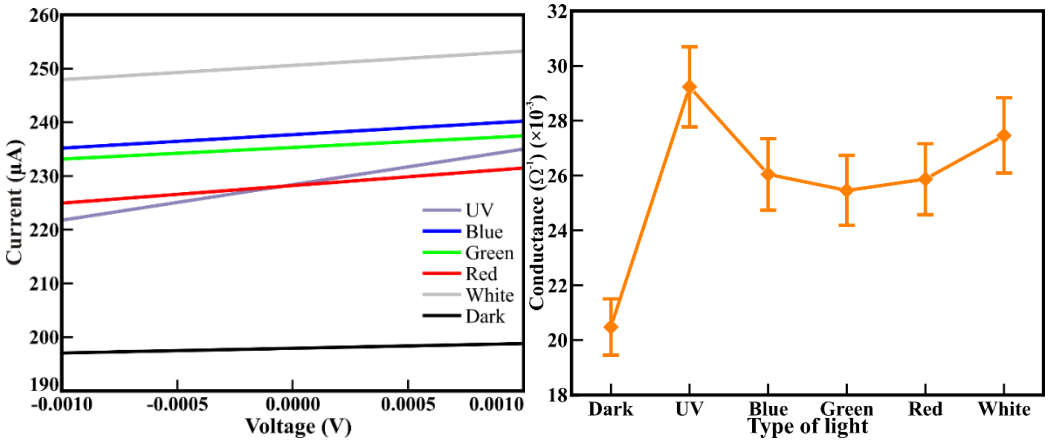

Figure 5.8 I-V curve under dark and illumination at 0 bias (Left panel). Probing wavelength-dependent variation in conductance evaluated from I-V curves of NiO/MAPI heterojunction (Right panel).

The key parameters, such as responsivity and detectivity, were evaluated further to investigate the performance of NiO/MAPI heterojunction PD. Fig. 5.7(b) shows a typical plot of applied bias (0 to +1 V) dependent variation in the responsivity and detectivity under white light illumination. The maximum photo responsivity of 5.79 mA/W and 29.2 A/W were observed for white light at zero bias and +1 V, respectively. The variation in the photo responsivity in the applied voltage range of +1 V to -1 V is shown in (Fig. 5.9).

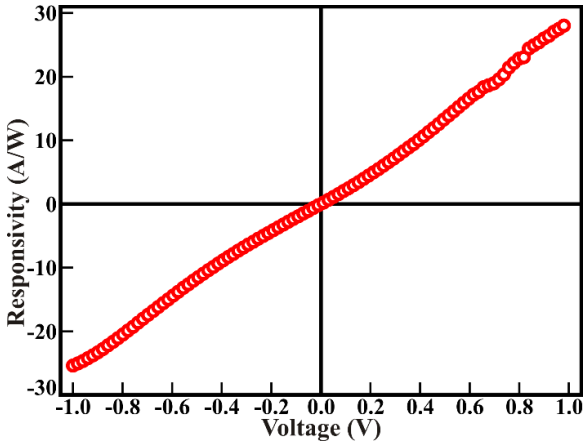

Figure 5.9 Variation of photo responsivity of NiO/MAPI heterojunction under white light illumination at an applied bias of +1 V to -1 V.

Furthermore, photo detectivity is one of the critical figures of merit for PD and is calculated to be 2.3×10^{10} Jones at zero bias and 2.2×10^{11} Jones at +1 V for visible light. The values of responsivity and detectivity for NiO/MAPI heterojunction PD are analogous to the conventional perovskite-based PDs consisting of multilayers of ETL-perovskite-HTL, which include NiO as a front HTL contact layer.[47-48] Further, the NiO/MAPI heterojunction was subjected to 30 s illumination cycles with different probing wavelengths under self-powering mode (i.e., zero bias). Fig. 5.10 shows the light-sensing cycles of the as-fabricated devices under illumination wavelength of different regions/colors. The square wave-like sensing cycles were obtained for all the measurements, which confirms reversible and reproducible temporal photoresponse at zero bias. Six continuous cycles involving 60 s dark and light illuminations were performed to examine the stable light current at zero bias. The highest light current (i.e., I_{light}) was obtained for UV illumination, followed by blue, green, and red-light illumination, which is akin to the absorption spectrum of NiO and MAPI thin films. Further, these transient measurements were used to evaluate the difference between I_{light} and I_{dark} (i.e., ΔI), (Fig. 2.5.**)** and rise (T_r) & fall (T_f) time at 90 % of I_{light} (Table 5.1**)** for each illuminating wavelength**.** The evaluated response time of 300 to 400 ms is akin to that of thin-film assembled perovskite-based PDs.[49-50] The low values of rise and fall time are not yet well understood. Still, they are believed to arise from the non-uniformity of NiO and MAPI

(pinholes), which leads to scattering of the incident illumination and a decrease in the shunt resistance of the heterojunction.

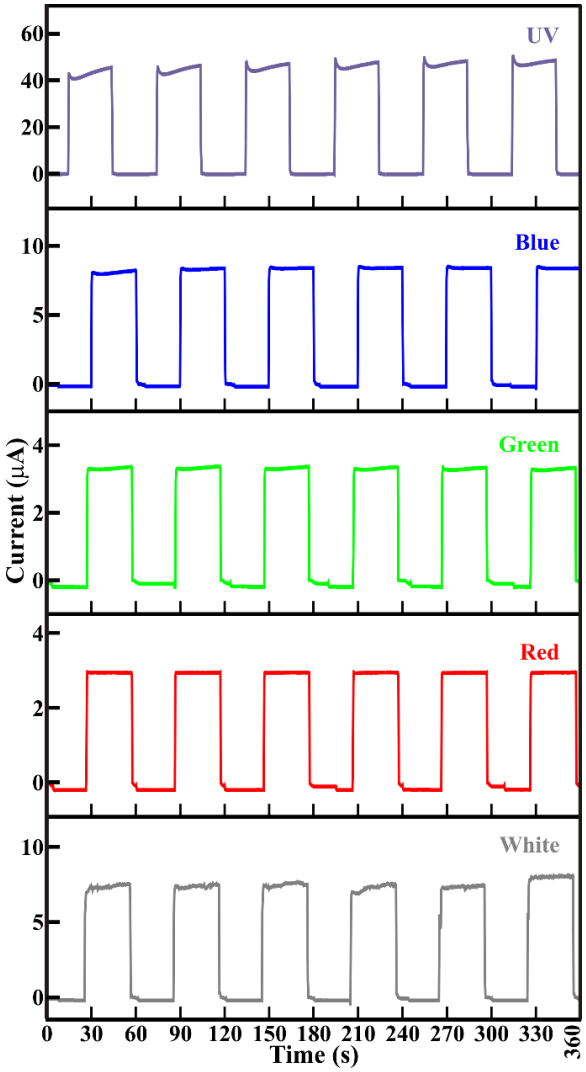

Figure 5.10 Probing wavelength-dependent photo-response cycles of NiO/MAPI heterojunction. (Day1)

Table 5.1 Summary of T_r and T_f calculated from the response cycles for self-powered NiO/MAPI heterojunction on the 1st day.

Probing wavelength (nm)	Tr (ms)	T_f (ms)
290±5 (UV)	452±10	363±10
450±5 (Blue)	345±10	290±10
540±5 (Green)	332±10	319±10

640±5 (Red)	369±10	320±10
White	320±10	305±10

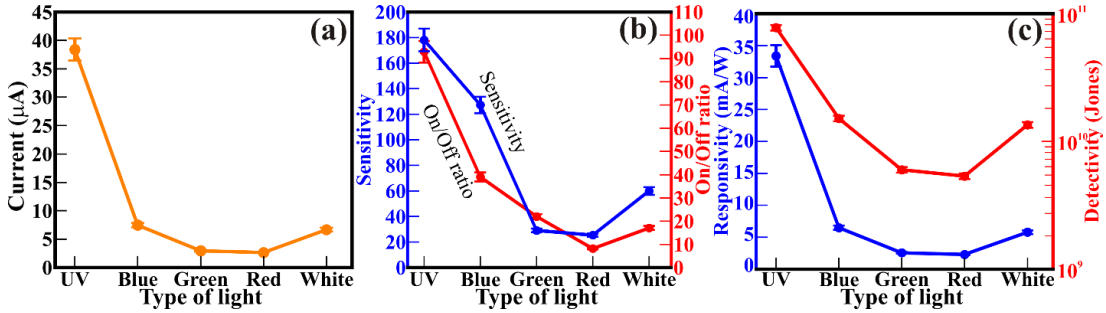

Figure 5.11 Probing wavelength-dependent variation in the (a) difference between Ilight and Idark (i.e., ΔI), (b) sensitivity and On/Off ratio, and (c) responsivity and detectivity of NiO/MAPI heterojunction PD.

The difference between I_{light} and I_{dark} (i.e., ΔI), sensitivity, On/Off ratio, responsivity, and detectivity of the NiO/MAPI heterojunction PDs are thoroughly investigated from the temporal response shown in Fig. 5.11. Fig. 5.11(a) shows the wavelength-dependent variation in the difference between I_{light} and I_{dark} (i.e., ΔI). The self-powered NiO/MAPI heterojunction PD showed the highest ΔI of 38.4 μA for UV light at zero bias. However, the increase in the probing wavelength has decreased ΔI. The probing wavelength of 450±5 nm (i.e., blue), 540±5 nm (green), and 640±5 nm (red) have resulted in reduced ΔI of 7.46, 2.96, and 2.64 μA, respectively. Nevertheless, white light, a mixture of all wavelengths of visible lights, showed ΔI of 6.66 μA. The probing wavelength-dependent variation in ΔI is in accordance with the measured conductance shown in Fig. 5.8 (Right panel). Fig. 5.11(b) reveals the variation in sensitivity and On/Off ratio of the self-powered NiO/MAPI heterojunction PDs. The highest sensitivity and On/Off ratio of 169 and 98, respectively, were observed for UV sensing. The probing wavelength relevant to blue, green, and red light has decreased the sensitivity to 71, 40, and 15, respectively. Similarly, the On/Off ratio has reduced from 98 to 14 after increasing the probing wavelength from UV to red. However, the sensitivity and On/Off ratio of 31 and 33 for white light-sensing of self-powered NiO/MAPI PDs are in line with ΔI for different lights.

Fig. 5.11 (c) shows the probing wavelength-dependent variation in responsivity and detectivity of self-powered NiO/MAPI heterojunction PD. NiO/MAPI heterojunction delivered a maximum responsivity of 33.39 mA/W at 0 bias for UV light, followed by 6.48, 2.57, 2.29, and 5.79 mA/W for blue, green, red, and white lights, respectively. Hu *et al.*[11] have reported similar responsivity for UV light illumination, which decreased with increasing wavelength. It is argued that incident light with a smaller wavelength has higher energy to generate more electron-hole pairs under the same applied bias. However, in our case, it is worth mentioning that the NiO front contact layer contribution in the photocurrent under UV light illumination at the NiO/MAPI interface cannot be denied, as in NiO heterojunctions with silicon[51] and ZnO[52-53]. Further, the detectivity in order 10^{11} Jones was achieved for UV light. Further increase in probing wavelength to the visible region led to decreased detectivity (order of 10^{10} Jones). The high values of responsivity (above 1 mA/W) and detectivity (order of 10^{10} Jones) reveal the good functionality of our device in the entire UV and visible spectrum.

The MAPI perovskite can lead to deterioration in the performance of the PD. The moisture-induced degradation of MAPI can result in the formation of PbI_2 and aqueous CH_3NH_3I, which fundamentally change the charge transport characteristics in MAPI films.[54] Therefore, to understand the temporal stability of ambient stored and self-powered NiO/MAPI heterojunction PD, the temporal cycles for each probing wavelength were measured at random intervals for 58 days. The sensing performance of NiO/MAPI self-powered heterojunction measured at zero bias for different probing wavelengths during the 4^{th}, 14^{th}, $28^{th,}$ $38^{th,}$ and 58^{th} day is shown in Fig. 5.12 and 5.13, respectively. The cyclic temporal performance degraded as the days progressed and disfigured on the 58^{th} day (Fig. 5.14).

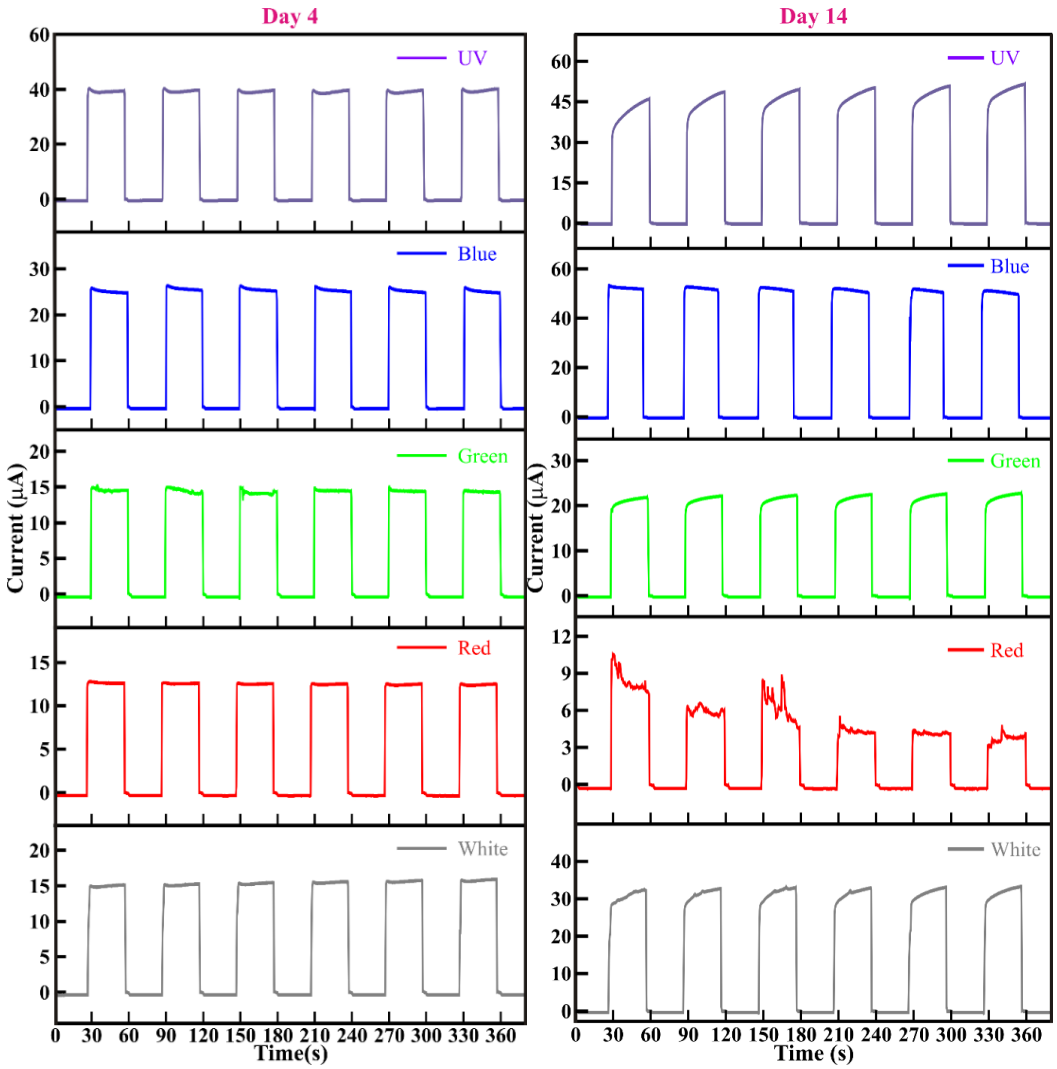

Figure 5.12 Probing wavelength-dependent photo-response cycles of NiO/MAPI heterojunction on the 4th (Left panel) and 14th (Right Panel) day.

Therefore, the photodetection parameters for each incident wavelength were calculated up to 38 days (Fig. 5.15). As the days progressed, ΔI of self-powered NiO/MAPI heterojunction PD increased up to 14 days and decreased after that till 58 days (Fig. 5.15(a)). However, the 14th-day rise in ΔI for the blue light might be due to the wavelength proximity of the blue and UV region. The optimal content of PbI_2 resulted from the degradation of perovskite might be behind the maximum values of ΔI on the 14th day. Similarly, high values of light current and responsivity were observed for a wide range of PbI_2 content. It was concluded that the higher conduction band edge and lower valence band edge

energy levels of PbI_2 than that of MAPI further suppress the electron injection from MAPI into the NiO (Fig. 5.2(c)). The MAPI degrades with time, and the evolution of PbI_2 in MAPI takes place, resulting in suppressed dark current and increased responsivity. These observations are akin to literature reporting the enhanced photocurrent in NiO_x: PbI_2-based perovskite PDs.[47] Further, the sensitivity (Fig. 5.15(b)) and On/Off ratio (Fig. 5.15(c)) variation observed for probing wavelength (i.e., UV and Vis) on day 1 was continued till day 38. it is observed that both sensitivity and On/Off ratio were increased for white light from day 1 to the 38th day. This increase might be attributed to the reduction in $I_{dark,}$ though the decrease in I_{light} can be witnessed after the 14th day.[47]

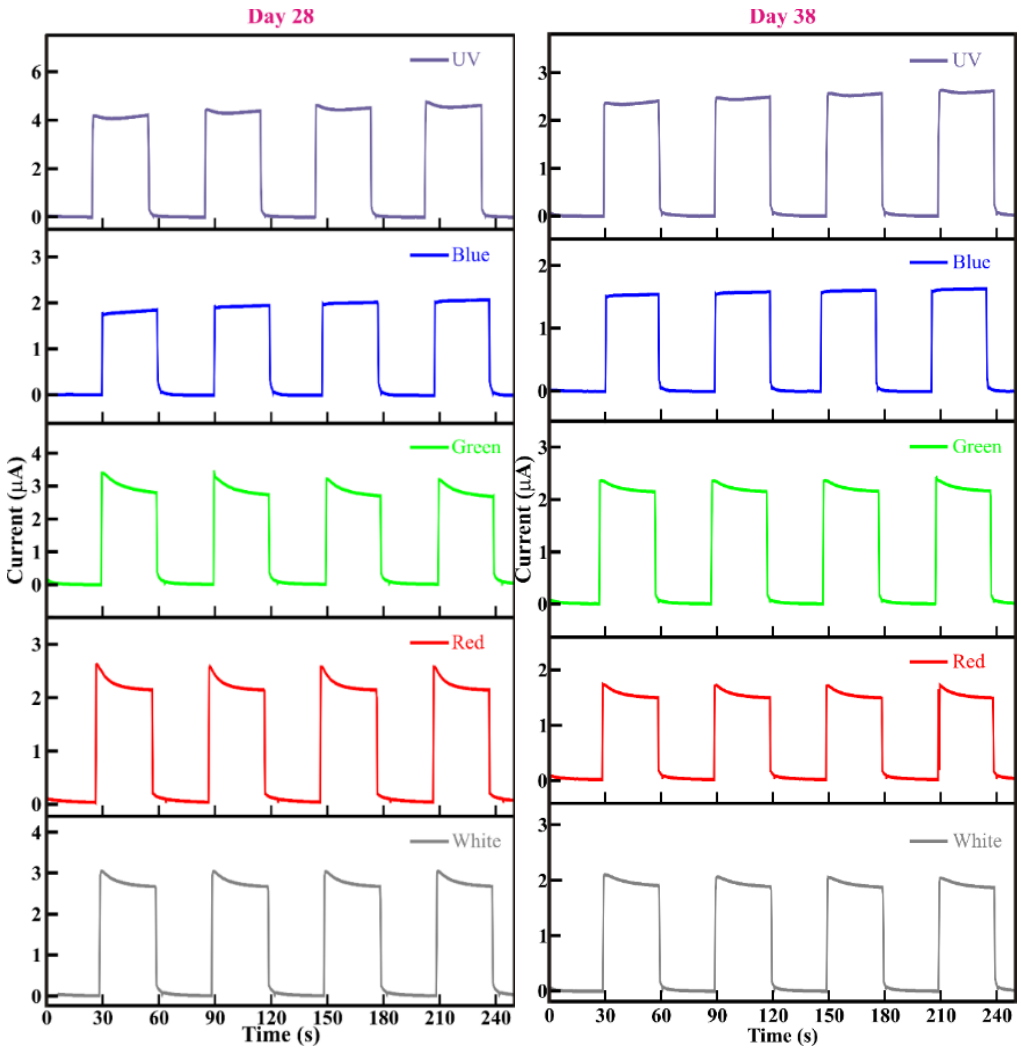

Figure 5.13 Probing wavelength-dependent photo-response cycles of NiO/MAPI heterojunction on the 28th (Left panel) and 38th (Right panel) day.

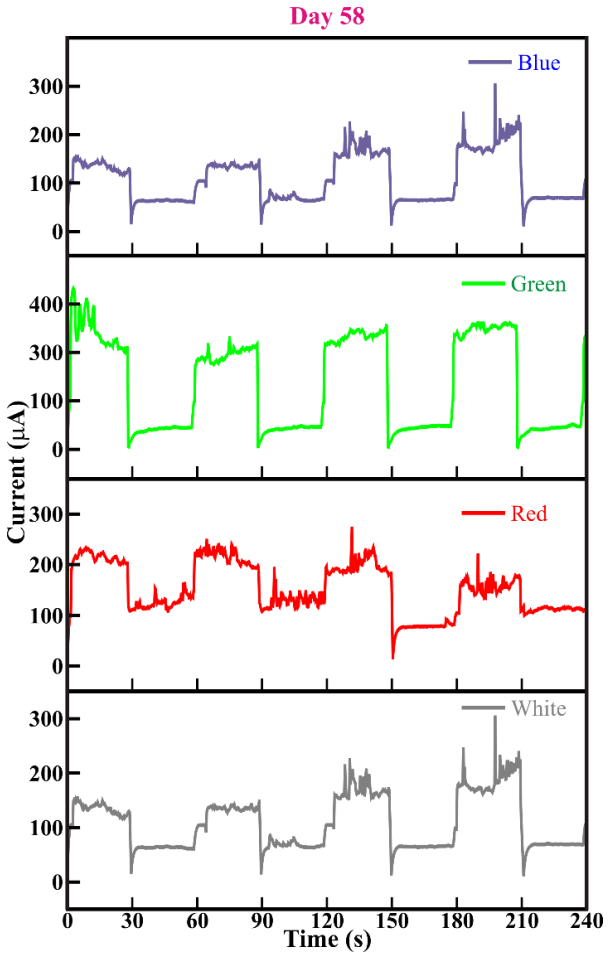

Figure 5.14 Probing wavelength-dependent photo-response cycles of NiO/MAPI heterojunction on the 58th day.

Table 5.2 Values of T_r and T_f in ms calculated for each probing wavelength as the days progressed. All the values are to be read with ±10 ms error.

	Day 1		**Day 4**		**Day 14**		**Day 28**		**Day 38**	
	Tr	**Tf**	**Tr**	**Tf**	**Tr**	**Tf**	**Tr**	**Tf**	**Tr**	**Tf**
UV	452	363	290	288	292	286	284	488	380	253
Blue	345	290	302	293	289	295	289	218	386	253
Green	332	319	301	286	305	289	287	237	475	258
Red	369	320	299	289	302	287	282	252	286	245
White	320	305	320	379	475	382	286	332	383	336

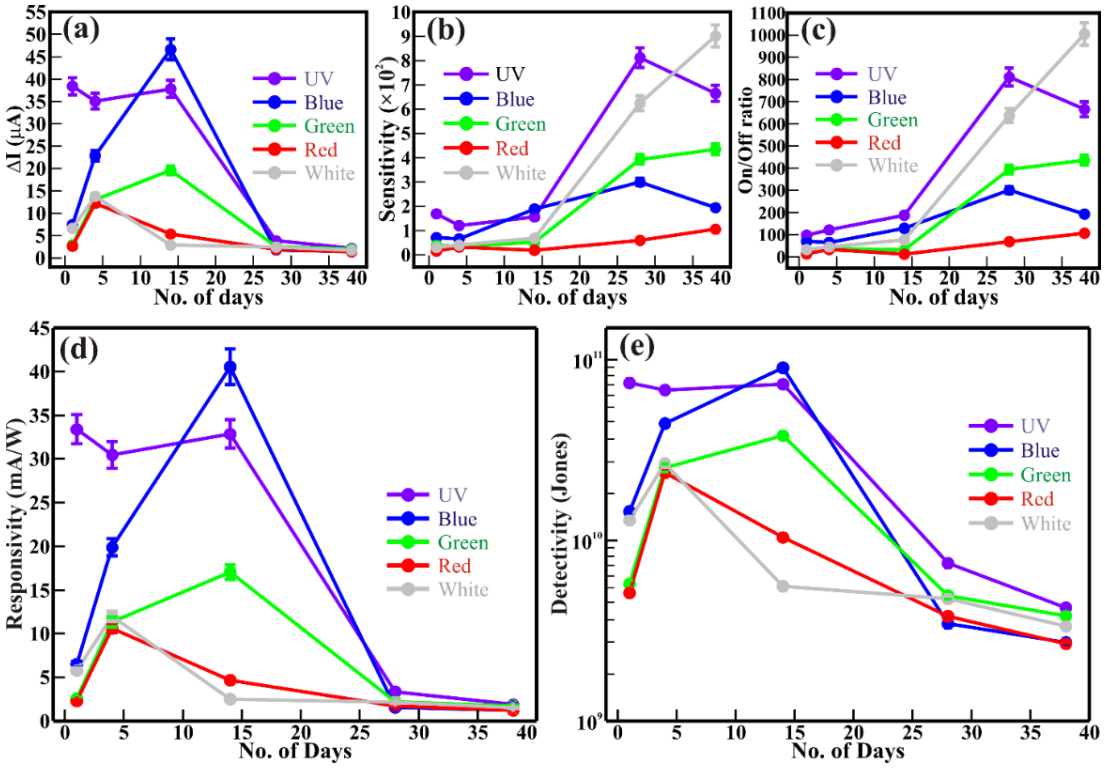

Figure 5.15 Time-dependent variation in the (a) difference between I_{light} and I_{dark} (i.e., ΔI), (b) sensitivity, (c) On/Off ratio, (d) responsivity, and (e) detectivity for NiO/MAPI heterojunction PD.

Furthermore, transient characteristics such as rise (T_r) and fall (T_f) were investigated for different probing wavelengths between day 1 to the 38th day and are listed in supporting Table 5.2. The response time depends on the RC time constant and carrier transit time at the depletion width, and hence the response time has not changed significantly even though the degradation occurred in perovskite during the 38 days.[8,55] The slow response of the device might be because developed photodetectors are hole-only devices, and depletion width present at both sides of the perovskite. Moreover, the pinholes in MAPI and NiO films offer low shunt resistance, which can be improved further by forming a uniform and compact NiO underlayer and processing perovskite in a controlled environment. The improvement in the shunt resistance will drastically reduce the response time. Time-dependent variation of responsivity and detectivity of self-powered NiO/MAPI heterojunction PDs is shown in Fig. 5.15(d) and Fig. 5.15(e)**,** respectively. The maximum responsivity of 40.56 mA/W was observed

on the 14th day for blue light, followed by UV, green, red, and white wavelengths. This is in line with the variation of ΔI reaching peak value at the 14th day and suggest optimized PbI_2 content was developed on the 14th day. Additionally, Fig. 5.15(e) shows excellent detectivity in the order of 10^{10} Jones for NiO/MAPI heterojunction up to 38 days.

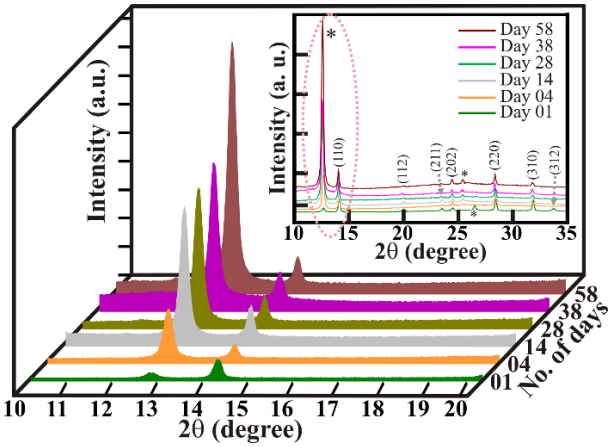

Figure 5.16 Illumination days dependent XRD pattern of MAPI films. (inset shows XRD up to 35°).

The moisture-induced degradation of MAPI films strongly influences the photoresponse of the self-powered NiO/MAPI heterojunction PDs. Consequently, it is important to understand the structural changes resulting from perovskite degradation with passing days in an ambient atmosphere. XRD patterns of MAPI films in NiO/MAPI heterojunction shown in Fig. 5.16 were measured before each sensing cycle on respective days. The XRD pattern of MAPI films in the inset of Fig. 5.16 reveals that the tetragonal phase is consistent with the JCPDS card no. 41-1445 and reported literature.[44,56-58] The signature peak observed at 12.65° (identified as *) represents the existence of PbI_2.[59] The intensity of the peak at 12.65° was insignificant for as prepared NiO/MAPI heterojunction thin film on day 1, indicating the negligible existence of PbI_2. However, a gradual increase in intensity reflects the formation of PbI_2 as the days progressed. The distinguishable existence of PbI_2 was observed on day 4. The highest intensity of the PbI_2 peak was observed on the 58th day. The peak intensity ratio of PbI_2 (i.e., I_{Dx}/I_{D1}, where x = 4, 14, 28, 38, and 58) has

increased from 11.46 to 35.58 from day 4 to day 58. The formation of the larger amount of PbI_2 on day 58 might have disfigured the sensing cycle and drastically degraded the PD performance. The presence of an optimal amount of PbI_2 in MAPI films might have resulted in an increase in ΔI up to 14 days. The content of PbI_2 in MAPI films on the 14th day was calculated with Eq. 5.7 and found to be 61±2 %. However, after 14 days, the degradation progressed further, and > 62 % PbI_2 content was observed in MAPI. The larger PbI_2 content has suppressed optoelectronic properties of the MAPI perovskite light absorber (i.e., reduced I_{dark} and I_{light}) and gives rise to lower ΔI. These observations are akin to literature reporting the enhanced photocurrent in NiOx: PbI_2-based perovskite PDs.[47] In total, it is observed that high-performance PDs can be fabricated by tailoring the concentration/formation of PbI_2 in MAPI films.

Table 5.3 Comparison of some important metal oxide-based self-powered MAPI perovskite-based PDs reported in the literature.

S/N	Device configuration	Detectable λ (nm)	Synthesis	Detectivity (Jones)	Ref.
1.	FTO/NiO/MAPI/Au	290 - 800	Ambient	10^{10}	This study
2.	ITO/$(FAPbI_3)_{0.97}(MAPbBr_3)_{0.03}$/spiro-OMeTAD/Au	254	Glove box	10^{11}	[60]
3.	FTO/ZnO/MAPI/MoO_3/Au	300-800	Glove box	10^{11}	[22]
4.	FTO/TiO_2/Al_2O_3/PCBM/MAPI/spiro-OMeTAD/Au/Ag	400-800	Glove box	10^{12}	[13]
5.	FTO/TiO_2/MAPI/Spiro-OMeTAD/Au	300-800	-	10^{10}	[23]
6.	FTO/ZnO-NR array/MAPI/MoO_3/Au	250-800	Ambient	10^{14}	[24]
7.	ITO/PTAA/MAPI/C_{60}/BCP/Cu	350-800	-	10^{12}	[25]

Further, the developed PD uses a p-n junction, unlike n-i-p or p-i-n junctions reported in the literature (Table 5.3). Recently, Nguyen et al. [60] demonstrated self-powered perovskite-based PD delivering performance similar to the present study, but the use of complex perovskite composition and an expensive spiro-OMeTAD is not cost-effective. On the other hand, the present

studies provide a candid guide to understand the effect of intrinsic modifications on the optoelectronic properties of organic-inorganic perovskites for application in self-powered PDs.

5.4 Conclusion

In conclusion, we have successfully fabricated a self-powered NiO/MAPI heterojunction PD in ambient conditions. NiO thin films were synthesized by thermal evaporation followed by oxidation, and the MAPI overlayer was coated with a two-step deposition process in the ambient. The multifunctional NiO film provided PD with both built-in potentials and also acted as a template to enhance the light absorption of the MAPI films. Thus, self-powered NiO/MAPI heterojunction PD showed high detectivity in the order of 10^{10} Jones. Further, the performance parameters of self-powered PD for each probing wavelength from UV to Visible were studied for up to 58 days stored in ambient. The x-ray diffraction (XRD) was recorded for up to 58 days to analyze the degradation of MAPI. The changes in performance parameters of self-powered PD were related to the degradation of MAPI films. These results not only explain the degradation of MAPI w.r.t. performance of PDs but also help in understanding the influence of intrinsic modifications of hybrid perovskite on the photoresponse of such perovskite heterojunctions used in other optoelectronic devices. This study will instigate the researchers to modulate the optoelectronic properties of metal halide perovskite through intrinsic modifications.

5.5 References

[1] Leung, S.-F.; Ho, K.-T.; Kung, P.-K.; Hsiao, V. K. S.; Alshareef, H. N.; Wang, Z. L.; He J. H., (2018), A self-powered and flexible organometallic halide perovskite photodetector with very high detectivity. Adv. Mater., 30, 1704611, (DOI: 10.1002/adma.201704611).

[2] Jena A. K., Kulkarni A., Miyasaka T., (2019), Halide Perovskite Photovoltaics: Background, Status, and Future Prospects, Chem. Rev., 119, 3036-3103, (DOI: 10.1021/acs.chemrev.8b00539).

[3] Gonzalez-Pedro V., Juarez-Perez E. J., Arsyad W.-S., Barea E. M., Fabregat-Santiago F., Mora-Sero I., Bisquert J., (2014), General working principles of

$CH_3NH_3PbX_3$ perovskite solar cells, Nano Lett., 14, 888-893, (DOI: 10.1021/nl404252e).

[4] Alsalloum A. Y., Turedi B., Almasabi K., Zheng X., Naphade R., Stranks S. D., Mohammed O. F., Bakr O. M., (2021), 22.8%-Efficient single-crystal mixed-cation inverted perovskite solar cells with a near-optimal bandgap, Energy Environ. Sci., (DOI: 10.1039/D0EE03839C).

[5] Maniarasu S., Korukonda T. B., Manjunath V., Ramasamy E., Ramesh M., Veerappan G., (2018), Recent advancement in metal cathode and hole-conductor-free perovskite solar cells for low-cost and high stability: A route towards commercialization, Renew. Sust. Energy Rev., 82, 845-857, (DOI: 10.1016/j.rser.2017.09.095).

[6] Manjunath V., Bimli S., Parmar K. H., Shirage P. M., Devan R. S., (2019), Oxidized nickel films as highly transparent HTLs for inverted planar perovskite solar cells, Sol. Energy, 193, 387-394, (DOI: 10.1016/j.solener.2019.09.070).

[7] Gu Z., Wang K., Sun W., Li J., Liu S., Song Q., Xiao S., (2016), Two-photon pumped $CH_3NH_3PbBr_3$ perovskite microwire lasers, Adv. Opt. Mater., 4, 472-479, (DOI: 10.1002/adom.201500597).

[8] Wang, H.-P.' Li, S.; Liy, X.; Shi, Z.F; Fang, X. S.; He, J. H., (2021), Low-dimensional metal halide perovskite photodetectors, Adv. Mater., 33, 2003309, (DOI: 10.1002/adma.202003309)

[9] Tan Z.-K., Moghaddam R. S., Lai M. L., Docampo P., Higler R., Deschler F., Price M., Sadhanala A., Pazos L. M., Credgington D., Hanusch F., Bein T., Snaith H. J., Friend R. H., (2014), Bright light-emitting diodes based on organometal halide perovskite, Nat. Nanotechnol., 9, 687-692, (DOI: 10.1038/nnano.2014.149).

[10] Cho H., Jeong S.-H., Park M.-H., Kim Y.-H., Wolf C., Lee C.-L., Heo J. H., Sadhanala A., Myoung N., Yoo S., Im S. H., Friend R. H., Lee T.-W., (2015), Overcoming the electroluminescence efficiency limitations of perovskite light-emitting diodes, Science, 350, 1222, (DOI: 10.1126/science.aad1818).

[11] Hu X., Zhang X., Liang L., Bao J., Li S., Yang W., Xie Y., (2014), High-performance flexible broadband photodetector based on organolead halide perovskite, Adv. Funct. Mater., 24, 7373-7380, (DOI: 10.1002/adfm.201402020).

[12] Dou L., Yang Y., You J., Hong Z., Chang W.-H., Li G., Yang Y., (2014), Solution-processed hybrid perovskite photodetectors with high detectivity, Nat. Commun., 5, 5404, (DOI: 10.1038/ncomms6404).

[13] Sutherland B. R., Johnston A. K., Ip A. H., Xu J., Adinolfi V., Kanjanaboos P., Sargent E. H., (2015), Sensitive, fast, and stable perovskite photodetectors exploiting interface engineering, ACS Photonics, 2, 1117-1123, (DOI: 10.1021/acsphotonics.5b00164).

[14] Dong Y., Gu Y., Zou Y., Song J., Xu L., Li J., Xue J., Li X., Zeng H., (2016), Improving all-inorganic perovskite photodetectors by preferred orientation and plasmonic effect, Small, 12, 5622-5632, (DOI: 10.1002/smll.201602366).

[15] Zhang T., Wu J., Zhang P., Ahmad W., Wang Y., Alqahtani M., Chen H., Gao C., Chen Z. D., Wang Z., Li S., (2018), High speed and stable solution-processed triple cation perovskite photodetectors, Adv. Opt. Mater., 6, 1701341, (DOI: 10.1002/adom.201701341).

[16] Liu B., Gutha R. R., Kattel B., Alamri M., Gong M., Sadeghi S. M., Chan W.-L., Wu J. Z., (2019), Using silver nanoparticles-embedded silica metafilms as substrates to enhance the performance of perovskite photodetectors, ACS Appl. Mater. Interfaces, 11, 32301-32309, (DOI: 10.1021/acsami.9b10706).

[17] Li F., Ma C., Wang H., Hu W., Yu W., Sheikh A. D., Wu T., (2015), Ambipolar solution-processed hybrid perovskite phototransistors, Nat. Commun., 6, 8238, (DOI: 10.1038/ncomms9238).

[18] Saidaminov M. I., Adinolfi V., Comin R., Abdelhady A. L., Peng W., Dursun I., Yuan M., Hoogland S., Sargent E. H., Bakr O. M., (2015), Planar-integrated single-crystalline perovskite photodetectors, Nat. Commun., 6, 8724, (DOI: 10.1038/ncomms9724).

[19] Alwadai N., Haque M. A., Mitra S., Flemban T., Pak Y., Wu T., Roqan I., (2017), High-performance ultraviolet-to-infrared broadband perovskite photodetectors achieved via inter-/intraband transitions, ACS Appl. Mater. Interfaces, 9, 37832-37838, (DOI: 10.1021/acsami.7b09705).

[20] Zheng Z., Zhuge F., Wang Y., Zhang J., Gan L., Zhou X., Li H., Zhai T., (2017), Decorating perovskite quantum dots in TiO_2 nanotubes array for broadband response photodetector, Adv. Funct. Mater., 27, 1703115, (DOI: 10.1002/adfm.201703115).

[21] Gao T., Zhang Q., Chen J., Xiong X., Zhai T., (2017), Performance-enhancing broadband and flexible photodetectors based on perovskite/ZnO-nanowire hybrid structures, Adv. Opt. Mater., 5, 1700206, (DOI: 10.1002/adom.201700206).

[22] Zhu, Y.; Song, Z.; Zhou, H.; Wu, D.; Lu, R.; Wang, R.; Wang, H., (2018), Self-powered, broadband perovskite photodetector based on ZnO microspheres as scaffold layer. Appl. Surf. Sci., 448, 23-29, (DOI: 10.1016/j.apsusc.2018.04.047).

[23] Zhou, H.; Song, Z.; Tao, P.; Lei, H.; Gui, P.; Mei, J.; Wang, H.; Fang, G., (2016), Self-powered, ultraviolet-visible perovskite photodetector based on TiO_2 nanorods. RSC Adv., 6, 6205-6208, (DOI: 10.1039/C5RA27840F).

[24] Yu, J.; Chen, X.; Wang, Y.; Zhou, H.; Xue, M.; Xu, Y.; Li, Z.; Ye, C.; Zhang, J.; van Aken, P. A.; Lund, P. D.; Wang, H., (2016), A high-performance self-powered broadband photodetector based on a $CH_3NH_3PbI_3$ perovskite/ZnO nanorod array heterostructure. J. Mater. Chem. C, 4, 7302-7308, (DOI: 10.1039/C6TC02097F).

[25] Shen, L.; Fang, Y.; Wang, D.; Bai, Y.; Deng, Y.; Wang, M.; Lu, Y.; Huang, J., (2016), A self-powered, sub-nanosecond-response solution-processed hybrid perovskite photodetector for time-resolved photoluminescence-lifetime detection. Adv. Mater., 28, 10794-10800, (DOI: 10.1002/adma.201603573).

[26] Li J., Yuan S., Tang G., Li G., Liu D., Li J., Hu X., Liu Y., Li J., Yang Z., Liu S. F., Liu Z., Gao F., Yan F., (2017), High-performance, self-powered photodetectors based on perovskite and graphene, ACS Appl. Mater. Interfaces, 9, 42779-42787, (DOI: 10.1021/acsami.7b14110).

[27] Liu Y., Jia R., Wang Y., Hu Z., Zhang Y., Pang T., Zhu Y., Luan S., (2017), Inhibition of zero drift in perovskite-based photodetector devices via [6,6]-Phenyl-C61-butyric acid methyl ester doping, ACS Appl. Mater. Interfaces, 9, 15638-15643, (DOI: 10.1021/acsami.7b02413).

[28] Qin L., Wu L., Kattel B., Li C., Zhang Y., Hou Y., Wu J., Chan W.-L., (2017), Using bulk heterojunctions and selective electron trapping to enhance the responsivity of

perovskite–graphene photodetectors, Adv. Funct. Mater., 27, 1704173, (DOI: 10.1002/adfm.201704173).

[29] Patil R. A., Devan R. S., Lin J.-H., Ma Y.-R., Patil P. S., Liou Y., (2013), Efficient electrochromic properties of high-density and large-area arrays of one-dimensional NiO nanorods, Sol. Energy Mater. Sol. Cells, 112, 91-96, (DOI: 10.1016/j.solmat.2013.01.003).

[30] Devan R. S., Patil R. A., Lin J.-H., Ma Y.-R., (2012), One-dimensional metal-oxide nanostructures: Recent developments in synthesis, characterization, and applications, Adv. Funct. Mater., 22, 3326-3370, (DOI: 10.1002/adfm.201201008).

[31] Dalavi D. S., Devan R. S., Patil R. S., Ma Y.-R., Patil P. S., (2013), Electrochromic performance of sol-gel deposited NiO thin film, Mater. Lett., 90, 60-63, (DOI: 10.1016/j.matlet.2012.08.108).

[32] Dalavi D. S., Devan R. S., Patil R. S., Ma Y.-R., Kang M.-G., Kim J.-H., Patil P. S., (2013), Electrochromic properties of dandelion flower like nickel oxide thin films, J. Mater. Chem. A, 1, 1035-1039, (DOI: 10.1039/C2TA00842D).

[33] Lu H., Tian W., Cao F., Ma Y., Gu B., Li L., (2016), A self-powered and stable all-perovskite photodetector–solar cell nanosystem, Adv. Funct. Mater., 26, 1296-1302, (DOI: 10.1002/adfm.201504477).

[34] Zhou H., Zeng J., Song Z., Grice C. R., Chen C., Song Z., Zhao D., Wang H., Yan Y., (2018), Self-powered all-inorganic perovskite microcrystal photodetectors with high detectivity, J. Phys. Chem. Lett., 9, 2043-2048, (DOI: 10.1021/acs.jpclett.8b00700).

[35] Li F., Liu M., (2017), Recent efficient strategies for improving the moisture stability of perovskite solar cells, J. Mater. Chem. A, 5, 15447-15459, (DOI: 10.1039/C7TA01325F).

[36] Divitini G., Cacovich S., Matteocci F., Cinà L., Di Carlo A., Ducati C., (2016), In situ observation of heat-induced degradation of perovskite solar cells, Nat. Energy, 1, 15012, (DOI: 10.1038/nenergy.2015.12).

[37] Zhang Z., Suchan K., Li J., Hetherington C., Kiligaridis A., Unger E., Scheblykin I. G., Wallentin J., (2021), Vertically aligned $CsPbBr_3$ nanowire arrays with template-

induced crystal phase transition and stability, J. Phys. Chem. C, 125, 4860-4868, (DOI: 10.1021/acs.jpcc.0c11217).

[38] Gu L., Tavakoli M. M., Zhang D., Zhang Q., Waleed A., Xiao Y., Tsui K.-H., Lin Y., Liao L., Wang J., Fan Z., (2016), 3D Arrays of 1024-pixel image sensors based on lead halide perovskite nanowires, Adv. Mater., 28, 9713-9721, (DOI: 10.1002/adma.201601603).

[39] Bao C., Yang J., Bai S., Xu W., Yan Z., Xu Q., Liu J., Zhang W., Gao F., (2018), High performance and stable all-inorganic metal halide perovskite-based photodetectors for optical communication applications, Adv. Mater., 30, 1803422, (DOI: 10.1002/adma.201803422).

[40] Li C., Han C., Zhang Y., Zang Z., Wang M., Tang X., Du J., (2017), Enhanced photoresponse of self-powered perovskite photodetector based on ZnO nanoparticles decorated $CsPbBr_3$ films, Sol. Energy Mater. Sol. Cells, 172, 341-346, (DOI: 10.1016/j.solmat.2017.08.014).

[41] Qi Z., Fu X., Yang T., Li D., Fan P., Li H., Jiang F., Li L., Luo Z., Zhuang X., Pan A., (2019), Highly stable lead-free $Cs_3Bi_2I_9$ perovskite nanoplates for photodetection applications, Nano Res., 12, 1894-1899, (DOI: 10.1007/s12274-019-2454-0).

[42] Hussain A. A., Rana A. K., Ranjan M., (2019), Air-stable lead-free hybrid perovskite employing self-powered photodetection with an electron/hole-conductor-free device geometry, Nanoscale, 11, 1217-1227, (DOI: 10.1039/C8NR08959K).

[43] Park J. H., Seo J., Park S., Shin S. S., Kim Y. C., Jeon N. J., Shin H.-W., Ahn T. K., Noh J. H., Yoon S. C., Hwang C. S., Seok S. I., (2015), Efficient $CH_3NH_3PbI_3$ perovskite solar cells employing nanostructured p-type NiO electrode formed by a pulsed laser deposition, Adv. Mater., 27, 4013-4019, (DOI: 10.1002/adma.201500523).

[44] Song J., Zheng E., Bian J., Wang X.-F., Tian W., Sanehira Y., Miyasaka T., (2015), Low-temperature SnO_2-based electron selective contact for efficient and stable perovskite solar cells, J. Mater. Chem. A, 3, 10837-10844, (DOI: 10.1039/C5TA01207D).

[45] Shi Y., Xing Y., Li Y., Dong Q., Wang K., Du Y., Bai X., Wang S., Chen Z., Ma T., (2015), $CH_3NH_3PbI_3$ and $CH_3NH_3PbI_{3-x}Cl_x$ in planar or mesoporous perovskite solar

cells: Comprehensive insight into the dependence of performance on architecture, J. Phys. Chem. C, 119, 15868-15873, (DOI: 10.1021/acs.jpcc.5b02784).

[46] Wang K., Tian Y., Jiang H., Chen M., Xu S., (2019), Surface treatment on nickel oxide to enhance the efficiency of inverted perovskite solar cells, Int. J. Photoenergy, 2019, 4360816, (DOI: 10.1155/2019/4360816).

[47] Zhu H. L., Cheng J., Zhang D., Liang C., Reckmeier C. J., Huang H., Rogach A. L., Choy W. C. H., (2016), Room-temperature solution-processed NiO_x:PbI_2 nanocomposite structures for realizing high-performance perovskite photodetectors, ACS Nano, 10, 6808-6815, (DOI: 10.1021/acsnano.6b02425).

[48] Afzal A. M., Bae I.-G., Aggarwal Y., Park J., Jeong H.-R., Choi E. H., Park B., (2021), Highly efficient self-powered perovskite photodiode with an electron-blocking hole-transport NiO_x layer, Sci. Rep., 11, 169, (DOI: 10.1038/s41598-020-80640-3).

[49] Xia H.-R., Li J., Sun W.-T., Peng L.-M., (2014), Organohalide lead perovskite based photodetectors with much enhanced performance, ChemComm., 50, 13695-13697, (DOI: 10.1039/C4CC05960C).

[50] Deng H., Dong D., Qiao K., Bu L., Li B., Yang D., Wang H.-E., Cheng Y., Zhao Z., Tang J., Song H., (2015), Growth, patterning and alignment of organolead iodide perovskite nanowires for optoelectronic devices, Nanoscale, 7, 4163-4170, (DOI: 10.1039/C4NR06982J).

[51] Al-Hardan N. H., Ahmed N. M., Almessiere M. A., Aziz A. A., (2020), Low-intensity UV light sensor based on p-NiO/n-Si heterojunction, Mater. Res. Express, 6, 126332, (DOI: 10.1088/2053-1591/ab5dfc).

[52] Zhang Y., Ji T., Zou R., Ha E., Hu X., Cui Z., Xu C., He S. a., Xu K., Zhang Y., Hu J., (2020), An efficiently enhanced UV-visible light photodetector with a Zn:NiO/p-Si isotype heterojunction, J. Mater. Chem. C, 8, 3498-3508, (DOI: 10.1039/C9TC06199A).

[53] Echresh A., Chey C. O., Zargar Shoushtari M., Khranovskyy V., Nur O., Willander M., (2015), UV photo-detector based on p-NiO thin film/n-ZnO nanorods heterojunction prepared by a simple process, J. Alloys Compd., 632, 165-171, (DOI: 10.1016/j.jallcom.2015.01.155).

[54] Toloueinia P., Khassaf H., Shirazi Amin A., Tobin Z. M., Alpay S. P., Suib S. L., (2020), Moisture-induced structural degradation in methylammonium lead iodide perovskite thin films, ACS Appl. Energy Mater., 3, 8240-8248, (DOI: 10.1021/acsaem.0c00638).

[55] Li C., Wang H., Wang F., Li T., Xu M., Wang H., Wang Z., Zhan X., Hu W., Shen L., (2020), Ultrafast and broadband photodetectors based on a perovskite/organic bulk heterojunction for large-dynamic-range imaging, Light: Sci. Appl., 9, 31, (DOI: 10.1038/s41377-020-0264-5).

[56] Jassim S. M., Bakr N. A., Mustafa F. I., (2020), Synthesis and characterization of $MAPbI_3$ thin film and its application in C-Si/perovskite tandem solar cell, J. Mater. Sci.: Mater. Electron., 31, 16199-16207, (DOI: 10.1007/s10854-020-04084-1).

[57] Tavakoli M. M., Gu L., Gao Y., Reckmeier C., He J., Rogach A. L., Yao Y., Fan Z., (2015), Fabrication of efficient planar perovskite solar cells using a one-step chemical vapor deposition method, Sci. Rep., 5, 14083, (DOI: 10.1038/srep14083).

[58] Peng H., Lan C., Chen S., Fan P., Liang G., Lan H., (2019), N,N-dimethylformamide vapor effect on microstructural and optical properties of CH3NH3PbI3 film during solvent annealing, Surf. Coat. Technol., 359, 162-168, (DOI: 10.1016/j.surfcoat.2018.12.069).

[59] Zhang H., Tao M., Gao B., Chen W., Li Q., Xu Q., Dong S., (2017), Preparation of $CH_3NH_3PbI_3$ thin films with tens of micrometer scale at high temperature, Sci. Rep., 7, 8458, (DOI: 10.1038/s41598-017-09109-0).

[60] Nguyen T. M. H., Kim S., Bark C. W., (2021), Solution-processed and self-powered photodetector in vertical architecture using mixed-halide perovskite for highly sensitive UVC detection, J. Mater. Chem. A, 9, 1269-1276, (DOI: 10.1039/D0TA08738F).

Chapter 6

NiO thin films-based perovskite solar cell

6.1 Introduction

Recently, organic-inorganic hybrid PSCs have shown remarkable light-harvesting owing to their desired PV properties. With long charge diffusion lengths, high absorption coefficient, ease of processing, etc., researchers have achieved efficiencies close to 23 %.[1] Miyasaka reported an initial description of the light-harvesting capabilities of organic-inorganic perovskite.[2] Then, these solar cells evolved through various modifications such as the use of solid electrolytes, tuning the bandgap of the light harvester, use of multiple organic transport layers, and utilization of different inorganic nanostructures as transport layers, and development of new device configurations, etc.[3-9] In the case of device architectures, PSCs are broadly classified as mesoporous, planar, and carbon-based architectures. Further, PSCs are categorized depending on the sequence of deposition and type of transport layer as n-i-p and p-i-n configuration.[10] Owing to the fact that PSCs are the evolution of DSSCs, the majority of all device architectures and configurations use semiconducting transport layers.[11-17] Semiconducting transport layers are selected based on conduction band edge levels, mobilities of charge carriers, and absorption range, because conduction band edge mismatch could lead to recombination of photo-generated charge carriers, the difference in mobilities of the transport layer and light harvester will cause charge accumulation at their interface, and the absorption range decides the optical transparency to irradiate the light harvester respectively.[18] Therefore, many inorganic HTLs are developed and checked for their suitability in PSCs. Additionally, a variety of thin film techniques are used to coat the HTL. Despite such progress in inorganic transport layers, high-efficiency PSCs are realized by using expensive organic HTLs such as PTAA or spiro-MeOTAD, which hinder their use in PSCs owing to the use of hygroscopic dopants that trigger degradation of the perovskite layer, and the requirement of an inert atmosphere for processing.[19] Thus, to get through this problem, among all the inorganic transport layers, NiO is of prime importance and found to be a more promising candidate for optoelectronic and energy storage/conversion studies because of its chemical stability [20-23]. The use of NiO nanoparticle suspensions for the formation of NiO film produces residual ligands at low temperatures and hampers the performance of PSCs by controlling the coverage of overlaying perovskite absorber.[24] Even though the physical deposition methods, such as ALD, sputtering, laser deposition,

etc., ensures uniformity and reproducibility, involves high processing cost. However, low-cost thermal evaporation of Ni followed by oxidation has gained recent interest to make optimized NiO thin films. Lai et al.[25] used e-beam evaporation to form bi-layer films of Ni and Au (5~10 nm) over a glass substrate, which was further oxidized in an oxygen (O_2) atmosphere to increase the conductivity of NiO film through the inter-diffusion. Further, the incorporation of Cu in the bi-layer of Ni-Au resulted in an efficiency of 11.1 % after thermal oxidation.[26] However, the formation of thermally oxidized bi-layer and tri-layer may result in a chemically non-homogenous layer, reduced transmittance in the visible region, and also, usage of the O_2 environment increases the cost. Recently, Abzieher et al.[27] used e-beam for direct evaporation of NiO thin film over transparent conducting oxide films, which involved the incorporation of excess O_2 in the deposition process to obtain highly transparent NiO films. On the other hand, the utilization of reactive electron beam evaporation for the synthesis of NiO films conceived an efficiency of 11.5%.[28] Thus, the usage of O_2 limits the steps toward low-cost film formation. Nevertheless, O_2 deficiency in the vacuum-processed NiO films possesses low transparency and limits the short circuit current density (J_{SC}) of PSCs.[29-31]

In this chapter, we report the engineering of a highly transparent NiO film using thermal evaporation of Ni metal followed by oxidation in a muffle furnace maintained at 580°C in an ambient atmosphere without any additional inclusion of O_2. MAPI, a light harvester in the ambient atmosphere accompanied by thermally oxidized Ni films, is utilized to fabricate PSCs. The device fabricated conceived an efficiency of 9.71% with an enhanced J_{SC} of 20.66 mA/cm^2.

6.2 Experimental details

6.2.1 Materials and reagents

Nickel (99.5%, Alfa Aesar), Lead Iodide (99.9985%, Alfa Aesar), Methylamine Hydroiodide (TCI), [6, 6]-Phenyl C_{61} Butyric Acid Methyl Ester (PCBM) (Sigma Aldrich), N, N-Dimethylformamide (DMF) (Sigma Aldrich), Dimethyl Sulfoxide (DMSO) (Sigma Aldrich), Chlorobenzene (99.8%, Sigma Aldrich), Ethanol (SRL Chem) and Isopropyl Alcohol (SRL Chem) were used as received.

6.2.2 Formation of NiO films

Fluorine-doped tin oxide coated glass (FTO) was cleaned sequentially with soap solution, DI water, acetone, and isopropyl alcohol and dried with hot air. After that, these films were loaded in the customized thermal evaporator maintained at a high vacuum of $6x10^{-6}$ Torr and treated further under an argon plasma to maintain the high purity. The masked FTO was loaded over the substrate holder and kept vertically above at a distance of 10 cm from the Ni target. The Ni target was evaporated at an optimized temperature of ~1200℃ at various times, i.e., 70, 100, and 130 sec. and identified as N70, N90, and N130, respectively. Post-evaporated Ni films were further thermally oxidized in a muffle furnace at 580℃ for 3 hours without purging O_2 gas externally into the furnace to obtain NiO thin films of various morphologies.

6.2.3 PSCs fabrication

MAPI was deposited in the ambient with a modified two-step deposition method. 1.2 M lead iodide was dissolved in 19:1 (DMF: DMSO) for optimized time and filtered through a 0.45 μm Nylon filter. Lead iodide was spin-coated on NiO films at 1500 rpm for 30 secs and further dried at 75℃ for 60 sec. Further, the lead solution was reloaded at 4500 rpm for 10 secs and dried at 75℃ for 60 secs to ensure pin-hole-free compact films. Lead iodide-coated films were dipped in methylamine hydroiodide solution in isopropyl alcohol for 20 sec (10mg/ml) to obtain reddish-brown films, which were rinsed in isopropyl alcohol to remove excess deposition and immediately spin-coated at 4500 rpm for 10 sec to form smooth, transparent films. Transparent thin films converted into reddish-brown films upon heating at 100℃ for 30 min were allowed to cool at room temperature, and PCBM solution in chlorobenzene (15mg/ml) was spin-coated at 3500 rpm for 20 sec over the perovskite layer to form the ETL. In the end, the Au was thermally evaporated through a shadow mask to form the metal contacts.

6.2.4 Characterization

Absorption spectroscopy of NiO films was recorded using a UV-Vis spectrophotometer (Shimadzu, UV-2600) to confirm the absorption and band-

edge evaluations. The morphology of pristine and perovskite over-layer loaded NiO films was confirmed using Field Emission Scanning Electron Microscopy (FESEM, JEOL, JSM-7610 F). Energy dispersive x-ray spectra (EDS, Oxford Instruments, X-Max^N) of NiO film were recorded to identify the elements in the films. The thickness of the NiO films was confirmed from AMBIOS XP-1 Profiler with a stylus tip radius of 2 microns and vertical resolution of 1Å at 10 μm. Samples were probed from the substrate onto Nickel film to obtain the film thickness. The large area 3D surface topography of oxidized films was recorded in tapping mode utilizing atomic force microscopy (AFM, PARK NX 10). Photoluminescence (PL, Dongwoo Optron DM 500i) spectra were obtained by a photoluminescence analyzer to understand the hole transfer kinetics at the perovskite/NiO interface. Current-voltage (I-V) characterization of PSCs was measured with simulated solar light conditions (Photo Emission Tech., CT50AAA) calibrated to 1 sun condition (AM 1.5G) using NREL certified silicon reference cell. All the mentioned solar cell performance values were averaged for 6 cells.

6.3 Results and discussions

6.3.1 Microstructure of NiO thin film

Thermal evaporated Ni film followed by oxidation to form NiO film is employed in the planar inverted hetero-junction PSCs. The thermally evaporated Ni film was annealed at 580°C to transform into NiO. Fig. 1 shows the surface morphology of thermally oxidized Ni film evaporated for 70, 100, and 130 sec. The optimized evaporation time of 70, 100, and 130 sec resulted in the formation of ~15, ~30, and ~35 nm thin layers, respectively, over the FTO. The keen observation of the top view FESEM image illustrates that the evaporation of the Ni target at 70 sec resulted in the formation of Ni islands-like films (Fig. 6.1(a)) over the FTO-coated glass substrate. The supply of Ni vapors with an increased evaporation time of 100 sec resulted in the formation of large numbers of islands converging to form a continuous film (Fig. 6.1(b)). Moreover, those individual islands of NiO have grown further with an increase in the evaporation time of

130 sec (Fig. 6.1(c)) and form the porous NiO thin film of nanoparticles with clearly visible textural boundaries. The formation of NiO islands over the FTO is schematically represented in Fig. 6.1(d).

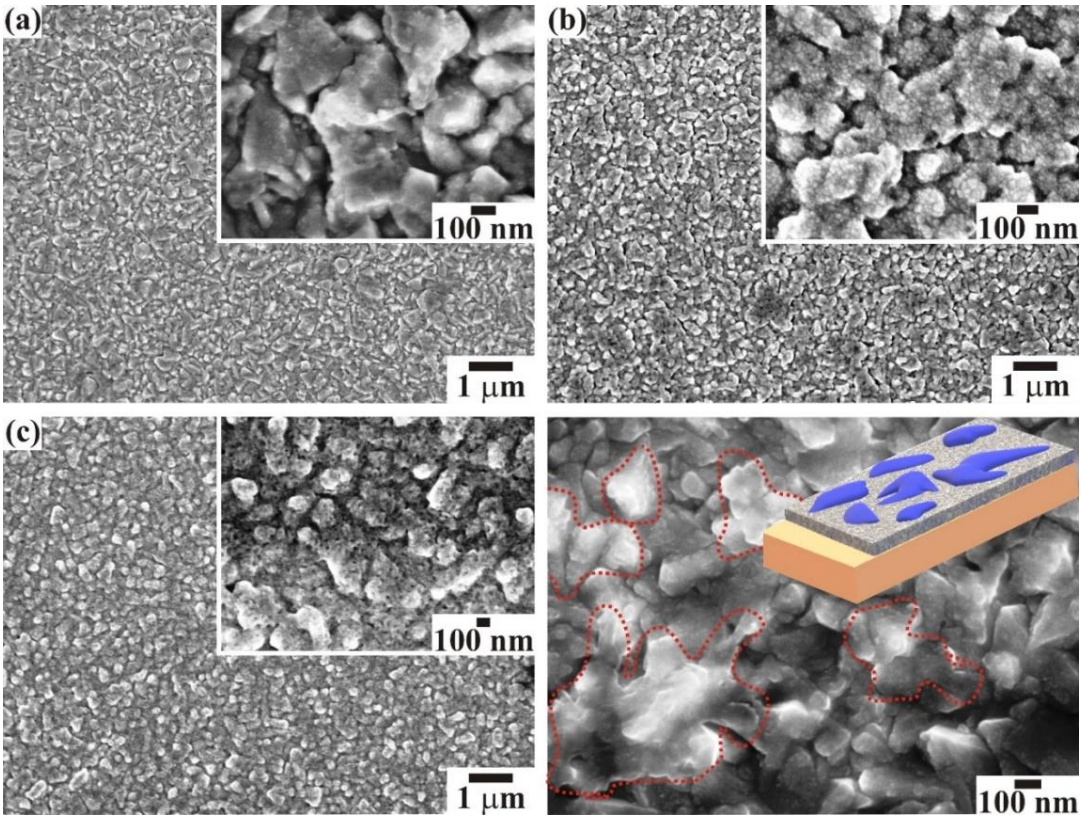

Figure 6.1 Top view FESEM images of the NiO films obtained after the oxidization of pure Ni films synthesized at an evaporation time of (a) 70 sec. (i.e., N70), (b) 100 sec (i.e., N100), and (c) 130 sec (i.e., N130). Inset shows their respective high-magnification images. (d) High-magnification FESEM image showing the growth of island-like NiO morphology (i.e., N70). Island-like morphologies are traced with dotted red lines. The inset shows the correlated schematic of island-like features of N70.

6.3.2 Energy dispersive x-ray spectroscopy

The energy dispersive x-ray spectra of the films N70, N100, and N130, were recorded to confirm the time-dependent variation in the NiO content and the presence of the elements Ni and O. Fig. 2 confirms the formation of NiO films without any impurities. The peaks of only O and Ni, along with F, Sn, and Si observed for all NiO films (Fig. 6.2(a)), confirm the absence of any kind of

impurities in the NiO films. Moreover, the intensity of the Ni peaks (Fig. 6.2(b)) increased with respect to evaporation time. The formation of the discontinued island-like growth of NiO in N70 films has resulted in a less intense Ni peak, and it increased further for N100, where the convergence of island-like features forms unbroken NiO films. The pronounced peaks of Ni and O were observed in N130 films due to a further increase in the thickness of porous NiO films. The atomic % of Ni increased to 1.6 %, 8.3 %, and 9.1 % with the time of evaporation for N70, N100, and N130, respectively. These observations confirm the increase in the quantity of NiO, which means the increase in the formation of islands and/or thickness of the NiO film. Moreover, the apparent reduction in the intensity of Sn and Si peak for the N70, N100, and N130 films with an increase in the evaporation time reconfirms the increase in the thickness of NiO film, respectively.

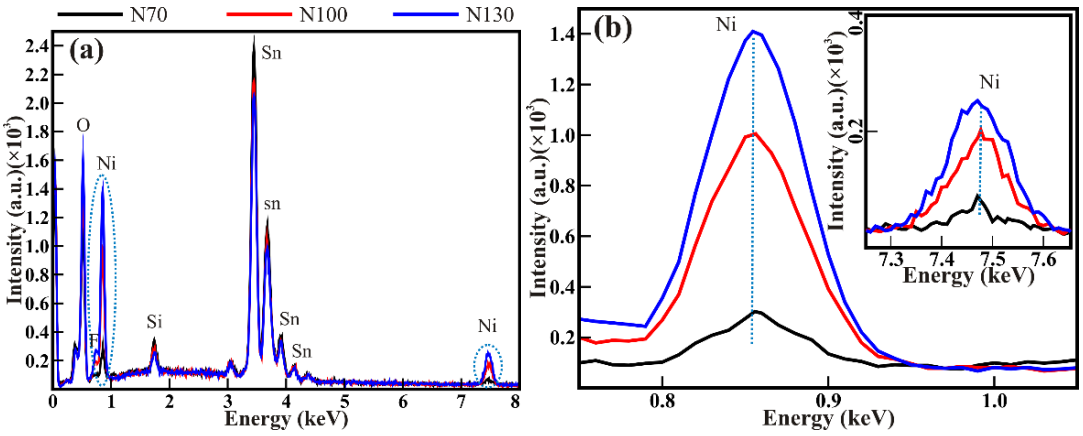

Figure 6.2 (a). EDS spectra of the oxidized N70, N100, and N130 NiO films. (b) magnified EDS spectra of the Ni peaks highlighted in figure (a) indicate the increase in NiO with an evaporation time.

6.3.3 Atomic force microscopy

The topographic images obtained by AFM in tapping mode over the area of 5 μm^2 of all oxide films developed on the FTO-coated glass substrates (Fig. 6.3). The topographic images of N70 oxide film confirm the discontinued growth of island-like features on FTO (Fig. 6.3(a)). The growth of islands of approximate width of 900 nm over the large area resulted in surface roughness

of 21.56 nm. However, the increase in the evaporation time to 100 sec illustrates the growth of more numbers of islands (Fig. 6.3(b)). The increase in the number of islands has been reflected in the better coverage over the FTO surface, with negligible change in roughness (i.e., 22.65 nm). However, the individual NiO islands have grown further for an evaporation time of 130 sec and produced a more compact appearance than N100 (Fig. 6.3(c)). The topography of N130 oxide films illustrates the formation of thin NiO film with a small increase in roughness (i.e., 22.77 nm). These observations are akin to the FESEM analysis provided in Fig. 6.1. Therefore, the proposed technique shows promise toward scaling up highly transparent NiO for their unitization in the real-time fabrication of solar cells.

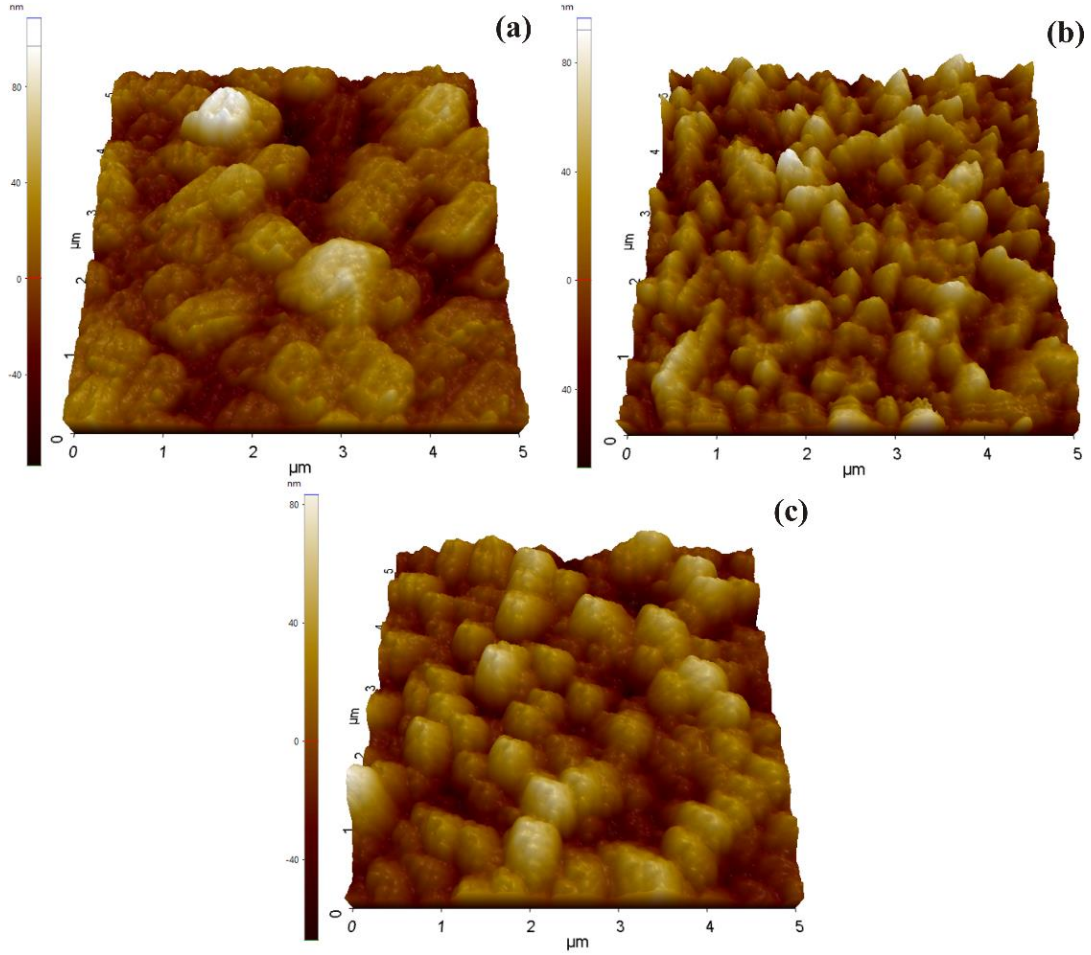

Figure 6.3 Surface topography images of the NiO films obtained after the oxidization of pure Ni films synthesized at an evaporation time of (a) 70 sec. (i.e., N70), (b) 100 sec (i.e., N100), and (c) 130 sec (i.e., N130).

6.3.4 UV-visible spectroscopy

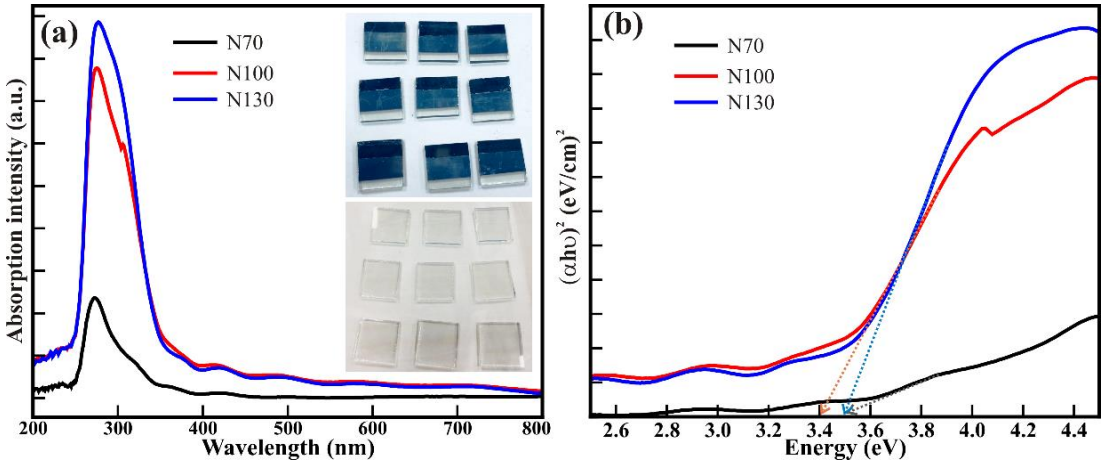

Figure 6.4 (a) UV-Vis absorption spectra and corresponding (b) Tauc's plot of oxidized Ni films. Inset to photographs in (a) shows the transformation of metallic grey Ni films into highly transparent NiO films

A thin transparent layer of NiO is one of the prerequisites to ensure the absorption of light for better solar energy conversion. Fig. 6.4(a) shows the absorption of NiO films in the ultra-violet and visible range. The thermal evaporated Ni films appear shiny grey (upper inset of Fig. 6.4(a)) and are converted into transparent NiO films (lower inset of Fig. 4(a)) after the annealing at 580°C. The film N70 showed the lowest absorption in both the visible and ultra-violet regions than that of the films N100 and N130. The island-like discontinued morphology of NiO in the film N70 has resulted in the lowest absorption in the visible range, which is further increased with an increase in the size of islands and thickness of the film in N100 and N130. Furthermore, the evaporation for 100 and 130 seconds showed significant absorption in the ultra-violate region and confirmed the increase in the thickness of the films with increased evaporation time. Thus, the highly transparent island-like morphology of N70 samples synthesized utilizing thermal evaporation in the ambient atmosphere without any inclusion of external O_2 during annealing confirms the suitability of thermal evaporation for the fabrication of low-cost solar cells. Furthermore, the bandgap of all the samples was estimated from absorption spectra. The bandgap evaluated from Tauc's plot in Fig. 4(b) is 3.48 eV, 3.40

eV, and 3.44 eV for the films evaporated at 70 (i.e., N70), 100 (i.e., N100), and 130 (i.e., N130) sec., respectively. The bandgap values obtained are in agreement with the literature [32] and again confirm the formation of NiO thin films.

6.3.5 Microstructure of perovskite over layer

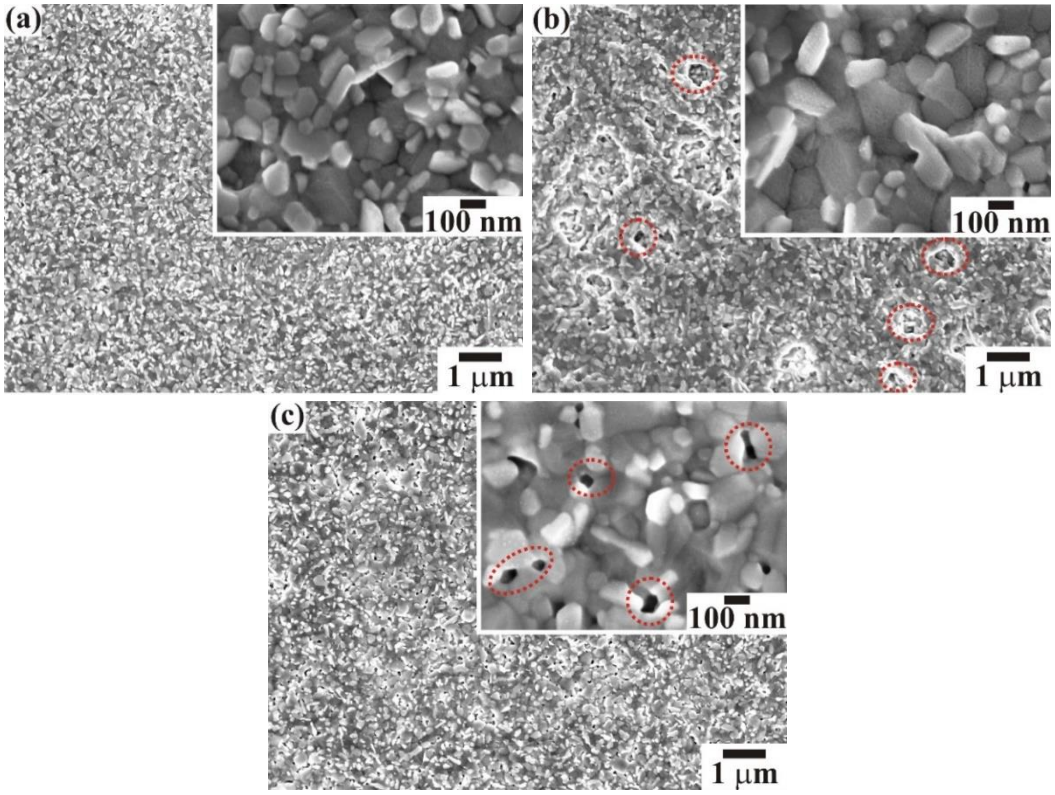

Figure 6.5 FESEM image of an overlayer of $CH_3NH_3PbI_3$ perovskite absorber coated on the (a) N70, (b) N100, and (c) N130 films. Inset shows their respective high-magnification FESEM images. Pinholes are marked with red circles.

The well-optimized transparent NiO films are further subjected to the coating of the absorber overlayer of the perovskite materials. Fig. 6.5 shows the surface morphology of the single cationic perovskite absorber overlayer coated with a modified two-step method along the surface of the NiO films. The perovskite absorbers overlayer on N70 film resulted in the complete coverage of the NiO (Fig. 6.5(a)) with uniform secondary grains due to the modified coating method used to deposit the perovskite absorber. Although a similar perovskite absorbers overlayer was formed on the N100 films, few pinholes are observed in the absorber overlayer (Fig. 6.5(b)). The number of pinholes increased further for the N130 film (Fig. 6.5(c)). The pinholes in the

perovskite absorber overlayer might be propagated from the rough and porous structure of underneath NiO film. Thus, a relatively smooth, uniform, and pinhole-free perovskite over layer on the NiO islands (i.e., N70) is the preferred texture to gain high solar energy conversion.

6.3.6 Photoluminescence spectroscopy

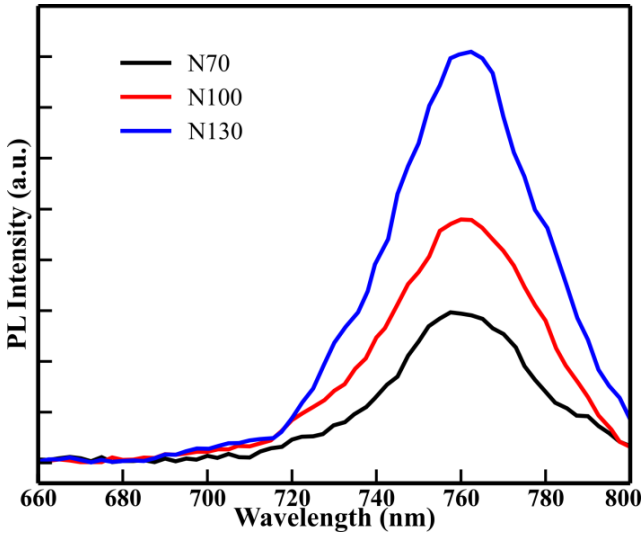

Figure 6.6 Steady-state photoluminescence (PL) spectra of $CH_3NH_3PbI_3$ perovskite absorber coated over N70, N100, and N130 films.

PL spectroscopic measurements provide insights into charge separation at the perovskite/ HTL interface. The sample preparation was done by coating the perovskite absorber over multiple NiO films. The PL peak intensities for all the samples were recorded at around 760 nm. This value is in accordance with the literature [33] confirming the formation of a MAPI perovskite absorber. The variations in the intensity of the PL peaks describe the extent of charge injection from the perovskite absorber to that of NiO films, i.e., the degree of hole quenching property of NiO films. PL intensities of perovskite absorber overlayer on the NiO thin films (i.e., N70, N100, and N130) are shown in Fig. 6.6. PL spectroscopy was used to study the carrier dynamics at the perovskite/NiO interface, i.e., the hole quenching property of NiO films. PL intensities of perovskite absorber overlayer on the NiO thin films (i.e., N70, N100, and N130) is shown in Fig. 6.6. The PL intensity has varied with the quantity and thickness of the NiO island and film. The highest intensity of PL was observed for the

N130 film, where isolated islands were converted into the porous thin film. Further reduction for the N100 film confirms the improvement in the junctions of the perovskite absorber overlayer with the discontinuous film of NiO islands. The largest quenching observed in N70 samples is assigned to the infiltration of the perovskite absorber into the island-like NiO film, increasing the effective junction area between the perovskite absorber overlayer and the NiO film. Thus, low PL intensity with N70 films indicates fast hole injection by removing an excess hole from the perovskite absorber, avoiding recombination in the absorber. A similar hole-quenching behavior is reported in spiro-MeOTAD and CuSCN, which were further observed to have a conclusive effect on the PCE.[15]

6.3.7 PV studies

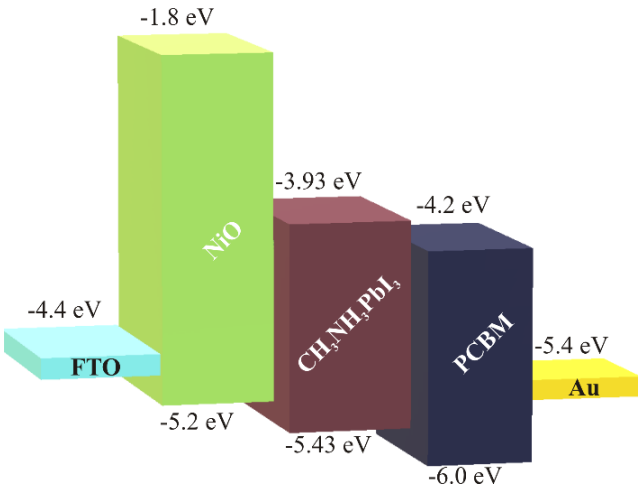

Figure 6.7 Schematic illustration of the energy band levels of the fabrication prototype solar cell.

The performance of thermally oxidized Ni metal films as an HTL in inverted PSCs was examined for the device with the configuration of FTO/NiO/MAPI/PCBM/Au. Fig. 6.7 illustrates the schematic of the energy band diagram of the solar cell encompassing the controlled NiO, MAPI, and PCBM over layers. Well-aligned energy levels of each layer facilitate the charge extraction to the external circuit. The values of energy levels of each layer considered in the schematic representation are reported in the literature.[34] The J-V measurements were performed over the active area of 0.15 cm^2 of well-

designed cells. The J-V curves of the champion cells are shown in Fig. 6.8. The higher J_{sc} observed for the film N70 has reduced further with the increase in the thickness of NiO film (i.e., N100 and N130) after illumination. The performance of the champion cells fabricated with different NiO films is given in Table 6.1. The cells fabricated of single cationic MAPI absorber overlayer coated island-like NiO film (i.e., N70) delivered the highest PCE of 9.71% with J_{SC} of 20.66 mA/cm^2, open circuit voltage (V_{OC}) of 973 mV, and FF of 48 %. The high efficiency in N70-based cells is mainly due to an optically engineered island-like film.

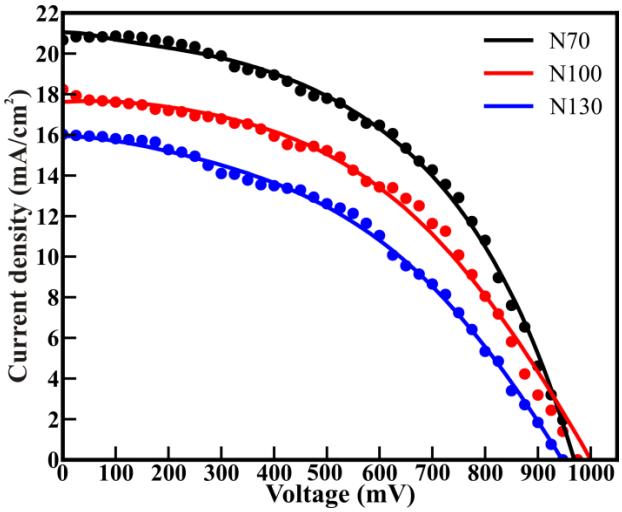

Figure 6.8 J-V curves of the champion cells consisting of $CH_3NH_3PbI_3$ perovskite absorber overlayer and NiO films, i.e., N70, N100, and N130. Solid lines in the J-V curves are guidelines for the eye.

Table 6.1 Performance parameters of champion cells consisting of $CH_3NH_3PbI_3$ perovskite absorber overlayer and NiO films.

Device	Current Density (mA/cm^2)	Open Circuit Voltage (V_{OC})	Fill Factor (%)	Efficiency (%)
N 70	20.66	973	48	9.71
N 100	18.24	975	47	8.33
N 130	16.02	947	47	6.97

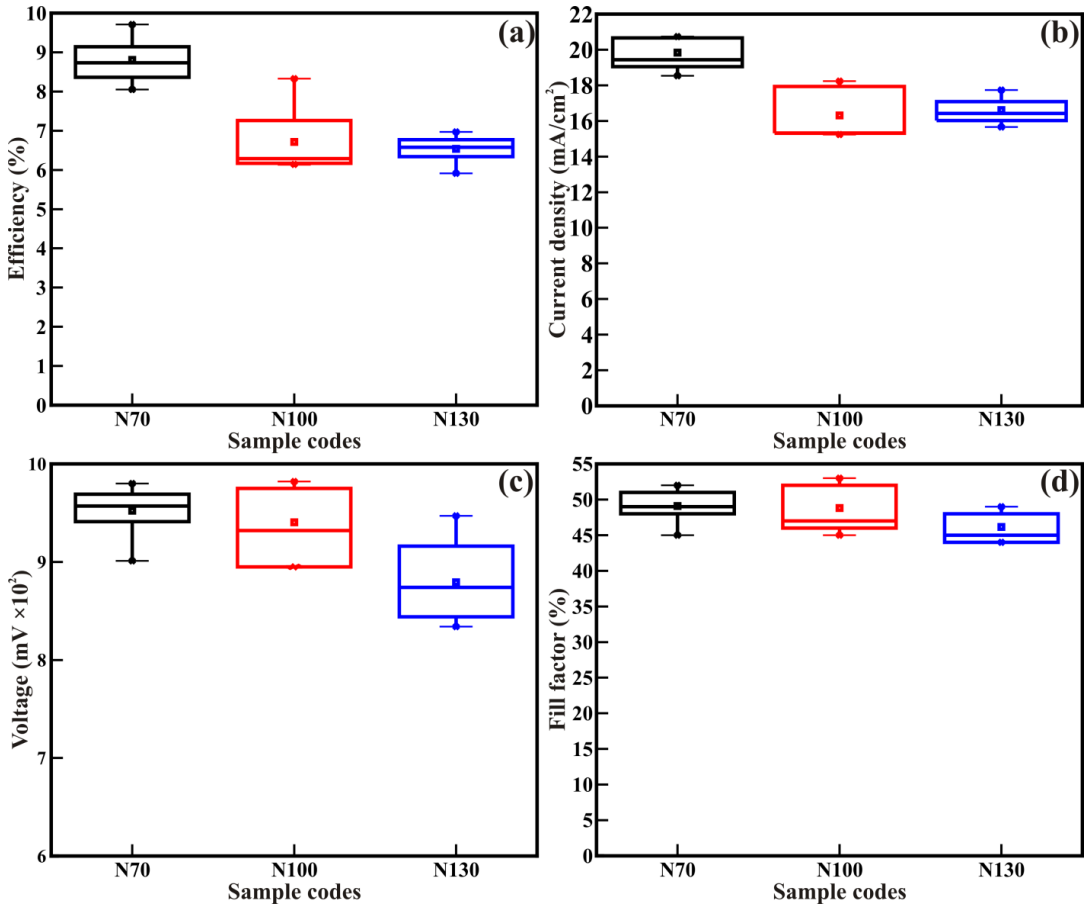

Figure 6.9 Distribution of (a) efficiency, (b) current density, (c) open circuit voltage, and (d) fill factor obtained for the 6 independent cells consisting of $CH_3NH_3PbI_3$ perovskite absorber coated N70, N100, and N130 films.

The statistic of the performance of the six independent cells consisting of NiO films, i.e., N70, N100, and N130, is represented in Fig. 6.9. The variation in efficiency for cells fabricated with various NiO films is as shown in Fig. 6.9(a). Optically managed NiO (N70) films have shown higher efficiency as compared to N100 and N130 films. The cells with N70 showed an increase of 39.3 % in PCE compared to the N130 film. The increase in efficiency is directly related to the corresponding rise in $J_{SC,}$ as shown in Fig. 6.9(b). The highest J_{SC} obtained for tailored N70 films is a resultant of its transparency in the visible region, which is 41.4 % larger than the N130 film. This high increment in J_{SC} was strategically achieved with island-like features obtained in N70 films. Further, the variation in V_{OC} for cells with different NiO films is shown in Fig. 9(c). The V_{OC} of PSCs with N70 and N100 samples remained almost akin but

decreased further with N130 films. This decrease observed in V_{OC} might be the contribution of the roughness and holes identified in the N130 film. The series resistance (R_S) and shunt resistance contribute to FF. The variation in FF for various devices is shown in Fig. 9(d). FF for all champion cells remained almost the same. The lower values of FF factors can originate from the quality of the perovskite and PCBM films deposited in ambient conditions. Therefore, a further increase in FF is possible to achieve if one fabricates the solar cells in an inert atmosphere. Further, the stability studies were performed for 144 h to understand the stability of solar cells composed of NiO, MAPI, and PCBM.

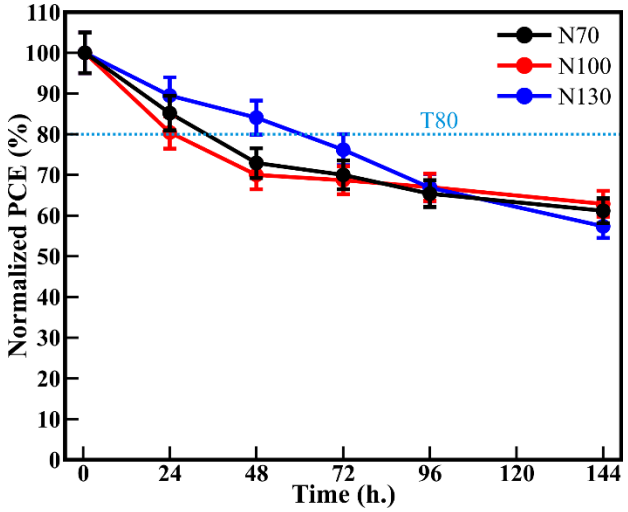

Figure 6.10 The stability study performed on the champion cells consisting of NiO, $CH_3NH_3PbI_3$, and PCBM.

Champion cells fabricated using N70, N100, and N130 oxides films were considered for stability studies. Fig. 6.10 shows the variation of normalized PCE with time. Even though all the cells fabricated in ambient conditions contain PCBM as ETL, the T80 lifetime (i.e., the time at which a solar cell operates at 80% of its initial performance)[35] of solar cells fabricated with N70, N100, and N130 oxide films is 24 hr, 34 hr, and 60 hr, respectively. Further, the measurements were performed for the next 144 hr and found a retention value of 60 % for all the devices. In the present work, thin films of NiO were accomplished by thermal evaporation of Ni metal only. The bi-layer and tri-layer of noble metals like Au or Ag [25, 26] were not engaged to enhance the conductivity of NiO. Routledge et al. [28] reported a high efficiency of 11.5 %

for NiO thin films, which were obtained by providing an in-situ O_2 atmosphere during the evaporation of the Ni target. Further, those cells were processed in an inert atmosphere with high-yield absorbers. Moreover, few recent reports on the direct evaporation of NiO compound for PSCs have employed O_2 during deposition to attain transparency.[27] However, in the present study on the use of a single cationic MAPI perovskite light absorber, the efficiency of 9.71% fits into the highest values reported with undoped NiO films obtained from the thermal evaporation of Ni followed by oxidation. Further optimization shall lead to higher performance.

6.4 Conclusion

In conclusion, Ni films were thermally evaporated at optimized evaporation times and further oxidized to form a highly transparent NiO thin film. The optimized evaporation time of 70 min leads to the formation of an island-like NiO feature without the inclusion of O_2 during both evaporation and oxidation. The increase in evaporation time has resulted in the growth of porous films at the expanses of island-like features. The NiO films show competent solar cell performance when processed with single-cation MAPI perovskite as a light absorber in an ambient atmosphere. The high transparency of the island-like NiO films and its complete coverage by perovskite absorbers overlayer resulted in the enhanced value of J_{SC} and hence in the efficiency of 9.71%. Further, the method proposed here for the formation of highly transparent metal oxide films can be extended for other inorganic transport layers helping in the optical management of the thin films to improve efficiency.

6.5 References

[1] Jung E. H., Jeon N. J., Park E. Y., Moon C. S., Shin T. J., Yang T.-Y., Noh J. H., Seo J., (2019), Efficient, stable and scalable perovskite solar cells using poly(3-hexylthiophene), Nature, 567, 511-515, (DOI: 10.1038/s41586-019-1036-3).

[2] Kojima A., Teshima K., Shirai Y., Miyasaka T., (2009), Organometal halide perovskites as visible-light sensitizers for photovoltaic cells, J. Am. Chem. Soc., 131, 6050-6051, (DOI: 10.1021/ja809598r).

[3] Kim H.-S., Lee C.-R., Im J.-H., Lee K.-B., Moehl T., Marchioro A., Moon S.-J., Humphry-Baker R., Yum J.-H., Moser J. E., Grätzel M., Park N.-G., (2012), Lead

iodide perovskite sensitized all-solid-state submicron thin film mesoscopic solar cell with efficiency exceeding 9%, Sci. Rep., 2, 591, (DOI: 10.1038/srep00591)

[4] Hao F, Stoumpos C. C., Cao D. H., Chang R. P. H., Kanatzidis M. G., (2014), Lead-free solid-state organic-inorganic halide perovskite solar cells. Nat. Photonics., 8, 489, (DOI: 10.1038/nphoton.2014.82).

[5] Ameen S., Rub M. A., Kosa S. A., Alamry K. A., Akhtar M. S., Shin H.-S., Seo H.-K., Asiri A. M., Nazeeruddin M. K., (2016), Perovskite solar cells: Influence of hole transporting materials on power conversion efficiency, ChemSusChem, 9, 10-27, (DOI: 10.1002/cssc.201501228).

[6] Malinkiewicz O., Yella A., Lee Y. H., Espallargas G. M., Graetzel M., Nazeeruddin M. K., Henk J. B., (2013), Perovskite solar cells employing organic charge-transport layers. Nat. Photonics., 8, 128, (DOI: 10.1038/nphoton.2013.341).

[7] Singh R., Singh P. K., Bhattacharya B., Rhee H.-W., (2019), Review of current progress in inorganic hole-transport materials for perovskite solar cells, Applied Mater. Today, 14, 175-200, (DOI: 10.1016/j.apmt.2018.12.011).

[8] Stranks S. D., Nayak P. K., Zhang W., Stergiopoulos T., Snaith H. J., (2015), Formation of thin films of organic-inorganic perovskites for high-efficiency solar cells, Angew. Chem. Int. Ed., 54, 3240-3248, (DOI: 10.1002/anie.201410214).

[9] Maniarasu S., Korukonda T. B., Manjunath V., Ramasamy E., Ramesh M., Veerappan G., (2018), Recent advancement in metal cathode and hole-conductor-free perovskite solar cells for low-cost and high stability: A route towards commercialization, Renew. Sust. Energy Rev., 82, 845-857, (DOI: 10.1016/j.rser.2017.09.095).

[10] Mali S. S., Hong C. K., (2016), p-i-n/n-i-p type planar hybrid structure of highly efficient perovskite solar cells towards improved air stability: synthetic strategies and the role of p-type hole transport layer (HTL) and n-type electron transport layer (ETL) metal oxides, Nanoscale, 8, 10528-10540, (DOI: 10.1039/c6nr02276f).

[11] Mousavi-Kamazani M., Salavati-Niasari M., Sadeghinia M., (2015), Facile hydrothermal synthesis, formation mechanism and solar cell application of $CuInS_2$ nanoparticles using novel starting reagents, Mater. Lett., 142, 145-149, (DOI: 10.1016/j.matlet.2014.12.014).

[12] Mousavi-Kamazani M., Salavati-Niasari M., Hosseinpour-Mashkani S. M., Goudarzi M., (2015), Synthesis and characterization of $CuInS_2$ quantum dot in the presence of novel precursors and its application in dyes solar cells, Mater. Lett., 145, 99-103, (DOI: 10.1016/j.matlet.2015.01.076).

[13] Karthikeyan V., Maniarasu S., Manjunath V., Ramasamy E., Veerappan G., (2017), Hydrothermally tailored anatase TiO_2 nanoplates with exposed {111} facets for highly efficient dye-sensitized solar cells, Sol. Energy, 147, 202-208, (DOI: 10.1016/j.solener.2017.03.049).

[14] Ramasamy E., Lee J., (2011), Ordered mesoporous Zn-doped SnO_2 synthesized by exotemplating for efficient dye-sensitized solar cells, Energy Environ. Sci., 4, 2529-2536, (DOI: 10.1039/C1EE01123E).

[15] Arora N., Dar M. I., Hinderhofer A., Pellet N., Schreiber F., Zakeeruddin S. M., Grätzel M., (2017), Perovskite solar cells with CuSCN hole extraction layers yield stabilized efficiencies greater than 20%, Science, 358, 768, (DOI: 10.1126/science.aam5655).

[16] Ganapathy V., Kong E.-H., Park Y.-C., Jang H. M., Rhee S.-W., (2014), Cauliflower-like SnO_2 hollow microspheres as anode and carbon fiber as cathode for high-performance quantum dot and dye-sensitized solar cells, Nanoscale, 6, 3296-3301, (DOI: 10.1039/C3NR05705D).

[17] Didwal P. N., Pawar K. S., Chikate P. R., Abhyankar A. C., Pathan H. M., Devan R. S., (2016), Titania sensitized with SPADNS dye for dye sensitized solar cell, J. Mater. Sci.: Mater. Electron., 27, 12446-12451, (DOI: 10.1007/s10854-016-5431-3).

[18] Jung H. S., Park N.-G., (2015), Perovskite solar cells: From materials to devices, Small, 11, 10-25, (DOI: 10.1002/smll.201402767).

[19] Rong Y., Liu L., Mei A., Li X., Han H., (2015), Beyond efficiency: the challenge of stability in mesoscopic perovskite solar cells, Adv. Energy Mater., 5, 1501066, (DOI: 10.1002/aenm.201501066).

[20] Patil R. A., Devan R. S., Lin J.-H., Ma Y.-R., Patil P. S., Liou Y., (2013), Efficient electrochromic properties of high-density and large-area arrays of one-dimensional NiO nanorods, Sol. Energy Mater. Sol. Cells, 112, 91-96, (DOI: 10.1016/j.solmat.2013.01.003).

[21] Dalavi D. S., Devan R. S., Patil R. S., Ma Y.-R., Patil P. S., (2013), Electrochromic performance of sol-gel deposited NiO thin film, Mater. Lett., 90, 60-63, (DOI: 10.1016/j.matlet.2012.08.108).

[22] Dalavi D. S., Devan R. S., Patil R. S., Ma Y.-R., Kang M.-G., Kim J.-H., Patil P. S., (2013), Electrochromic properties of dandelion flower like nickel oxide thin films, J. Mater. Chem. A, 1, 1035-1039, (DOI: 10.1039/C2TA00842D).

[23] Devan R. S., Patil R. A., Lin J.-H., Ma Y.-R., (2012), One-dimensional metal-oxide nanostructures: Recent developments in synthesis, characterization, and applications, Adv. Funct. Mater., 22, 3326-3370, (DOI: 10.1002/adfm.201201008).

[24] Qiu W., Paetzold U. W., Gehlhaar R., Smirnov V., Boyen H.-G., Tait J. G., Conings B., Zhang W., Nielsen C. B., McCulloch I., Froyen L., Heremans P., Cheyns D., (2015), An electron beam evaporated TiO_2 layer for high efficiency planar perovskite solar cells on flexible polyethylene terephthalate substrates, J. Mater. Chem. A, 3, 22824-22829, (DOI: 10.1039/C5TA07515G).

[25] Lai W. C., Lin K. W., Wang Y. T., Chiang T. Y., Chen P., Guo T. F., (2016), Oxidized Ni/Au transparent electrode in efficient $CH_3NH_3PbI_3$ perovskite/fullerene planar heterojunction hybrid solar cells, Adv Mater, 28, 3290-3297, (DOI: 10.1002/adma.201504621).

[26] Lai W.-C., Lin K.-W., Guo T.-F., Chen P., Liao Y.-Y., (2018), Efficient $CH_3NH_3PbI_3$ perovskite/fullerene planar heterojunction hybrid solar cells with oxidized Ni/Au/Cu transparent electrode, Appl. Phys. Lett., 112, 071103, (DOI: 10.1063/1.5006513).

[27] Abzieher T., Moghadamzadeh S., Schackmar F., Eggers H., Sutterlüti F., Farooq A., Kojda D., Habicht K., Schmager R., Mertens A., Azmi R., Klohr L., Schwenzer J. A., Hetterich M., Lemmer U., Richards B. S., Powalla M., Paetzold U. W., (2019), Electron-beam-evaporated nickel oxide hole transport layers for perovskite-based photovoltaics, Adv. Energy Mater., 9, 1802995, (DOI: 10.1002/aenm.201802995).

[28] Routledge T. J., Wong-Stringer M., Game O. S., Smith J. A., Bishop J. E., Vaenas N., Freestone B. G., Coles David M., McArdle T., Buckley A. R., Lidzey D. G., (2019), Low-temperature, high-speed reactive deposition of metal oxides for perovskite solar cells, J. Mater. Chem. A, 7, 2283-2290, (DOI: 10.1039/C8TA10827G).

[29] Islam M. B., Yanagida M., Shirai Y., Nabetani Y., Miyano K., (2017), NiOx hole transport layer for perovskite solar cells with improved stability and reproducibility, ACS Omega, 2, 2291-2299, (DOI: 10.1021/acsomega.7b00538).

[30] Li G., Jiang Y., Deng S., Tam A., Xu P., Wong M., Kwok H.-S., (2017), Overcoming the limitations of sputtered nickel oxide for high-efficiency and large-area perovskite solar cells, Adv. Sci., 4, 1700463, (DOI: 10.1002/advs.201700463).

[31] Pae S. R., Byun S., Kim J., Kim M., Gereige I., Shin B., (2018), Improving uniformity and reproducibility of hybrid perovskite solar cells via a low-temperature vacuum deposition process for NiO_x hole transport layers, ACS Appl. Mater. Interfaces, 10, 534-540, (DOI: 10.1021/acsami.7b14499).

[32] Al-Ghamdi A. A., Abdel-wahab M. S., Farghali A. A., Hasan P. M. Z., (2016), Structural, optical and photo-catalytic activity of nanocrystalline NiO thin films, Mater. Res. Bull., 75, 71-77, (DOI: 10.1016/j.materresbull.2015.11.027).

[33] Stoumpos C. C., Malliakas C. D., Kanatzidis M. G., (2013), Semiconducting tin and lead iodide perovskites with organic cations: phase transitions, high mobilities, and near-infrared photoluminescent properties, Inorg. Chem., 52, 9019-9038, (DOI: 10.1021/ic401215x).

[34] Park J. H., Seo J., Park S., Shin S. S., Kim Y. C., Jeon N. J., Shin H.-W., Ahn T. K., Noh J. H., Yoon S. C., Hwang C. S., Seok S. I., (2015), Efficient $CH_3NH_3PbI_3$ perovskite solar cells employing nanostructured p-type NiO electrode formed by a pulsed laser deposition, Adv. Mater., 27, 4013-4019, (DOI: 10.1002/adma.201500523).

[35] Christians J. A., Habisreutinger S. N., Berry J. J., Luther J. M., (2018), Stability in perovskite photovoltaics: A paradigm for newfangled technologies, ACS Energy Lett., 3, 2136-2143, (DOI: 10.1021/acsenergylett.8b00914).

Chapter 7

Theoretical analysis of all-oxide solar cells

7.1 Introduction

Energy harvesting is one of the major modern-day problems for attaining a sustainable future. Among the various approaches introduced, the effective harnessing of renewable solar energy can satisfy the upcoming energy demands.[1] Various photovoltaic technologies have been introduced since the discovery of crystalline silicon solar cells. The CIGS,[2] CZTS,[3] CdTe,[4], etc., established to find a better alternative to the crystalline Si solar cells, are suffering from complex processing protocols. Therefore, DSSCs [5] and organic PSCs [6, 7] introduced with heterojunctions to generate and transport carriers [8] are fascinating modern-day. Even though various encapsulation techniques are established for PSCs, the poor long-term stability has slow-down their commercialization. [9, 10] Therefore, engineering a novel light harvester that can provide both high PCE and long-term stability is of utmost importance.

Recently, spinel-structured p-type copper bismuth oxide (CBO) with AB_2O_4 formula where a 3D array of $[CuO_4]^{6-}$ distributed along the c-axis and isolated by Bi^{3+} ions show excellent panchromatic visible light absorption (E_g = ~1.5 eV).[11,12] The valence band of CBO comprising hybrid Bi(6s), Cu(3d), and O(2p) orbitals offers accelerated mobility of photogenerated charge carriers showing excellent efficiency in photocatalytic hydrogen evolution and photocatalytic organic dye-degradation applications.[13,14] The light-harvesting capability of CBO is comparable with Si and perovskite absorber material. Therefore, it is possible to achieve efficiency comparable to Si and perovskite-based solar cells (Fig. 7.1(a)). Unlike perovskite, CBO, an inorganic material, is resistant to moisture and UV degradation, which improves the long-term stability of the device. Therefore, it is necessary to evaluate the capability of CBO as a light harvester in thin-film solar cells. On the other hand, in the ABO_3 PO structures, where the A-site ion is usually a rare-earth element or an alkaline earth metal situated at the center of the lattice, the B-site ion is a transition metal positioned at the lattice corners and possesses a bandgap ranging from 1.4 to 3.8 eV. Additionally, POs offer tunable physical, chemical, and optoelectronic properties, depending on the substitution of the ions and distortion in the ABO_3 structure.[15] The POs are synthesized in numerous morphology using different techniques such as sol-gel, electrospinning, co-precipitation, hydrothermal, sonochemical, microemulsion, etc.[16] are employed in various multifunctional applications, namely

solar cells,[17,18] photocatalysis,[19] light-emitting diodes,[20] electrochemical devices,[21] etc. Moreover, POs are used in solar cells as the n-type buffer/transport layers or photoanodes to form a p-n junction. Transparency to visible spectra, compatible band energy level alignment with absorber, and minimum recombinations at the interface with absorbers are critical factors for selecting a suitable POs buffer layer for the solar cells. Among various POs buffer layers, $SrTiO_3$ (STO), $BaTiO_3$ (BTO), $SrSnO_3$ (SSO), and $BaSnO_3$ (BSO) are found suitable to fulfill the requirements of an excellent transport layer in PSCs. The maximum efficiencies obtained using these PO transport layers vary between 12-21 % in the PSCs (Fig. 7.1(b). However, the intervention of the lead iodide layer at the interface between the transport and perovskite absorber layer degrades the performance drastically. Therefore, the solar cell fabricated using CBO light harvesters with these PO buffer layers will be highly stable and environmentally friendly, unlike PSC, which is hazardous, moisture and UV sensitive, and suffer from long-term stability (Figure 1(c)).[22] Therefore, evaluating the potential of CBO light harvesters and PO buffer layers is of scientific importance. Several morphologies of CBO nanostructures are synthesized using various techniques, namely sol-gel,[23] solid-state,[24] hydrothermal,[25] electro-deposition,[24], etc. However, experimentally evaluating the performance of kusachiite solar cells with various PO buffer layers is a myriad task. Nevertheless, researchers utilize several software packages, namely finite difference time domain method (FDTD), SILVACO ATLAS, wxAMPS, AFORS-HET, etc., to simulate solar cells.[26] Among these software packages, SCAPS-1D, developed at Gent University, Belgium, offers a simulation of heterojunction and multi-junction solar cell devices. Hosen et al. simulated the capabilities of CBO as an absorber layer in thin-film solar cells with Al/FTO/CdS/CBO/Ni device architecture and estimated 26 % PCE for optimum thickness (i.e., 2000 nm) of the CBO light absorber.[27] However, complex device architecture involving the toxic metal sulfide buffer layer demotivated the scientific community to explore the practical implementation of CdS/CBO-based devices. Therefore, all oxide solar cell consisting of CBO absorber and AB_2O_4 buffer layers is of scientific importance. To our best knowledge, the CBO-based kusachiite solar cell devices comprising different buffer PO films and CBO light harvester is not yet reported in the literature.

In this chapter, we use the SCAPS-1D program to assess the potential of CBO light harvester with different POs buffer layers, namely STO, BTO, SSO, and BSO. The device configuration and schematics of the band diagram of kusachiite solar cells comprising ITO/PO/CBO/metal contacts are shown in Fig. 7.1(c). The solar cell performance parameters of the proposed kusachiite solar cells, such as PCE, V_{OC}, J_{SC}, and FF, are analyzed by varying the thickness, doping, and defect densities of the subsequent films. Additionally, several rear metal contact or counter electrode are implemented to understand its feasibility. The variation in the device performance at elevated operating temperatures is studied to gauge their real-time viability. The well-optimized kusachiite solar cells comprising the SSO buffer layer deliver a PCE of ~23%, which is competitive with its counterparts like SI, CIGS, and PSCs.

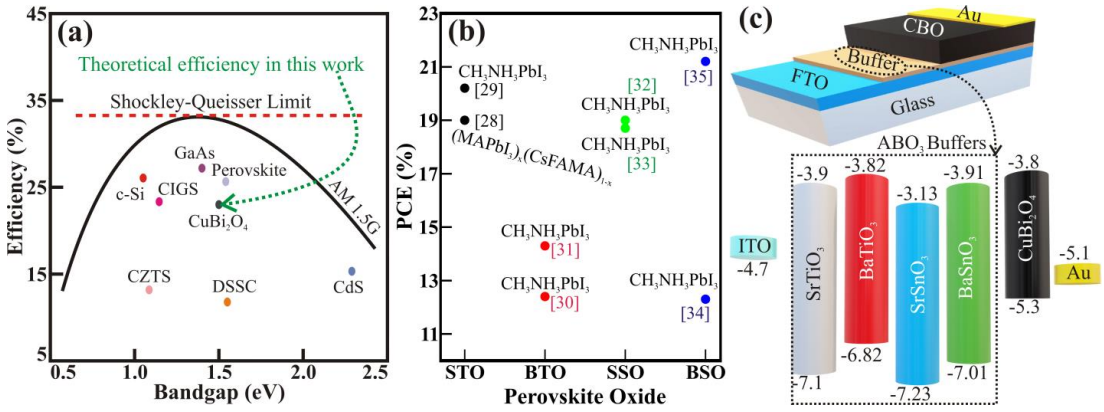

Figure 7.1 Schematics of (a) comparison of Shockley-Queisser efficiency limits of various light harvesters, (b) comparison of PCE for perovskite solar cells with different perovskite transport materials, and (c) solar device architecture (upper panel) and band alignment (lower panel) of the p-type CBO light absorber and various n-type ABO_3 buffer layers (The values in the lower panel are in eV).

7.2 Device modeling and simulation

The device architecture of all oxide solar cells with ITO/PO/$CuBi_2O_4$/Au considered in this study is shown in Fig. 7.1(c). The ITO-covered glass substrate is the transparent conducting electrode, and Au is the rear metal contact. Various n-type perovskite buffer layers are studied with a p-type CBO kusachiite light harvester. The Energy band diagram of p-type CBO with respect to the n-type PO buffer layers is shown in Fig. 7.2. The lower conduction band offset between CBO absorber and STO, BTO, SSO,

and BSO buffer layers are 0.32 eV, 0.34 eV, 0.18 eV, and 0.47 eV, respectively, offers smooth charge transportation and higher charge collection efficiency at CBO/MO interface. The lowest conduction band offset for CBO/SSO results in higher device performance for solar cells with an SSO buffer layer. The high potential barrier between the valence band maximum of CBO and STO, BTO, SSO, and BSO buffer layer of 2.22, 2.25, 2.74, and 2.05 eV, respectively, are sufficiently high to restrict the flow of positive carriers towards POs. Also, the high energy barrier minimizes recombination at the CBO/PO interface. The simulations of all oxide solar cells are carried out with AM 1.5G at an incident power density of 100 mW/cm^2.SCAPS 1D programming is an incredible asset that breaks down and reproduces heterojunction and multijunction solar cells. The fundamental semiconductor equations utilized in the SCAPS 1D programming are discussed in Chapter 2 (Eq. 2.16 to 2.20). SCAPS-1D simulation includes loading the required material and physical properties of subsequent layers of CBO and POs to solve these equations in one direction by applying boundary conditions at the interfaces. The physical and defect parameters used in the simulation of solar devices consisting of CBO and POs are tabulated in Table 7.1.

Table 7.1. The physical parameters used to analyze and optimize solar cell properties.

Parameter	**ITO**	**STO**	**BTO**	**SSO**	**BSO**	**CBO**
Bandgap Eg (eV)	3.5	3.2	9	4.1	3.1	1.5
Electron affinity χ (eV)	4	4	3.76	3.64	4.2	3.72
Dielectric constant ε	9	8.7	60	17.8	22.3	34
CB effective density of states N_c (/cm^3)	2.2×10^{18}	1.7×10^{19}	1.19×10^{20}	6.37×10^{18}	6.37×10^{18}	1.2×10^{19}
VB effective density of states N_v (/cm^3)	1.8×10^{18}	2×10^{20}	1.34×10^{20}	6.37×10^{19}	6.37×10^{18}	5×10^{19}
Thermal velocity of electrons $V_{th,e}$ (cm/s)	1×10^{7}	1×10^{7}	1×10^{7}	1×10^{7}	1×10^{7}	1×10^{7}
Thermal velocity of holes $V_{th,p}$ (cm/s)	1×10^{7}	1×10^{7}	1×10^{7}	1×10^{7}	1×10^{7}	1×10^{7}
Electron Mobility μ_n (cm^2/Vs)	20	5300	1	55.8	150	1.1×10^{-3}
Electron mobility μ_p (cm^2/Vs)	10	660	0.3	55.8	150	1.2×10^{-3}
Shallow uniform donor density N_D (/cm^3)	1×10^{18}	2×10^{16}	10^{19}	3.7×10^{18}	1.4×10^{19}	0

Shallow uniform acceptor density N_A (/cm^3)	0	0	0	0	0	3.7×10^{18}
Ref.	[36]	[37]	[38, 39]	[40, 41]	[42-44]	[27]

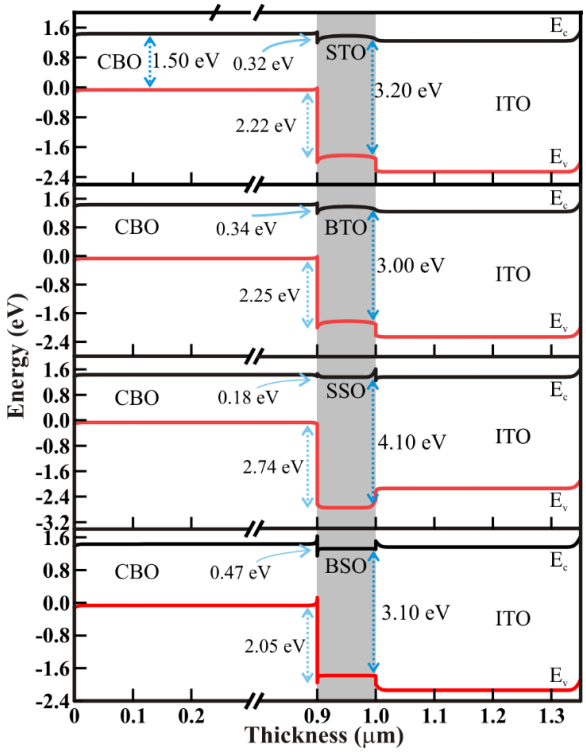

Figure 7.2 Energy band diagram of p-type CBO light absorber and various ABO_3 buffer layers utilized for kusachiite solar cells.

7.3 Results and discussions

7.3.1 Effect of CBO thickness

Optimization of the thickness of subsequent layers of thin-film solar cells is the essential criterion for achieving high performance. With all the all-physical parameters as tabulated in Table 7.1, the kusachiite CBO light harvester thickness is varied from 100 to 1400 nm. As the thickness of CBO films increases to 1400 nm, the corresponding rise in the PCE is observed for all perovskite buffer layers (Fig. 7.3), which results in a PCE of 22.53 %, 23.11 %, 23.04 %, and 20.73 % for STO, BTO, SSO, and BSO, respectively. Nevertheless, when the thickness of the CBO light harvester is increased beyond 900 nm, the PCE saturates for all perovskite buffer films. The V_{OC} of the device changed marginally with the increase in absorber thickness because the band offset

between CBO/POs is independent of the thickness of the absorber layer and does not contribute to the increment in the PCE. FF can be defined by the presence of parasitic resistance within the equivalent diode model. However, here we only changed the absorber layer thickness; the marginal change in FF should be addressed primarily as bulk-induced changes, or losses, rather than conventional parasitic changes.[45] The increase in PCE with increasing the thickness of the CBO light harvester results mainly from a corresponding rise in J_{SC} originating due to higher photogeneration in thicker CBO absorber films. However, increasing the thickness of CBO absorber films beyond their charge diffusion length will lead to carrier recombination declining performance.[46] The thin films of the CBO buffer layers can be synthesized using various thin-film techniques, but highly reproducible techniques which can be scaled up for batch processing should be considered.

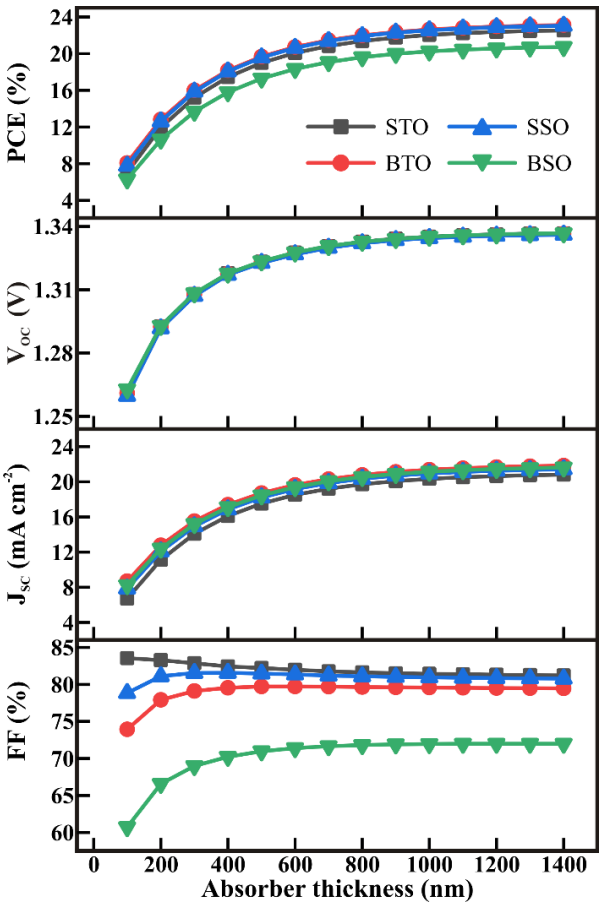

Figure 7.3 The effect of CBO light absorber thickness on the performance of solar cells comprising 100 nm thick buffer layers of various PO buffer layers.

7.3.2 Effect of PO buffer layer thickness

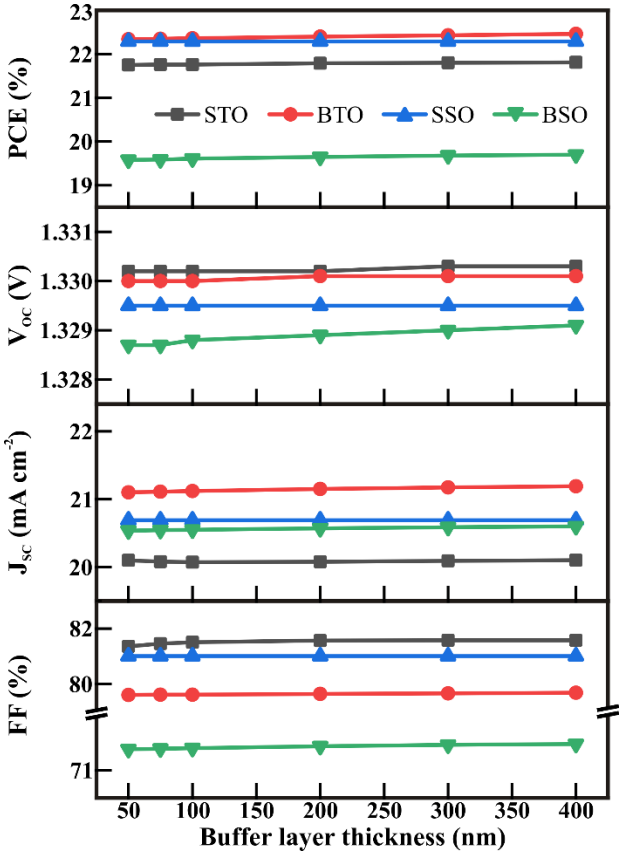

Figure 7.4 The effect of PO buffer layers thickness on the performance of solar cells with optimized 900 nm thick CBO absorber layer.

Given the experimentally feasible thin-film techniques, the thickness of the n-type PO layer is varied (with CBO 900 nm) from 50 to 400 nm (Fig. 7.4). Further increase in thickness beyond this range will lead to blinding of the irradiation striking the perovskite absorber. Moreover, a further increase in the thickness of the PO buffer layer has not affected the V_{OC}, J_{SC}, and FF of the device; thus, PCE remains unchanged. The V_{OC} and FF depend on the band offset energy level and the internal parasitic resistance, which is independent of the buffer layer thickness.[45] The POs buffer layer is transparent to visible light due to its large wide bandgap, and the increase in thickness has not shown an effect on the photogenerated charge carrier; thus, J_{SC} remains constant. However, different perovskite buffers of STO, BTO, SSO, and BSO offered PCEs of 21.81, 22.46, 22.29, and 19.7 %, respectively, at the thickness of 400 nm. The V_{OC}, FF,

and J_{SC} vary for different buffer layers depending on the intrinsic carrier conductivity and mobility.[47] Various thin-film techniques ranging from wet chemical deposition to vacuum deposition can be used to deposit PO films. However, the techniques which offer low-temperature synthesis with high uniformity and reproducibility should be adopted.[48]

7.3.3 Effect of acceptor and donor doping density

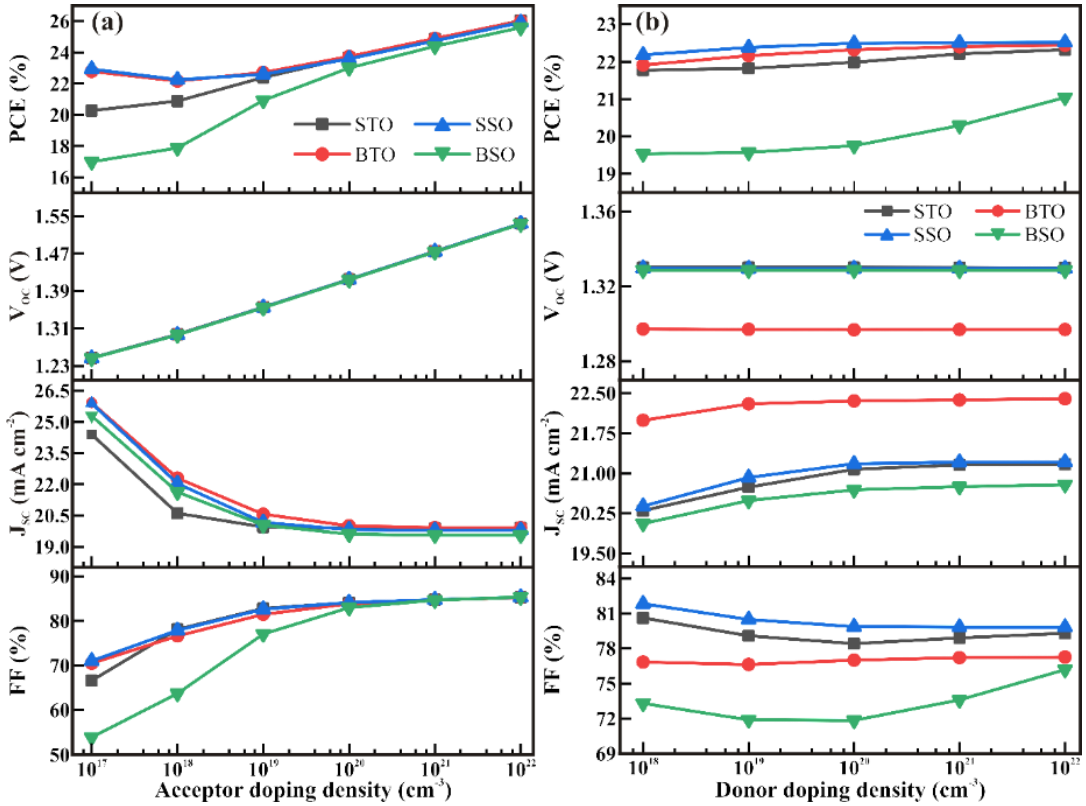

Figure 7.5 The effect of (a) acceptor doping density in CBO absorber films and (b) donor doping density in perovskite buffer films on the performance of kusachiite solar cells.

Further, to enhance the electrical properties of the p-type CBO light harvester, the acceptor density of the CBO light absorber is varied from 10^{17} to 10^{22} cm^{-3}, as shown in Fig. 7.5(a). Practically, the doping densities are controlled using suitable dopants. Various synthesis protocols can assist in increasing the doping density in both n-type POs buffer and CBO absorber layers. As the acceptor doping density increases, the PCE of the device increases for all PO buffer layers. PCEs of 26.03, 26, 25.91, and 25.59 % are obtained for STO, BTO,

SSO, and BSO, respectively, at a CBO acceptor density of 10^{22} cm^{-3}. The increase in PCE is credited to the corresponding increase in V_{OC} and FF, originating from the change in band offsets at the perovskite buffer and CBO absorber interface arising with the increase in CBO acceptor doping concentration.[49] The reduction in J_{SC} for all POs buffer films is ascribed to the higher recombination rate and a reduction in charge carrier mobility.[50]

Similar to CBO light harvester, the donor doping density in n-type PO is varied from 10^{18} to 10^{22} cm^{-3} (Fig. 7.5(b)). The donor density can be tailored by doping at the possible A or B site in the ABO_3 perovskite, which can alter the electrical, morphological, and optical properties of the compounds.[51] The donor doping density modification has shown negligible variation in PCE for most of the perovskite buffer layers. The adequate change in the PCE of the device consisting of the BSO buffer layer is attributed to the change in FF possibly arising due to the increased electrical mobility of the charge carriers in doped BSO.[52] V_{OC}, J_{SC}, and FF also remain constant with increasing the donor doping concentration of the n-type buffer layers. However, depending on the intrinsic carrier properties of the perovskite buffer layers, the variation in cell parameters is observed. Practically, the doping densities are varied by using suitable dopants. Various synthesis protocols can increase the doping density in n-type buffer and CBO absorber films.

7.3.4 Effect of bulk defect density in CBO layer

Different synthesis techniques offer distinct bulk defect densities, which play a crucial role in photogeneration and charge recombination in CBO absorbers films, influencing the performance of the device. Therefore, the bulk defect density in CBO absorber films is varied from 10^{12} to 10^{16} cm^{-3} for cells with distinct perovskite buffer layers (Fig.7. 6). The PCE declined with increased bulk defect density for all perovskite buffer layers. The reduction in J_{SC} and V_{OC} can be attributed to defect-assisted recombination in CBO absorber film and change in band offsets at perovskite buffer/CBO interface derived from the change in conduction and valence band levels of CBO films with an increase in

bulk defect density, respectively.[53] A higher defect density also reduces the lifetime of carriers, and thus the carrier diffusion length also decreases.[49] Though the FF for solar cells with STO remained constant for an unknown reason, the reduction in the FF is observed for cells with BTO, SSO, and BSO buffer layers.

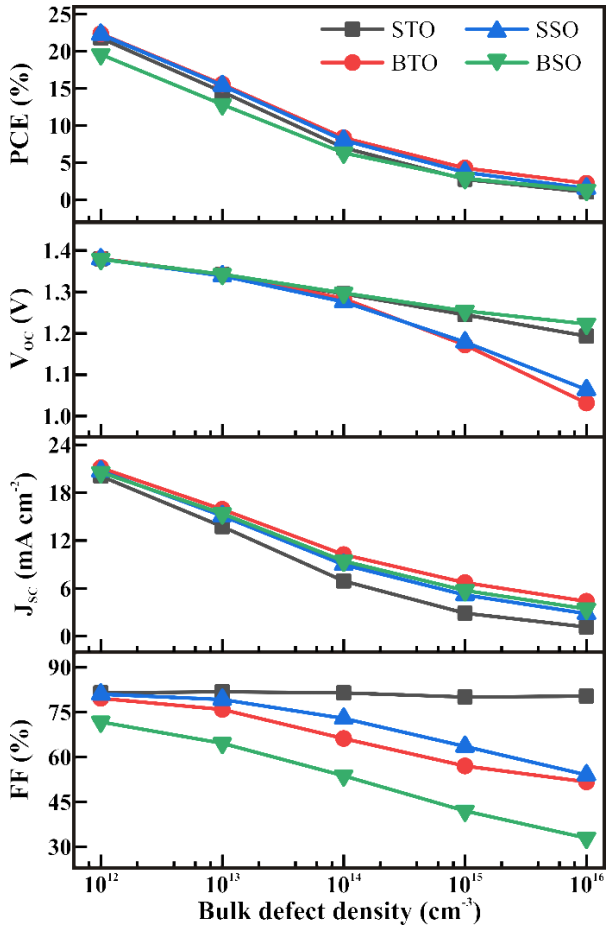

Figure 7.6 The effect of bulk defect density in CBO films on the performance of solar cells consisting of various n-type PO buffer layers.

7.3.5 Effect of interfacial defect density at CBO/PO interface

Fig. 7.7 shows the effect of variation of defect density at the CBO/PO interface on the performance parameters of the solar cell. The interfacial defect density varied from 10^{10} to 10^{12} cm^{-3} and has shown a dramatic reduction in the PCE, FF, and $V_{oc,}$ but negligible variation is observed in the J_{sc}. The increased defect density at the interface alters the energy level alignment; therefore, the V_{OC} of the device reduces. Moreover, increased interfacial defect density at the

interface alters the parasitic resistance and results in low FF. Overall, the reduction in Voc and FF instigates the deterioration of the PCE. However, the cause for the negligible variation in the J_{SC} of the device even after increasing the interfacial defect density is still unknown but can be assigned to the negligible variation in the series resistance.

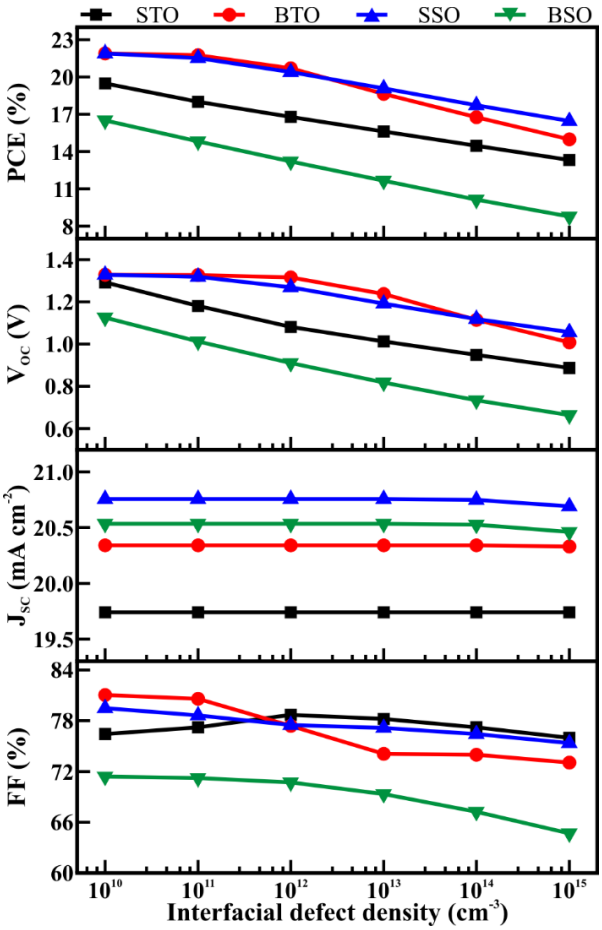

Figure 7.7 Effect of variation of defect density at CBO/PO interface on the performance of the solar cell.

7.3.6 Effect of work function of rear metal contact

The metals like Fe, Cu, Au, Ni, and Pt exhibiting distinct work functions have been explored as the counter electrode or metal back contacts for the commercial solar cells. Their conductivity, cost, and physical and chemical reactivity directly impact the cost and performance of solar cells.[54] Therefore, the effect of the work function of metal back contact on the overall performance of solar cells is explored and shown in Fig.7.8. The work function of electron-

rich metal back contact has revealed a direct influence on the performance of kusachiite solar cells. The PCE of the device with various POs increases with increasing the work function of rear metal contact. With Pt as rear metal contact, the kusachiite solar cells comprising n-type STO, BTO, SSO, and BSO buffer layers showed a PCE of 19.92, 23.57, 23.76, and 16.63 %, respectively. Corresponding V_{OC}, J_{SC}, and FF varied with increased rear metal contact work function. However, the performance parameters for all PO layers change depending on the intrinsic effective hole transfer at the interface of the metal back contacts and CBO absorber layer.[55]

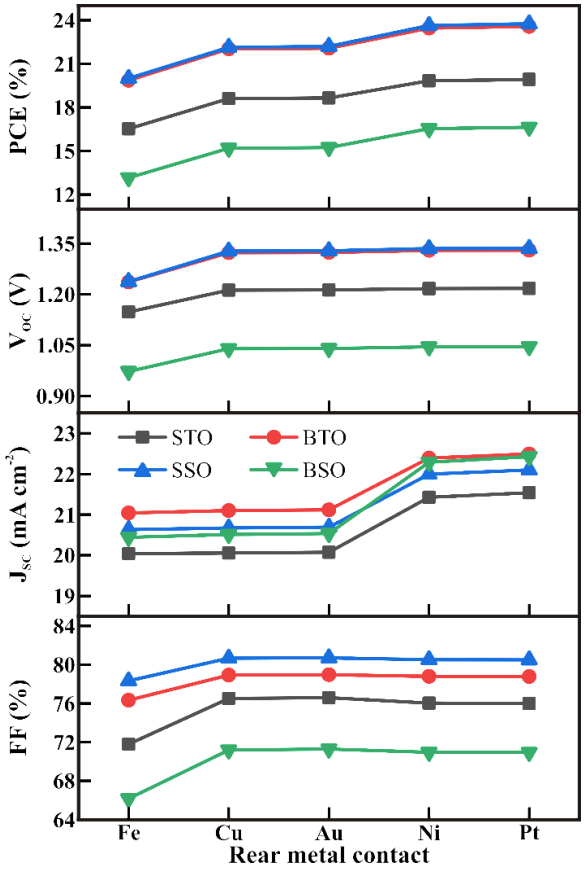

Figure 7.8 The effect of work-function of rear metal contact on the performance of device consisting of CBO absorber layer and PO buffer layers.

7.3.7 Effect of operating temperature

During the real-time application of kusachiite solar cells, elevated operating temperatures increase the stresses related to thermal expansion and thus play a noticeable part in impacting the performance of the solar cells.

Consequently, the impact of the operating temperature is examined for the temperature ranging from 300 to 380 K, and the relative simulated J-V curve is displayed in Fig. 7.9. The rise in temperature from 300 to 380 K declines V_{OC} by increasing the reverse saturation current, which decreases the PCE of the device. Though the PCE drops with the temperature rise, a reasonable higher efficiency of 20.51 % (at 380 K) is still achieved theoretically for kusachiite solar cells formed by bringing together the 900 nm thick CBO absorber and n-type SSO buffer layer of 100 nm thickness.

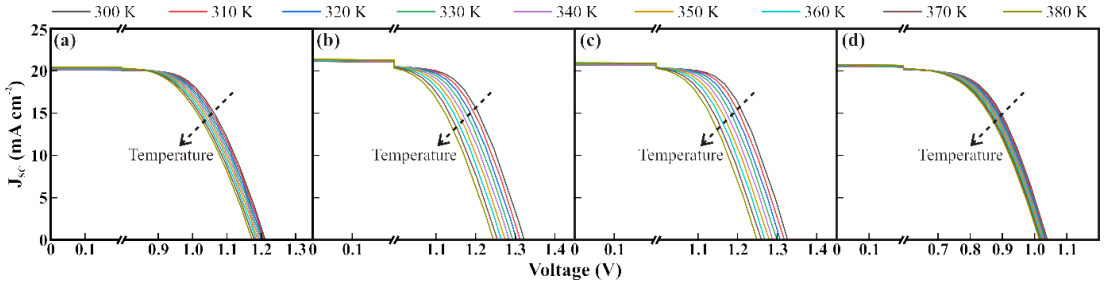

Figure 7.9 Temperature-dependent J-V curves of the kusachiite solar cells containing n-type (a) STO, (b) BTO, (c) SSO, and (d) BSO buffers layers and CBO light harvester.

7.3.8 IPCE spectra of $CuBi_2O_4$/PO based kusachiite solar cells

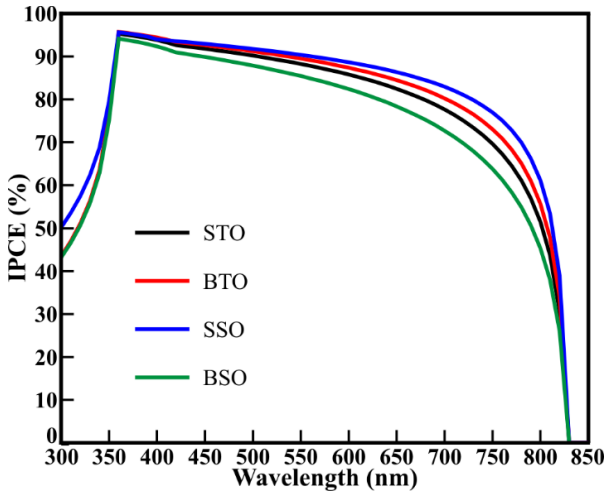

Figure 7.10 IPCE spectra of $CuBi_2O_4$-based kusachiite solar cells with various perovskite oxide buffer layers.

Evaluating the spectral response of the CBO and PO-based solar cells is crucial to understanding the incident photon to current efficiency (IPCE). Fig.

7.10 shows the IPCE of the solar cell with different PO as the buffer layer. The Higher IPCE of the device corresponds to the high performance of the solar cell. The CBO being an excellent absorber material provides a wide absorption of the visible spectra around 600-800 nm, which results in excellent IPCE (> 85 %) of the device. The slight dip around 400-450 nm is attributed to the interface with the different POs, which also helps in increasing the IPCE of the device in the UV spectrum of the irradiated light.

7.3.9 Optimum J-V characteristics of CuBi2O4/PO solar cells

The optimum solar cell parameters evaluated for the base value of acceptor density, donor density, and defect density of transport land absorber layers offering a series resistance of 5 Ω-cm^2 are shown in Fig. 7.11. CBO absorber layer based kusachiite solar cells shows high V_{OC}, J_{SC}, FF, and PCE for all ABO_3 buffer layers under investigation. The optimum PCE observed for STO, BTO, SSO, and BSO buffer layers is 18.65, 22.07, 22.19, and 15.23%, respectively. SSO based kusachiite solar cells show a marginally higher value of PCE in comparison with other PO buffer layers, which originates from their lower bandgap. Apart from the bandgap, the intrinsic charge conductance and mobility of the buffer layers decide the PCE of CBO based Kusachiite solar cells.

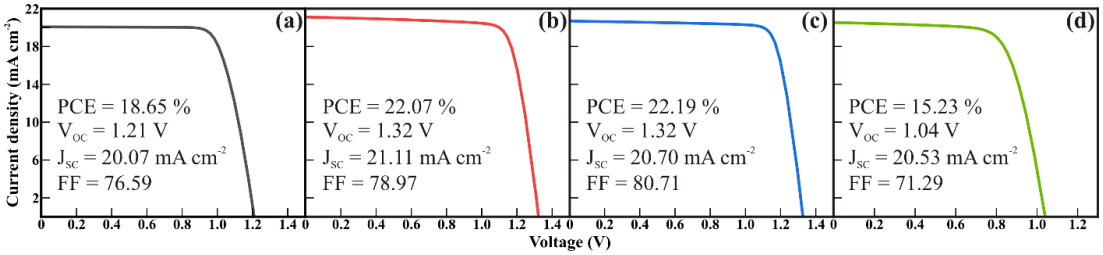

Figure 7.11 Optimum J-V of the device consisting of 100 nm thick (a) STO, (b) BTO, (c) SSO, and (d) BSO buffer layers along with an optimized CBO absorber layer of 900 nm.

7.4 Conclusion

In conclusion, kusachiite solar cells consisting of a CBO absorber and PO buffer layers are theoretically scrutinized for their best performance as visible light harvesters. Various n-type PO buffer layers of STO, BTO, SSO, and BSO are analyzed with a p-type

kusachiite CBO light harvester to theoretically evaluate (using SCAPS-1D) the performance of CBO based solar cells. We optimized different parameters like thickness, doping density, bulk defect density, and work function, which play a significant role in the performance of a practically feasible PV device. The effect of operating temperature is also studied in this simulation. All the POs buffer layers coupled with CBO absorber have shown efficiencies greater than 15 %. SSO and BTO based device has shown the maximum PCE of ~22 % among all the PO buffer layers. Therefore, this study proposes stable and economic BTO and SSO as the most promising candidate as a PO buffer layer and CBO as an absorber harvester. However, one needs to focus on using facile and economical synthesis techniques to obtain the pure phase of both n-type SSO or BTO and p-type CBO films containing minimum defect densities. Overall, this study provides the guidelines to fabricate high efficiency all oxide solar cells using CBO absorber and SSO or BTO transport layer, which can be experimentally viable, cheap, stable, and environmentally friendly.

7.5 References

[1] Panwar N. L., Kaushik S. C., Kothari S., (2011), Role of renewable energy sources in environmental protection: A review, Renew. Sust. Energy Rev., 15, 1513-1524, (DOI: 10.1016/j.rser.2010.11.037).

[2] Jeong H., Nandi R., Cho J. Y., Pawar P. S., Lee H. S., Neerugatti K. E., Kim J. H., Heo J., (2021), CZTSSe/Zn(O,S) heterojunction solar cells with 9.82% efficiency enabled via $(NH_4)_2S$ treatment of absorber layer, Prog. Photovolt.: Res. Appl., 29, 1057-1067, (DOI: 10.1002/pip.3439).

[3] Gour K. S., Karade V. C., Lee M., Jang J. S., Jo E., Babar P., Shim H., Yun J. S., Park J., Kim J. H., (2022), Engineering of interface and bulk properties in $Cu2ZnSn(S,Se)_4$ thin-film solar cells with ultrathin $CuAlO_2$ intermediate layer and ge doping, ACS Appl. Energy Mater., 5, 2024-2035, (DOI: 10.1021/acsaem.1c03569).

[4] Bista S. S., Li D.-B., Awni R. A., Song Z., Subedi K. K., Shrestha N., Rijal S., Neupane S., Grice C. R., Phillips A. B., Ellingson R. J., Heben M., Li J. V., Yan Y.,

(2021), Effects of Cu precursor on the performance of efficient CdTe solar cells, ACS Appl. Mater. Interfaces, 13, 38432-38440, (DOI: 10.1021/acsami.1c11784).

[5] Karthikeyan V., Maniarasu S., Manjunath V., Ramasamy E., Veerappan G., (2017), Hydrothermally tailored anatase TiO_2 nanoplates with exposed {111} facets for highly efficient dye-sensitized solar cells, Sol. Energy, 147, 202-208, (DOI: 10.1016/j.solener.2017.03.049).

[6] Manjunath V., Bimli S., Parmar K. H., Shirage P. M., Devan R. S., (2019), Oxidized nickel films as highly transparent HTLs for inverted planar perovskite solar cells, Sol. Energy, 193, 387-394, (DOI: 10.1016/j.solener.2019.09.070).

[7] Wadsworth A., Hamid Z., Kosco J., Gasparini N., McCulloch I., (2020), The bulk heterojunction in organic photovoltaic, photodetector, and photocatalytic applications, Adv. Mater., 32, 2001763, (DOI: 10.1002/adma.202001763).

[8] Di Giacomo F., Fakharuddin A., Jose R., Brown T. M., (2016), Progress, challenges and perspectives in flexible perovskite solar cells, Energy Environ. Sci., 9, 3007-3035, (DOI: 10.1039/C6EE01137C).

[9] Ren M., Qian X., Chen Y., Wang T., Zhao Y., (2022), Potential lead toxicity and leakage issues on lead halide perovskite photovoltaics, J. Hazard. Mater., 426, 127848, (DOI: 10.1016/j.jhazmat.2021.127848).

[10] Manjunath V., Mishra P. K., Dobhal R., Bimli S., Shirage P. M., Sen S., Shaikh P. A., Devan R. S., (2021), Perovskite-based facile $NiO/CH_3NH_3PbI_3$ heterojunction self-powered broadband photodetector, ACS Appl. Electron. Mater., 3, 4548-4557, (DOI: 10.1021/acsaelm.1c00679).

[11] Sharma G., Zhao Z., Sarker P., Nail B. A., Wang J., Huda M. N., Osterloh F. E., (2016), Electronic structure, photovoltage, and photocatalytic hydrogen evolution with p-$CuBi_2O_4$ nanocrystals, J. Mater. Chem. A, 4, 2936-2942, (DOI: 10.1039/C5TA07040F).

[12] Bhat S. S. M., Jang H. W., (2017), Recent advances in bismuth-based nanomaterials for photoelectrochemical water splitting, ChemSusChem, 10, 3001-3018, (DOI: 10.1002/cssc.201700633).

[13] [13] Mao J.-X., Wang J.-C., Gao H., Shi W., Jiang H.-P., Hou Y., Li R., Zhang W., Liu L., (2022), S-scheme heterojunction of $CuBi_2O_4$ supported Na doped P25 for

enhanced photocatalytic H_2 evolution, Int. J. Hydrog. Energy, 47, 8214-8223, (DOI: 10.1016/j.ijhydene.2021.12.133).

[14] Yang L., Quan S., Li T., Shi X., Liu C., (2020), A new La-doped $CuBi_2O_4$ catalysts for the reduction of nitroaromatic compounds and toxic organic dyes, ChemistrySelect, 5, 14935-14942, (DOI: 10.1002/slct.202003867).

[15] Sun C., Alonso J. A., Bian J., (2021), Recent advances in perovskite-type oxides for energy conversion and storage applications, Adv. Energy Mater., 11, 2000459, (DOI: 10.1002/aenm.202000459).

[16] Walton R. I., (2020), Perovskite oxides prepared by hydrothermal and solvothermal synthesis: A review of crystallisation, chemistry, and compositions, Chem. Eur. J., 26, 9041-9069, (DOI: 10.1002/chem.202000707).

[17] Liu J., Guan Y., Liu S., Li S., Gao C., Du J., Qiu C., Li D., Zhang D., Wang X., Wang Y., Hu Y., Rong Y., Mei A., Han H., (2021), Modulating oxygen vacancies in $BaSnO_3$ for printable carbon-based mesoscopic perovskite solar cells, ACS Appl. Energy Mater., 4, 11032-11040, (DOI: 10.1021/acsaem.1c01966).

[18] Purushothamreddy N., Kovendhan M., Dileep R. K., Veerappan G., Kumar K. S., Joseph D. P., (2020), Synthesis and characterization of nanostructured La-doped $BaSnO_3$ for dye-sensitized solar cell application, Mater. Chem. Phys., 250, 123137, (DOI: 10.1016/j.matchemphys.2020.123137).

[19] Li X., Zhao H., Liang J., Luo Y., Chen G., Shi X., Lu S., Gao S., Hu J., Liu Q., Sun X., (2021), A-site perovskite oxides: An emerging functional material for electrocatalysis and photocatalysis, J. Mater. Chem. A, 9, 6650-6670, (DOI: 10.1039/D0TA09756J).

[20] Huang Z., Ouyang D., Shih C.-J., Yang B., Choy W. C. H., (2020), Solution-processed ternary oxides as carrier transport/injection layers in optoelectronics, Adv. Energy Mater., 10, 1900903, (DOI: 10.1002/aenm.201900903).

[21] Samtham M., Singh D., Hareesh K., Devan R. S., (2022), Perspectives of conducting polymer nanostructures for high-performance electrochemical capacitors, J. Energy Stor., 51, 104418, (DOI: 10.1016/j.est.2022.104418).

[22] Leijtens T., Eperon G. E., Pathak S., Abate A., Lee M. M., Snaith H. J., (2013), Overcoming ultraviolet light instability of sensitized TiO_2 with meso-superstructured

organometal tri-halide perovskite solar cells, Nat. Commun., 4, 2885, (DOI: 10.1038/ncomms3885).

[23] Najafian H., Manteghi F., Beshkar F., Salavati-Niasari M., (2019), Fabrication of nanocomposite photocatalyst $CuBi_2O_4/Bi_3ClO_4$ for removal of acid brown 14 as water pollutant under visible light irradiation, J. Hazard. Mater., 361, 210-220, (DOI: 10.1016/j.jhazmat.2018.08.092).

[24] Elaziouti A., Laouedj N., Bekka A., (2016), Synergetic effects of Sr-doped $CuBi_2O_4$ catalyst with enhanced photoactivity under UVA– light irradiation, Environ. Sci. Pollut. Res., 23, 15862-15876, (DOI: 10.1007/s11356-015-4946-0).

[25] Wang Y., Cai F., Guo P., Lei Y., Xi Q., Wang F., (2019), Short-time hydrothermal synthesis of $CuBi_2O_4$ nanocolumn arrays for efficient visible-light photocatalysis, Nanomaterials, 9, 1257, (DOI: 10.3390/nano9091257).

[26] Alla M., Manjunath V., Chawki N., Singh D., Yadav S. C., Rouchdi M., Boubker F., (2022), Optimized $CH_3NH_3PbI_{3-X}Cl_X$ based perovskite solar cell with theoretical efficiency exceeding 30%, Opt. Mater., 124, 112044, (DOI: 10.1016/j.optmat.2022.112044).

[27] Hosen A., Mian M. S., Ahmed S. R. A., (2021), Simulating the performance of a highly efficient $CuBi_2O_4$-based thin-film solar cell, SN Appl. Sci., 3, 544, (DOI: 10.1007/s42452-021-04554-z).

[28] Neophytou M., De Bastiani M., Gasparini N., Aydin E., Ugur E., Seitkhan A., Moruzzi F., Choaie Y., Ramadan A. J., Troughton J. R., Hallani R., Savva A., Tsetseris L., Inal S., Baran D., Laquai F., Anthopoulos T. D., Snaith H. J., De Wolf S., McCulloch I., (2019), Enhancing the charge extraction and stability of perovskite solar cells using strontium titanate ($SrTiO_3$) electron transport layer, ACS Appl. Energy Mater., 2, 8090-8097, (DOI: 10.1021/acsaem.9b01567).

[29] Tsvetkov N., Moon B. C., Lee J., Kang J. K., (2020), Controlled synthesis of nanocrystalline Nb:$SrTiO_3$ electron transport layers for robust interfaces and stable high photovoltaic energy conversion efficiency in perovskite halide solar cells, ACS Appl. Energy Mater., 3, 344-351, (DOI: 10.1021/acsaem.9b01592).

[30] Okamoto Y., Suzuki Y., (2016), Mesoporous $BaTiO_3/TiO_2$ double layer for electron transport in perovskite solar cells, J. Phys. Chem. C, 120, 13995-14000, (DOI: 10.1021/acs.jpcc.6b04642).

[31] Luo X., Li Y., Liu K., Zhang J., (2020), Electron transport enhancement of perovskite solar cell due to spontaneous polarization of Li^+-doped $BaTiO_3$, Solid State Sci., 108, 106387, (DOI: 10.1016/j.solidstatesciences.2020.106387).

[32] Guo H., Chen H., Zhang H., Huang X., Yang J., Wang B., Li Y., Wang L., Niu X., Wang Z., (2019), Low-temperature processed yttrium-doped $SrSnO_3$ perovskite electron transport layer for planar heterojunction perovskite solar cells with high efficiency, Nano Energy, 59, 1-9, (DOI: 10.1016/j.nanoen.2019.01.059).

[33] Guo H., Zhang H., Yang J., Gong W., Chen H., Wang H., Liu X., Hao F., Niu X., Zhao Y., (2020), Lanthanum-doped strontium stannate for efficient electron-transport layers in planar perovskite solar cells, ACS Appl. Energy Mater., 3, 6889-6896, (DOI: 10.1021/acsaem.0c00978).

[34] Zhu L., Shao Z., Ye J., Zhang X., Pan X., Dai S., (2016), Mesoporous $BaSnO_3$ layer based perovskite solar cells, ChemComm., 52, 970-973, (DOI: 10.1039/C5CC08156D).

[35] Shin S. S., Yeom E. J., Yang W. S., Hur S., Kim M. G., Im J., Seo J., Noh J. H., Seok S. I., (2017), Colloidally prepared La-doped $BaSnO_3$ electrodes for efficient, photostable perovskite solar cells, Science, 356, 167-171, (DOI: doi:10.1126/science.aam6620).

[36] Rai N., Rai S., Singh P. K., Lohia P., Dwivedi D. K., (2020), Analysis of various ETL materials for an efficient perovskite solar cell by numerical simulation, J. Mater. Sci.: Mater. Electron., 31, 16269-16280, (DOI: 10.1007/s10854-020-04175-z).

[37] Singh N., Agarwal A., Agarwal M., (2021), Performance evaluation of lead–free double-perovskite solar cell, Opt. Mater., 114, 110964, (DOI: 10.1016/j.optmat.2021.110964).

[38] McCormick M. A., Slamovich E. B., (2003), Microstructure development and dielectric properties of hydrothermal $BaTiO_3$ thin films, J. Euro. Ceram. Soc., 23, 2143-2152, (DOI: 10.1016/S0955-2219(03)00022-0).

[39] Yang F., Lin S., Yang L., Liao J., Chen Y., Wang C.-Z., (2017), First-principles investigation of metal-doped cubic $BaTiO_3$, Mater. Res. Bull., 96, 372-378, (DOI: 10.1016/j.materresbull.2017.03.023).

[40] Truttmann T. K., Zhou J.-J., Lu I. T., Rajapitamahuni A. K., Liu F., Mates T. E., Bernardi M., Jalan B., (2021), Combined experimental-theoretical study of electron mobility-limiting mechanisms in $SrSnO_3$, Commun. Phys., 4, 241, (DOI: 10.1038/s42005-021-00742-w).

[41] Zhang W., Tang J., Ye J., (2007), Structural, photocatalytic, and photophysical properties of perovskite MSnO3 (M = Ca, Sr, and Ba) photocatalysts, J. Mater. Res., 22, 1859-1871, (DOI: 10.1557/jmr.2007.0259).

[42] Wang Y., Sui R., Bi M., Tang W., Ma S., (2019), Strain sensitivity of band structure and electron mobility in perovskite $BaSnO_3$: First-principles calculation, RSC Adv., 9, 14072-14077, (DOI: 10.1039/C9RA02146A).

[43] Bévillon É., Chesnaud A., Wang Y., Dezanneau G., Geneste G., (2008), Theoretical and experimental study of the structural, dynamical and dielectric properties of perovskite $BaSnO_3$, J. Phys.: Condens. Matter, 20, 145217, (DOI: 10.1088/0953-8984/20/14/145217).

[44] Sanchela A. V., Onozato T., Feng B., Ikuhara Y., Ohta H., (2017), Thermopower modulation clarification of the intrinsic effective mass in transparent oxide semiconductor $BaSnO_3$, Phys. Rev. Mater., 1, 034603, (DOI: 10.1103/PhysRevMaterials.1.034603).

[45] Liu Y., Jin B., Zhang H., Zhang Y., Kim Y., Wang C., Wen S., Xu B., Im C., Tian W., (2019), Efficiency of $MAPbI_3$-based planar solar cell analyzed by its thickness-dependent exciton formation, morphology, and crystallinity, ACS Appl. Mater. Interfaces, 11, 14810-14820, (DOI: 10.1021/acsami.9b01952).

[46] Xing G., Mathews N., Sun S., Lim S. S., Lam Y. M., Grätzel M., Mhaisalkar S., Sum T. C., (2013), Long-range balanced electron- and hole-transport lengths in organic-inorganic $CH_3NH_3PbI_3$, Science, 342, 344-347, (DOI: doi:10.1126/science.1243167).

[47] Yang D., Yang R., Wang K., Wu C., Zhu X., Feng J., Ren X., Fang G., Priya S., Liu S., (2018), High efficiency planar-type perovskite solar cells with negligible

hysteresis using EDTA-complexed SnO_2, Nat. Commun., 9, 3239, (DOI: 10.1038/s41467-018-05760-x).

[48] Lhermitte C. R., Polo A., Yao L., Boudoire F. A., Guijarro N., Sivula K., (2020), Generalized synthesis to produce transparent thin films of ternary metal oxide photoelectrodes, ChemSusChem, 13, 3645-3653, (DOI: 10.1002/cssc.202000926).

[49] Rai S., Pandey B. K., Dwivedi D. K., (2021), Designing hole conductor free tin–lead halide based all-perovskite heterojunction solar cell by numerical simulation, J. Phys. Chem. Solids, 156, 110168, (DOI: 10.1016/j.jpcs.2021.110168).

[50] Duan Q., Ji J., Hong X., Fu Y., Wang C., Zhou K., Liu X., Yang H., Wang Z.-Y., (2020), Design of hole-transport-material free $CH_3NH_3PbI_3/CsSnI_3$ all-perovskite heterojunction efficient solar cells by device simulation, Sol. Energy, 201, 555-560, (DOI: 10.1016/j.solener.2020.03.037).

[51] Mizoguchi H., Chen P., Boolchand P., Ksenofontov V., Felser C., Barnes P. W., Woodward P. M., (2013), Electrical and Optical Properties of Sb-Doped $BaSnO_3$, Chem. Mater., 25, 3858-3866, (DOI: 10.1021/cm4019309).

[52] Kim H. J., Kim U., Kim T. H., Kim J., Kim H. M., Jeon B.-G., Lee W.-J., Mun H. S., Hong K. T., Yu J., Char K., Kim K. H., (2012), Physical properties of transparent perovskite oxides $(Ba,La)SnO_3$ with high electrical mobility at room temperature, Phys. Rev. B, 86, 165205, (DOI: 10.1103/PhysRevB.86.165205).

[53] Moon M. M. A., Ali M. H., Rahman M. F., Hossain J., Ismail A. B. M., (2020), Design and simulation of FeSi-based novel heterojunction solar cells for harnessing visible and near-infrared light, Phys. Status Solidi (A), 217, 1900921, (DOI: 10.1002/pssa.201900921).

[54] Maniarasu S., Korukonda T. B., Manjunath V., Ramasamy E., Ramesh M., Veerappan G., (2018), Recent advancement in metal cathode and hole-conductor-free perovskite solar cells for low-cost and high stability: A route towards commercialization, Renew. Sust. Energy Rev., 82, 845-857, (DOI: 10.1016/j.rser.2017.09.095).

[55] Minemoto T., Murata M., (2014), Impact of work function of back contact of perovskite solar cells without hole transport material analyzed by device simulation, Curr. Appl. Phys., 14, 1428-1433, (DOI: 10.1016/j.cap.2014.08.002).

Chapter 8
Summary and conclusion

8.1 Summary and conclusion

The global energy demand will be 30 TW by 2050, which is expected to increase to 46 TW by 2100. With ever-increasing energy demand, conventional energy sources such as coal, oil, natural gas, etc., are not sustainable to reach the expectations. Therefore, renewable and sustainable energy sources need to be extensively inspected to administer future massive energy demand. Of the several available renewable energy systems, producing hydrogen fuel through water splitting and generating electricity from sunlight using PV cells are two prominent attractions to the scientific and industrial community. Likewise, photodetectors that convert photons into electrical signals attract scientists and industrialists for utilization in various modern applications. Considering the limitation of sunshine timing; the excess solar energy can be stored in the form of hydrogen fuel by putting PV panels and water electrolyzers in tandem, i.e., the electrical output from the PV panels can be fed as input to water electrolyzers to produce hydrogen fuel which can be converted back to electricity using fuel cells or internal combustion engines. Moreover, photodetectors can be used with PV panels in self-powered mode to monitor the intensity of incident solar radiations and align the PV panels for better efficiency throughput over the year. Overall, photodetectors, PV panels, and electrocatalytic hydrogen generation will be efficient approaches to sustainably serve future energy demands.

Oxides of transitional metals, namely Ti, Sn, Mn, Fe, Co, Ni, Cu, and Zn, have been utilized for water splitting, photodetection, and solar cell applications. Different doping and composite formation strategies are explored to tailor the physicochemical and electronic properties benefiting those applications. The downscaling of the transition metal oxides in various nanostructure morphological forms provide control over the defects and interface at the nanoscale. Therefore, metal oxide nanostructures are used as electrocatalysts for water splitting and the buffer layers in thin-film solar cells and photodetectors. Nevertheless, the morphology and size of the nanostructures decide the number of exposed active sites which control the efficiency during electrochemical water splitting. Similarly, the roughness, thickness, uniformity, pinholes, etc., of metal oxide thin films directly influence the photoconversion efficiency in solar cells and photodetectors. Especially in the case of metal oxide thin films, the synthesis technique and its repeatability are highly important.

Therefore, investigating the influence of morphologies of metal oxides on the efficiency of electrocatalytic water splitting is essential to improve the performance in green hydrogen generation. Various metal oxide nanostructures and their composites have been developed for electrocatalytic water splitting, but the influence of NiO nanostructure morphologies and porosity in achieving lower overpotential is not well understood. Moreover, self-powered perovskite-based PDs have attracted intense attention due to their independence, less complicated circuitry, and self-sufficient potential for device operation. These PDs depend on PV behavior to produce light current at 0 V bias, which is achieved by forming Schottky junctions with single perovskite crystals and p-i-n junctions. These materials are thermally unstable and degrade in the ambient atmosphere. This becomes a critical issue inhibiting device performance for real-time applications such as optical communication, imaging, sensing, etc. Therefore, a systematic study on degradation mechanisms and intrinsic modification within metal halide perovskite in the presence of a metal oxide, like NiO, transport layer is highly desirable.

Despite the use of MOTLs, high-efficiency PSCs are realized by using expensive organic HTLs, which trigger degradation of the perovskite layer and require an inert atmosphere for processing. Therefore, to overcome the problem of perovskite degradation, among all inorganic transport layers, NiO is found to be a more promising and important candidate for optoelectronic properties because of its excellent chemical stability. Various wet chemical techniques, namely, spin coating, blade coating, spray coating, metric rod coating, etc., are used to synthesize metal oxide thin films, but residual ligands present in it impede the performance. Although the physical deposition methods, such as atomic layer deposition, sputtering, laser deposition, etc., ensure uniformity and reproducibility of the thin films, it involves high processing costs. Therefore, synthesizing NiO thin films using industrially matured thermal evaporation will be an economical solution to the above-cited problems in PSCs. Moreover, the intervention of the lead iodide layer at the interface degrades the PCE performance drastically. The solar cell consisting of metal oxide light harvesters and buffer layers is expected to be highly stable and environmentally friendly, unlike the PSC, which is hazardous, moisture and UV sensitive, and suffers from long-term stability. Therefore, evaluating the potential of metal oxide light harvesters and PO buffer layers is of scientific importance. However, experimentally evaluating the performance of

solar cells with various buffer layers and light harvesters is a myriad task. The heterojunction and multi-junction solar cell devices simulation using the SCAPS-1D package shall give the prime information about the influence of thickness, defect/impurity levels, temperature, interfacial resistance, etc., of the selected metal oxide buffer and light harvester layers for the solar cell fabrications.

Therefore, we have addressed the following objective in this thesis work.

- Synthesis and characterization of morphology-controlled NiO nanostructures using the cost-effective technique for hydrogen and oxygen generation applications through electrocatalytic water splitting.
- The industrially scalable synthesis protocol for transparent NiO thin films to use as a transport layer in the solar cells and photodetector processed at ambient atmospheric conditions
- The influence of perovskite degradation at the interface (due to the formation of PbI_2) on the overall performance of the solar cells and photodetector.
- Simulation of heterojunction and multi-junction oxide solar cell devices consisting of various metal oxide buffers and light harvester layers to identify the best suitable combination for efficient all oxide solar cells.

Developing a single electrocatalyst effective for both oxygen and hydrogen evolution remains challenging. Although an attempt to utilize a single electrocatalyst for overall water splitting is made, there still exist several issues of efficiency and stability of the electrocatalyst. Hence, the present study reports on morphology-controlled NiO electrocatalyst, a single electrocatalyst for oxygen and hydrogen evolution (Fig. 8.1). The cubic phase NiO nanoparticles and nanoplates of diameter and thickness < 10 nm delivered surface-to-volume ratios of 0.078 and 0.083, respectively. XRD and TEM confirm the formation of NiO nanostructures, where morphology transformed independently of the chemical composition. XPS and EXAFS confirm the 2+ oxidation state of Ni ions and their octahedral coordination with oxygen. The 0D nanoparticles providing a larger surface area and active sites offered the overpotentials of 373 and 268 mV for OER and HER activity, respectively, and performed well than the 2D porous NiO nanoplates. The CA and repetitive LSV cyclic studies confirmed the excellent long-term stability of 0D NiO

nanoparticles in basic and acidic mediums during electrocatalytic water splitting reactions, owing to its increased electrochemically exposed active sites.

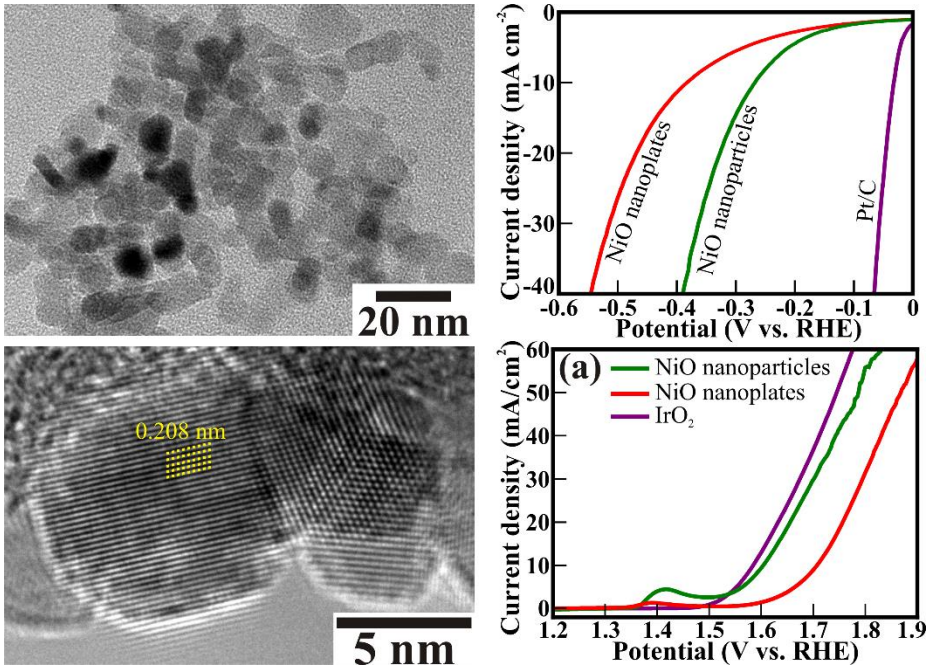

Figure 8.1 Morphology-controlled bi-functional 0D NiO nanoparticles (left upper panel) of cubic crystalline (lower left panel) phase delivered excellent electrocatalytic hydrogen (upper right panel) and oxygen (lower right panel) evaluation.

A porous 1D nanostructure provides much shorter electron transport pathways, thereby helping to improve the life cycle of the device as well as to overcome poor ionic and electronic conductivity, the interfacial impedance between electrode-electrolyte interface, and low volumetric energy density. In view of this, we report on the feasibility of 1D porous NiO nanorods comprising interlocked NiO nanoparticles as an active electrode for capturing green-house CO_2, effective supercapacitor, and efficient electrocatalytic water splitting applications (Fig. 8.2). The nanorods with size less than 100 nm were formed by the stacking of cubic crystalline NiO nanoparticles having a dimension less than 10 nm providing the necessary porosity. XPS and EXAFS confirm the presence of Ni^{2+} and octahedral coordination with O^{2-}. The SAXS profile and BET analysis showed a surface area of 84.731 m^2/g for the porous NiO nanorods. The NiO nanorods providing significant surface area and hence active surface sites offered the CO_2 uptake of 63 mmol/g at 273 K via physisorption, the specific capacitance of 368 F/g with 76.84% retention after

2500 cycles, and excellent electrocatalytic water splitting with over potential of 441 and 345 mV for OER and HER activity, respectively. Therefore, the porous 1D NiO as an active electrode shows multifunctionality toward sustainable environmental and energy applications.

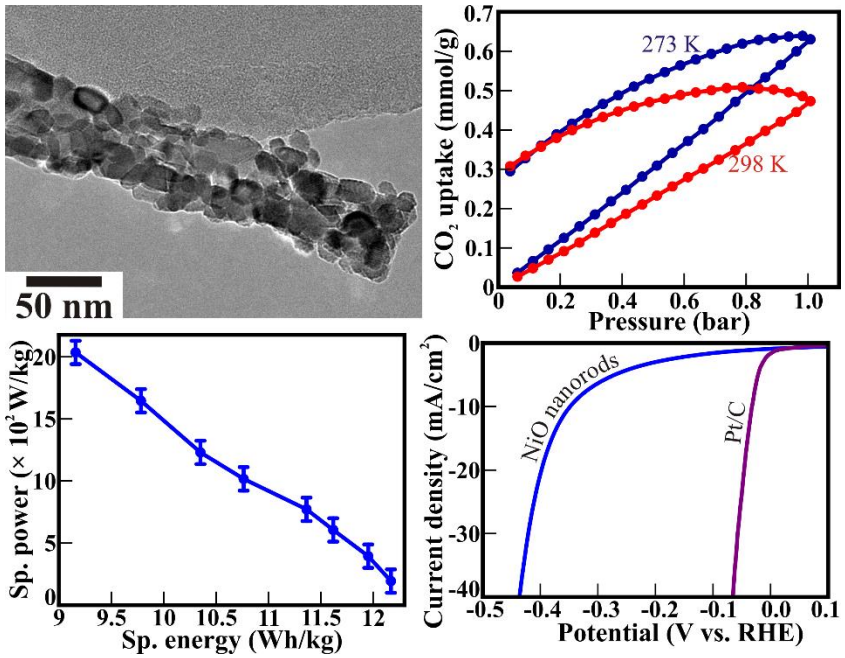

Figure 8.2 The Porous nanorods by stacked NiO nanoparticulate exhibiting corn-like structure (upper left panel) show multifunctionality towards sustainable applications in CO_2 capture (upper right panel), energy storage (lower left panel), and electrocatalytic H_2/O_2 evolution through water splitting (lower right panel).

Optoelectronic devices based on perovskite light absorbers have drawn worldwide attention owing to solution processible photovoltaic, high carrier mobility, broad spectral range, integration with a wide range of substrates, etc. A facile $NiO/CH_3NH_3PbI_3$ heterojunction was fabricated in the ambient environment for self-powered and high-performance photodetector (PD) application. The self-powered PD showed a high responsivity of 33.39 mAW^{-1} for UV light and 5.79 mAW^{-1} for white light at zero bias, which further increases up to 28.6 AW^{-1} for UV light and 29.2 AW^{-1} for white light at + 1 V. Subsequently, the detectivity for an entire region of UV light and the visible spectrum was observed to be above 10^{10} Jones at zero bias. Interestingly, the stability study in the air for PD up to 38 days revealed the highest photoresponsivity of 40.56 mAW^{-1} at zero bias (Fig. 8.3, right panel). This enhancement is attributed to the intrinsic modification within

metal halide perovskites that lead to optimized PbI_2 content. Additionally, a systematic study of XRD patterns at an interval of days revealed the presence of PbI_2 content (Fig. 8.3, left panel). Further, the photodetection ability was retained for up to 58 days with a decrease in light current without encapsulation. Our results indicate that $NiO/CH_3NH_3PbI_3$ heterojunction-based PD paves the way for ambient-friendly, high-performance, self-powered, stable optoelectronic applications.

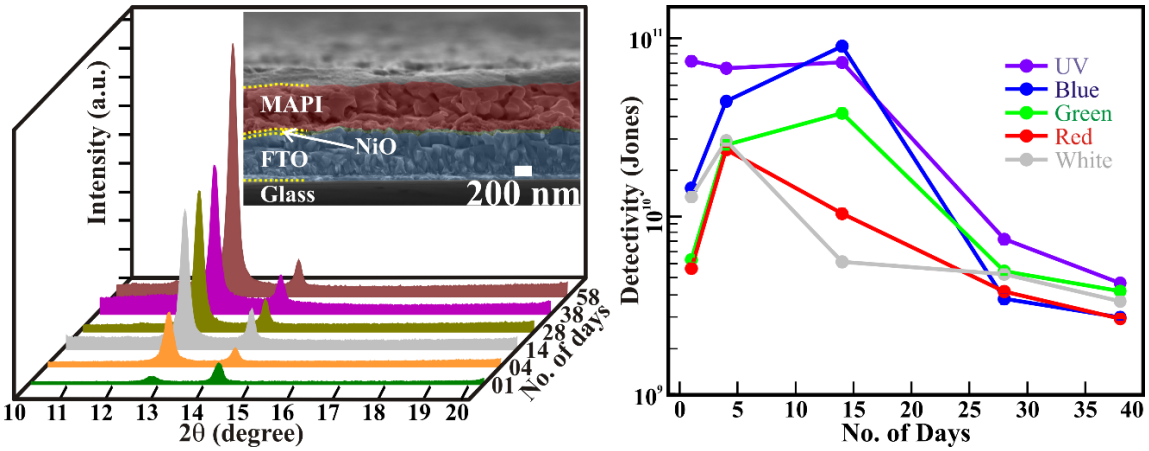

Figure 8.3 The time-dependent increase in the ratio of PbI_2 content in $CH_3NH_3PbI_3$ films (left panel), FESEM cross-sectional image depicting the facile $NiO/CH_3NH_3PbI_3$ heterojunction (left panel inset). Time and probing wavelength-dependent variation of detectivity of ambient synthesized and stored $NiO/CH_3NH_3PbI_3$ heterojunction (right panel).

Inverted planar PSCs with nickel oxide (NiO) as a hole-transporting layer were fabricated in an ambient atmosphere. Nickel (Ni) film films synthesized at optimized evaporation conditions using low-cost thermal evaporation were transformed from island-like structures to compact porous thin films of NiO after oxidation at 580°C. The formation of highly transparent NiO films without impurity was confirmed from UV-visible spectroscopy and energy dispersive x-ray analysis. These optically tailored NiO films with island-like morphology conceived minimum absorption to the visible light than that of compact porous thin films (Fig. 8.4, right panel). The NiO island-like films coated with a single cationic MAPI perovskite overlayer in ambient conditions via a modified two-step method showed higher hole quenching than the compact porous NiO thin films. PSCs consisting of NiO island-like films showed a 39.3 % improvement in PCE (Fig. 8.4, left

panel) and a 41.4 % enhancement in current density (J_{SC}) compared to the compact porous NiO thin film films. Overall, the present approach of utilizing optically engineered island-like inorganic films with a single cationic MAPI perovskite overlayer has opened up a novel approach toward the improvement of high-performance optoelectronic devices fabricated in an ambient atmosphere.

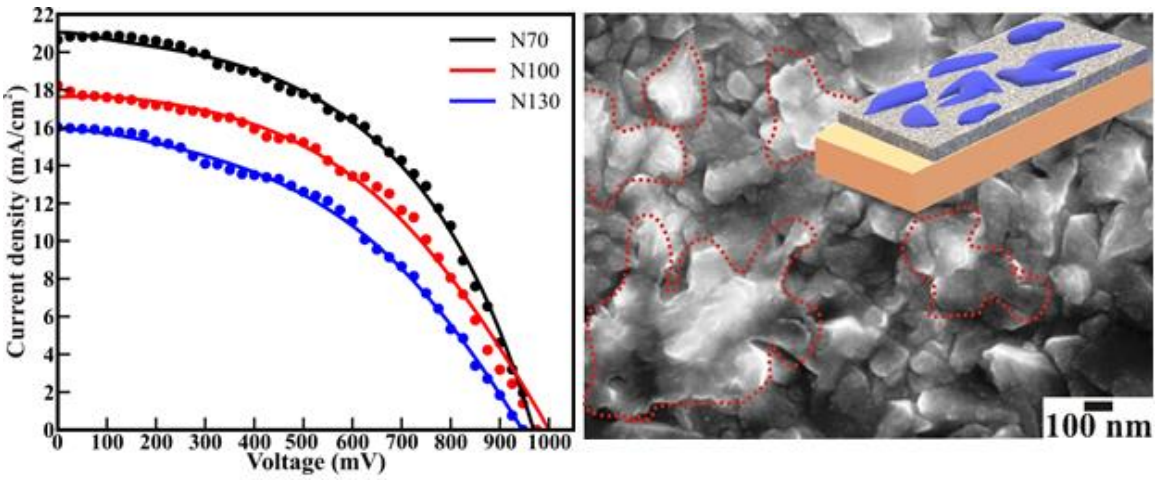

Figure 8.4 The NiO island-like films coated with a single cationic $CH_3NH_3PbI_3$ perovskite overlayer in ambient conditions (right panel) delivered 39.3 % improvement in power conversion efficiency (PCE) and 41.4 % enhancement in current density (J_{SC}) compared to the compact porous NiO thin film films (left panel).

Thin film solar cells have gained tremendous interest due to their easy processing and packaging at low costs, but most of them suffer from long-term stability. Therefore, in the quest to find a novel thin film harvester with both high efficiency and long-term stability, the capabilities of cheap and stable copper bismuth oxide or $CuBi_2O_4$ (CBO) are comprehensively investigated as an efficient light harvester (Fig. 8.5, left panel). SCAPS-1D software is used to optimize the performance of CBO-based kusachiite solar cells with various n-type ABO_3 PO buffer layers (such as $SrTiO_3$, $BaTiO_3$, $SrSnO_3$, and $BaSnO_3$) (Fig. 8.5, right panel). The variation in the thickness, doping density, and defect density of the CBO light absorber showed the utmost control over PCE and other solar cell parameters. The effect of the work function of metal back contact and operating temperature on the performance of solar cells is also analyzed to assess the real-time application of the proposed PO buffer and CBO light harvester-based kusachiite solar cells. Among all

investigated solar cell device structures, ITO/$SrSnO_3$/CBO/Au optimized in terms of thickness and doping density has shown a theoretical PCE of 22.19%.

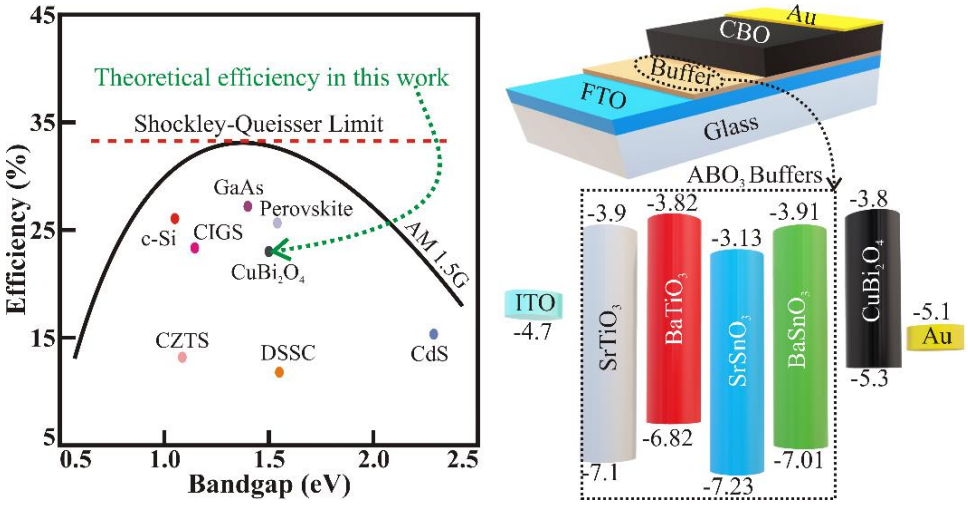

Figure 8.5 Kusachiite Solar Cells of p-type $CuBi_2O_4$ light absorber in combination with n-type perovskite oxide buffer layer achieving reasonable efficiency. The schematics of the modeled Kusachiite solar cells and the corresponding band diagram.

8.2 Future scope

The increased energy consumption will support economic development; however, it will give rise to greenhouse gas emissions and other issues, namely, environmental pollution, global warming, and other allied problems. Therefore, sustainable energy applications are the only way toward a greener future. Sustainable energy applications such as electrolytic water splitting, solar cells, photodetectors, etc., will play a prominent role in attaining zero carbon footprint. The production of green hydrogen fuel can be directly used in industries or can drive internal combustion with zero pollution to assist modern-day transport. Similarly, the output of PV panels can act as isolated sources or be integrated into existing grids which will soften the dependence on natural gas. The photodetectors can monitor and optimize the effective outcome when such renewable systems work in tandem. Therefore, one should put efforts into improving the overall performance of materials for these sustainable energy applications. The present study signifies that the pristine NiO nanostructures and thin films are excellent multifunctional materials for applications in water splitting, light sensing, and photoconversion. However, some of the key findings provide directions for future work, such as:

1. Explore the hetero-architecture of the morphology-controlled p-type NiO nanostructures with metal oxides or chalcogenides to enhance the overall splitting efficiencies.
2. Study the effect of porous 1D NiO nanostructures and conducting polymers such as polyaniline, polypyrrole, PEDOT, etc., on the overpotential for water splitting.
3. Study how the surface post-treatments of the NiO thin films control the formation of the PbI_2 layer at the NiO/perovskite interface and assist in improving the stability of photodetector and solar cells can
4. Explore the effect of transition metals doping in NiO to improve the transport phenomenon for higher efficiency PSCs.
5. Experimental investigation on the theoretically well-performing all-oxide-solar cells consisting of $CuBi_2O_4$ light harvester and suitable n-type binary metal oxides transport layer.